博士論文

Experimental study on acoustic emissions during pile penetration in sand

（砂地盤への杭貫入に伴うAE 特性に関する模型実験）

毛 無衛
MAO Wuwei

博士論文

Experimental study on acoustic emissions during pile penetration in sand

［砂地盤への杭貫入に伴う AE 特性に関する模型実験］

by

毛 無衛
Wuwei MAO

A dissertation submitted in partial fulfillment of the requirements for the degree of

Doctor of Philosophy

in

Civil Engineering

東京大学大学院工学系研究科
社会基盤学専攻
Department of Civil Engineering,
The University of Tokyo, Tokyo, Japan
September, 2015

THESIS APPROVAL

Student Name	:	Wuwei Mao
Student I.D.	:	37-127190
Institute	:	The University of Tokyo
Department	:	Civil Engineering
Laboratory	:	Geotechnical Engineering
Subject	:	Experimental study on acoustic emissions during pile penetration in sand
Submission	:	September, 2015

This is to certify that we have read this thesis and that in our opinion it is fully adequate, in scope and quality, as a thesis for the degree of Doctor of Philosophy.

Research Supervisor:

Prof. Dr. Ikuo TOWHATA _____

Prof. Dr. Junichi KOSEKI _____

Advisory Committee Members:

Prof. Dr. Taro UCHIMURA _____

Prof. Dr. Reiko KUWANO _____

Prof. Dr. Yoshiaki KIKUCHI _____

Department of Civil Engineering,
The University of Tokyo, Tokyo, Japan
September, 2015

Experimental study on acoustic emissions during pile penetration in sand

［砂地盤への杭貫入に伴う AE 特性に関する模型実験］

毛 無衛

Wuwei Mao

Ph.D. Thesis – Civil Engineering

September 2015

Supervisor: Prof. Ikuo Towhata

Prof. Junichi Koseki

ABSTRACT

This study introduces a new technique to investigate the behavior of stressed soils by means of Acoustic Emission (AE). AE refers to the energy dissipations in form of elastic waves from a stressed material, which accounts for partial or the total released energies. In case of pile installation, the sands immediately below the pile tip and around the pile shaft are stressed and the energy is dissipated due to particle sliding or crushing in the form of elastic waves. Information carried within these AE signals is supposed to provide direct insights to the subsoil response during pile penetration.

Firstly, AE testing method was applied to monitor the processes of sand crushing and sand sliding. It was found that the spectra of AE signals originated from the fracture failure of the particles is characterized by high frequency components (>100 kHz), while AE signals originated from sliding generally dominated by low frequency components. Therefore, it is possible to reveal the sand crushing process based on the high frequency AE component. This feature meets the practical demand for an easy and effective monitoring approach on the sand crushing problems.

Secondly, experiments were carried out in a pile loading system equipped with AE instrumentation. Two types of AE tests were conducted. One was aimed to capture the

AE evolution characteristics including count, amplitude and energy by using a single AE sensor attached on pile surface. The other was the localization of AE signal sources by using an eight-sensor array set around the pile tip.

Based on AE testing results, it is found that the process of pile penetration was highly distinguished by AE activities. In generally, dense ground was more emissive than loose ground. And silica sand was more emissive than coral sand. The evolution tendency of the AE count, AE amplitude and AE energy showed high similarity with load-settlement curves. The test results showed that the yield settlements obtained from both load and AE data were close. This suggests a new method of studying the yielding of soil other than the traditional stress-strain-based method.

In addition, significant difference revealed in the frequency domain of AE signals was used for distinguishing of sand crushing and sand sliding events. It is found that sand crushing occurred throughout the pile penetration process and became significant after the ground yielding. Dense ground was subjected to more crushing. This is evidenced by both AE analysis and grain size distribution analysis.

Thirdly, the AE source location were performed. This includes the development of an automatic signal arrival time determination method based on AR-AIC model, and an AE source location algorithm based on time of difference of arrival. It is found that AE sources were not uniformly distributed below the pile tip, but concentrated within a region about 0.5~1D below pile tip. AE distribution in dense ground was more concentrated, while in loose ground was more scattered. In addition, AE sources in coral sand were distributed within a more limited region, suggesting a higher level of stress concentration. Microscopic observation of subsoil below pile tip after tests showed that the sand crushing mostly occurred in the shear zone, while the compression zone immediately below the pile tip had insignificant crushing. The lower limit of sand crushing zone located approximately 1D below the pile tip. This is consistent with AE source concentration results.

Finally, the AE monitoring method was applied to the group pile testing. Two different pile spacing, 2.5D and 5D, were tested. It is found that the center pile in case of 2.5D group pile showed much higher level of AE activity compared with the corner and middle pile. While in case of 5D group pile, the center pile showed no obvious difference compared with the other piles. This suggests greater interactions between piles in case of narrower pile spacing. The effect of individual loading on the group pile behaviors was not evident in view of AE for both 2.5D and 5D group pile. It seems that

AE may not be quite effective when it is discussed in the exact values. Rather, it is more useful to reveal certain transition point (e.g. ground yielding) where significant changes of AE activity can be identified.

The AE features revealed herein provide new insights into the energy dissipation of subsoil subjected to pile load. The features of energy dissipation is closely related with the ground bearing capacity development. The characteristics of subsoil behaviors revealed in the current study including extent of crushing as well as the location of crushing can be further utilized to modify the traditionally developed pile bearing theories, e.g. the cavity expansion theory, to achieve a better prediction of the pile bearing capacity. Potential application of the technique to field pile monitoring is promising as well.

Keywords: Acoustic emission; pile; yielding; sand crushing; FFT; TDOA.

ACKNOWLEDGEMENTS

I would like to express my deepest appreciation to my supervisor Prof. Ikuo Towhata, for his consistent encouragement and valuable guidance during these past three years. The completion of this thesis would not be possible without his full support since the beginning of this topic. Prof. Towhata is a lively, enthusiastic and energetic man. His rigorous academic attitude as well as the generous hospitality outside the academic environment will continue inspiring my future life.

My sincere gratitude also goes to Prof. Junichi Koseki, my co-advisor, who guided me with his insightful suggestions about the research. Our long and stimulating discussions have greatly deepen my understanding of soil mechanics, and enhanced the achievement of this thesis.

I express my grateful thanks to the members of my research advisory committee Prof. Yoshiaki Kikuchi (Tokyo University of Science), Prof. Reiko Kuwano and Assoc. Prof. Taro Uchimura for their enlightening discussions and constructive comments. I am grateful that they took time out of their busy schedules to be part of the evaluation committee. Assoc. Prof. Taro Uchimura is especially acknowledged for his help in solving issues related to the sensors used in this research.

I also appreciate Dr. Shigeru Goto, my team leader in pile group, for his great support and help during the preparation of AE instrumentation. It is really a great time for us working together.

Special thanks to Mr. Shogo Aoyama, my research partner and best friend in Japan, for all the help regarding my research and my daily life during all these three years. My PhD study could not have been so smooth without his kind help. I wish him a happy life and bright future.

My special appreciation goes to Dr. Nana Yoshimitsu, who helped me without any reservation concerning acoustic emission techniques. Her kindness made it possible for me to proceed my research smoothly.

I would like to thank all members in geotechnical lab who helped to conduct my model pile tests. Special appreciation is extended to Takaki Matsumaru sensei, Mr. Junya

Tanaka (Fudotetra Corparation), Doctoral student Chuang Zhao, Yulong Chen, Jirat Teparaksa for their assistance whenever it was required.

Special appreciation is extended to my senior lab members Dr. Hongling Tian, Dr. Bangan Liu, Dr. Xuefeng Nong, Dr. Fangwei Yu, Dr. Hailong Wang, Dr. Rouzbeh, Dr. Yolanda Alberto, Monoi, Masahide Otsubo, Luki Danardi, from whom I learned research skills covering a wide range of topics in the field of geotechnical engineering.

My years in Univ. of Tokyo would not have been the same without the friendship of my fellows from geotechnical/Koseki/Kuwano lab, especially Sunshine, Duyen, Ghani, Ahmad Naveed, Ali Falak, Shintaku, Gunji, Tanaka, Usama, Aoyagi. Special thanks to Yang Yang, for the company and friendship shared with me to achieve the successful completion of this thesis.

I would like to thank my host family in Japan, Dr. Koji Ohta, for his generous kindness and support during my stay. His guidance has broaden my eyes to the people, scenery, food and traditional cultures of Japan.

Many thanks are extended to administrative staff of Civil Engineering Department, Foreign Student Officers and Japanese Language teachers for their guidance and support during my stay in Japan. Special appreciate is also extended to Ms. Hirano, secretary of Geotechnical Laboratory, who always took care of administrative matters related to my research and travel.

My three years at the University of Tokyo were made possible by the scholarship funded by the Ministry of Education, Culture, Sports, Science & Technology (MEXT) of Government of Japan, which is greatly acknowledged.

I have received continuous encouragement and love from my family members in China, my parents and my sisters, to whom I would like to dedicate this thesis

Finally, I would like to thank everybody who has been an important part during my stay in Tokyo. It has been a memorable experience that I could not have successfully completed without every single help from you.

Thank you all, and may we meet again!

Wuwei Mao

September 2015

Tokyo, Japan

TABLE OF CONTENTS

LIST OF FIGURES

LIST OF TABLES

CHAPTER 1

DISSERTATION OVERVIEW

1.1. PROBLEM STATEMENT

Pile foundations are extensively used in modern infrastructural constructions in order to provide a better performance in ground bearing capacity or displacement behavior. The practice of pile foundation design basically relies on the determination of the bearing capacity of the pile shaft or pile groups. In general, current design guidelines estimate the ground bearing capacity from either in-situ testing or theoretical calculations based on laboratory testing, combined with empirical modifications by considering local ground conditions and foundation types. An accurate prediction of pile bearing capacity requires a profound understanding of the underlying mechanisms governing the behavior of piles in sand. However, up to now, it is still a subject of great uncertainty in foundation design to determine the bearing capacity of piles in sand. Despite various modification approaches were established in order to correlate the testing parameters (e.g. the cone resistance q_c) to the end-bearing resistance (q_b) of a pile. Nevertheless, the bearing mechanism of the subsoil exhibits complicated cluster of situations which are not well understood, thus the proposed correlations have inevitably been confronted with unreliability, and some of the criteria are even not consistent with the physical processes involved. Therefore, there is an ongoing demand to clarify the mechanism of subsoil behaviors and the inner interactions between the pile and the surrounding soils.

Traditionally, pile studies focus on the load settlement measurement. However, such approaches provide only a general information on the soil bearing capacity which is not sensitive to the inner grain-level response of the soil, and consequently, difficult to reveal the mechanism of the gradual straining process during the pile loading. In

addition, previous pile tests have revealed the importance of particle crushing in evolution of pile tip resistance. It is also difficult to use traditional method to evaluate the onset and extent of crushing. In this study, an idea to monitor the subsoil and location of most stress/strain developed by using acoustic emission monitoring is presented. AE refers to the energy release from stressed materials. As a non-destructive method, AE testing has been successfully applied to the fracture process in rocks, composite materials and concretes. It is generally observed that the impending failure of the tested specimen is featured by an increasing rate of AE activity. In case of pile installation, the sands immediately below the pile tip and around the pile shaft are stressed and the energy is dissipated due to particle sliding or fracture in form of elastic waves. Information carried within these AE signals is supposed to provide direct insights to the subsoil response during pile penetration. This study is an attempt to deepen the current understanding of subsoil response under pile loading.

1.2. AIMS & OBJECTIVES

This research is aimed towards developing the fundamental understanding of AE in stressed soils with reference to pile loading conditions. Clear and comprehensive understanding of the source and characteristics of AE activity during pile penetration are illustrated. The crushing of particles in evolution of pile tip resistance is studied by means of AE as well. In general, the main objectives of this study can be outlined as follows;

- Explore the frequency characteristics of AE signals from crushing and sliding.
- Explore the AE evolution behavior during pile penetration.
- Explore the effects of soil type/condition on AE activities.
- Explore the feature of AE activity and its relationship with ground yielding.
- Explore the locations of AE signals by a multiple sensor array, which includes developing of :
    a. An automatic signal onset pick up algorithm based on Auto-Regressive/ AIC Model
    b. A three-dimensional AE source localization algorithm based on Time Difference of Arrival (TDOA)

- Extend the AE monitoring to group pile conditions.

1.3. SCOPE OF WORK AND LIMITATIONS

The scope of this research encompasses comprehensive studies to explore the activities of AE associated with soil density, soil yielding and soil crushability, as well as the locations of the AEs aiming to reveal the stress/strain localization. The objective of this research is to explore the pile bearing mechanism using AE correlating. Hence, it is firstly desired to explore the evolution tendency of the AE activity during pile penetration. A series of tests have been conducted with different types of sand and different density conditions. In order to have an insight into the sand crushing, a separate study is required to explore the frequency features originating from source of crushing and sliding. The finding was subsequently applied to analyze the sand crushing behavior during pile penetration. At last, another series of experiments was conducted to localize the position of generated AE below a penetrating pile tip. Based on the above results, an integrated understanding of subsoil reaction subjected to pile penetration can be obtained.

Due to the limitation of time, findings of this research could not be expanded to other aspects which may better represent the in-situ ground conditions, such as anisotropy, water content effect and wave attenuation. In addition, the pile end bearing mechanism revealed herein is derived from indirect analysis based on AE activity and its locations. Validity of said findings in actual pile penetration conditions is yet to be done.

1.4. UNIT SYSTEM

The SI system of measurement units, acronymically known as “International System of Units” was employed for this study. Following the usual sign convention adopted in soil mechanics, stresses and strains in compression were designated as positive, whereas those in tension were represented as negative.

1.5. THESIS ORGANIZATION

Considering the desired objectives and scope of this research work, the thesis is arranged in nine chapters providing a detailed overview of the work done and the main findings of this research program. A broad outline of the thesis is as follows.

Chapter 1 is an introduction of this research, and provides a broad synopsis of this research. The research curriculum is elucidated by discussing in detail, the problem statement and its significance, objectives and specific aims as well as the scope of work and its limitations.

Chapter 2 provides a brief review of previous studies related to subsoil behavior subjected to pile loading. Followed by an introduction of AE testing, a brief review made on AE testing in the field of geotechnical engineering.

Chapter 3 presents the detailed description of the experimental setup employed for this study.

Chapter 4 describes the overall research methodology. The physical properties of test material, detailed experimental plan and step by step procedure for the performance of each type of experiment are outlined in this chapter.

In Chapter 5 the frequency characteristic of AE signals originating from source of sand particle crushing and sliding are studied. A detailed description of AE generating from the process of sand crushing and sand sliding is outlined in this chapter. Signal discrimination based on dominant frequency characterizing is suggested.

Chapter 6 summarizes the results of AE testing during a series of tests concerning two different types of sand as well as different ground conditions. Detailed descriptions of AE evolution during loading and unloading, sequential loading and insights into sand particle crushing are outlined.

In Chapter 7, the results of AE source location tests on different ground conditions are presented and the corresponding insights on pile bearing mechanism are discussed.

Chapter 8 extends the application of AE testing method to the group pile conditions.

Finally, Chapter 9 summarizes the conclusion drawn from this research along with the associated recommendations for future studies.

CHAPTER 2

LITERATURE REVIEW

2.1. REVIEW ON SUBSOIL BEHAVIOR SUBJECTED TO PILE LOADING

Pile foundation is extensively used in modern infrastructural constructions in order to provide a better performance in ground bearing capacity or displacement behavior (Poulos and Davis 1980). During pile foundation design, the bearing capacity of the pile shaft or pile groups is one of the key governing parameters. In general, current design guidelines estimate the ground bearing capacity from either in-situ tests or theoretical calculations based on laboratory testing, combined with empirical modifications by considering local ground conditions and foundation types. However, up to now, it is still a subject of great uncertainty in foundation design to determine the bearing capacity of piles in sandy ground (Foray et al. 1998; Zhang and Chen 2012; Burlon et al. 2014). Despite various modification approaches were established in order to correlate the testing parameters (e.g. the cone resistance *Qc*) to the end-bearing resistance (*Qb*) of a pile. Nevertheless, the bearing mechanism of the subsoil exhibits complicated cluster of situations which are not well understood, thus the proposed correlations have inevitably been confronted with unreliability, and some of the criteria are even not consistent with the physical processes involved (Randolph et al. 1994). Therefore, there is an ongoing demand to clarify the mechanism of subsoil reactions and the inner interactions between the pile and the surrounding soils (Randolph, 2003).

Establishing the stress and strain conditions developed around the pile tip are crucial to improve the understanding of pile bearing mechanism. In some recent studies, several attempts have been made to investigate the subsoil behavior adjacent to the pile tip.

Jardine et al. (2009, 2013a, 2013b) deployed dozens of soil stress sensors in sand to measure the vertical, radial and circumferential stresses around a closed-ended model pile (Figure 2.1). It was observed that the stress was concentrated and emanated from the pile tip, and a high-level of stress existed for sand located within ten radii of the pile. Despite a number of sensor used, it should be noted that such measurement was based on point tracing, and consequently further interpolation was required to estimate the stress condition of other positions. Particular, for soils immediately below the pile tip, such measurement becomes extremely difficult.

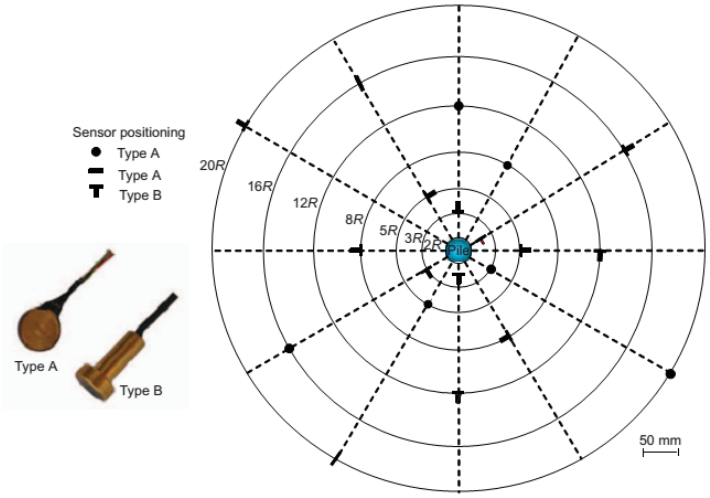

Figure 2.1 Soil stress sensors at one level (Jardine et at. 2013)

Ekisar et al. (2012) used the X-ray CT to investigate the soil arching of pile foundation. As a non-destructive technique, it is possible to examine the load distribution of a target region quantitatively. Therefore, the effect of load transfer inside the ground subjected to external load was able to be observed. It is evident from his study that the soil arching in a reinforced embankment system with rigid pile foundation can be visualized.

The image correlation technique, commonly applied in fluids experiments to infer the flow field (Willert and Gharib 1991, Adrian 2005), allows real time observation of particle trajectories, which has also been recognized as an efficient method for investigation of granular materials (Sadek et al. 2003, White et al. 2001, White et al. 2003, Rechenmacher 2006). White and Bolton (2004) applied the Particle Image Velocimetry (PIV) method to investigate the ground settlement and strain path development in a pile penetration test. The PIV results provided a direct vision of sand

particle movement through a transparent window, and the displacement field of soil around the pile can be observed (Figure 2.2). Similar method was also adopted by Arshad et al. (2014) to investigate the soil behavior during cone penetration.

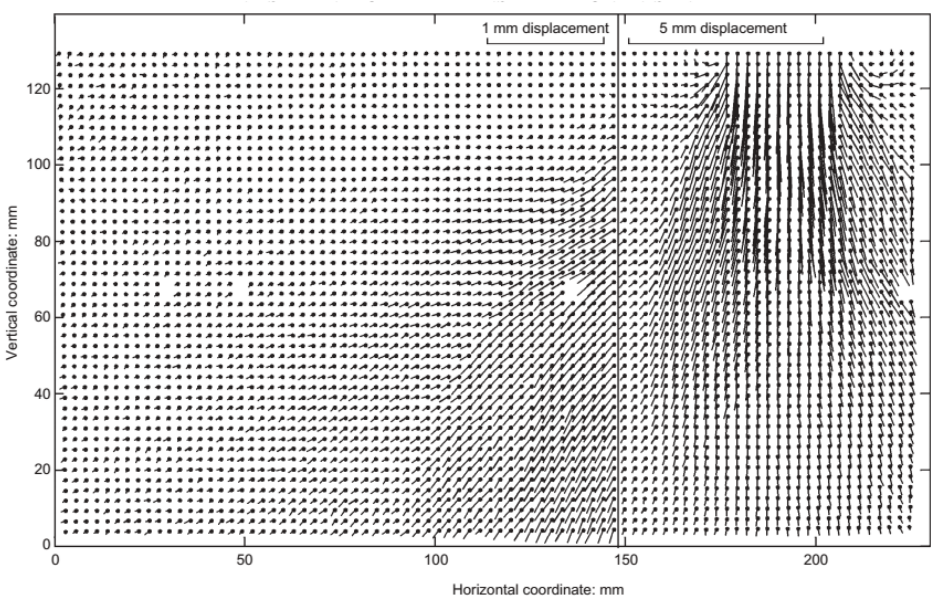

Figure 2.2 Displacement filed of sand around pile tip (White and Bolton, 2004)

2.2.PARTICLE CRUSHING DURING PILE PENETRATION

The mechanical property of highly stressed sands is one of the fundamental concerns in soil mechanics. It is commonly recognized that particle breakage becomes remarkable in highly stressed soils related to particle crushability, and will eventually affect the mechanical behavior of the materials (Casini et al., 2013). In the field of geotechnical engineering, such a kind of situation is involved in various engineering processes, e.g. the footing of large dams or embankments (Sadrekarimi, 2012), and soils around pile end (Jardine et al., 2013a, b; Yasufuku and Hyde, 1995), or natural hazard processes, e.g. particle fragmentation during rockslides (Imre, 2010). Breakage of particulate materials has become one of the most intractable topics in geoscience (Einav 2007).

Many attempts have been made to quantify the degree of crushing and evaluate the effect of particle crushing on the mechanical behavior of granular materials. For example, it is found that particle crushing has significant influence on shear strength,

dilatancy, stress path, friction angle and critical state of the tested samples (Lade and Yamamuro, 1996; Hyodo et al., 2002; Sadrekarimi and Olson, 2010; Carrera et al., 2011). However, it should be noted that the particle breakage factors used in the above studies were mostly based on the modification of grain size distributions (GSD) before and after the tests, either based on a specific grain size or the full range size distributions (Hardin, 1985; Lade et al., 1996). Such measurements are difficult to be preferred as a routine methodology for process monitoring, since only the ultimate conditions of particle crushing can be investigated, and consequently, the onset and crushing rate development that happen inside the soils remain unclear (Marketos and Bolton, 2007).

The effect of sand crushing on the bearing capacity of piles is most likely to act in term of a changed value of friction angle. Sadrekarimi and Olson (2010) performed ring shear tests to observe shear band formation and correlated it with particle crushing. It was found that the mobilized friction angle increased after very large share displacements (critical state). They argued that this may because of a more uniform particle size distribution and more angular and rougher particles produced due to crushing. In contrast, at smaller shear displacement, the friction angle decreased due to compensated dilation by crushing induced contraction.

Yu (2014) quantitatively evaluated the effect of particle crushing and resultant variation of friction angle by a series of high pressure triaxial tests. The results showed that the friction angle of the original sand (silica No.5, same material as used in the current study) decreased with increasing particle crushing (Figure 2.3). It was also found that dilatancy had more significant effect on the friction angles under lower confining pressure, as can be seen from CD tests in Figure 2.3 that under 0.2Mpa confining pressure, friction angle showed a larger reduction compared with 0.5Mpa confining pressure condition.

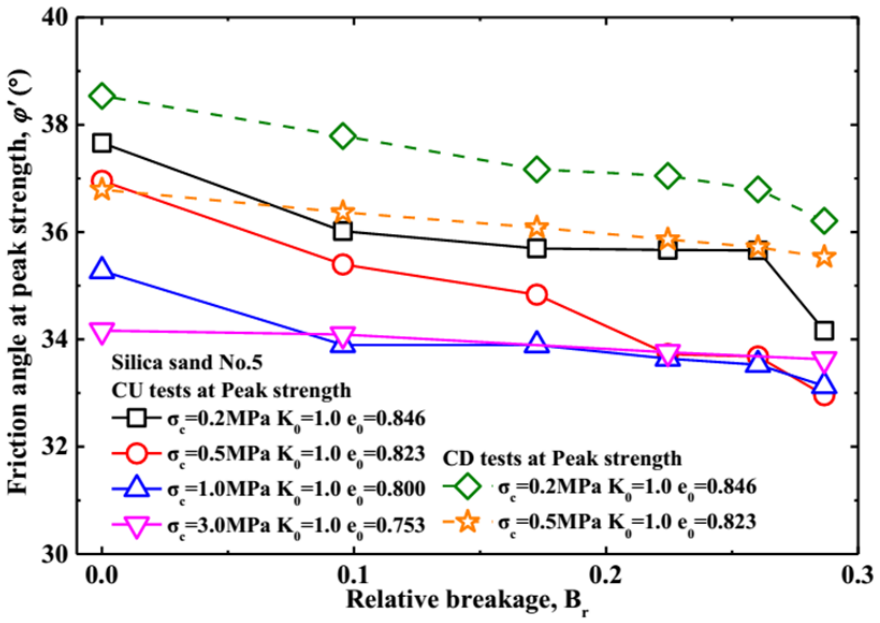

Figure 2.3 Friction angle at peak against relative breakage factor (Yu 2014)

Attempts have also been made to evaluate the effects of particle crushing on pile end bearing capacity. Kuwajima et al. (2009) conducted model pile tests on carbonate sand and silica sand to evaluate the pile bearing capacity and soil crushability. It was found that under higher confining pressure, substantial increasing of bearing capacity was found for silica sand. In contrast, the bearing capacity of carbonate sand ceased increasing due to considerable crushing (Figure 2.4). Consequently, it is believed that the friction angle is reduced by carbonate sand crushing (Dogs Bay sand in figure below is carbonate sand).

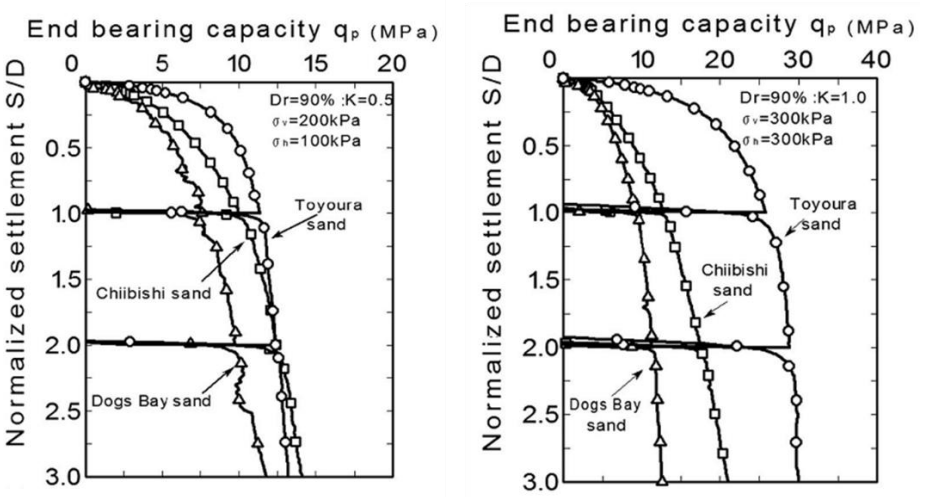

Figure 2.4 Pile end bearing capacity-settlement behaviors for different sands at high and low stress level (Kuwajima et al. 2009)

In theoretical analysis, Yasufuku et al. (1995) used the spherical cavity expansion method to predict the end bearing capacities of piles by considering soil crushability. The reduced rigidity index was used to compute the decreased bearing capacity by taking account of soil compressibility, which is related to soil crushability. However, such relation is empirically determined through laboratory tests by linking the volumetric strain and the internal friction angle of the soils. Therefore, the extent of soil crushing was not directly evaluated.

Zhang et al. (2012, 2014) developed a new model based on particle breakage mechanics theory for calculating end bearing capacity of piles in crushable soils. The proposed method, initially formulated by Einav (2007a, 2007b), described the evolution of the grain size distribution due to particle crushing with only physically meaningful parameters. The key point was connecting the Grain Size Distribution (GSD) modification with breakage energy dissipation by introducing a breakage factor *B*. The current GSD: ($F(x,B)$) was a linear combination of the initial $F_0(x)$ and the ultimate GSD: $BF_u(x)$;

$$F(x,B) = (1-B)F_0(x) + BF_u(x) \tag{2-1}$$

The accurate determination of breakage factor *B* in the above formula is important to ensure promising results. In reality, the breakage of soil is closely related to its stress condition as well as the geometry of the crushing zone.

White and Bolton (2004) reported a "nose cone" beneath the pile tip (Figure 2.5). They argued that the soils within the "nose cone" underwent severest crushing. Yang et al. (2010) classified the crushing zone into three zones based on the stress conditions of each zone (Figure 2.6). The soils in the shear band subjected to extreme normal and shear stress underwent highest crushing rate, followed by the non-shear band zone with high normal stress (significant crushing) and reduced normal stress (moderate crushing). Due to the cone-shaped pile end, the crushing status of sand immediately below a flat ended pile was not observed. A debatable point lies in the shear zone located around the pile side. According to White and Bolton (2014), the soil below a penetrating pile can be regarded as a soil stream flowing passing the pile shaft (Figure 2.7). As the pile kept advancing, the shear zone around the pile side will be coated with fine, crushed sand (Bolton and Cheng 2002). The crushed fines should be mainly originated from the crushing zone below pile tip, while the crushing around the pile side may be limited due to stress relaxation. Such argument was also evidenced by discrete element modeling, where the zone of crushing is mainly concentrated in the pile end (Vallejo and Lobo-Guerrero, 2005).

Figure 2.5 "nose cone" of crushed soil below pile tip (White and Bolton 2004)

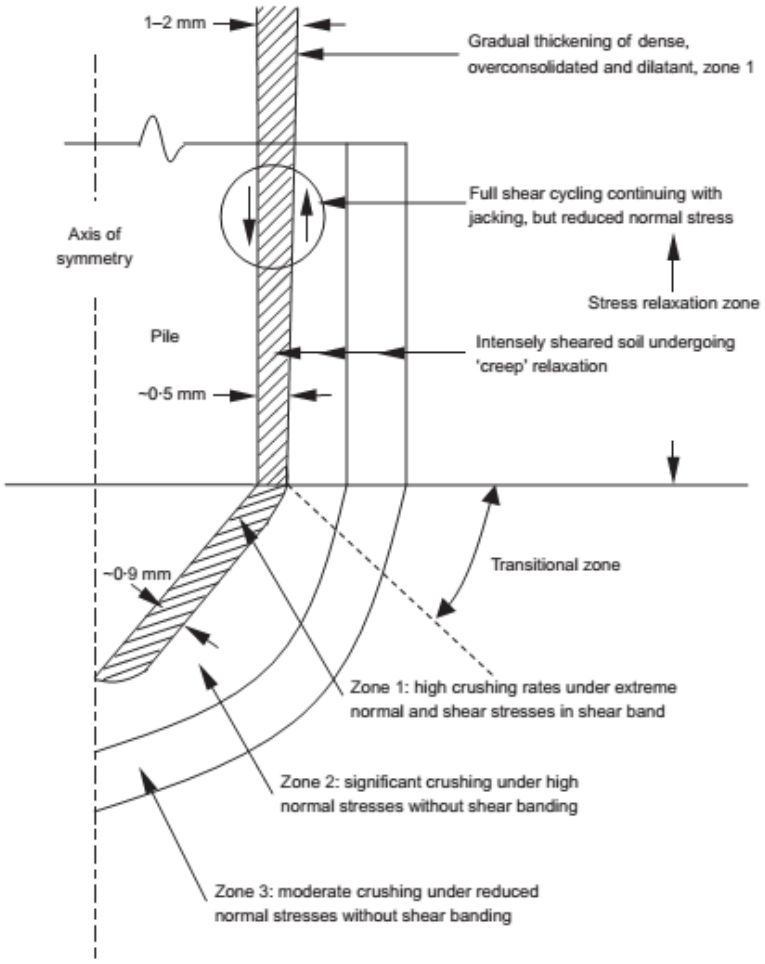

Figure 2.6 Schematic zones of soil below a pile end (Yang et al. 2010)

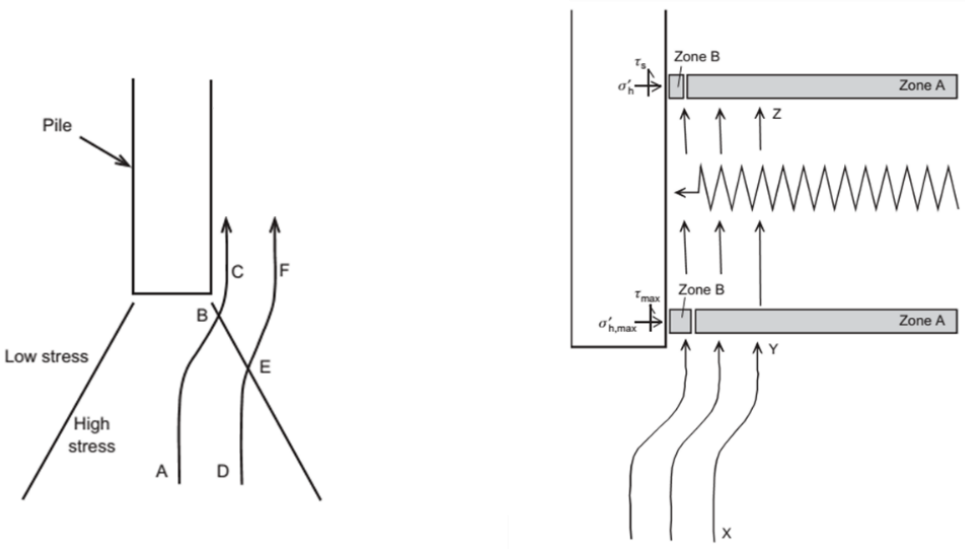

Figure 2.7 Schematic illustration of soil stream and friction fatigue close to pile tip (White and Bolton 2004)

2.3.INTRODUCTION OF ACOUSTIC EMISSION

Acoustic Emission (AE) refers to the transient elastic waves generated by the rapid release of energy from a stressed material (ASTM-E1316 2014). It concerns with the micro "noises" emitted from the source material, which is usually ignored, and also difficult to be evaluated through traditional testing methods. In the theory of plasticity, the plastic straining of a stressed material is accompanied by irrecoverable energy dissipations in forms of heat, vibration and elastic waves (Tanimoto and Tanaka 1986). The elastic waves here, accounting for partial or the total released energies, can be picked by an AE sensor (mostly piezoelectric type) and converted to an electrical signal. Figure 2.8 shows the schematic view of a typical AE monitoring system. The elastic waves triggered by the external forces may propagate through the medium to the sensor, subsequently amplified by a preamplifier and recorded by a data logger. The captured signals are characterized by a number of parameters in terms of amplitude, count, energy, etc., which directly reflect the signal source mechanisms.

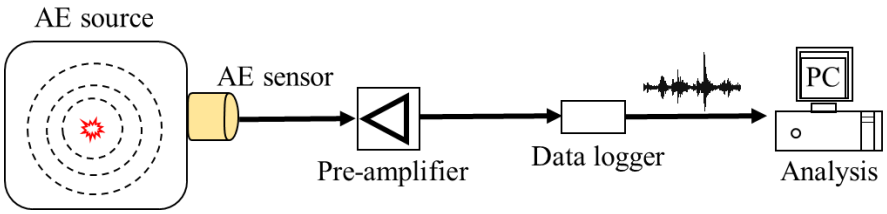

Figure 2.8 Schematic representation of a typical AE monitoring system

As a non-destructive testing (NDT) method, AE testing has been successfully applied to the studies of steelwork, concrete, rock, wood and composite materials (Bassim et al. 1994, Labuz et al. 2001, Ohtsu et al. 2001, Aicher et al. 2001, Lei et al. 2004, Liu et al. 2012). These applications have been involved in a variety of mechanical aspects including damage assessment, crack growth, flaw localization or failure mechanism, and have led to many new findings.

AE technique is considered quite unique from the conventional methods in several aspects. First, it is a passive dynamic inspection method that detects the active defects inside a material (Boyd and Varley 2001). Therefore, it is usually applied when the material is subjected to load or other stimulus, e.g. the presence of external force,

temperature variation or fatigue break, etc. Second, it is more sensitive to the signal source characteristics (usually determined by material itself) while being less sensitive to the geometry of the materials (ASM Handbook 1992). This is particularly meaningful when monitoring a specific type of mechanical process or dealing with complex-shaped objects. Third, the arrangement of AE sensor is considerably flexible. Because of the propagation characteristics of elastic waves, the sensor is free from being installed to a prescribed region of interest. This makes the method applicable when it is difficult to access to the test location using conventional approaches, for example, in a high pressure or high temperature environment. By using multiple sensor arrays, it is even possible to localize the defect position (Baud et al 2004). In view of the above features, the AE testing method has become a powerful tool in monitoring complex material problems.

2.4. AE FUNDAMENTALS

Figure 2.9 shows a typical AE signal, along with relevant signal parameters of interest. A variety of parameters can be defined to characterize the captured signals (ASM Handbook 1992), among which the most widely used ones are listed below.

- Amplitude: represents the highest peak voltage of a signal wave. The amplitude is an important parameter indicating the signal strength. It can be expressed in voltage or on a decibel scale, where 1μV corresponds to 0 dB_{AE}.
- Count: represents the number of hits with a maximum amplitude crossing a predefined threshold. The hits here can be a ring down hit or event hit as illustrated in Figure 2.9. Note that event count is mainly used in the current study because further analysis based on individual events are conducted.
- Energy: The AE energy is measured by integrating the squared AE signal voltage within a signal duration. This is also referred as the true energy sometimes. Another widely used energy parameter is the E_{MARSE}, or known as energy counts, which is the integral of the rectified AE signal voltage within the duration of the signal.
- Duration: refers to the elapsed time from the first threshold crossing to the last.

- Rise time: refers to the elapsed time from the first threshold crossing to the peak value.

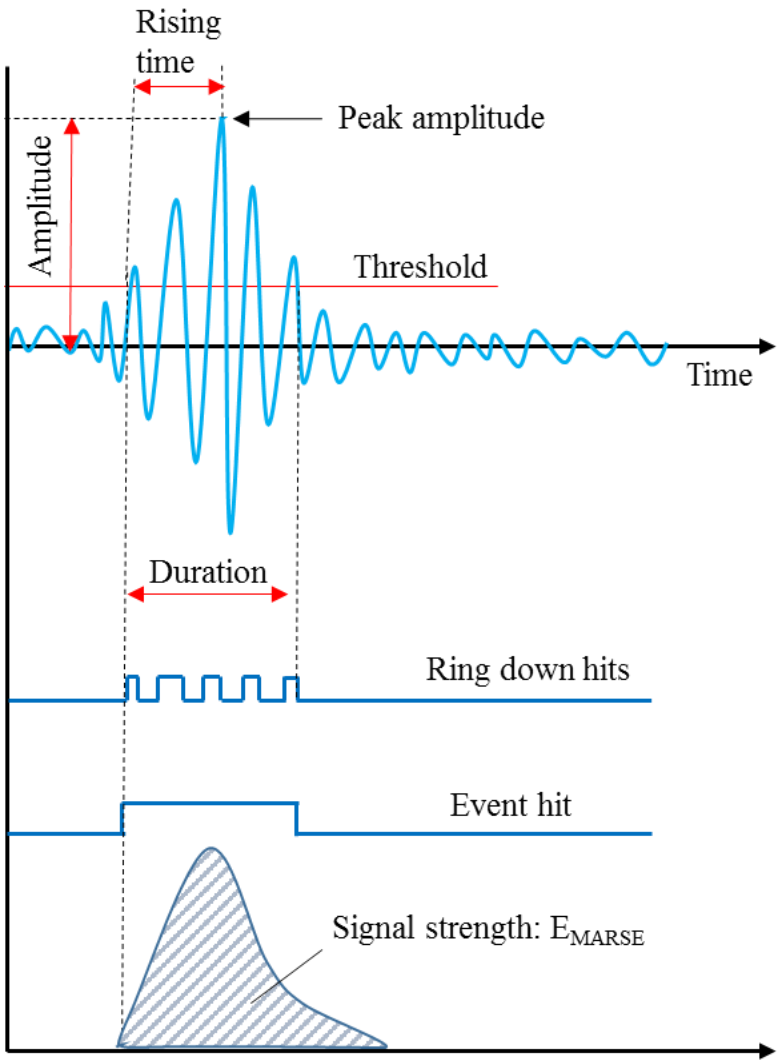

Figure 2.9 Parameters of a typical AE signal

2.5.ELASTIC WAVE PROPAGATION IN SOIL

The elastic waves propagating through soil in forms of body waves involve ground dilation and distortion. In compression waves (also known as primary waves, longitudinal or *P*-waves), particle vibrations are in the direction of wave propagation. In shear waves (also known as secondary waves or *S*-waves), vibration of particles is perpendicular to the direction of propagation (Figure 2.10). For AE monitoring, usually a *P*-type transducer is used since the *S*-type wave is usually submerged in the *P*-wave

and becomes difficult to identify.

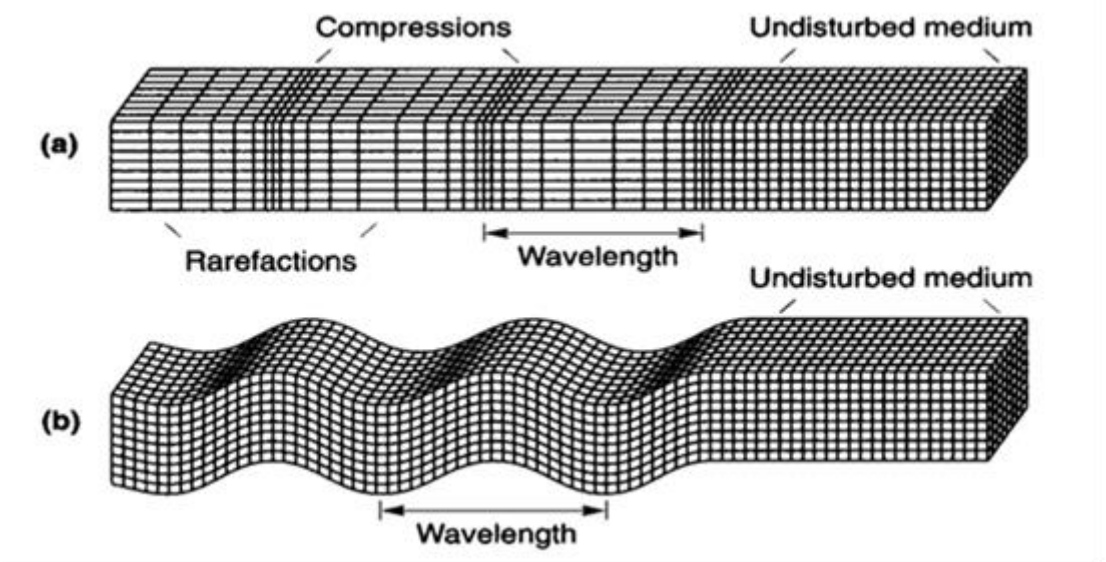

Figure 2.10 Particle motions associated with (a) Compression waves; (b) Shear waves (Kramer 1996)

Elastic wave measurements have been widely used for investigation of mechanically stressed geomaterials. However, majority of geotechnical laboratory studies are focused on shear wave velocity measurement, which is supposed to be linked with the material's shear modulus (Hardin and Richart 1963, Ohta and Goto 1978, Brignoli et al. 1996, Cho and Santamarina 2001, Mancuso et al. 2002). A significant difference between AE monitoring and conventional wave velocity measurements lies in the source of signal. AE testing is a passive measurement that captures the signals generated by external disturbance. A main issue that prevent the AE method from wide range application is the signal attenuation. The attenuation of a wave signal can be expressed using the following equation (Koerner et al. 1981).

$$\alpha = \frac{20}{x}\log\frac{A_1}{A_2} \tag{2-2}$$

Where α =attenuation coefficient in dB/distance,

x =distance between pickup points,

A_1 = amplitude of first wave, and

A_2 = amplitude of second wave.

The attenuation of wave depends on the signal frequency, and also the propagating medium. As can be seen in Figure 2.11, iron and steel has much lower rate of attenuation compared with sands. Therefore, in practical applications, the metals are usually used as wave guide to bring the AE within the soil mass to the external sensors.

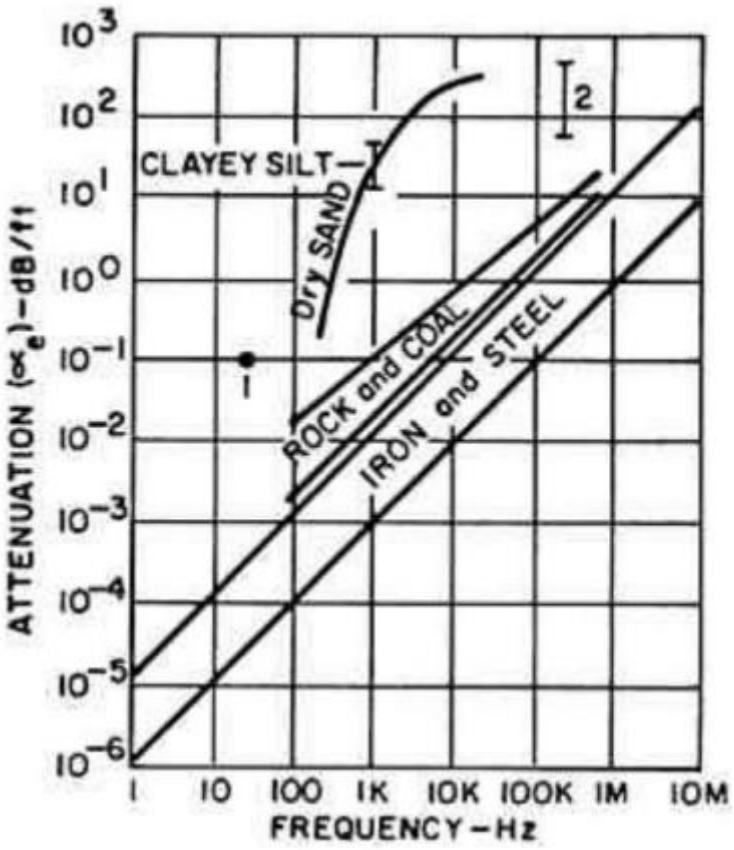

Figure 2.11 Wave attenuation as a function of frequency of various materials (Koerner et al. 1981)

2.6.DEVELOPMENT OF AE TESTING METHOD

AE signals are emitted through a wide band of frequencies, ranging from several hertz to kilo hertz. Figure 2.12 shows the different range of frequencies employed for different purpose of testing. The highest frequency was only applied to the study of metal and ceramics. This may be attributed to its good performance in view of wave

attenuation. For laboratory AE studies concerning geologic materials, the frequency is mostly ranged from 100 Hz to 500 kHz. However, as is going to be revealed in the current study, the upper limit of the AE signals for laboratory testing may reach 1MHz.

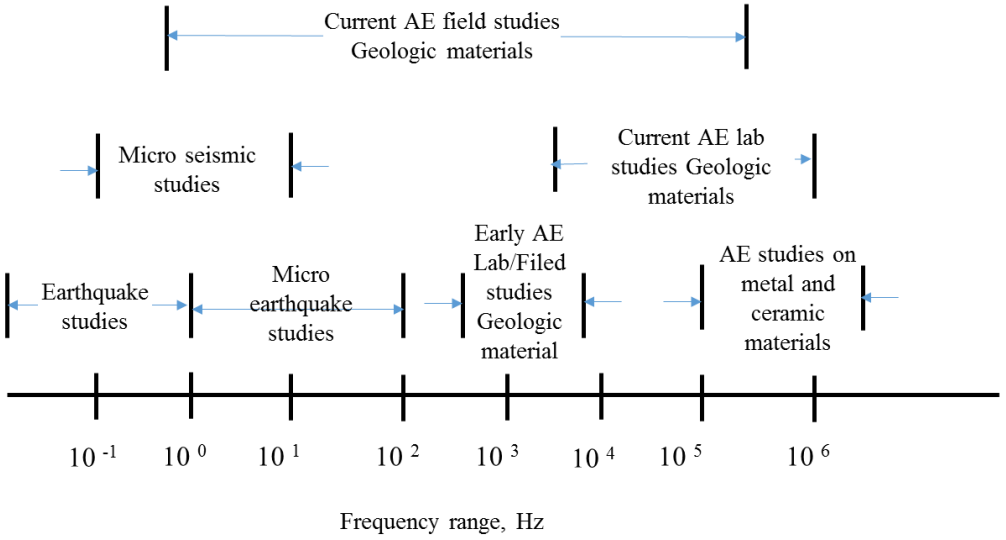

Figure 2.12 Frequency range of AE monitoring (Hardy 1975)

In order to capture the desired signals, a proper type of AE sensor needs to be selected. Commonly used ones include geophones, accelerometers and AE transducers. For the first two types, the frequency response range is usually limited, mostly up to 10-20 kHz, and consequently, they were more frequently used during the earlier time of AE application (Koerner et al. 1981). Due to its economic efficiency, they were also commonly used for field monitoring or laboratory testing when the high frequency signals are not of the primary interest (Ohtsu 1991; Cai et al. 2001; Senfaute et al. 2009). On the other hand, the piezoelectric ceramic type AE transducers, featured by broad band response and high sensitivity, have been a dominant choice for laboratory testing in the current time (Godin et al. 2004, Yoshimitsu et al. 2009, Asamene and Sundaresan 2012, Mao et al. 2015).

Referring to the field of geophysics, however, the application of AE method is very limited in spite of the long history of research (Paparo et al. 2002). The main reason is attributed to the propagation complexity and high attenuation of elastic waves in porous geomaterials (Koerner et al. 1981). For example, the rate of magnitude attenuation (as shown in Figure 2.11) of a signal at frequency of 1 kHz in dry sand is about ten thousand

times as great as in steel. Such behavior prevents the potential implementation of AE in large scale. In order to enhance the signal strength captured by AE transducers, a metal waveguide was employed when investigating the generation of AE in soils, especially in large scale field studies. In several recent studies, active wave guides were developed for AE monitoring of slope deformation (Dixon et al. 2003, Dixon et al. 2014). The "silent" slope displacement were amplified by "noisy" materials placed in the wave guide which deform together with the slope movement. Such applications broaden the potential application of AE method in geologic materials.

2.7.SUMMARY

The overall discussion presented in this chapter is categorized in two broad fields; *(i)* subsoil behaviors below a pile tip, and *(ii)* acoustic emission measurements in soil. In the first section, the problem of subsoil behavior and related investigation methods, as well as the significance of sand crushing are discussed. The second half of this chapter presents a potential method based on AE monitoring was introduced. A detailed description of AE fundamentals, elastic wave propagation in soils and development of AE testing method for geologic materials were presented.

2.8.REFERENCES

Aicher, S., Höfflin, L., & Dill-Langer, G. (2001). Damage evolution and acoustic emission of wood at tension perpendicular to fiber. European Journal of Wood and Wood Products, 59(1), 104-116.

Arshad, M. I., Tehrani, F. S., Prezzi, M., & Salgado, R. (2014). Experimental study of cone penetration in silica sand using digital image correlation. Géotechnique, 64(7), 551-569.

Asamene, K., & Sundaresan, M. (2012). Analysis of experimentally generated friction related acoustic emission signals. Wear, 296(1), 607-618.

A. S. M. Handbook. (1992). Nondestructive evaluation and quality control. American Society of Metals, Metals Park, Ohio, USA, 200.

ASTM E1316-14e1. (2014). Standard Terminology for Nondestructive Examinations, ASTM International, West Conshohocken, PA.

Adrian, R. J. (2005). Twenty years of particle image velocimetry. Experiments in fluids, 39(2), 159-169.

Bassim, M. N., Lawrence, S. S., & Liu, C. D. (1994). Detection of the onset of fatigue crack growth in rail steels using acoustic emission. Engineering Fracture Mechanics, 47(2), 207-214.

Baud, P., Klein, E., & Wong, T. F. (2004). Compaction localization in porous sandstones: spatial evolution of damage and acoustic emission activity. Journal of Structural Geology, 26(4), 603-624.

Bolton, M. D., & Cheng, Y. P. (2002). Micro-geomechanics. Constitutive and centrifuge modelling: Two extremes (ed. SM Springman), 59-74.

Boyd, J. W., & Varley, J. (2001). The uses of passive measurement of acoustic emissions from chemical engineering processes. Chemical Engineering Science, 56(5), 1749-1767.

Brignoli, E. G. M., Gotti, M., & Stokoe, K. H. (1996). Measurement of shear waves in laboratory specimens by means of piezoelectric transducers. ASTM geotechnical testing journal, 19(4), 384-397.

Burlon, S., Frank, R., Baguelin, F., Habert, J., & Legrand, S. (2014). Model factor for the bearing capacity of piles from pressuremeter test results-Eurocode 7 approach. Geotechnique, 64(7), 513-525.

Cai, M., Kaiser, P. K., & Martin, C. D. (2001). Quantification of rock mass damage in underground excavations from microseismic event monitoring. International Journal of Rock Mechanics and Mining Sciences, 38(8), 1135-1145.

Carrera, A., Coop, M., & Lancellotta, R. (2011). Influence of grading on the mechanical behaviour of Stava tailings. Géotechnique, 61(11), 935-946.

Casini, F., Viggiani, G. M., & Springman, S. M. (2013). Breakage of an artificial crushable material under loading. Granular matter, 15(5), 661-673.

Cho, G. C., & Santamarina, J. C. (2001). Unsaturated particulate materials—particle-level studies. Journal of geotechnical and geoenvironmental engineering.

De Rosa, I. M., Santulli, C., & Sarasini, F. (2009). Acoustic emission for monitoring the mechanical behaviour of natural fibre composites: a literature review. Composites Part A: Applied Science and Manufacturing, 40(9), 1456-1469.

Dixon, N., Hill, R., & Kavanagh, J. (2003). Acoustic emission monitoring of slope instability: development of an active waveguide system.

Dixon, N., Spriggs, M. P., Smith, A., Meldrum, P., & Haslam, E. (2014). Quantification of reactivated landslide behaviour using acoustic emission monitoring. Landslides, 1-12.

Einav, I. (2007a). Breakage mechanics—part I: theory. Journal of the Mechanics and Physics of Solids, 55(6), 1274-1297.

Einav, I. (2007b). Breakage mechanics—Part II: Modelling granular materials. Journal of the Mechanics and Physics of Solids, 55(6), 1298-1320.

Foray, P., Balachowski, L., & Colliat, J. L. (1998). Bearing capacity of model piles driven into dense overconsolidated sands. Canadian Geotechnical Journal, 35(2), 374-385.

Godin, N., Huguet, S., Gaertner, R., & Salmon, L. (2004). Clustering of acoustic emission signals collected during tensile tests on unidirectional glass/polyester composite using supervised and unsupervised classifiers. Ndt & E International, 37(4), 253-264.

Hardin, B. O. (1985). Crushing of soil particles. Journal of Geotechnical Engineering, 111(10): 1177-1192.

Hardin, B. O., & Richart Jr, F. E. (1963). Elastic wave velocities in granular soils. Journal of Soil Mechanics & Foundations Div, 89(Proc. Paper 3407).

Hardy Jr, H. R. (1975). Evaluating the Stability of Geologic Struc tures Using Acoustic Emission. Monitor ing Structural Integrity by Acoustic Emission, ASTM STP, 571, 80-106.

Hyodo, M., Hyde Adrian F.L., Aramaki N., & Nakata Y. (2002). Undrained monotonic and cyclic shear behavior of sand under low and high confining stresses. Soils and Foundations, 42(3):63-76.

Imre, B., Laue, J., & Springman, S. M. (2010). Fractal fragmentation of rocks within sturzstroms: insight derived from physical experiments within the ETH geotechnical drum centrifuge. Granular matter, 12(3), 267-285.

Jardine, R. J., Zhu, B. T., Foray, P., & Yang, Z. X. (2013a). Interpretation of stress measurements made around closed-ended displacement piles in sand. Géotechnique, 63(8), 613-627.

Jardine, R. J., Zhu, B., Foray, P., & Yang, Z. X. (2013b). Measurement of stresses around closed-ended displacement piles in sand. Geotechnique, 63(1), 1-17.

Jardine, R. J., Zhu, B., Foray, P., & Dalton, C. P. (2009). Experimental arrangements for investigation of soil stresses developed around a displacement pile. Soils and Foundations, 49(5), 661-673.

Koerner, R. M., McCabe, W. M., & Lord, A. E. (1981). Acoustic emission behavior and monitoring of soils. Acoustic Emissions in Geotechnical Engineering Practice, ASTM STP, 750, 93-141.

Kramer, S. L. (1996). Geotechnical earthquake engineering (Vol. 80). Upper Saddle River, NJ: Prentice Hall.

Kuwajima, K., Hyodo, M., & Hyde, A. F. (2009). Pile bearing capacity factors and soil crushabiity. Journal of geotechnical and geoenvironmental engineering, 135(7), 901-913.

Labuz, J. F., Cattaneo, S., & Chen, L. H. (2001). Acoustic emission at failure in quasi-brittle materials. Construction and building materials, 15(5), 225-233.

Lade, P. V., & Yamamuro, J. A. (1996). Undrained sand behavior in axisymmetric tests at high pressures. Journal of Geotechnical Engineering, 122(2), 120-129.

Lade, P. V., Yamamuro, J. A., & Bopp, P. A. (1996). Significance of particle crushing in granular materials. Journal of Geotechnical Engineering, 122(4), 309-316.

Lei, X., Masuda, K., Nishizawa, O., Jouniaux, L., Liu, L., Ma, W., ... & Kusunose, K. (2004). Detailed analysis of acoustic emission activity during catastrophic fracture of faults in rock. Journal of Structural Geology, 26(2), 247-258.

Liu, P. F., Chu, J. K., Liu, Y. L., & Zheng, J. Y. (2012). A study on the failure mechanisms of carbon fiber/epoxy composite laminates using acoustic emission. Materials & Design, 37, 228-235.

Lockner, D. (1993). The role of acoustic emission in the study of rock fracture. International Journal of Rock Mechanics and Mining Sciences & Geomechanics Abstracts, 30(7): 883-899.

Mancuso, C., Vassallo, R., & d'Onofrio, A. (2002). Small strain behavior of a silty sand in controlled-suction resonant column torsional shear tests. Canadian Geotechnical Journal, 39(1), 22-31.

Mao, W., Aoyama, S., Goto, S., & Towhata, I. (2015). Acoustic emission

characteristics of subsoil subjected to vertical pile loading in sand. Journal of Applied Geophysics, 119, 119-127.

Marketos, G., & Bolton, M. D. (2007). Quantifying the extent of crushing in granular materials: a probability-based predictive method. Journal of the Mechanics and Physics of Solids, 55(10), 2142-2156.

Ohta, Y., & Goto, N. (1978). Empirical shear wave velocity equations in terms of characteristic soil indexes. Earthquake Engineering and Structural Dynamics, 6(2), 167-187.

Ohtsu, M., & Watanabe, H. (2001). Quantitative damage estimation of concrete by acoustic emission. Construction and Building Materials, 15(5), 217-224.

Ohtsu, M. (1991). Simplified moment tensor analysis and unified decomposition of acoustic emission source: application to in situ hydrofracturing test. Journal of Geophysical Research: Solid Earth (1978–2012), 96(B4), 6211-6221.

Poulos, H. G., & Davis, E. H. (1980). Pile foundation analysis and design (No. Monograph). New York, Wiley.

Paparo, G., Gregori, G. P., Coppa, U., De Ritis, R., & Taloni, A. (2002). Acoustic Emission (AE) as a diagnostic tool in geophysics. Annals of geophysics. 45(2), 401-416

Randolph, M. F. (2003). Science and empiricism in pile foundation design. Geotechnique, 53(10), 847-875.

Randolph, M. F., Dolwin, R., & Beck, R. (1994). Design of driven piles in sand. Geotechnique, 44(3), 427-448.

Rechenmacher, A. L. (2006). Grain-scale processes governing shear band initiation and evolution in sands. Journal of the Mechanics and Physics of Solids, 54(1), 22-45.

Sadek, S., Iskander, M. G., & Liu, J. (2003). Accuracy of Digital Image Correlation for Measuring Deformations in Transparent Media. Journal of Computing in Civil

Engineering, 17(2), 88-96.

Sadrekarimi, A. (2012). Effect of soil particle mineralogy on embankment dams. Proceedings of the ICE-Geotechnical Engineering, 165(3), 195-206.

Sadrekarimi, A., & Olson, S. M. (2010). Particle damage observed in ring shear tests on sands. Canadian Geotechnical Journal, 47(5), 497-515.

Senfaute, G., Duperret, A., & Lawrence, J. A. (2009). Micro-seismic precursory cracks prior to rock-fall on coastal chalk cliffs: a case study at Mesnil-Val, Normandie, NW France. Natural Hazards and Earth System Science, 9(5), 1625-1641.

Tanimoto, K., & Tanaka, Y. (1986). Yielding of soil as determined by acoustic emission. Soils and foundations, 26(3), 69-80.

Vallejo, L. E., & Lobo-Guerrero, S. (2005). DEM analysis of crushing around driven piles in granular materials. Géotechnique, (55), 617-623.

White, D. J., & Bolton, M. D. (2004). Displacement and strain paths during plane-strain model pile installation in sand. Géotechnique, 54(6), 375-397.

White, D. J., Take, W. A., & Bolton, M. D. (2001). Measuring soil deformation in geotechnical models using digital images and PIV analysis. In International Conference on Computer Methods and Advances in Geomechanics (No. 10, pp. 997-1002).

White, D. J., Take, W. A., & Bolton, M. D. (2003). Soil deformation measurement using particle image velocimetry (PIV) and photogrammetry. Geotechnique, 53(7), 619-631.

Willert, C. E., & Gharib, M. (1991). Digital particle image velocimetry. Experiments in fluids, 10(4), 181-193.

Yasufuku, N., & Hyde, A. F. L. (1995). Pile end-bearing capacity in crushable sands. Geotechnique, 45(4), 663-676.

Yang, Z. X., Jardine, R. J., Zhu, B. T., Foray, P., & Tsuha, C. H. C. (2010). Sand grain

crushing and interface shearing during displacement pile installation in sand. Géotechnique, 60(6), 469-482.

Yoshimitsu, N., Kawakata, H., & Takahashi, N. (2009). Broadband P waves transmitting through fracturing Westerly granite before and after the peak stress under a triaxial compressive condition. Earth, Planets and Space, 61(6), e21-e24.

Zhang, C., Nguyen, G. D., & Einav, I. (2012). The end-bearing capacity of piles penetrating into crushable soils. Géotechnique, 63(5), 341-354.

Zhang, C., Yang, Z. X., Nguyen, G. D., Jardine, R. J., & Einav, I. (2014). Theoretical breakage mechanics and experimental assessment of stresses surrounding piles penetrating into dense silica sand. Géotechnique Letters, 4(January-March), 11-16.

Zhang, L., & Chen, J. J. (2012). Effect of spatial correlation of standard penetration test (SPT) data on bearing capacity of driven piles in sand. Canadian Geotechnical Journal, 49(4), 394-402.

CHAPTER 3

EXPERIMENTAL SETUP

3.1. INTRODUCTION

The bearing capacity of a pile shaft or pile groups is one of the key concerns in pile foundation design. The underlying mechanisms of piles in sand depend on the subsoil behavior and the soil-pile interactions. As described in Chapter 2, a variety of laboratory and field tests are in practice nowadays for characterization of the pile performance (Randolph et al. 1994, Randolph, 2003, Jardine et al. 2013, Yang 2006). Distinct from the previous studies, this research focuses on the micro-scale energy dissipations in the form of elastic waves originating from the stressed sand subjected to pile loading. Therefore, an additional testing apparatus (AE monitoring) is assembled to an ordinary pile loading system to capture the elastic waves emitted from sand. Detailed description of both large and small pile loading apparatuses as well as the AE instrumentations for activity monitoring and source localization are discussed in this chapter.

3.2. SMALL PILE TESTING SYSTEM

3.2.1 General Layout

The small pile testing apparatus used in this study is a displacement-controlled loading system. The schematic diagram and the general layout of the testing apparatus are shown in Figure 3.1 and Figure 3.2. In general, the testing system consists of the following main parts:

a. Model box; containing model ground, with small dimensions which eases preparation of ground model.
b. Displacement-controlled loading system; controlling the axial load acting on the pile.
c. Measuring system; to obtain the axial load and the displacement of the pile.
d. Two amplifiers connected with load cell and EDT (external displacement transducer) respectively; to amplify output signals for improving measurement resolution.
e. *A/D* board; to convert electrical response of transducers from analogue to digital format.
f. Air balloons; to apply surcharge pressure to the model ground.
g. Reaction frame; to provide reaction force during pile loading.
h. Recording software; all data obtained by the load cell and the EDT is recoded using the data acquisitions package (Digitshow Basic), with a sampling interval of 1s.
i. An AE assemble is additionally instrumented with the pile loading system, and will be described next.

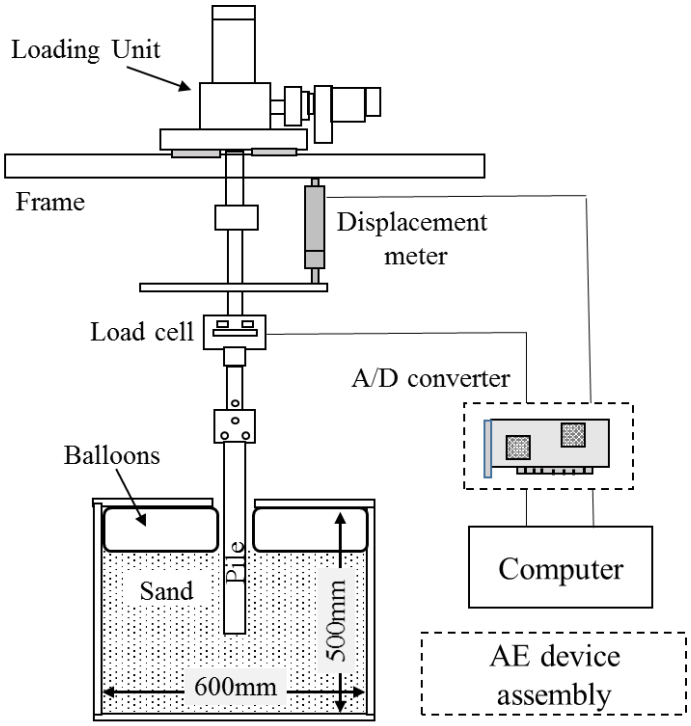

Figure 3.1 Schematic layout of small pile loading system

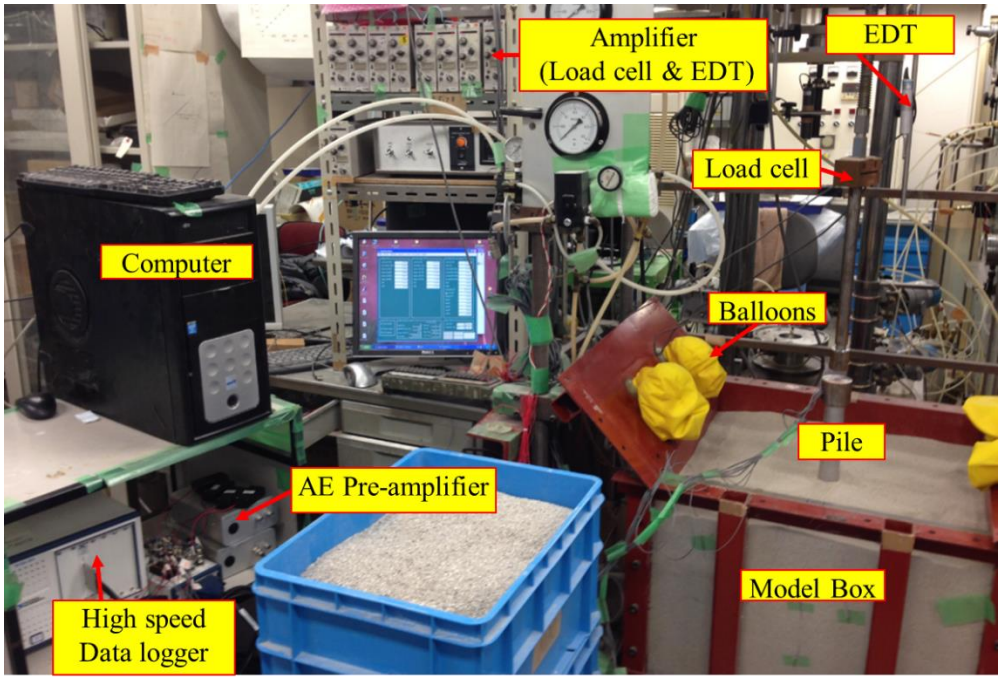

Figure 3.2 General layout of the small pile testing apparatus

3.2.2 Model Box

The internal dimension of the model box was 600mm long, 600mm wide and 500mm high. It should be noted that the size of this box was relatively small, and consequently, the boundary effect may exist. According to Kraft (1991), the boundaries of the soil container have effects on the stress and deformation patterns in the sand. In addition, the vertical stress in the sand can decrease due to the friction between the soil and container. It was also reported from several studies (Meyerhof, 1959; Kishida, 1963; Kishida, 1967; Robinsky and Morrison, 1964) that the zone affected by either installation of the pile or loading varies with soil density and method of pile installation. Yang (2006) suggested that for piles in clean sand, the influence zone is about 1.5-2.5D above the pile tip and 3.5-5.5D below the tip, where D is the pile diameter. This conclusion was based on the plastic zone analysis of the cavity expansion theory, and contrasted to the empirical estimation (0.7D-4D below pile tip and 6D-8D above pile tip) based on cone penetration tests (Robertson et al. 1985). In order to minimize the effect of boundary, a pile having an outer diameter of 40mm was used in this study. The pile end was 7.5D to the side wall, and 5D to the bottom. It is believed that the boundary effects should be limited to an acceptable

extent. Furthermore, this study is mainly targeted to investigate the AE characteristics of subsoil subjected to pile loading. Optimal results of the load-settlement behavior are not a primary consideration. Rather, the relationship between the AE activity and the load-settlement development during pile penetration is more interested in. Therefore, the small model box is used for most of the tests described next. Later, group pile tests were run in bigger box.

The model box is equipped with four air balloons fixed below the top cover of the box. With these, confining pressure or surcharge can be applied if desired ranging from 0kPa to 40kPa.

3.2.3 Axial Loading System

An electrical motor is fixed at the top of metal frame for applying the axial load to the pile. The loading motor has the maximum capacity of 25kN. The direction of loading can be both upward and downward. The loading speed of the motor is adjustable between 0.05mm/min to 7mm/min. Figure 3.3 shows the photo of the electrical motor (up) and its control unit (below) for speed adjustment.

Figure 3.3 Electrical motor and control unit

3.2.4 Measuring Devices

3.2.4.1 Load Cell

A load cell, an electronic-resistant strain gauge type transducer, was employed to measure the axial load (Figure 3.4). The load cell was screwed with the loading rod, with its upper side connected with the motor and lower side connected with pile. The capacity of the load cell is 50kN, and was calibrated before usage by applying a series of known dead loads on it. A correlation between the applied loads and the micro strains of the load cell was established. As is shown in Figure 3.5, perfect linearity can be observed from the load cell calibration plot.

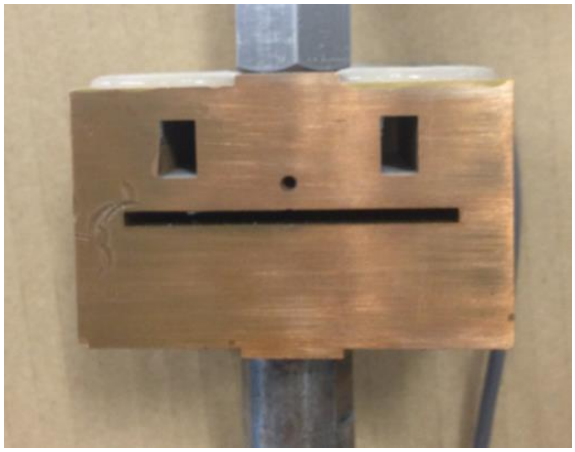

Figure 3.4 Axial load cell employed in small pile testing system

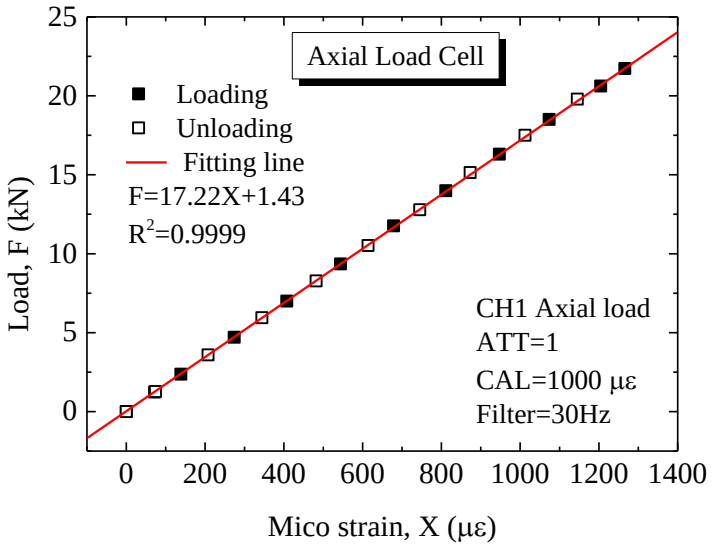

Figure 3.5 Calibration curve of the axial load cell

3.2.4.2 Displacement Measurement

The settlement of the pile during penetration was measured by an EDT (*External displacement transducer*) fixed on the upper plate of reaction frame. Figure 3.6 shows the photo of the EDT used in the small pile testing system. It measures the displacement of axial loading rod clamped to the motor. The EDT has the maximum capacity of 30 mm, and was calibrated before usage by applying a series of known displacements (a standard block gauge). It converts a mechanical displacement into a proportional electrical signal, subsequently amplified and recorded by the computer. As is shown in Figure 3.7, good linearity can be seen from calibration curve plot of EDT used in this study.

Figure 3.6 EDT used in small pile testing system

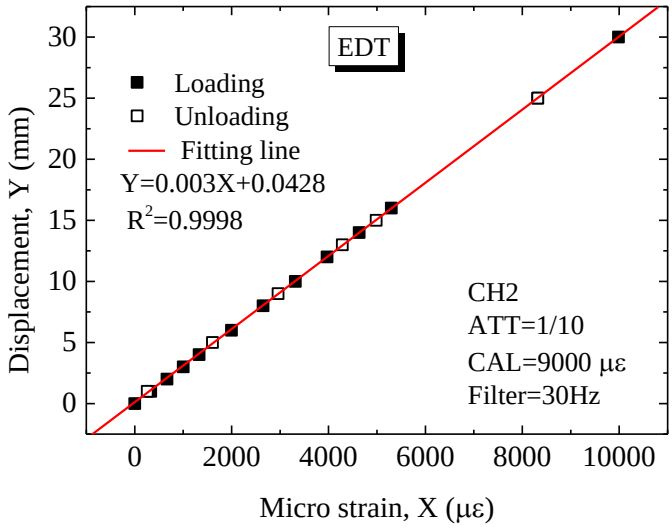

Figure 3.7 Calibration curve of the EDT

3.3. LARGE PILE TESTING SYSTEM

3.3.1 General Layout

In addition to the small pile testing system, a large pile machine was also employed in the current study. The internal dimension is approximately three times that of the small soil tank, and consequently, there is less boundary effect on the model ground. Moreover, a group pile testing assembly is available for the large pile machine. The AE testing technique is therefore further extended to investigate the group pile behavior. The schematic diagram and the general layout of the testing apparatus are shown in Figure 3.8. The working principles of the large testing machine are similar with the small loading system. Some new features of the pile machine are:

a. Large model box; with large dimensions to reduce the boundary effect.
b. Large loading capacity; powerful enough to penetrate a 9-pile group under 200kPa surcharge pressure at different loading speed into dense sand.
c. Group pile testing assembly; besides single pile testing, it is possible to conduct group pile test in 2.5D/5D pile spacing.
d. Surcharge pressure; apply up to 200kPa surcharge to the model ground.
e. Data acquisition system; capable of recording data up to 196 channels.

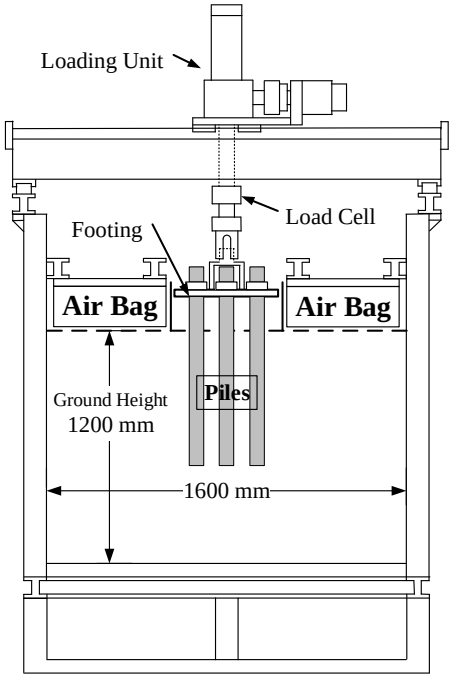

Figure 3.8 Schematic layout of large pile testing system

3.3.2 Large Model Box

Figure 3.9 shows the photo of model box used in large pile testing system. The soil tank has an inner dimension of 1600 (width) × 1600 (length) × 1680 (height). A Teflon sheet was placed on the sidewall to reduce the friction in sand-wall interface. For a pile with a diameter of 40mm, the horizontal distance to the sidewall is 20D when it is placed at the center. It is therefore believed that the boundary effects are negligible if not totally eliminated.

Figure 3.9 Photo of large model box

3.3.3 Axial Loading System

The electrical motor employed in the large model box has a maximum capacity of 500kN. As can be seen in Figure 3.10, the motor is placed on two perpendicular trails, and is movable in a 2D plane so that piles at different locations can be reached. The loading speed of the motor is adjustable from 0.1mm/min to 10mm/min.

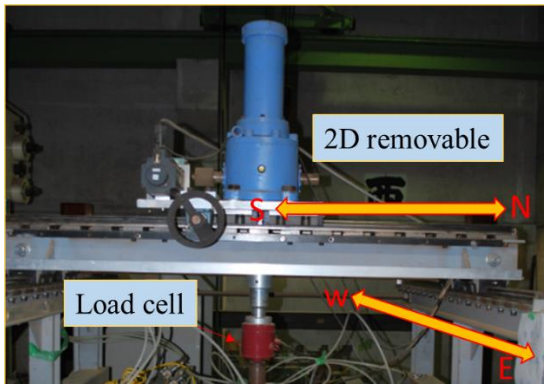

Figure 3.10 Photo of 2D moveable electrical motor

3.3.4 Air Bag System

Air bags were placed on the surface of the model ground in order to simulate a deeper foundation condition. The air bag used here was made of Dyneema Fibers fixed with a metal plate. Detailed design is shown in Figure 3.11. During the test, the bottom of the air bags were touched with the model ground surface and the upper side (metal plate) were confined by reactions beams. With the control valve, the surcharge pressure can be adjusted up to 200kPa. In order to cover all the ground surface except for the center region, reserved for piles, totally 8 air bags were used. The arrangement and the final configuration of the air bags are shown in Figure 3.12.

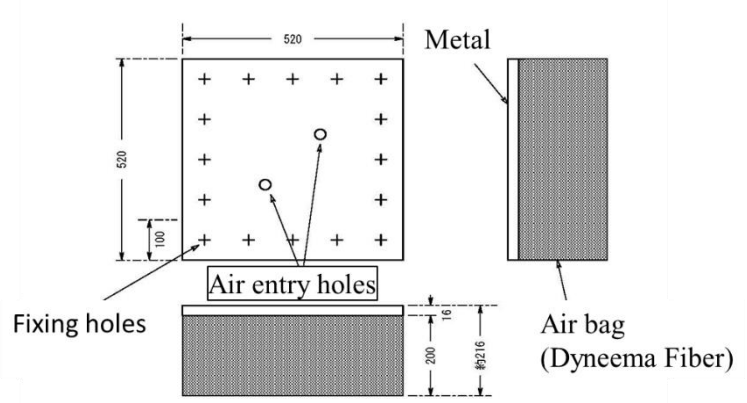

Figure 3.11 Schematic design of the air bag

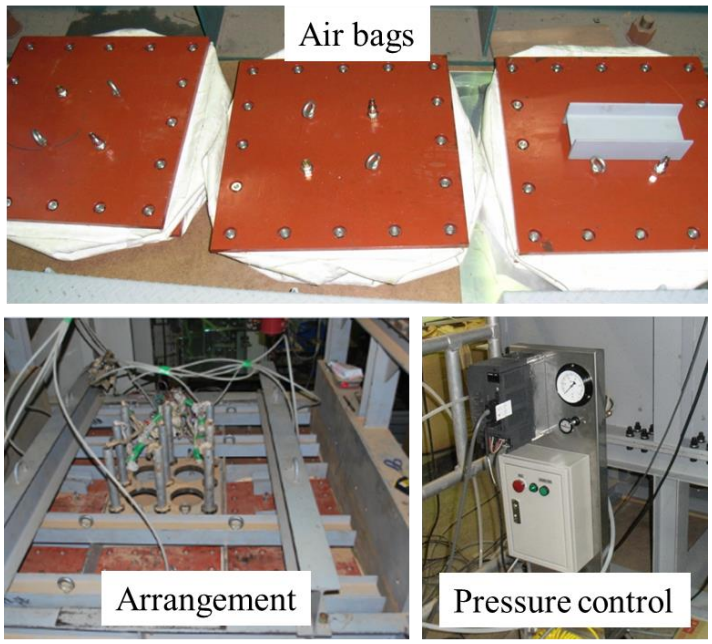

Figure 3.12 Air bags for applying surcharge pressure

3.3.5 Group Pile Assembly

The group pile model used in this study was constituted of 9 piles (3×3). A rigid steel footing associated with hoop accessories, as shown in Figure 3.13, was applied to connect the piles. In case of group pile loading, the axial force was applied directly on the footing via a loading head. Two types of footing corresponding to 2.5D and 5D pile spacing respectively are used. Detailed descriptions of the footing and the loading head are shown Figure 3.14.

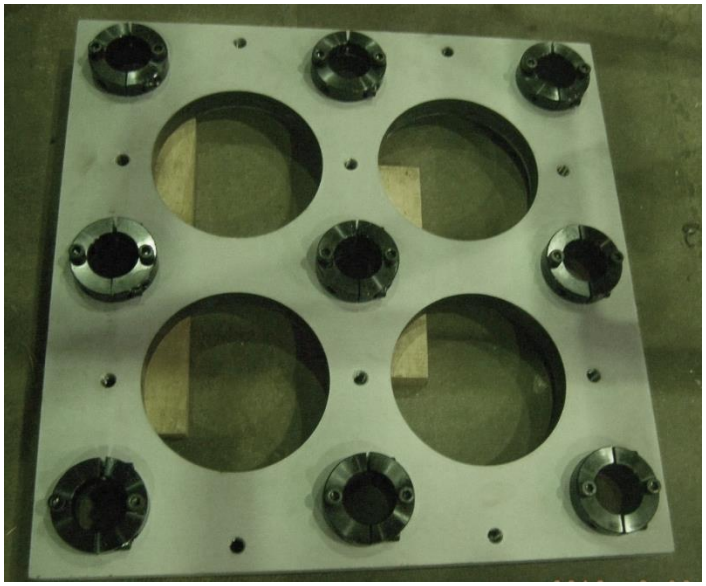

Figure 3.13 Photo of a load footing with hoop accessories

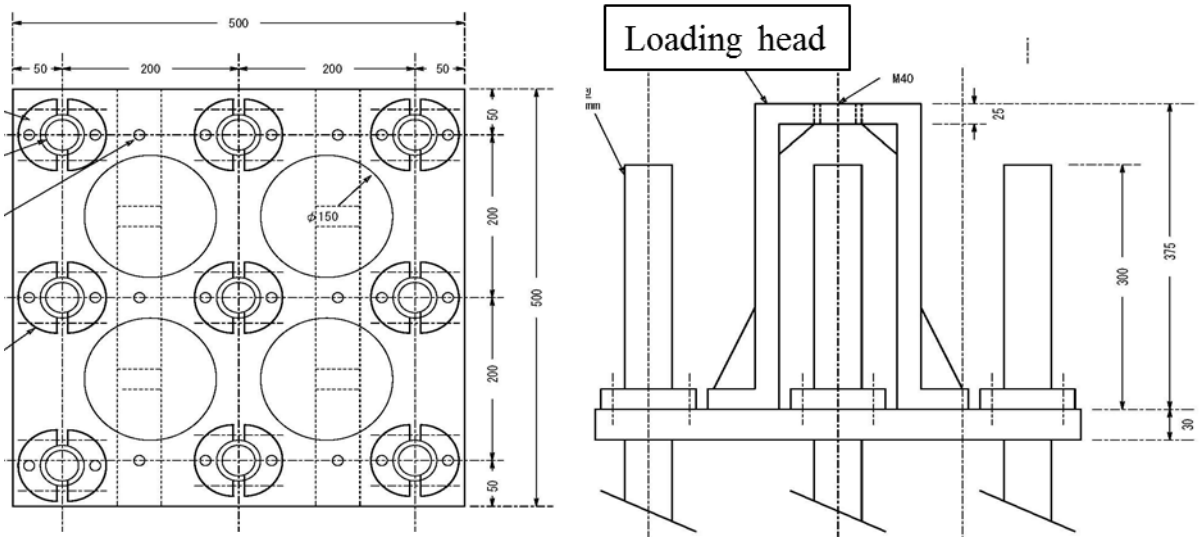

Figure 3.14 Schematic description of the footing and loading head

3.3.6 Data Acquisition System

The measured data from instrumented piles, load cell, EDT and earth pressure sensors were digitalized by a set of data acquisition system, which consists of one switch box (ASW-50C) and four data loggers (TDS-530), as shown in Figure 3.15. The piles were instrumented with strain gauges at different levels to measure the axial force in the pile shaft. There are 4 directions × 5 levels equaling 20 channels for each pile. A summary of 185 channels, with detailed description in Figure 3.16, are recorded at a time interval of 20s.

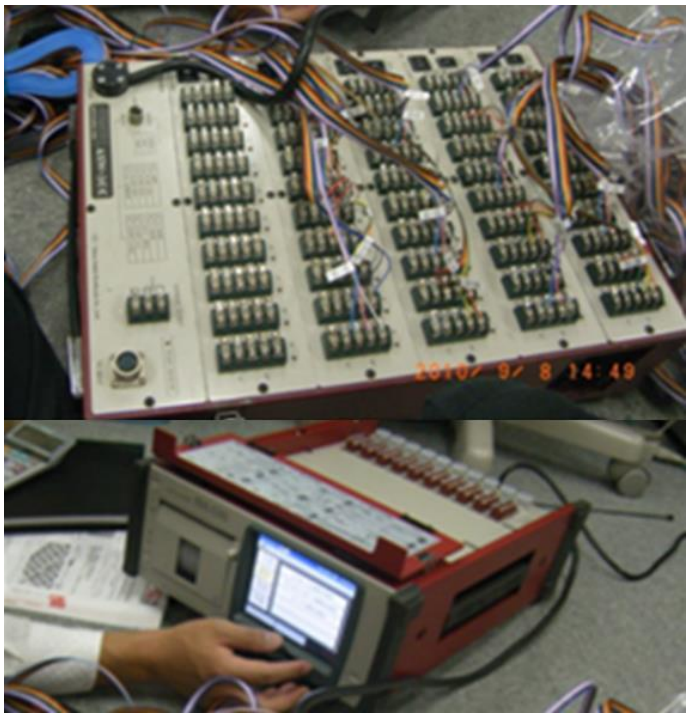

Figure 3.15 Photo of data logger

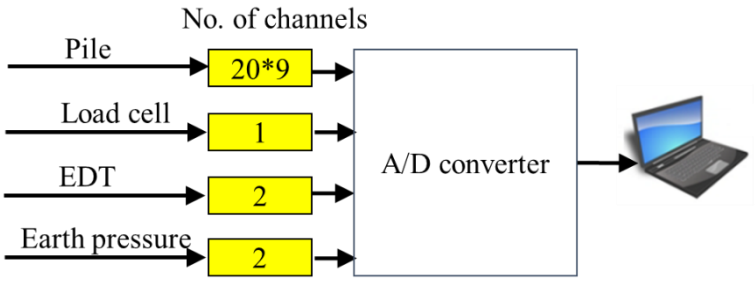

Figure 3.16 Schematic description of the data acquisition system

3.4. AE MONITORING SYSTEM

3.4.1 AE Sensor

For detection of AE signals, AE sensors manufactured by *Fuji Ceramics Corporation, Model R-cast M304A*, were used. The *R-cast* type AE sensor (referred as the AE sensor in the following sections), shown in Figure 3.17, was designed to detect microscopic destructions, and is capable of detecting cracks of several μm inside a material. Compared with conventional sensors, an FET (Field Effect Transistor) head amplifier was incorporated within the sensor case immediately after the piezo-ceramic, which significantly improves the sensitivity to low amplitude signals. With this design, the signal-noise ratio is almost twice as high as regularly designed models. The signal was subsequently amplified by the main amplifier. Figure 3.18 shows the schematic design of the structure and features of the AE sensor.

Figure 3.17 Photo of R-cast type AE sensor

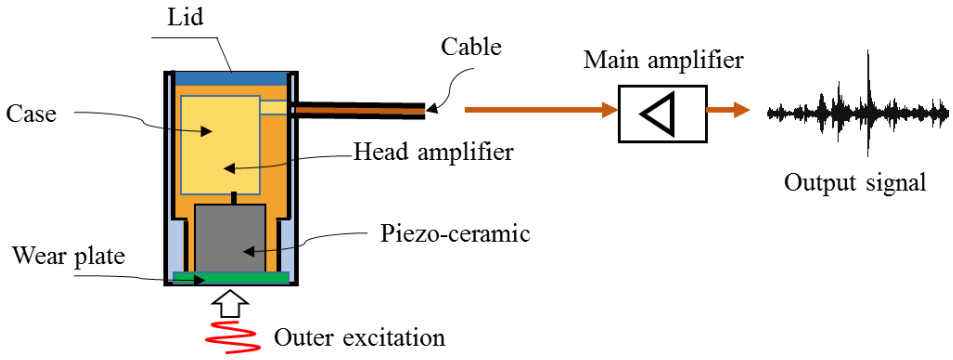

Figure 3.18 The structure and features of the AE sensor

Another type of vibration sensor, *Model VS-BV201*, manufactured by *NEC/TOKIN Corporation* was also used. A photograph of said sensor is shown Figure 3.19. This type of sensor (referred to as NEC type in the following sections) has a narrower working frequency band. It is therefore much cheaper to purchase, and is suitable for signal source location purpose where the total number of sensors is more important. A summary and comparison of R-cast type and NEC type sensors are listed in Table 3.1.

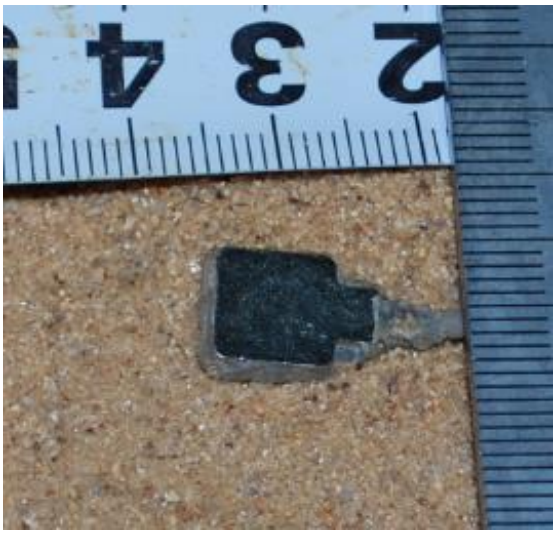

Figure 3.19 Photo of vibration sensor *VS-BV 201*

Table 3.1 Summary and comparison of R-cast type and NEC type sensors

Features	AE sensor (R-cast type)	NEC type
Measuring type	Velocity	Acceleration
Working frequency	10 kHz-2 MHz	10 Hz-15 kHz
Resonant frequency	300 kHz ±20%	——
Sensitivity (dB)	115±3	20
Size (mm)	φ5.5×10H	11.5×8.5×2.9
Weight (gm)	1	0.9

3.4.2 Pre-Amplifier

The initial amplitude of AE signal propagation through materials is very faint and consequently not enough to be discernible for further analysis. During AE testing, the captured signals are therefore amplified by a preamplifier before data saving. As

mentioned above, this study used a special AE sensor incorporated with a head amplifier and a main amplifier. The specifications of the head amplifier inside the sensor are listed in Table 3.2.

Table 3.2 Specifications of the head amplifier

Gain	20±2dB
Frequency range	20~2000 kHz
Output impedance	75Ω
Maximum output voltage	1Vpp
Power consumption	15m A
Power requirement	15V±10%

The main amplifier, manufactured by *Fuji Ceramics Corporation*, *Model A1201*, was further used, as shown in Figure 3.20. Each amplifier has two channels, and is possible to be connected with two sensors. When cooperated with R-cast AE sensor, it can yield a sensitivity of 115dB. In order to obtain high quality signals, a low-noise coaxial cable is required to connect the sensor to the amplifier.

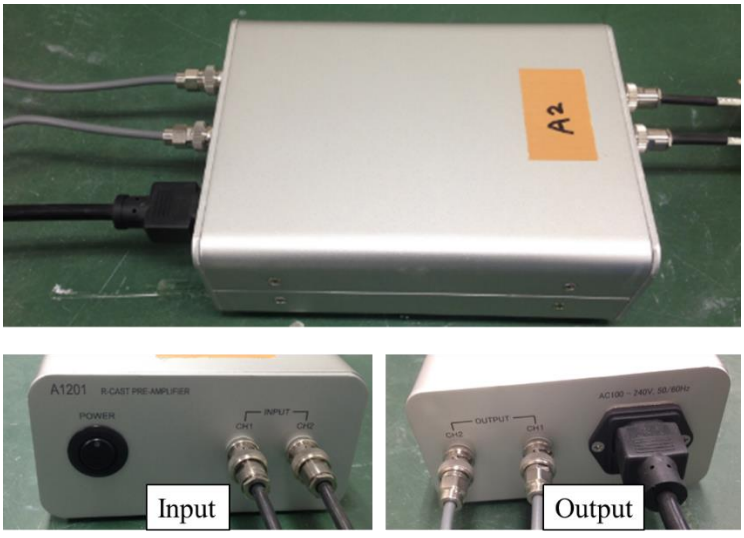

Figure 3.20 Photo of the main preamplifier

3.4.3 Recording Unit

As mentioned in Chapter 2, the frequency characteristics of AE signals originating from stressed soils may range from several hertz to hundreds of kilohertz. A high sampling rate is therefore required to capture full waveforms of very high frequency events. In the current study, a high performance data logger "*National Instruments Corporation, Model: PXIe-6366"* (Figure 3.21), was used for AE data recording. This device allows continuous recording of data flow from 8 simultaneous analog inputs at 2MS/s with 16 bit resolution. Detailed information of this data logger are summarized in Table 3.3.

Figure 3.21 Photo of *NI PXIe-6366* data logger

Table 3.3 Specification features of *NI PXIe-6366* data acquisition system

Feature	***Value***
Form factor	PXI/PXI Express
Max Analog input (AI) sampling rate	2MS/s (1-channel)
AI channels	8 (differential channels)
AI resolution	16 bits
Maximum voltage range	-10V~10V
Minimum voltage range	-1V~1V
Maximum working voltage	11V (channel to earth)
Highest sampling rate	2MS/s (simultaneous sampling in multiple channels)

3.4.4 Sensor Arrangement

The scope of this study covers two main aspects: AE activity evolution and AE source location respectively. To realize these goals, pertinent arrangements of AE sensors were made in order obtain optimal monitoring results. Figure 3.22 shows the schematic layout of AE sensor arrangements for the two different purposes mentioned above. For AE evolution monitoring, the sensor was directly attached to the pile surface so that the excessive attenuation of elastic wave within the sand could be avoided. Here, the pile shaft, which was made of aluminum, functioned as a wave guide. This method significantly enhanced the captured signals and was easier for installation compared with embedding the sensor in sand directly. It is also favorable for protecting the sensor from damage due to high pressure, which may happen when it is set close to the pile tip. For AE source location, 8 *NEC type* sensors were set around the pile tip aiming to capture a specific signal at the same time. It is important not to place the sensor too far away from the potential source region. Otherwise the signals may fail to be detected due to attenuation. A very close distance is also not preferred, since a wider area of coverage is desired so that all target region can be studied. By consideration of the above issues, the far side positions of sensors in this study were set about 1.75D to the pile center and 2.25D below the pile tip. The location of the detected signal can be subsequently computed using the developed algorithms, which will be described in the next chapter.

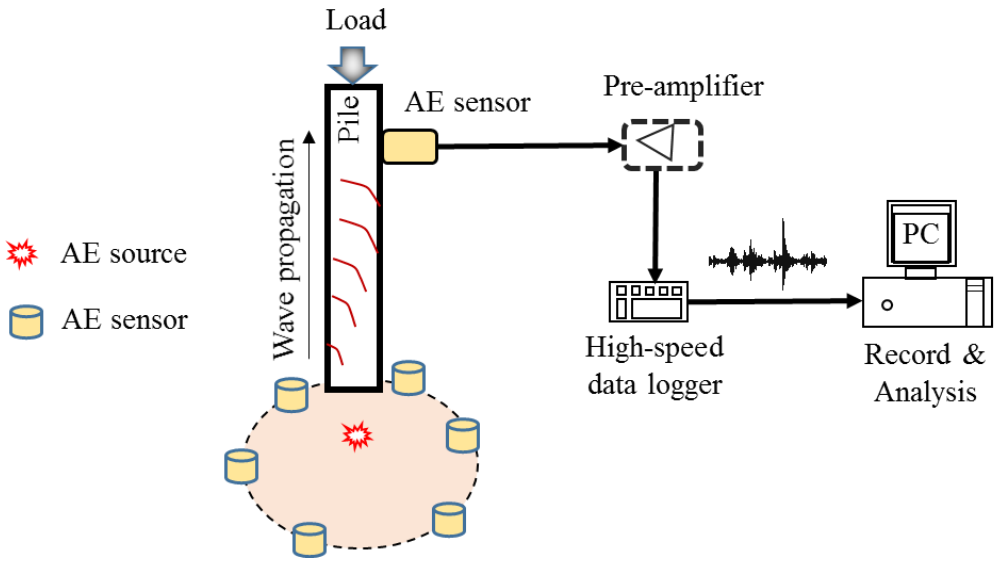

Figure 3.22 Schematic layout of AE sensor arrangements for different purposes

3.5. SUMMARY

This chapter discusses the details of the experimental apparatus used for this research. The functional description of the pile loading systems, including a small and a large loading system, as well as the AE instrumentation assembly have been presented in detail by means of photographs and schematic illustrations.

3.6. REFERENCES

Kishida, H. (1963). Stress distribution by model piles in sand. Soils and Foundations, 4(1), 1-23.

Kishida, H. (1967). Ultimate bearing capacity of piles driven into loose sand. Soils and Foundations, 7(3), 20-29.

Kraft Jr, L. M. (1991). Performance of axially loaded pipe piles in sand. Journal of Geotechnical Engineering.

Meyerhof, G. G. (1959). Compaction of sands and bearing capacity of piles. Journal of the Soil Mechanics and Foundations Division, 85(6), 1-30.

Robertson, P. K., Campanella, R. G., Brown, P. T., Grof, I., & Hughes, J. M. O. (1985). Design of axially and laterally loaded piles using in situ tests: A case history. Canadian Geotechnical Journal, 22(4), 518-527.

Robinsky, E. I., & Morrison, C. F. (1964). Sand displacement and compaction around model friction piles. Canadian Geotechnical Journal, 1(2), 81-93.

Yang, J. (2006). Influence zone for end bearing of piles in sand. Journal of geotechnical and geoenvironmental engineering, 132(9), 1229-1237.

CHAPTER 4

MATERIALS & METHODOLOGY

4.1. TESTED MATERIAL

This study aims to explore the subsoil behaviors subjected to pile penetration via AE monitoring. The understanding of such behaviors is deemed necessary to further clarify the pile bearing mechanism. In order to evaluate the effect of soil crushability, two different types of sands, silica sand No.5 and coral sand No.1, were used as the test material in this study. Silica sand is extensively used as construction materials in offshore engineering, and has been widely used in laboratory testing as well. Coral sand is more relevant in coastal areas and its particle strength is much weaker than the silica sand, which makes it more prone to breakage under stress. The following sections explain the physical properties and microscopic features of tested materials.

4.1.1 Physical Properties of Tested Material

The basic physical and mechanical properties of the tested sands are shown in Table 4.1, whereas Figure 4.1 shows the particle size distribution of sands. The determination of all index properties were performed according to Japanese Geotechnical Society (*JGS*) standards, where, e_{min} and e_{max} refer to minimum and maximum void ratios, D_{50} stands for mean particle diameter, *Cu* is the coefficient of uniformity defined as D_{60}/D_{10}, and *Cc* is the coefficient of curvature defined as $D_{30}^2/(D_{60}*D_{10})$, obtained from particle size distribution curves. It can be seen that the coral sand had larger mean particle diameter than the silica sand. The maximum and minimum void ratios of coral sand are also greater than the silica sand. The main reason is the porous structure of individual coral sand grains, which can be seen in the microscopic images shown in the next section.

Table 4.1 Physical and mechanical properties of tested material

Property	Silica sand No.5	Coral sand No.1
Specific gravity, G_s	2.651	2.803
Maximum void ratio, e_{max}	1.09	1.23
Minimum void ratio, e_{min}	0.66	0.84
D_{50}, mm	0.557	0.923
Coefficient of uniformity, *Cu*	1.692	2.096
Coefficient of curvature, *Cc*	1.051	1.026

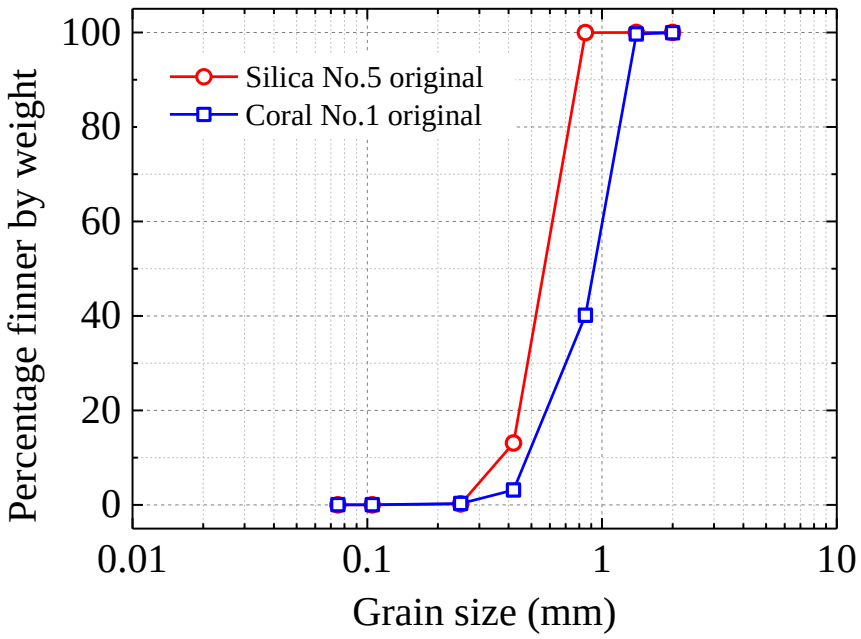

Figure 4.1 Grain size distribution of tested sands

4.1.2 Microscopic Image of Tested Material

The source of AE signal is mainly originated from micro scale straining of a material. Consequently, the micro structures of a material are supposed to have significant effect on its extrinsic AE characteristics when it is under stress. The microscopic images of silica sand and coral sand are shown in Figure 4.2(a) and Figure 4.2 (b) respectively. It can be seen that the surface of silica sand is rather angular, whereas the coral sand is much smoother. A closer observation is shown in Figure 4.3 through

laser illustration of a narrower area. The silica sand grain was found to be more "rough" and fragmentized with large amount of pre-existing fractures, while the coral sand grain demonstrated more uniform surface morphology but with large porous space which makes it softer. Previous studies generally found that calcareous sand was more crushable than siliceous sand (Coop et al. 2004, Kuwajima et al. 2009, Yu, 2014). It is therefore expected that a distinct behavior in term of AE activity also exist between the two materials. The features of the AE characteristics of these two types of sands will be revealed and compared in the following chapter.

(a) (b)

Figure 4.2 Microscopic images of (a) silica sand and (b) coral sand

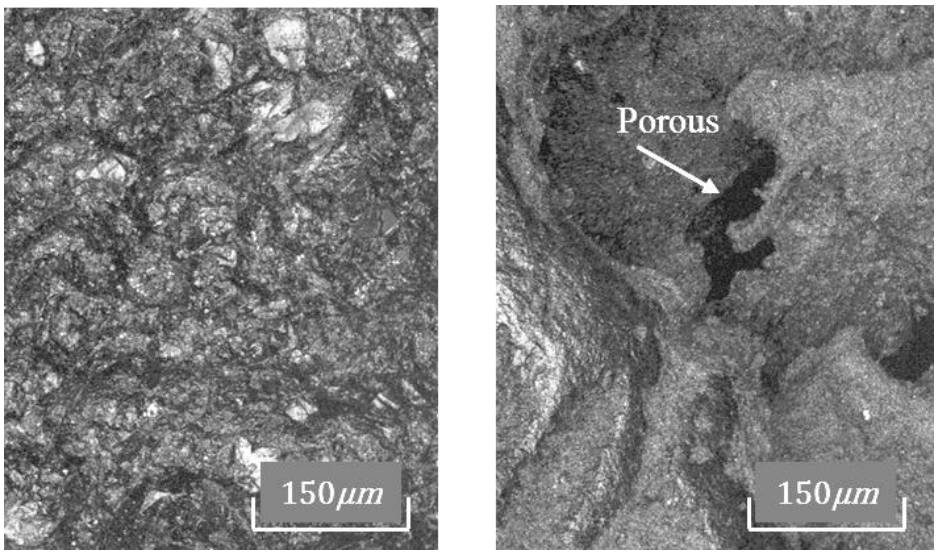

(a) (b)

Figure 4.3 Laser illustration of (a) silica sand and (b) coral sand

4.2.EXPERIMENTAL PROCEDURES

Although both large and small pile testing systems were used in this study, majority of tests conducted as part of this study were performed in the small pile testing system. Therefore, detailed descriptions of the experimental procedures are focused on the small pile testing system. A introduction of testing procedures in large model box is presented in the subsequent section as well.

4.2.1 AE Activity Monitoring

The following sections explain the general steps involved in AE evolution tests using small pile testing system.

4.2.1.1 Preparation of Model Ground

The model ground was prepared inside the soil tank. Before any test begins, make sure that the soil tank is clean and free from any impurities. Detailed steps for sample ground preparation are outlined below.

- The air-dried sand was poured in slowly and evenly in layers of every 50mm. After each layer, the sand was compacted by dropping (free fall) a 10kg weight all over the sand surface to attain the desired relative density (see Figure 4.4a). The weight of the sand should be weighted and recorded before pouring into the soil tank. In the current study, three types of ground conditions were tested, corresponding to loose, medium and dense ground conditions, with the times of compaction to be 1, 10 and 20 respectively.
- After the model ground reached the height of 200mm, the pile was placed at the center by clamping it against the guide bar while at the same time checking its vertical alignment (see Figure 4.4b).
- Continue pouring/compacting sand layers until reaching the final height of 400mm. The compaction of sand in this step should be very careful done due to the presence of pile. Violent disturbance should be avoided to assure that the position of the pile end remains unchanged. After reaching the uppermost layer, the guide bar was removed and the sand was flattened as in Figure 4.4c. followed by measuring the height of ground surface to the top of the box, and

calculating the relative density of the sample based on the total weight and sand volume.

- The cover with four air balloons was placed on the top of the box and secured with bolts and nuts, as shown in Figure 4.4d. Air was then supplied and controlled using a pressure regulator. Due to the limited capacity of air balloons, only 10kPa was applied throughout the tests.
- The axial loading rod was adjusted to reach the load head, and the EDT was properly placed. Furthermore, the measurement of axial load and displacement was initialized in the data acquisition software (DigitShow Basic).

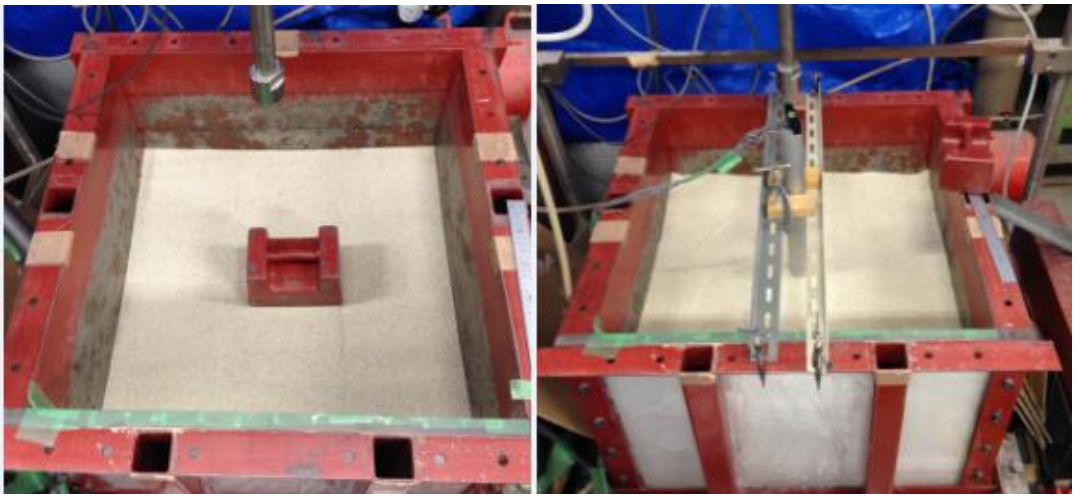

(a) (b)

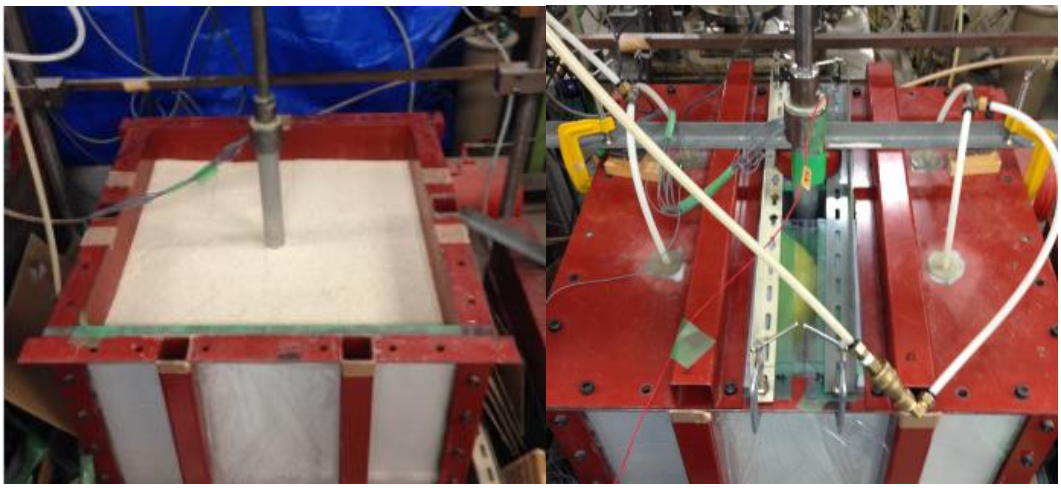

(c) (d)

Figure 4.4 Procedures of ground preparation: (a) sand compaction; (b) pile set up; (c) completed specimen; (d) closure the top cover and apply surcharge pressure

4.2.1.2 AE Sensor Set-up

For AE evolution monitoring, the AE sensor was attached to the pile shaft surface directly, and secured with tape, as shown in Figure 4.5. Preliminary testing showed that the mechanical noise from the loading motor significantly increased the signal noise level. Therefore, a noise barrier (Figure 4.6), by bonding together several layers of thin metal plates and membranes interactively, was made and placed between the loading rod and pile head. By this measure, the noise from the motor was reduced to a negligible level.

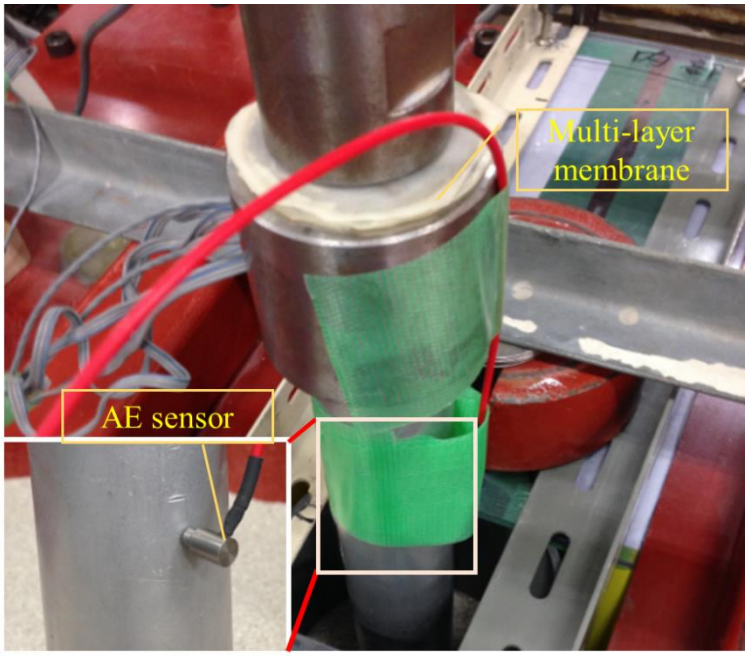

Figure 4.5 Photo of sensor set-up for AE evolution monitoring

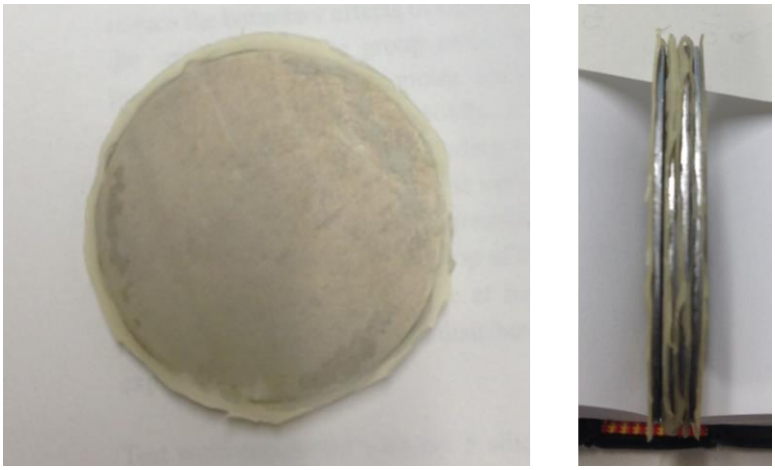

Figure 4.6 Structure of the noise barrier

Figure 4.7 shows a typical waveform of background noise, comparing with a noise signal when pile was loaded without the noise barrier. It can be seen that the magnitude of noise rose notably when the pile was loaded without the noise barrier. By contrast, when loaded with noise barrier, the recorded noise level showed no significant rising compared with the background noise (measured when the sensor was placed in the air), as shown in Figure 4.8. Therefore, the noise barrier was applied to all the tests described in the following sections.

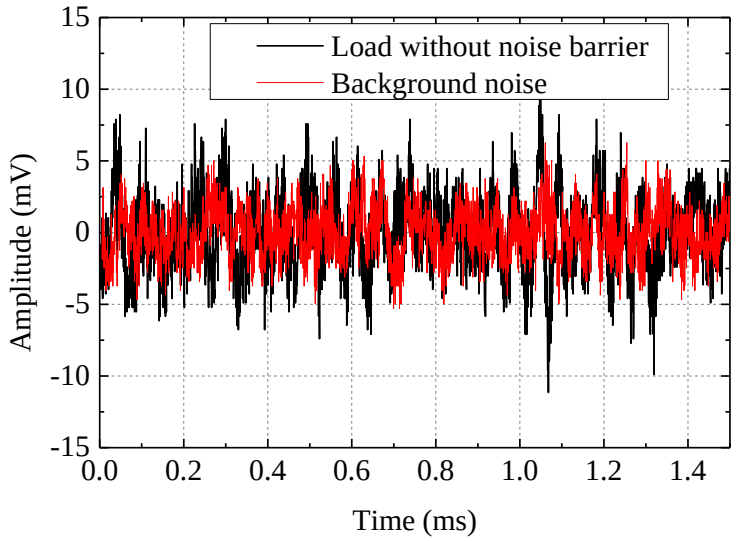

Figure 4.7 Comparison of noise level when pile is loaded without noise barrier

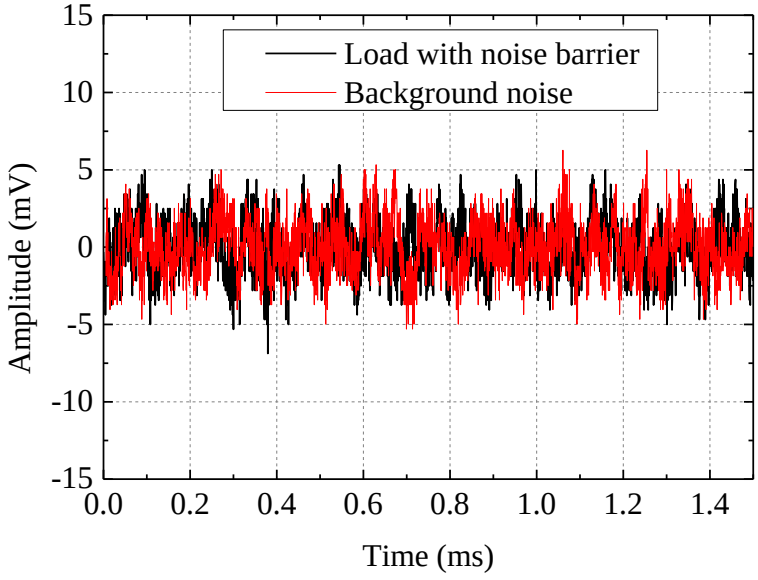

Figure 4.8 Comparison of noise level when pile is loaded with noise barrier

4.2.2 AE Source Location

For AE source location, the procedures for ground preparation and load cell & EDT settings are basically the same with AE evolution monitoring. Therefore, the AE sensor arrangement is focused in the following description.

All AE sensors are embedded directly in sand near the pile tip. The exact positions of the sensors are determined before test. When the model ground has been filled to the desired level, the sensors are placed properly before filling the next layer of sand, as is shown in Figure 4.9. The accurate position of sensor was assessed by its distance to the sidewall and the top of the soil tank. In general, all eight sensors were set at two levels, with each level containing four of them. The potential region of AE source was surrounded by the sensors. It is therefore important to set the active surface of the sensors toward source direction.

Figure 4.10 shows the schematic arrangement of sensors for source location tests. The sensors are placed at the eight corners of a virtual cuboid. With the pile end center set as the origin of a Cartesian coordinate, the coordinates of sensors can be derived. For a specific AE event, the signal may be captured by different sensors. Based on arrival time difference, it is possible to calculate the position of the event. Detailed mathematical descriptions will be presented in the next chapter. Figure 4.11 shows an overview of experimental setting for source location. The detected signals from eight channels are gathered through a BNC interface connected with data logger, and saved for further analysis. A schematic flowchart of the test is shown in Figure 4.12

Figure 4.9 Sensor set-up for AE source location

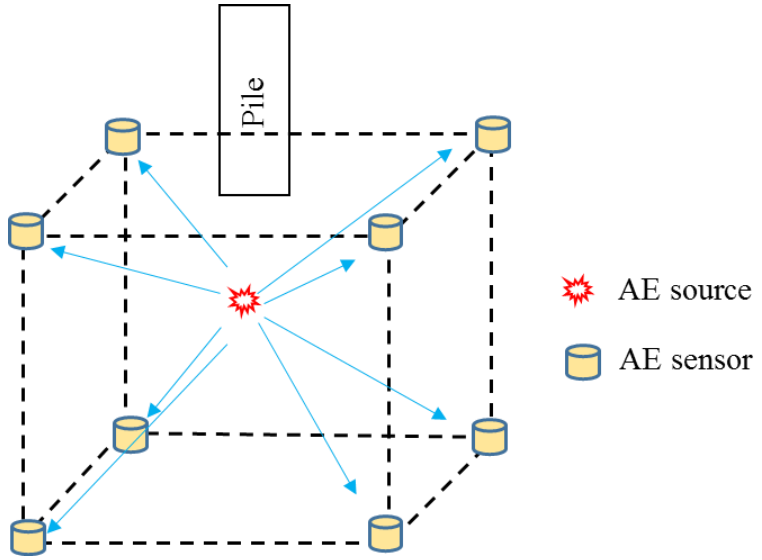

Figure 4.10 Schematic arrangement of sensors for source location

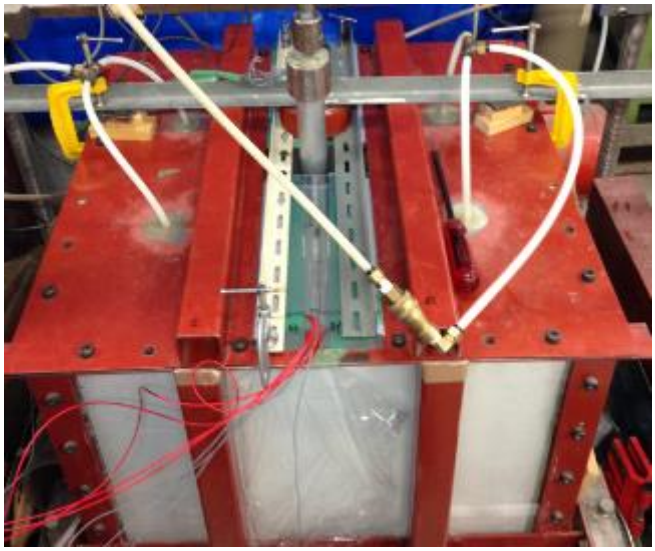

Figure 4.11 An overview of the setting for source location test

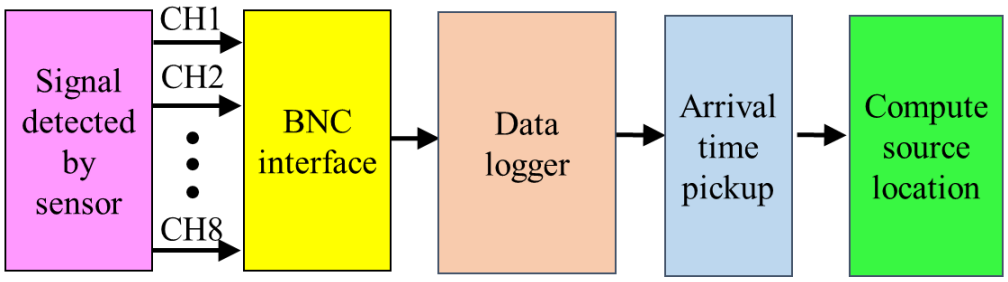

Figure 4.12 Schematic flowchart of source location test

4.2.3 AE Monitoring in Group Pile

The basic procedures for large pile loading tests are similar with small loading tests. Briefly, each experiment includes three main steps. First is model ground preparation; second is pile setting; third is AE sensor setting.

4.2.3.1 Model Ground Preparation and Pile Setting

The steps involved in preparing the model ground in large soil tank are outlined below;

- The model ground was prepared by air pluviation method (Figure 4.13 (a)) and manual compaction to a total height of 1200mm (Figure 4.13 (b)). The sand was compacted (10times using a wood stick) at every 150mm thickness. The total amount of sand and the height of the ground were measured when sand was poured. It is important to note that the sand inside group piles also needs compaction.
- After the model ground was constructed up to the initial elevation of the piles, the model piles were set on the ground surface and the ground was built again up to the 1200mm height. Before pile installation, the frame with footing (2.5D or 5D type) was fixed to the soil tank. Then the piles were installed carefully and kept in the vertical direction (Figure 4.13 (c-d)).
- Air bags (totally eight) were placed at the surface of the model ground (Figure 4.13 (e)). Reaction beams were placed on top of the air bags and connected to the soil tank (Figure 4.13 (f)).
- Air pressure was applied gradually. In this step, care was tanken to make sure that no wires lay between the reaction beam and the metal surface of the air bags.
- Two EDTs were set at two different locations to obtain the average value of pile settlement during penetration. The advantage of using two EDTs is that a tilting of loading plate can be observed if it happens.
- All piles were fastened very tight to the footing to make sure that no slip happens during loading.
- Finally, all cables from load cell, EDT and piles were connected to the data logger. The settings were then initialized and ready for recording.

(a)

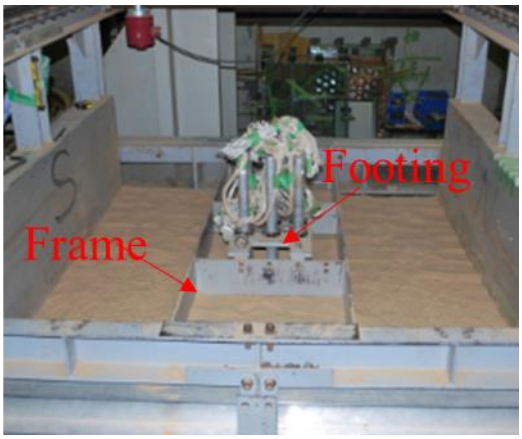

(b)

(c)

(d)

(e)

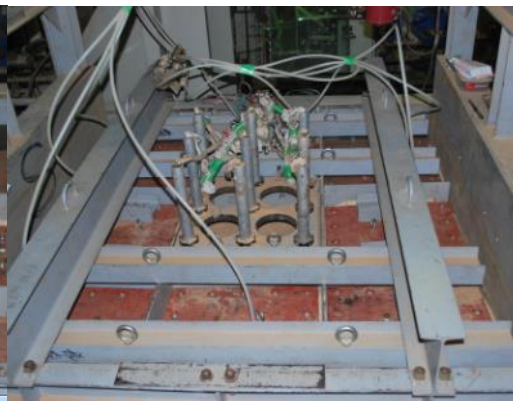

(f)

Figure 4.13 Procedures of ground preparation and pile setting in large model box: (a) sand pouring using air pluviation; (b) final configuration of model ground; (c) pile adjustment; (d) pile setting; (e) air bag setting; (f) reaction beam setting

4.2.3.2 AE Sensor Arrangement

In case of group pile loading, nine piles are connected to the footing. It is possible that the wave signals propagate from one pile to another through the metal footing. In order to reduce the disturbance from the surrounding piles, a membrane shim was placed between the footing and the fastening bolt to separate the pile from footing, as shown in Figure 4.14. For the description, the piles in the group were divided into 3 categories as shown in Figure 4.15. The middle and corner piles were in symmetric positions. Therefore, only one of them were monitored with AE sensor respectively.

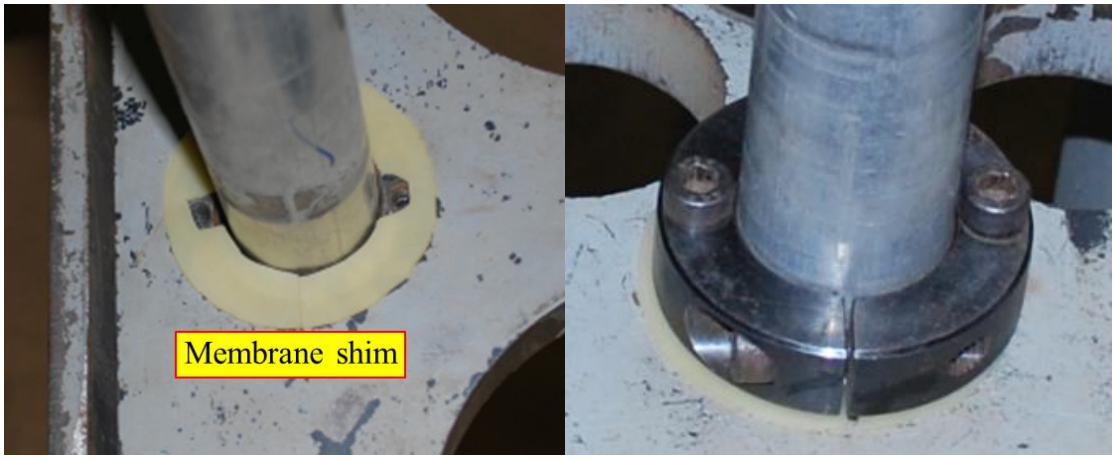

Figure 4.14 Membrane shim placed between footing and fastening bolt

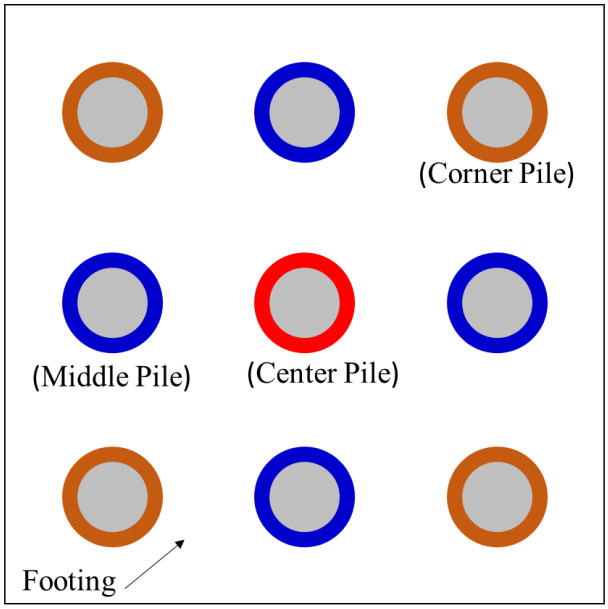

Figure 4.15 Definition of pile locations in the group

Four AE sensors were used in group pile monitoring. The arrangement of sensors is shown in Figure 4.16. Three of sensors were attached on the center, middle and corner pile surfaces respectively, and the forth sensor was attached to the footing to evaluate the influence of the surrounding piles. The final layout of the sensor setting is shown in Figure 4.17. The sensors were further connected to the data logger and ready for recording. After the sensors were set, a loading head was placed on the footing and connected to the loading motor. Figure 4.18 shows the overview of the experimental set up and data recording units.

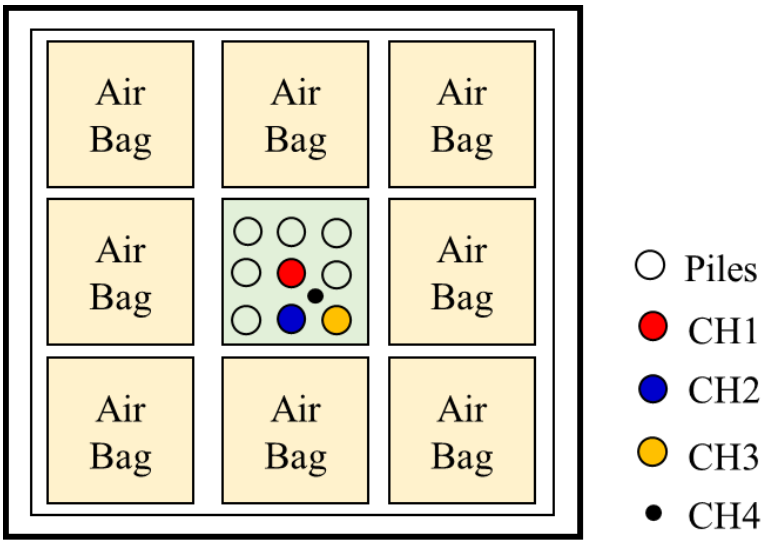

Figure 4.16 Sensor arrangement in group pile monitoring

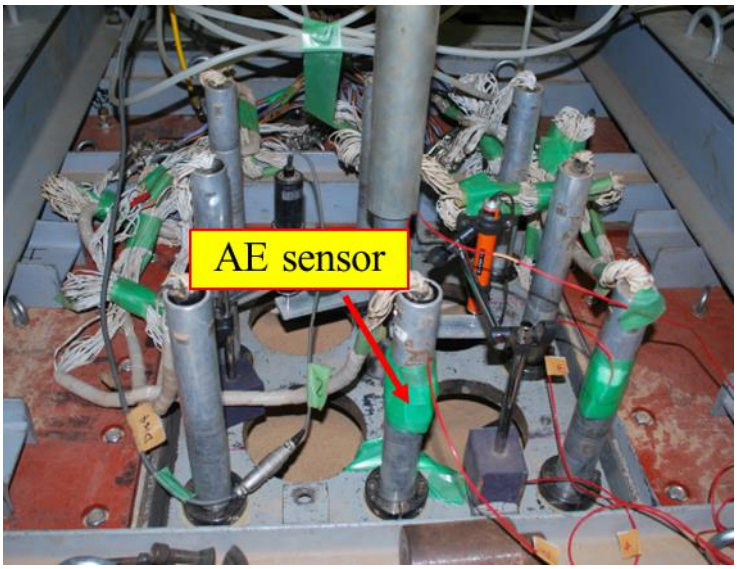

Figure 4.17 Photo of final layout of AE monitoring in group pile

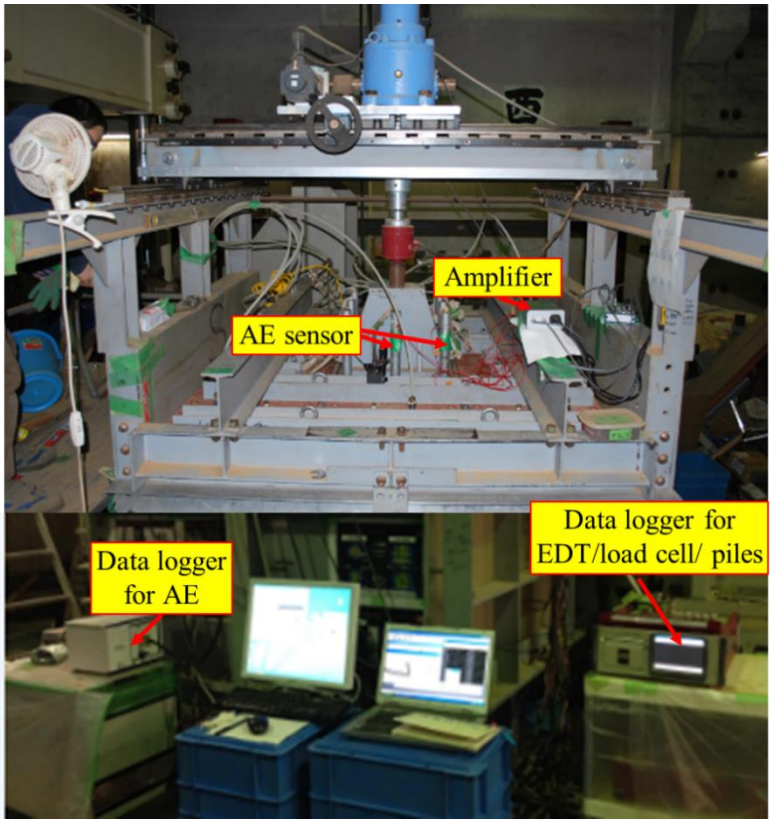

Figure 4.18 Overview of the experimental set up for group loading

4.2.3.3 Loading Procedures

The loading was performed in a displacement control manner and the loading rate was 1mm/min. The pile is loaded until fully yielded and the penetration depth was set around 20mm for each sequential cycle. Unloading was performed before the next loading step. There were two kinds of loading manners. One was “group loading” in which the footing was pushed down with all heads of piles connected to the footing, so that all piles settled into the ground together during the loading. Note that the footing never touched the ground surface throughout the tests. The other was “individual loading” in which each pile head was loaded individually by turns after the connection with footing at the each pile head was released. An illustration of the group loading and individual loading is shown in Figure 4.19. Usually two group loading cycles were followed by one individual loading in order to evaluate the effect of induced soil fabric. The data from the load cell and strain gauges inside the piles were recorded at a 20-second interval. Meanwhile, the data from AE sensors were recorded at a rate of 2M samples/second.

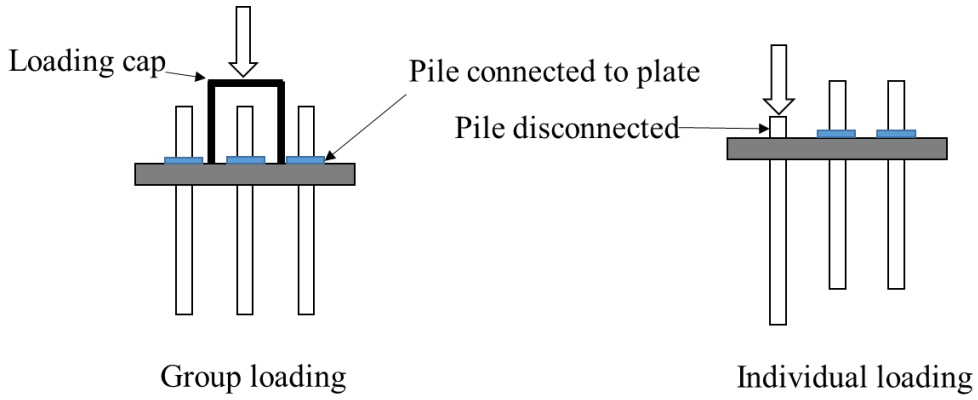

Figure 4.19 Illustration of group loading and individual loading

4.3.FUNDAMENTAL CALCULATIONS

4.3.1 Signal Interpretation

The AE signals in the current study were recorded in a continuous manner. As a result, the data file was extremely huge, making it impossible analyze entirely. Therefore, the source data file was further split into small files so that the data file can be loaded into MATLAB. This objective was achieved by coding an Express VI using Lab-view software. The developed code was attached in the appendix.

Figure 4.20 shows a typical wave data obtained from 0.5s recording. As the signal was sampled with 2MS/s, 2 million data points are included in the following sample data. Threshold was then applied to detect individual signals, and the further analysis such as count, FFT and signal arrival time, etc. were performed.

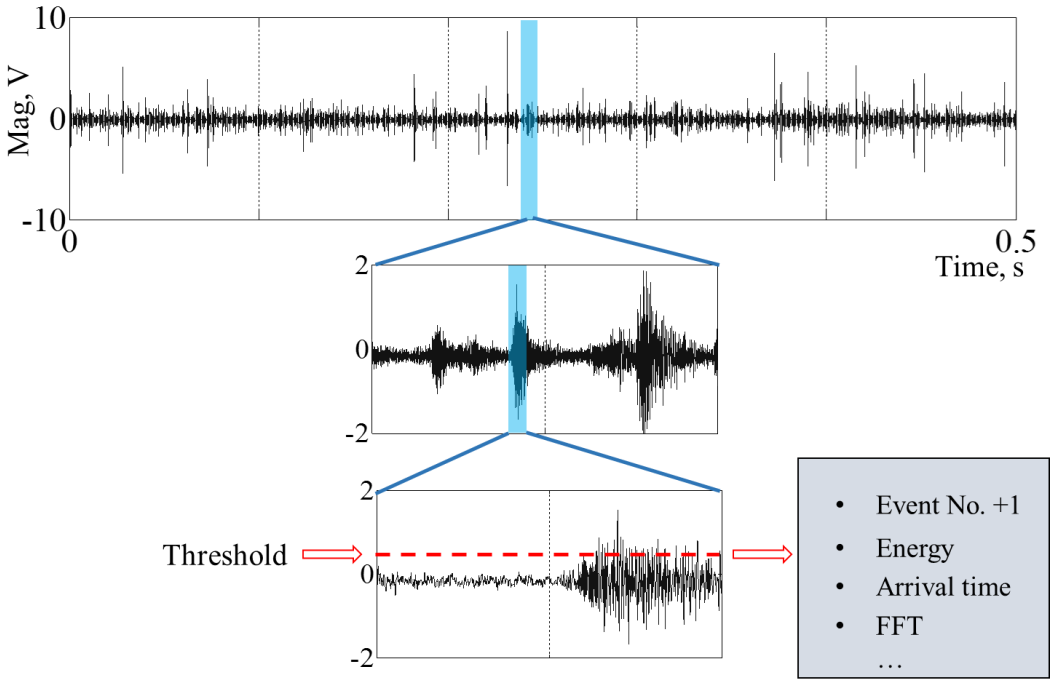

Figure 4.20 Illustration of signal processing

4.3.2 Signal Strength

As mentioned above, the released AE signal strength is calculated from the Measured Area under the Rectified Signal Envelop (MARSE) (ASM Handbook, 1992). Since the AE signals were recorded in discrete digital values, the following equation was used for calculation:

$$E_{MARSE} = \frac{1}{2}\sum_{t1}^{t2} V_{+}(t)\Delta t + \frac{1}{2}\sum_{t1}^{t2} \left|V_{-}(t)\right|\Delta t \qquad (4\text{-}1)$$

By contrast, the true signal energy, measured by integrating the squared AE signal voltage within signal duration, was calculated as following:

$$E_{\text{ture}} = \sum_{t1}^{t2} V^{2}(t)\Delta t \qquad (4\text{-}2)$$

where V is the measured voltage and $\triangle t$ is the signal sampling interval. An example comparison of the results from the above two equations is shown in Figure 4.21. As

expected, the general tendency of the two plots are similar to each other. In the following sections, if not indicated separately, only E_{MARSE} are used for plotting.

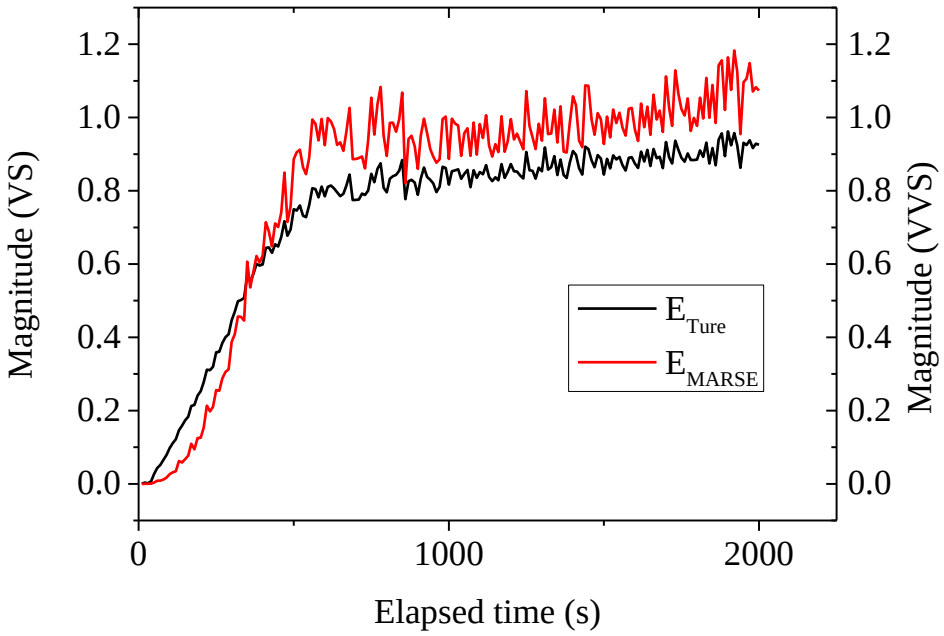

Figure 4.21 Comparison of E_{Ture} and E_{MARSE} plotting

4.3.3 Fast Fourier Transformation

By applying the Fast Fourier Transformation (FFT), the detected AE signals can be converted from time domain into frequency domain, and the frequency component with maximum amplitude in the spectrum was defined as the dominant frequency. Figure 4.22 shows a schematic illustration of FFT. In AE signal processing, the spectrum of a signal is believed to have intimate correlation with identical events, e.g. corresponding to particle crushing/sliding processes in the present study. A signal without any significant features in the time domain may show obvious characteristics in the frequency domain.

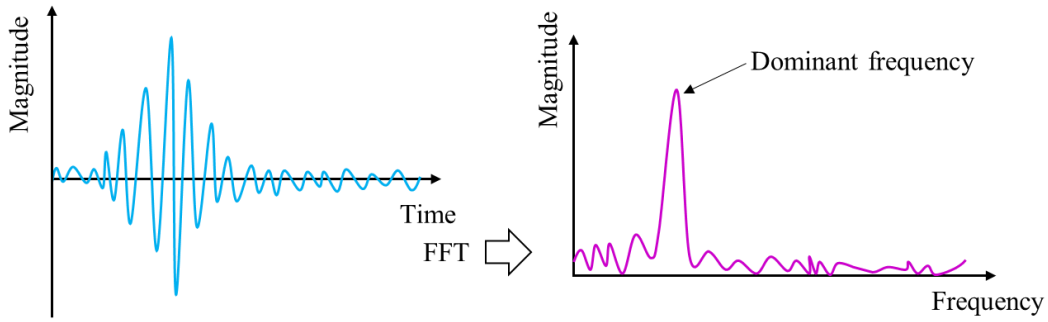

Figure 4.22 Schematic illustration of FFT

4.3.4 High-pass Filter

A signal wave is usually made of a serious of harmonic waves. A high-pass filter is able of cut off certain low-frequency components from the signal and remain the rest, as shown in Figure 4.23. For signals dominated by low frequency components, insignificant rising of high frequency component may be ignored from the above mentioned FFT analysis. Therefore, the high-pass filter provides an insight into high frequency components of AE signals. The detailed applications of this method will be presented in the following sections.

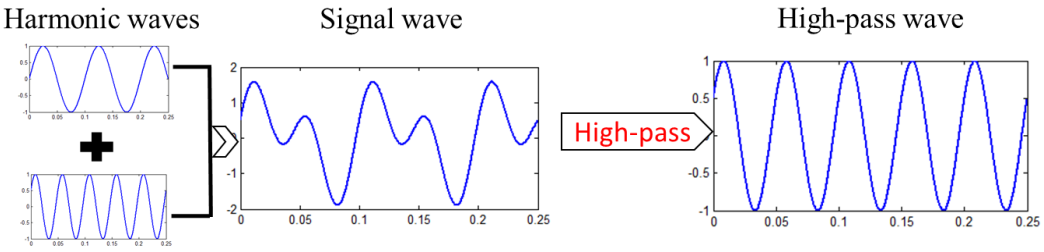

Figure 4.23 Schematic illustration of high-pass filter

4.4.SUMMARY

This chapter described the physical properties and microscopic images of tested materials used in this study. The detailed experimental program designed to achieve the objectives of this study was presented. Details of experimental procedures, including preparation model ground, pile set up and arrangement of AE sensors were

discussed. Some fundamental calculations related to AE signal analysis were discussed as well.

4.5. REFERENCES

Coop, M. R., Sorensen, K. K., Freitas, T. B., & Georgoutsos, G. (2004). Particle breakage during shearing of a carbonate sand. Géotechnique, 54(3), 157-163.

Kuwajima, K., Hyodo, M., & Hyde, A. F. (2009). Pile bearing capacity factors and soil crushabiity. Journal of geotechnical and geoenvironmental engineering, 135(7), 901-913.

Yu, F., (2014). Experimental study on particle breakage under high pressure (Doctoral dissertation). The University of Tokyo.

CHAPTER 5

FREQUENCY CHARACTERISTICS OF AE FROM PARTICLE CRUSHING AND SLIDING –

5.1. INTRODUCTION

The source of AE from a pile penetration test in sand comes from two main mechanical processes: sand particle crushing and sliding. As discussed in Chapter 2, the particle crushing may cause size reduction, and will eventually affect the bearing capacity of the ground due to a modified grain size distribution. Traditionally, the extent of crushing is quantified through comparison of the particle size distributions with original samples through destructive excavations after tests. Such measurements are difficult to be preferred as a routine methodology for process monitoring, since only the end conditions of particle crushing can be investigated. In addition, the excavation of soil sample is not always applicable especially in case of in-situ condition. A simple and effective investigation method is therefore desired.

AE technique is particularly helpful when dealing with specific type of mechanical process. Previous studies have shown that AE monitoring technique can be used for failure mode identification (Giordano et al. 1998, Ni and Iwamoto 2002, Gutkin et al. 2011). Among these studies, the dominant frequency of the AE event was often used as the defining parameter for signal differentiation, since it is less affected by testing conditions compared with amplitude or signal duration (De Groot et al. 1995). It is generally recognized that the frequency spectra of a signal is closely related to its source mechanism.

The sand particle crushing and sliding are two well defined source mechanisms for AE interpretation. Based on AE monitoring, it is possible to identify the occurrence of

crushing. Clarifying the AE characteristic involved within the crushing process is beneficial for further interpretation of AE results in pile testing. Therefore, prior to AE monitoring tests on pile, two different types of benchmark tests were performed to obtain a general information on the frequency characteristics of the said mechanical processes.

5.2. AE FROM SAND SLIDING

5.2.1 Experimental Design

For sand sliding tests, it is important to maintain a low stress level among particles, otherwise the grinding between contacting surfaces may be confused with particle fracturing. Three types of tests were designed to reproduce the process of sand sliding, with detailed description summarized in Table 5.1. Two particle sliding test may produce perfect individual sliding event, and the contacting stress can be approximately controlled by hand. Ruler moving test simulate the sand-metal interface sliding, which is similar to the pile-soil interface sliding. Hand stirring test produces massive inter-particle sliding under low stress level. It is believed that based on these three tests, the sliding of sand particles can be reasonably reproduced. Figure 5.1 shows the schematic illustrations of the mentioned tests.

Table 5.1 Summary of test conditions for sand sliding

Test type	Description	Illustration
Two particle sliding	One particle placed on the surface of a metal plate; put the other particle sliding against it. AE sensor attached on metal plate.	Figure 5.1 (a)
Ruler moving in sand	A sand box filled with sand; penetrate a ruler into sand; move ruler to cut sand. AE sensor attached on the ruler.	Figure 5.1 (b)
Hand stirring in sand	A sand box filled with sand; hand stirring in sand to generate sliding; AE sensor embedded in sand.	Figure 5.1 (c)

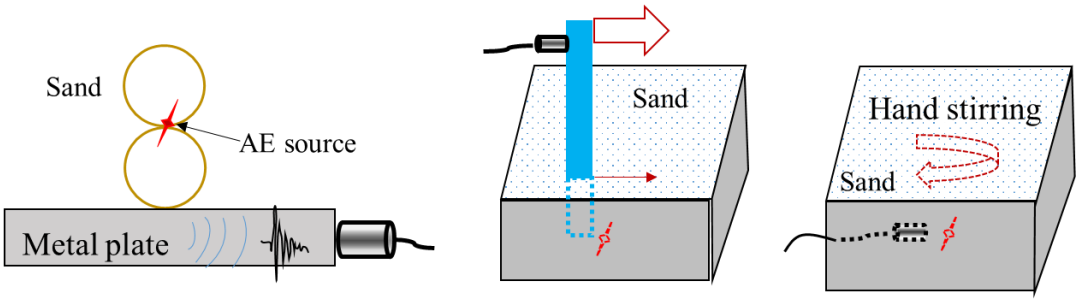

Figure 5.1 Schematic illustration of experimental design for sand sliding test

5.2.2 Background Noise

Electronic noise is unavoidable in AE monitoring testing. To evaluate the effect of background noise, a spectrum analysis is firstly applied to the noise signals. Figure 5.2 shows a waveform of the background noise and its spectrum features. Different frequency components are generally in a uniform distribution, with limited exceptions around 70 kHz, 500 kHz and 850 kHz. However, the peak amplitudes of the dominant components are less than 1mV. This low level of noise is believed to have negligible influence on the signal interpretation.

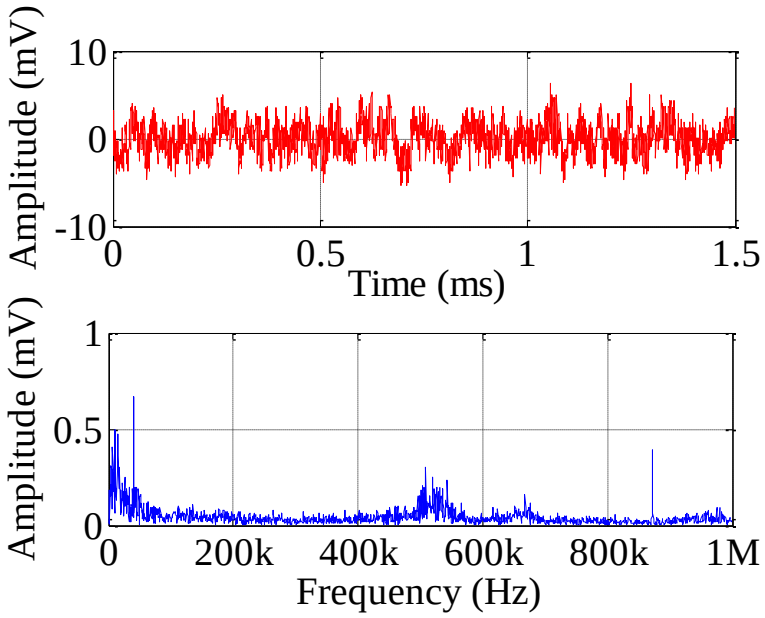

Figure 5.2 Background noise and its spectrum component

5.2.3 Frequency Characteristics of AE from Particle Sliding

Figure 5.3 shows a typical waveform and its spectrum component originating from two particle sliding. The dominant frequency resulting from process was relatively low (52 kHz), and the high frequency component was almost negligible as compared with the dominant frequency. Figure 5.4 shows the dominant frequency distributions of 150 continuous AE events. It is seen that most of the events have the dominant frequencies less than 100 kHz, with very few exceptions. The most typical range of dominant frequencies is between 4-40 kHz.

Figure 5.5 shows a waveform and its spectrum component generated by ruler moving in sand. Similar to the two particle sliding cases, the dominant frequency components were concentrated within the low frequency range. As can be seen in Figure 5.6, typical range of dominant frequencies is between 2-30 kHz.

Figure 5.7 shows a waveform and its spectrum component generated by hand stirring in sand. Again, low value of dominant frequency is observed. The typical range of dominant frequencies is between 2-20 kHz, as shown in Figure 5.8.

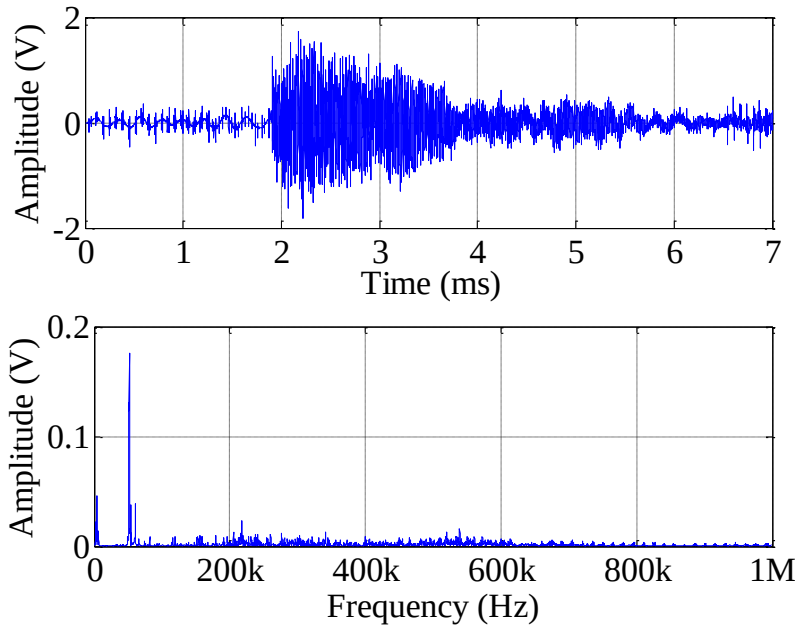

Figure 5.3 Waveform and spectrum component of an AE signal from two particle sliding

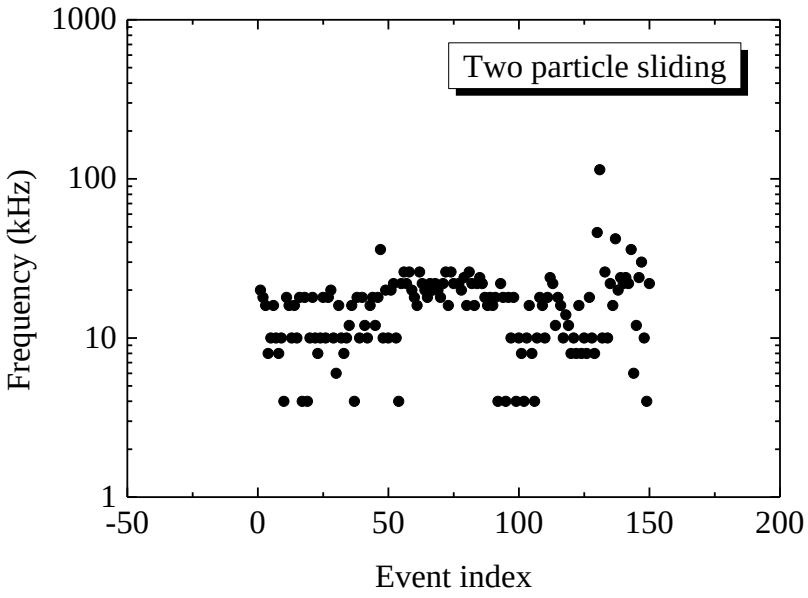

Figure 5.4 Dominant frequency distribution of 150 continuous events from two particle sliding

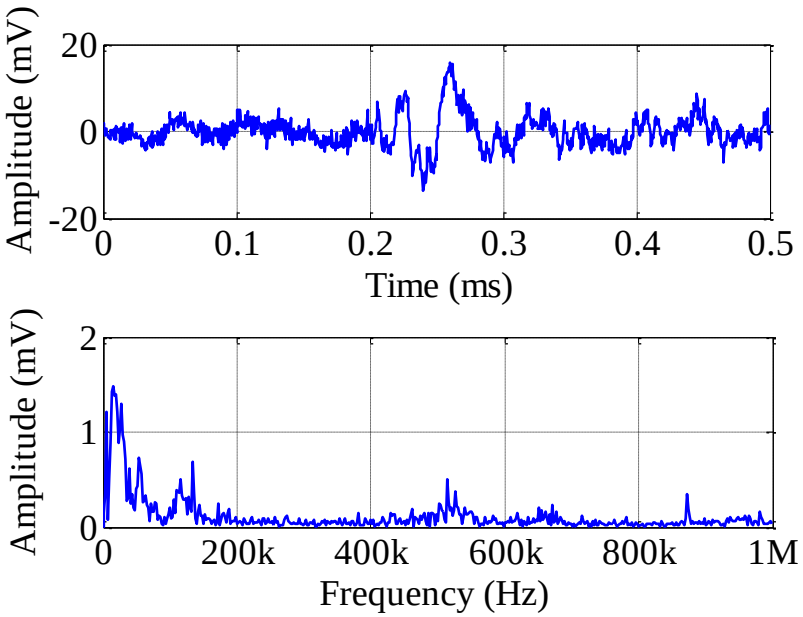

Figure 5.5 Waveform and spectrum component of an AE signal generated by ruler moving in sand

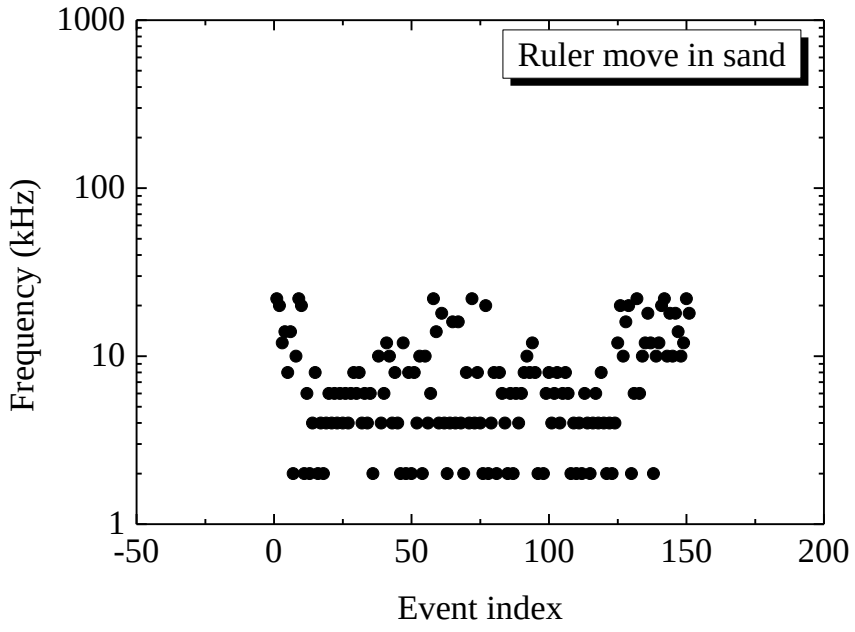

Figure 5.6 Dominant frequency distribution of 150 continuous events from ruler moving in sand

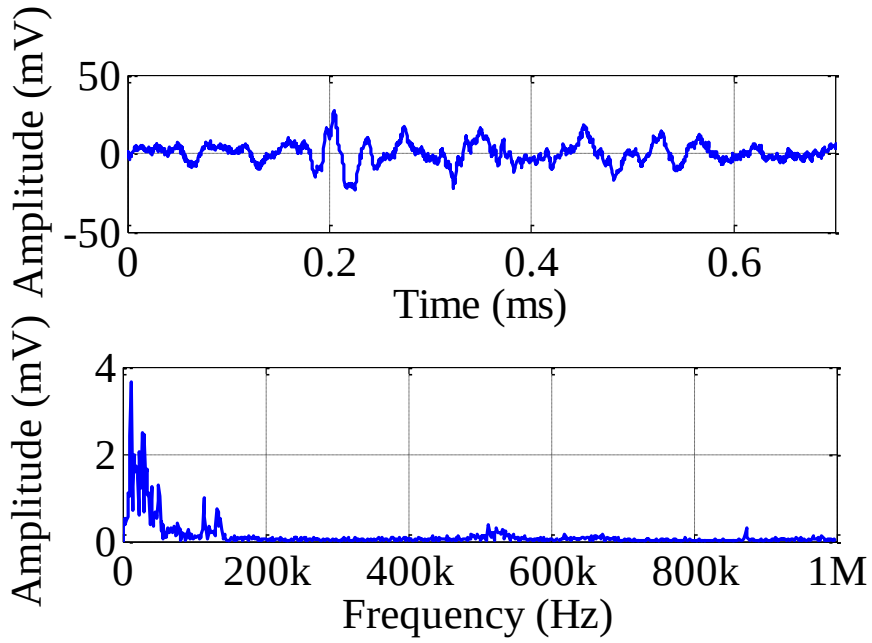

Figure 5.7 Waveform and spectrum component of an AE signal generated by hand stirring in sand

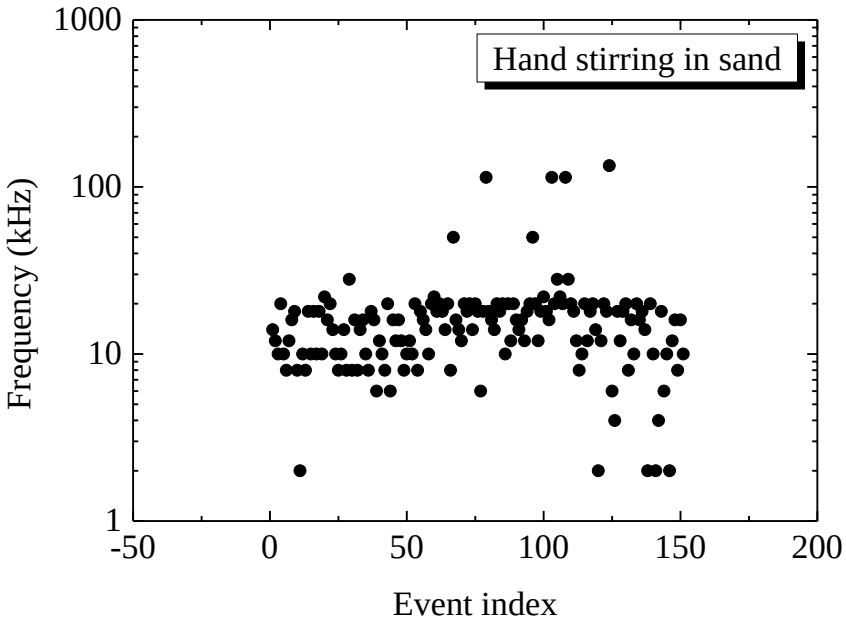

Figure 5.8 Dominant frequency distribution of 150 continuous events from hand stirring in sand

5.3. AE FROM SAND PARTICLE CRUSHING

5.3.1 Experimental Details

Figure 5.9 shows the test apparatus used for particle crushing. The particle for crushing was placed between two metal plates. The operating system was servo-controlled, with the maximum loading speed of 0.1mm/min and the minimum loading speeding of 0.001mm/min. A load cell and an EDT were used for load and displacement measurements, respectively. In this study, the axial loading speed of 0.1mm/min was used.

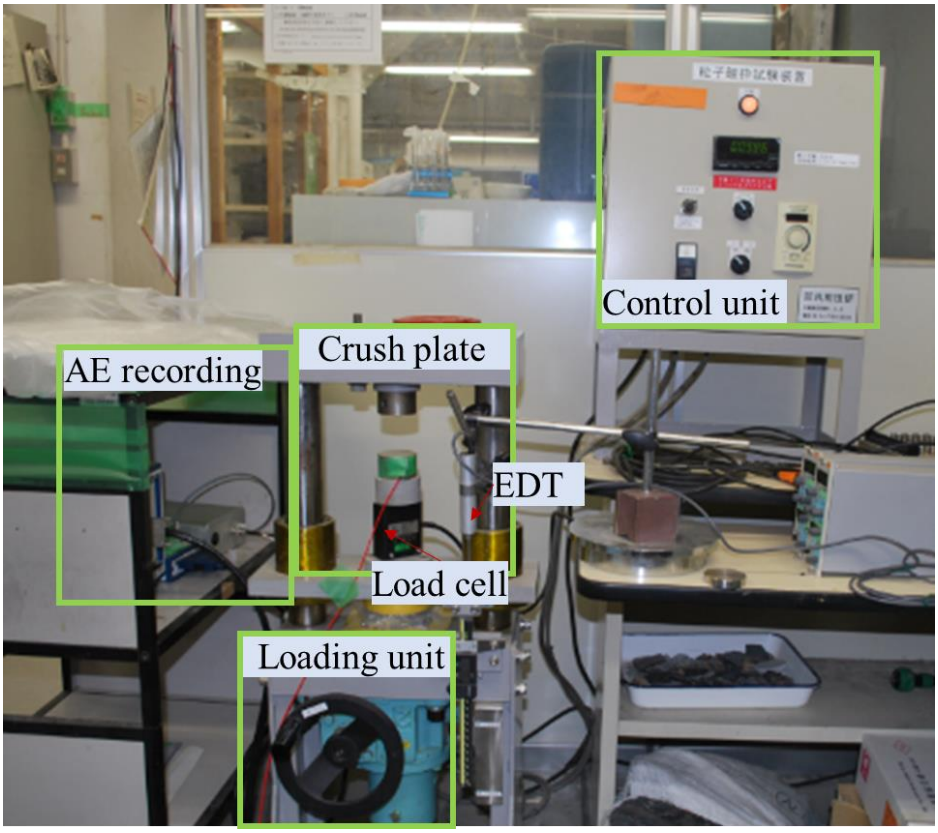

Figure 5.9 Experimental apparatus for particle crushing test

Since the tested particle was not well shaped and the size was relatively small, the AE sensor was not directly coupled to the surface of the tested grain but mounted on the metal plate as illustrated in Figure 5.10. High vacuum grease was used as the coupling material to fill the gap between the AE sensor and the metal plate. During the test, the AE signals generated inside the particle propagated to the metal loading plate and captured by the sensor. The data recording and analyzing are the same with pile loading testing as described in previous sections.

The materials used in crushing tests were selected from silica sand and coral sand, as shown in Figure 5.11, same material as used in pile tests but with larger sizes. Particles with different sizes were selected and tested.

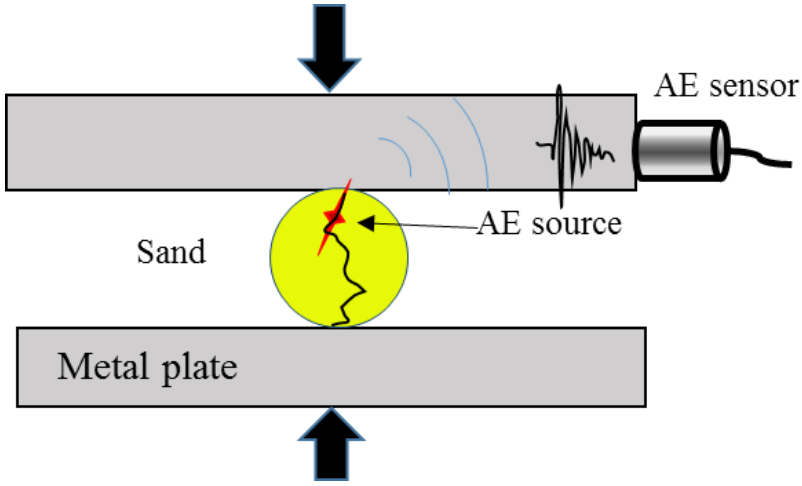

Figure 5.10 Schematic illustration of particle crushing and AE monitoring

Figure 5.11 Photo of sand particles used in crushing test

5.3.2 Particle Properties

The particle properties of the tested materials are summarized in Table 5.2. Particle sizes were measured in three different directions representing the maximum, medium and minimum size of the particle. Figure 5.12 shows the load-displacement profile from single particle crushing tests. A three-stage bearing load development was illustrated on the curve of Silica #2. At the beginning of loading, the particles underwent a readjustment period to obtain a better contact with the loading plates. Small fluctuations can be observed in the load-displacement curve in this stage. This stage was followed by an elastic deformation stage with bearing load increasing linearly. Finally, the particle failed, either suddenly or gradually.

Three types of samples exhibited significant difference in the stiffness property, as was revealed from the slope in the elastic part of the curves. Silica sand #2 (S5) was most stiff due to its good particle integrity, followed by Silica sand #1 (S1-S4). Coral sand was found to be the weakest (C6-C7). Silica #1 was similar in particle structure, but with different sizes. Silica #1 (S3-S4) was smaller in size and showed lower failure load, while their stiffness showed no obvious difference, e.g. S1 with larger size had similar stiffness with S4 with smaller size. Different particle properties will lead to different AE characteristics, which will be discussed in the next section.

Table 5.2 Summary of particle properties

Test No.	Sand type	Structure feature	Size (mm^3)	Load at main failure (N)
S1	Silica #1	With pre-existing fractures	5.4×6.1×6.3	236.7
S2			5.3×5.4×5.7	140.3
S3			1.4×1.5×1.9	64.7
S4			1.2×1.8×2.0	50.3
S5	Silica #2	Good integrity	3.4×4.9×8.5	428.4
C6	Coral	Porous	4.7×5.2×5.4	70.4
C7			3.6×4.0×5.4	55.5

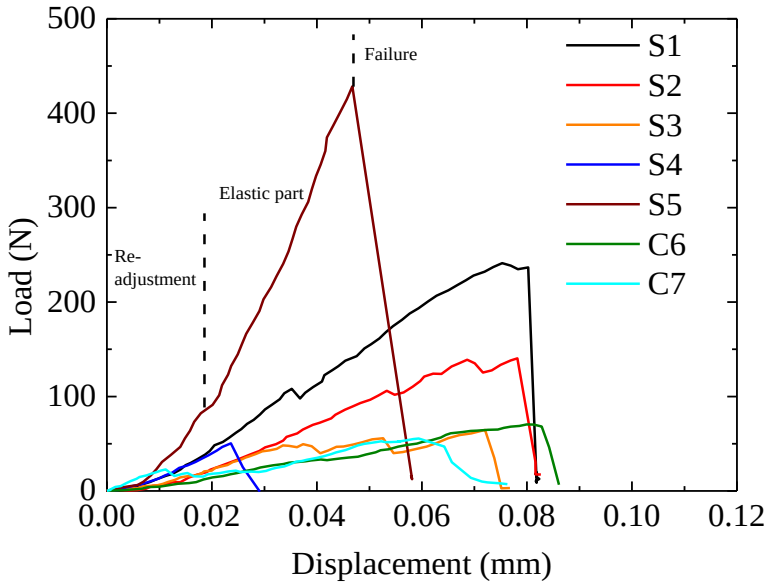

Figure 5.12 Load-displacement relationships for tested particles.

5.3.3 AE Activity during Particle Crushing

Figure 5.13 shows the AE activity and load history of the tested particles. It clearly shows that the AE was not uniformly distributed during the whole process of loading. In general, the AE was active when there was a stress drop of stress variation, and there were also "silent" periods with inactive AE. Overall, three stages of AE activity can be identified (identified in Test S2, which is more evident). The first stage started at the beginning of each loading and showed considerably high AE activity caused by grain densification, friction between loading plates and inner crack readjustment. The second stage was chartered by inactive AE activity corresponding to the elastic deformation of the particle. And the third stage was featured by substantial AE activity due to progressive crack growth corresponding to the plastic deformation of the particle. Similar observation of three stages was also reported by He et al. (2010) in triaxial compression tests of limestone. It is worth noting that the AE was observed not only at the failure stage of the particle fracture but also before the failure. The AE was detected even when no obvious variation was found in bearing load capacity, indicating that the AE monitoring was more sensitive to reflect the inner particle stress status. However, it did occur much more substantially when there was a significant decrease in the bearing load of the particle, which demonstrates that the process of particle fragmentation is consistent with previous studies that the failure of a material is usually featured by AE activity (Cai et al. 2007).

For the Siliceous sand, it is also found that the sample #1 (S1-S4) was more emissive than sample #2 (S5). This phenomenon can be explained by the micro structural features as revealed in the previous section. The source of AE mainly comes from the inner crack initiation and crack growth. Silica #1 was more fragmentized with massive weak interfaces and defects, while Silica #2 was better bonded. In contrast, the emission level of Coral sand was relatively low with maximum value of AE counts approximately one-tenth of siliceous sand. However, the general tendency was quite similar, with highly marked AE activity at the failure stage of the crushing.

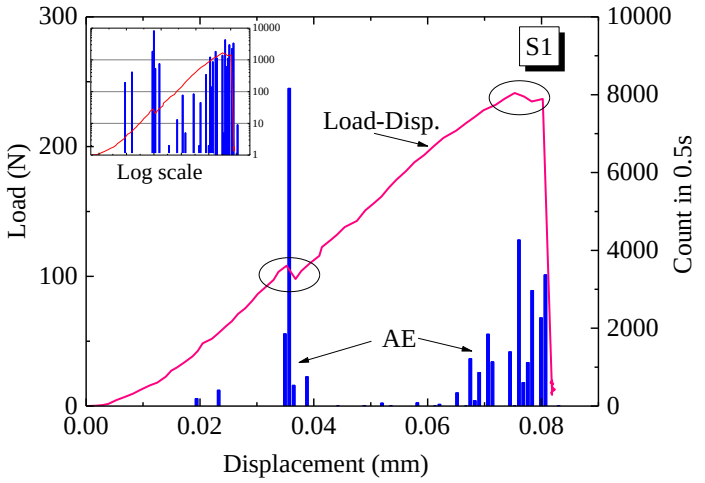
S1
Load-Disp.
AE
Log scale
Load (N)
Count in 0.5s
Displacement (mm)
0
100
200
300
0.00
0.02
0.04
0.06
0.08
2000
4000
6000
8000
10000
1
10
100
1000
10000

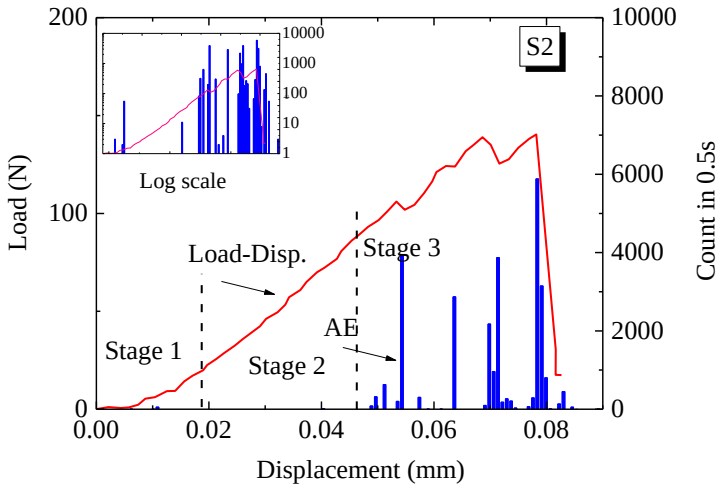
S2
Load-Disp.
Stage 1
Stage 2
Stage 3
AE
Log scale
Load (N)
Count in 0.5s
Displacement (mm)
0
100
200
0.00
0.02
0.04
0.06
0.08
2000
4000
6000
8000
10000
1
10
100
1000
10000

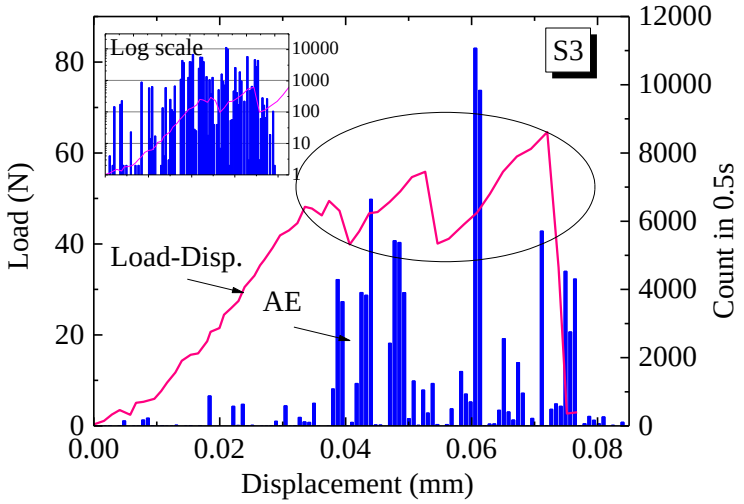
S3
Log scale
Load-Disp.
AE
Load (N)
Count in 0.5s
Displacement (mm)
0
20
40
60
80
0.00
0.02
0.04
0.06
0.08
2000
4000
6000
8000
10000
12000
1
10
100
1000
10000

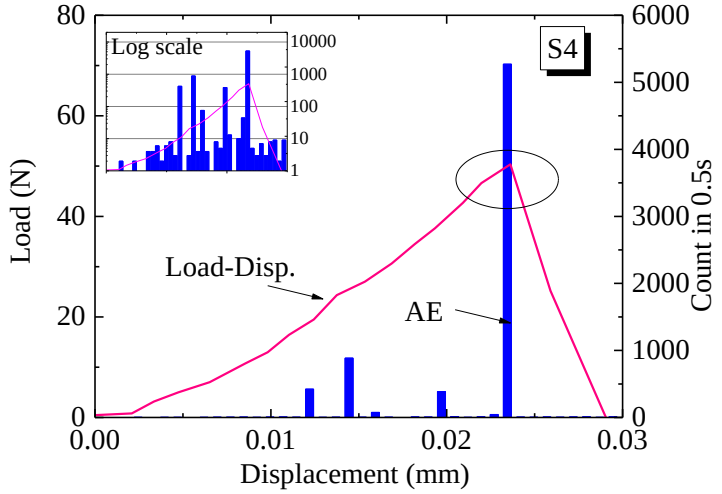
S4
Log scale
10000
1000
100
10
1
Load-Disp.
AE
Load (N)
Count in 0.5s
Displacement (mm)
0
20
40
60
80
0
1000
2000
3000
4000
5000
6000
0.00
0.01
0.02
0.03

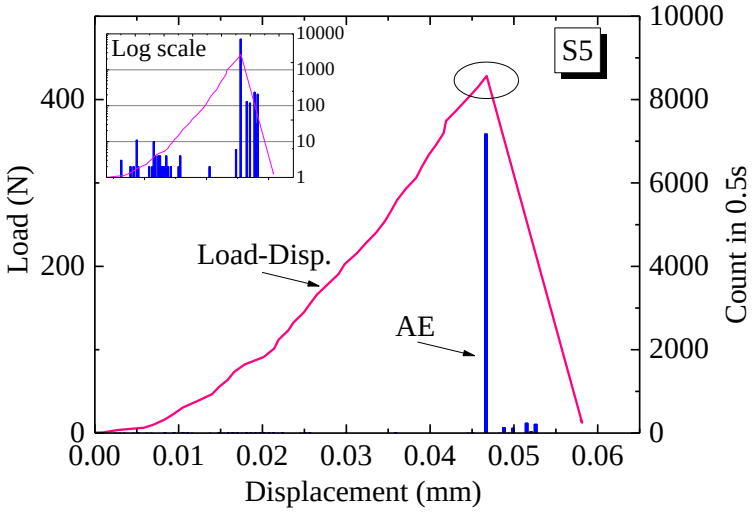
S5
Log scale
10000
1000
100
10
1
Load-Disp.
AE
Load (N)
Count in 0.5s
Displacement (mm)
0
200
400
0
2000
4000
6000
8000
10000
0.00
0.01
0.02
0.03
0.04
0.05
0.06

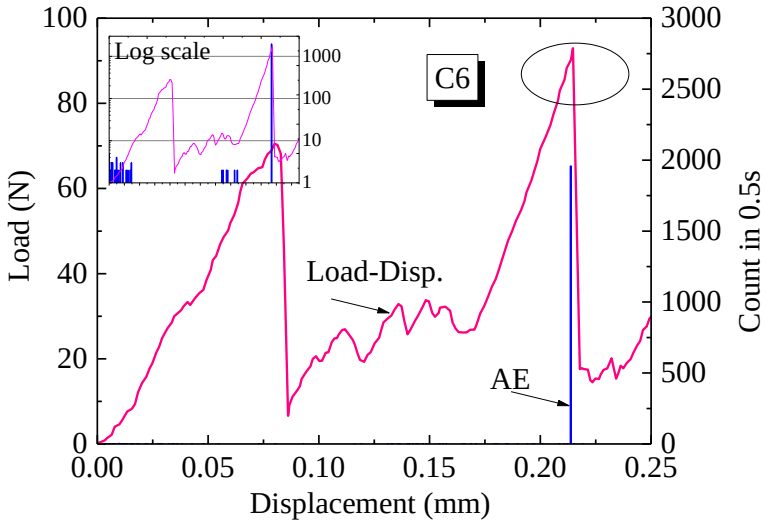
C6
Log scale
1000
100
10
1
Load-Disp.
AE
Load (N)
Count in 0.5s
Displacement (mm)
0
20
40
60
80
100
0
500
1000
1500
2000
2500
3000
0.00
0.05
0.10
0.15
0.20
0.25

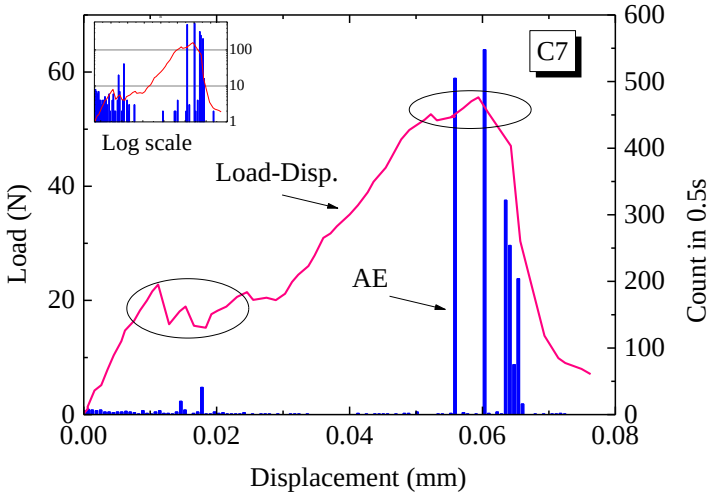

Figure 5.13 AE activity and load history for the tested materials.

5.3.4 Signal Waveforms and Spectral Analysis

As mentioned above, the detected AE may result from different sources, e.g. plate friction, crack closure, and crack growth, etc. The intensity of AE rate indicates the stress condition during the particle crushing. While the AE waveforms deliver more source information. Therefore, individual AE events are studied in this section.

In order to analyse the frequency characteristics during particle crushing, the obtained AE signals were converted from time domain to frequency domain by FFT. Figure 5.14 (a), (b) and (c) show the typical AE waveforms and the spectrums recorded during the main failure stage of particle crushing. It can be seen that the frequency component up to 600 kHz increased significantly. Some of the dominant frequency components can be easily identified.

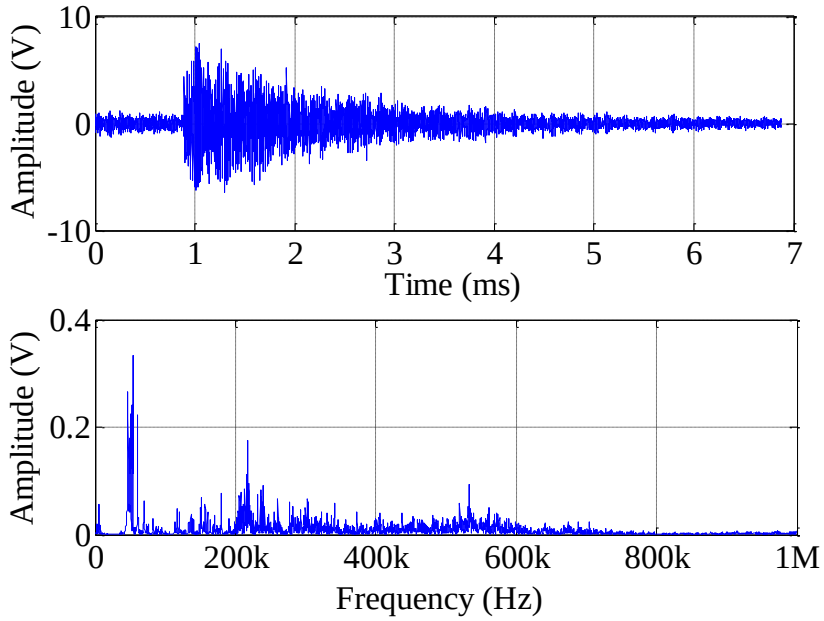
Amplitude (V)
10
0
-10
0
1
2
3
4
5
6
7
Time (ms)
Amplitude (V)
0.4
0.2
0
0
200k
400k
600k
800k
1M
Frequency (Hz)

(a)

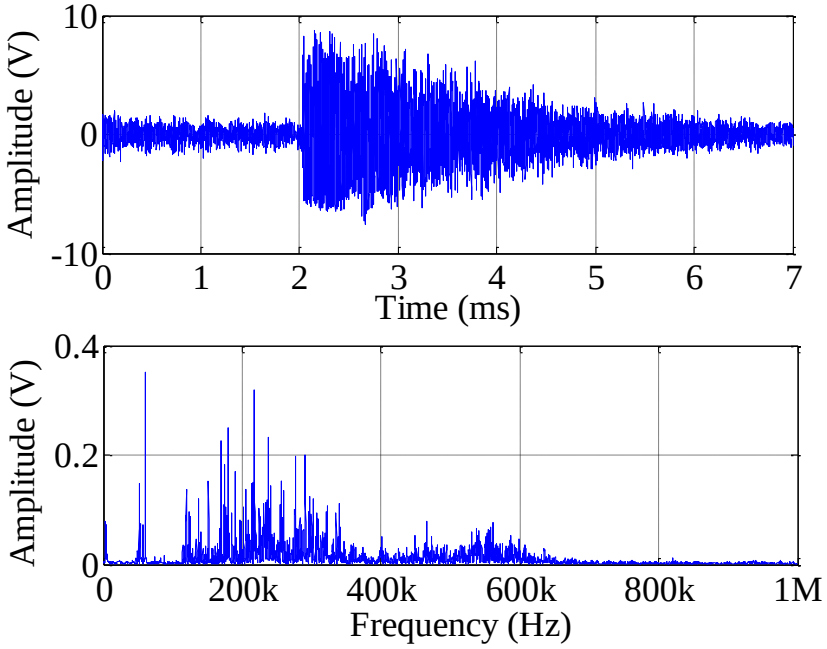
Amplitude (V)
10
0
-10
0
1
2
3
4
5
6
7
Time (ms)
Amplitude (V)
0.4
0.2
0
0
200k
400k
600k
800k
1M
Frequency (Hz)

(b)

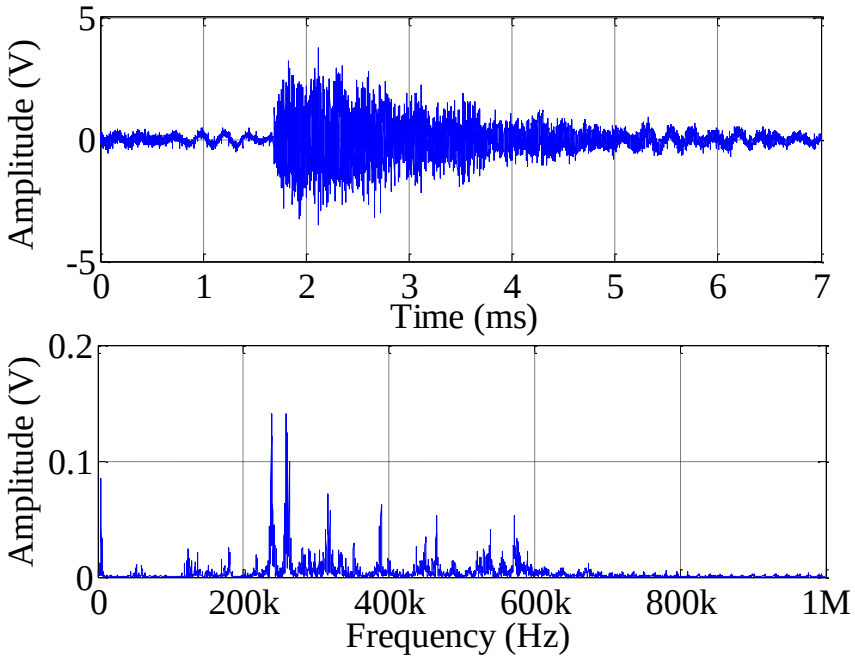

(c)

Figure 5.14 AE waveform and amplitude spectra of events during crushing failure: (a) Crushing failure of Silica sand #1; (b) Crushing failure of Silica sand #2; (c) Crushing failure of Coral sand

5.3.5 Frequency Characteristics of AE from Particle Crushing

In order to analyse the frequency characteristics during the whole particle crushing process, the FFT was applied to all AE waveforms recorded. Note that in Figure 5.14, low frequency component exists with considerable high amplitude value, which was likely to be caused by the sound blast of violent particle crushing at failure. This section aims to investigate the high frequency components during particle crushing, Therefore, to avoid this disturbance, the AE signals were treated with a high pass filter to eliminate low frequency component (<100 kHz). Figure 5.15 shows the dominant frequency distributions for the tested three types of samples. Each hollow circle in the figure represents one AE event. It is noted that the high frequency AEs were mostly observed at high stress level, particularly when there was obvious decrease in bearing load. A typical example is the Test S3, where notable fluctuation of the bearing load was observed, and consequently, resulting in substantial AE signals with high frequency within that period. Considering that high stress level will

cause the crack initiation and growth, it is suggested that the high frequency AEs were associated with inner crack development. The main bands of the dominant frequency lie between 200 kHz~400 kHz and 500 kHz~600 kHz for Silica sand #1, 200 kHz~250 kHz for Silica sand #2 and 250 kHz~300 kHz for Coral sand. However, it should be pointed out that the distribution of the dominant frequency value was rather scattering. As a matter of fact, the correlation between the appearance of high frequency and fracturing is more important from the above findings. A clustering of high frequency AEs indicates that certain fatal cracks were developing inside the particle, which will consequently result in bearing capacity loss or even complete failure.

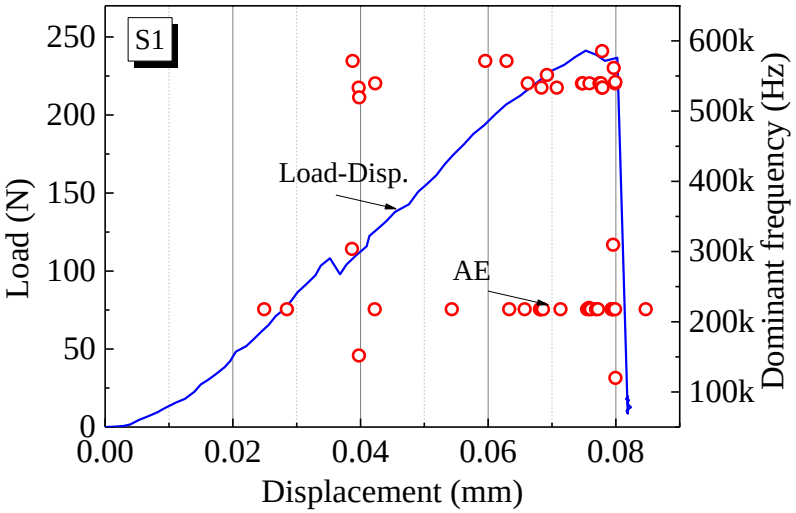

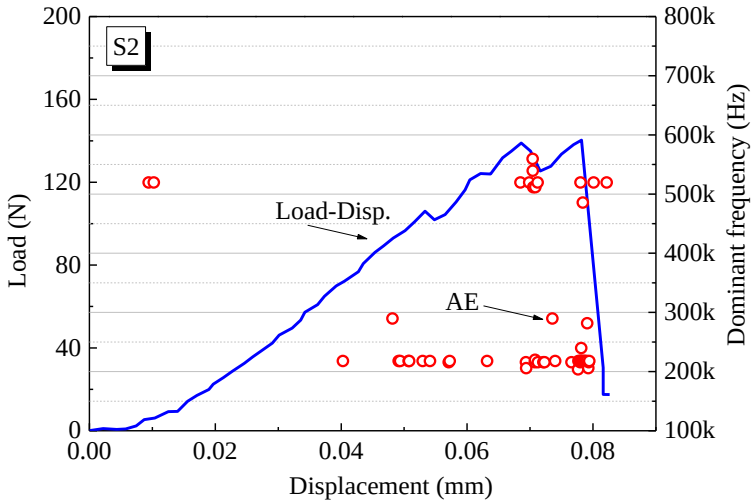

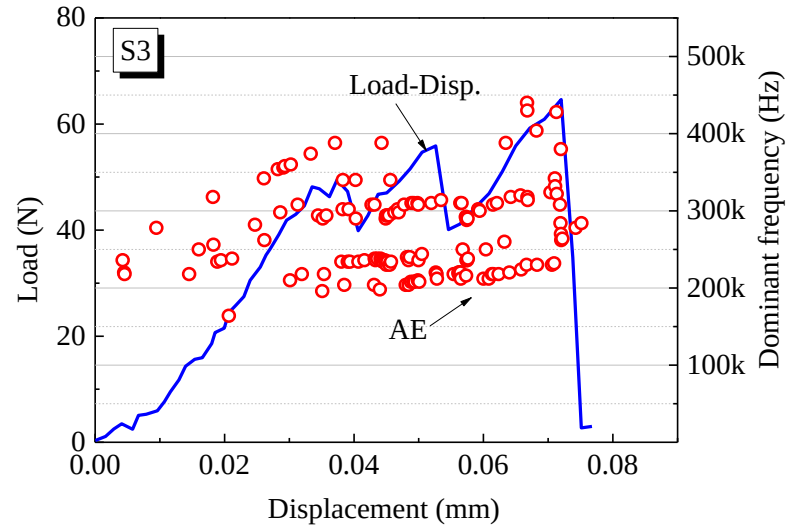
S3
Load-Disp.
AE
Load (N)
Dominant frequency (Hz)
Displacement (mm)
0
20
40
60
80
100k
200k
300k
400k
500k
0.00
0.02
0.04
0.06
0.08

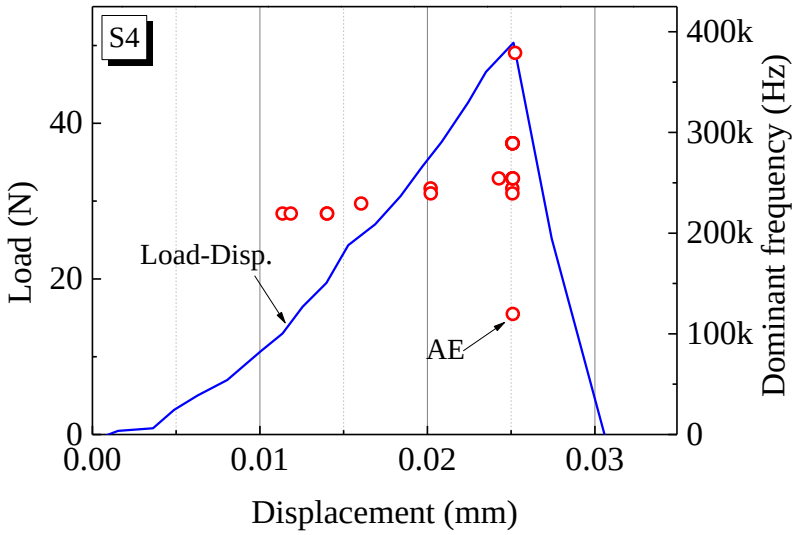
S4
Load-Disp.
AE
Load (N)
Dominant frequency (Hz)
Displacement (mm)
0
20
40
0
100k
200k
300k
400k
0.00
0.01
0.02
0.03

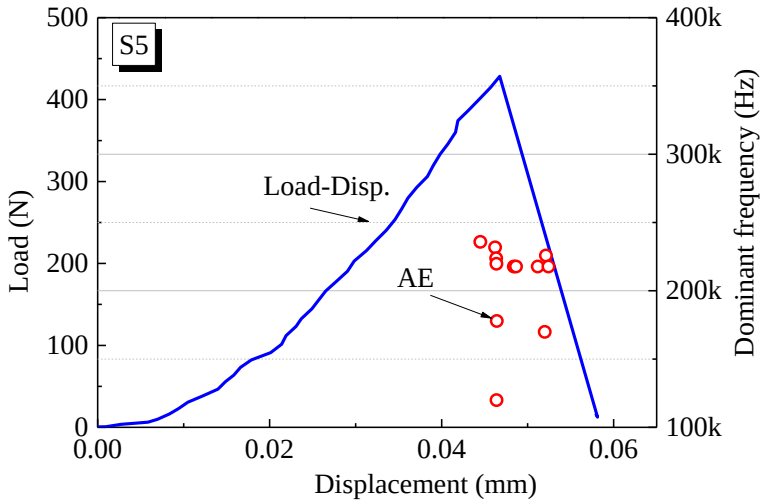
S5
Load-Disp.
AE
Load (N)
Dominant frequency (Hz)
Displacement (mm)
0
100
200
300
400
500
100k
200k
300k
400k
0.00
0.02
0.04
0.06

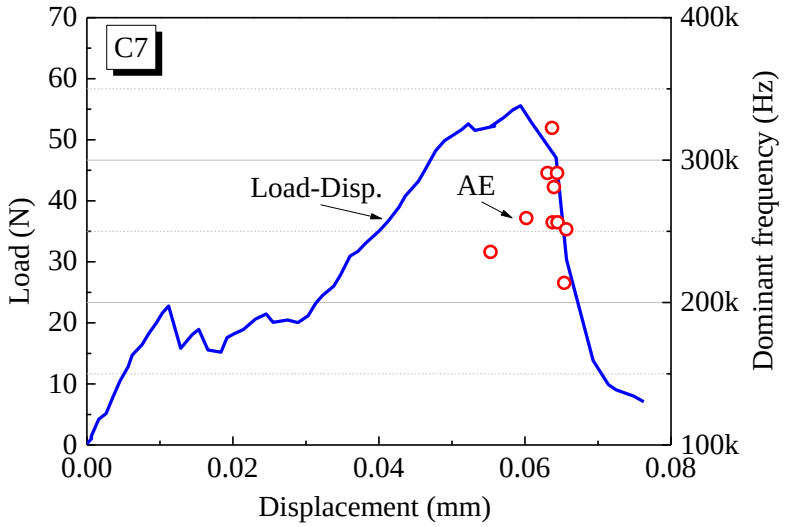

Figure 5.15 Dominant frequency (>100 kHz) distributions during particle crushing processes

5.4. SUMMARY AND DISCUSSION

From the above single crushing tests, it is clear that active AE occurs close to the peak stress. More specifically, AE activities were found to be associated with the increased level of damage in the particle. Compared with sand sliding tests, a significant rising of the high frequency component was observed associated with crushing AE events. In addition, previous studies from experiments with rock, concrete and sandstone samples confirmed that the AE spectra from fracture mechanisms is associated with high frequency AE (Masera et al. 2001, He et al. 2010, De Groot et al. 1995, Read et al. 1995). For example, Read et al. (1995) reported peak AE frequencies ranged between 100-600 kHz observed from triaxial testing of porous rock. This is highly consistent with the present study. As illustrated in Figure 5.14, the high frequency components (100-600 kHz) rose notably due to fracture failure. In contrast, the importance of frequency characteristics during particle crushing was highlighted in this study. The high frequency components of AE (say >100 kHz) can be regarded as a hallmark of the ongoing fracturing. With conventional methods, the fatal failure of the particle could only be identified from the major drop of bearing load. As observed in AE monitoring, however, it is possible to recognize the gradual straining process

based on the high frequency AE components originated from crack development. This feature meets the practical demand for an easy and effective monitoring approach on the grain fracture problems.

However, it should be noted that AE generated by frictional sliding under considerably high contacting stress may also result in high frequency, as reported by Kato et al. (1994), who observed the high-frequency elastic waves during laboratory shear rupture of granite samples. They argued that this process, however, is attributed to the brittle micro-fracture of asperities on the sliding surface. Therefore, it is more reasonable to classify such situations as fracture mode. In contrast, Dagois-Bohy et al (2010) conducted sand avalanches tests to make sand sliding on the flowing surface, and they were only able to detect rather low frequency AEs (<200 Hz). Michlmayr and Or (2014) observed up to 80 kHz AEs in direct shear tests under the confining pressure of 60kPa. Although different materials were involved, it seems that the confining pressure increased the dominant frequencies of AE. A summary of testing conditions and the observed AE frequencies in shown in Table 5.3 and Figure 5.16.

Another notable aspect from the above observation concerns with the particle type dependence. Among different types of particle samples, regardless of the exact value, it is found that they shared similar tendency of AE activity evolution and dominant frequency distribution, e.g. high frequency events were mostly observed during the impending failure. This suggests that AE can be used as a common tool for different granular types. Referring to coral sand grain, the total number of AE events is less than silica sand grains. It demonstrates the influence of material itself on the AE behavior. This difference is expected to be more evident while applying AE to highly stressed granular aggregates.

Based on the above knowledge, it is reasonable to regard high frequency spectrum (e.g. >100 kHz) as a hallmarking parameter for AE with fracture mechanism. Particle crushing by shear under high contact force is also accounted for high frequency AEs, which provides a new method for particle crushing evaluation in laboratory testing. This idea is further applied to AE monitoring in piles and will be discussed in detail in the following chapters

Table 5.3 Summary of AE dominant frequencies from different source mechanisms

Literature	AE mechanism	Contact stress	Material	Test procedure	Dominant freq.
Dagois-Bohy et al., 2010	Sliding of grains	1~2kPa	sand	Sand avalanche in a box	60 ~160 Hz
Michlmayr and Or, 2014	Sliding of grains	60kPa	Soda-lime glass beads	Direct shear test	30 ~80 kHz
Read et al., 1995	Rock cracking	20~100MPa	Sandstone	Triaxial compression	100 ~600 kHz
He et al., 2010	Rock burst	30~100Mpa	Limestone	True-triaxial unloading	60 ~100 kHz, 170 - 190 kHz
Kato et al., 1994	Frictional shearing	2.5~20Mpa	Granite	Shear	200 kHz~1 MHz
Current study	Particle crushing	20~60Mpa	Silica/Coral sand grain	Single particle crushing	100 ~600 kHz
Current study	Particle sliding	<10kPa	Silica/Coral sand grain	Particle-particle sliding	2-60 kHz

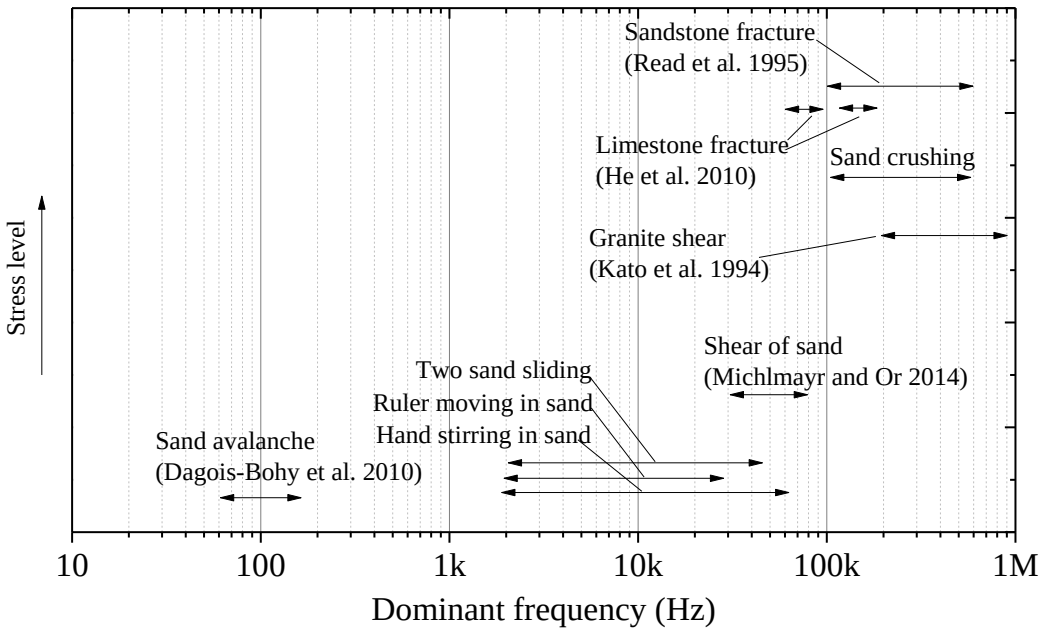

Figure 5.16 Illustration of dominant frequency and signal source mechanism

5.5. CONCLUDING REMARKS

This chapter presents the AE method to monitor the processes of sand crushing and sliding. The main objective is to characterize the AE signature in terms of dominant frequency during sand crushing. It is found that the spectra of AE originated from the fracture failure of the particles exhibited a significant rising of high frequency components (>100 kHz). The dominant frequency distributions of the tested samples further showed that high frequency components were mostly observed when the stress level was high, especially when there was an obvious decreasing in bearing load. This suggests a profound correlation between sand crushing and high frequency AEs. It is therefore argued that the high frequency AEs can be used to monitor and represent the extent of crushing in stressed sand.

5.6. REFERENCES

Cai, M., Morioka, H., Kaiser, P. K., Tasaka, Y., Kurose, H., Minami, M., & Maejima, T. (2007). Back-analysis of rock mass strength parameters using AE monitoring data. International Journal of Rock Mechanics and Mining Sciences, 44(4), 538-549.

Dagois-Bohy, S., Ngo, S., du Pont, S. C., & Douady, S. (2010). Laboratory singing sand avalanches. Ultrasonics, 50(2), 127-132.

De Groot, P. J., Wijnen, P. A., & Janssen, R. B. (1995). Real-time frequency determination of acoustic emission for different fracture mechanisms in carbon/epoxy composites. Composites Science and Technology, 55(4), 405-412.

Giordano, M., Calabro, A., Esposito, C., D'amore, A., & Nicolais, L. (1998). An acoustic-emission characterization of the failure modes in polymer-composite materials. Composites Science and Technology, 58(12), 1923-1928.

He, M. C., Miao, J. L., & Feng, J. L. (2010). Rock burst process of limestone and its acoustic emission characteristics under true-triaxial unloading conditions. International Journal of Rock Mechanics and Mining Sciences, 47(2), 286-298.

Kato, N., Yamamoto, K., & Hirasawa, T. (1994). Microfracture processes in the breakdown zone during dynamic shear rupture inferred from laboratory observation of near-fault high-frequency strong motion. pure and applied geophysics, 142(3-4), 713-734.

Masera, D., Bocca, P., & Grazzini, A. (2011, July). Frequency analysis of acoustic emission signal to monitor damage evolution in masonry structures. In Journal of Physics: Conference Series (Vol. 305, No. 1, p. 012134). IOP Publishing.

Michlmayr, G., & Or, D. (2014). Mechanisms for acoustic emissions generation during granular shearing. Granular Matter, 16(5), 627-640.

Ni, Q. Q., & Iwamoto, M. (2002). Wavelet transform of acoustic emission signals in failure of model composites. Engineering Fracture Mechanics, 69(6), 717-728.

Gutkin, R., Green, C. J., Vangrattanachai, S., Pinho, S. T., Robinson, P., & Curtis, P. T. (2011). On acoustic emission for failure investigation in CFRP: Pattern recognition and peak frequency analyses. Mechanical Systems and Signal Processing, 25(4), 1393-1407.

Read, M. D., Ayling, M. R., Meredith, P. G., & Murrell, S. A. (1995). Microcracking during triaxial deformation of porous rocks monitored by changes in rock physical properties, II. Pore volumometry and acoustic emission measurements on water-saturated rocks. Tectonophysics, 245(3), 223-235.

CHAPTER 6

AE CHARACTERISTICS DURING PILE PENETRATION

6.1. INTRODUCTION

The underlying behavior of subsoil subjected to pile loading is crucial to clarify the pile bearing mechanism. Typical instrumentation to indicate the subsoil status includes earth pressure sensors for stress determination, and displacement sensors for measurement of pile settlement (Altaee et al. 1992, Jardine et al. 2009, Zhu et al. 2009, Talesnick 2013). All such measurements are however based on load-settlement analysis, and provide relatively few information on the subsoil behavior due to low sensitivity for representing of micro-scale stress-strain variations. Toward a better insight to the intrinsic reactions of soils under stress, a sensitive detecting technique would therefore be desired. A novel idea of investigating soil behaviors by monitoring AE activity is presented in this chapter. This idea mainly comprises of installing a set of AE instrumentation assembly to the conventional pile testing apparatus, and monitoring the activity of AE during the process of pile penetration. Detailed results are presented in the following sections.

6.2. DESCRIPTION OF TEST CONDITION

This chapter covers laboratory model pile tests exploring the behavior of AE characteristics associated with pile penetration. Three series of pile loading tests were conducted to explore the effects of sand type and loading procedurals on AE behavior. In the first series of tests, three types of silica sand samples with different relative densities corresponding to loose, medium and dense ground conditions were prepared. The pile was loaded once to reach a penetration depth of 100mm. In order to explore

the effect of previous loading steps on the latter steps, another series of tests with silica sand were subsequently conducted. In this series of tests, the pile was loaded at every 20mm, and unloading was conducted before the next loading step. Totally five loading-unloading cycles were performed. In the third series of tests, coral sand with three different relative densities were tested. This series of tests aimed to explore the AE behavior in more crushable materials. The following sections explain the test results and corresponding discussions of these tests. Initial test conditions and other important parameters of each test series are summarized in Table 6.1.

Table 6.1: Test conditions in for AE activity monitoring

Test Designation	Material	Ground condition	Void ratio, e	Relative density, Dr	Loading procedure
T1-Si-D	Silica No.5	Dense	0.695	91.5%	100mm
T2-Si-M	Silica No.5	Medium	0.707	83.2%	100mm
T3-Si-L	Silica No.5	Loose	0.801	66.7%	100mm
T4-Si-Se-D	Silica No.5	Dense	0.683	94.5%	20mm*5
T5-Si-Se-M	Silica No.5	Medium	0.749	78.9%	20mm*5
T6-Si-Se-L	Silica No.5	Loose	0.794	68.3%	20mm*5
T7-Co-D	Coral No.1	Dense	0.841	99.6%	100mm
T8-Co-M	Coral No.1	Medium	0.888	87.8%	100mm
T9-Co-L	Coral No.1	Loose	1.010	56.3%	100mm

6.3. EXPERIMENTAL RESULTS ON SILICA SAND NO.5

6.3.1 Load-settlement Behavior

Figure 6.1 illustrates the evolutions of the ground resistance with the penetration of piles. Generally, an increased relative density of the model ground yielded an increased tip resistance. Note that the tip resistance herein represents the total ground resistance. Considering that the pile surface was smooth and the embedded depth was relatively shallow (200mm), the friction resistance is therefore not considered separately. In general, a rapid bearing load development can be seen during the first 10mm penetration, followed by a reduced gradient of load increment. However, no steady-state was observed for all three tested cases, as the ground resistance continuously increased gradually after ground yielding. Among different test conditions, it shows that the tip resistance of dense ground was almost twice as large as loose ground at the same penetration depth. The dependence of the AE characteristics on ground conditions will be discussed in the next section.

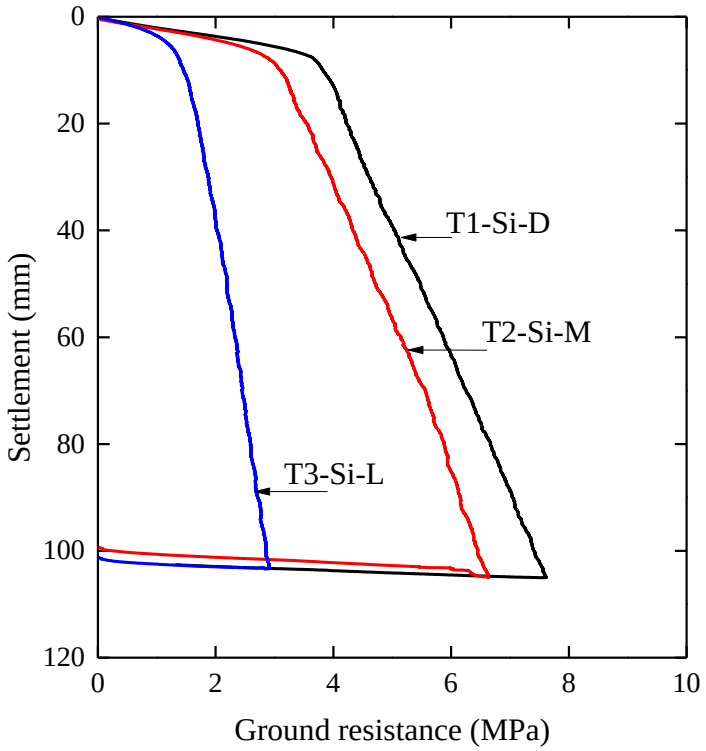

Figure 6.1 Ground resistance-settlement behaviors of the tested cases: T1-T3

6.3.2 AE Characteristics during Pile Loading in Silica Sand

6.3.2.1 AE Count

AE count is one of the most frequently used parameters characterizing the AE activity. The exact value of AE count depends on the intensity of the AE, as well as the preset threshold levels. However, the overall tendency of the result usually remain the same in spite of a different threshold. Figure 6.2 shows an illustration of the effect of the preset threshold and the corresponding AE count numbers for test T2-Si-M. It clearly shows that the amount of AE hits decreased with the increasing of threshold. However, all curves shared almost identical tendencies. It seems that the selection of threshold may not affect the results significantly, because in case of practical application, the tendency of the AE activity evolution is usually more interested in.

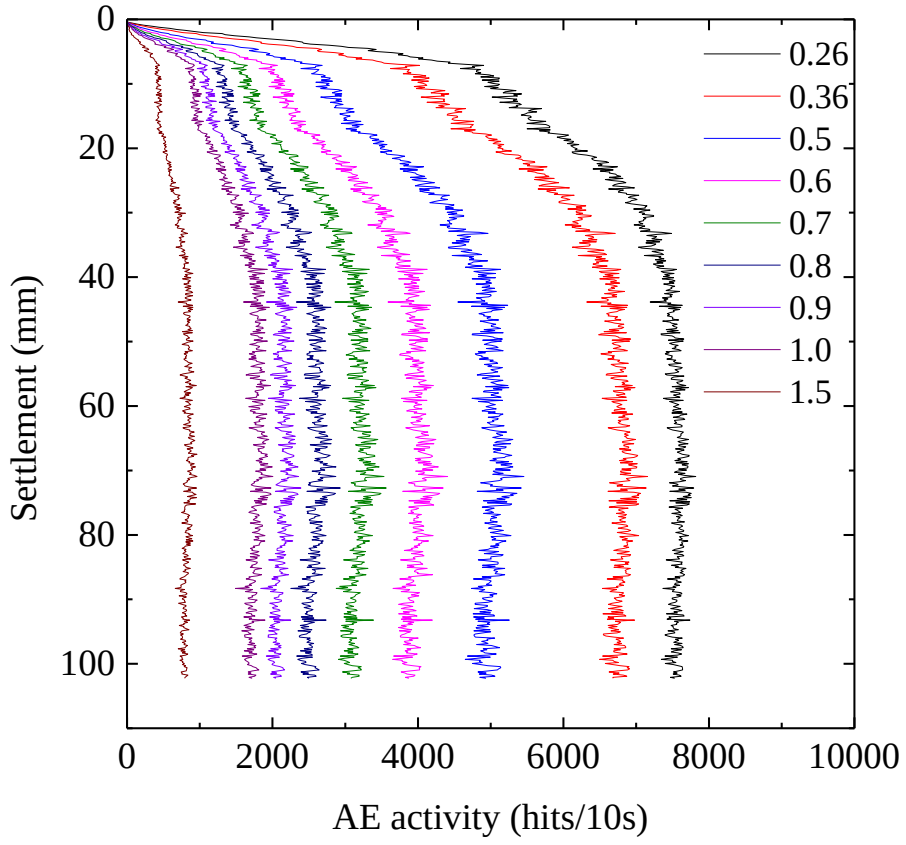

Figure 6.2 Influence of preset threshold on AE count

Figure 6.3 shows the results of AE count evolutions during the whole loading processes for test T1-Si-D, T2-Si-M and T3-Si-L, with the preset threshold of 0.36V. It shows that the activity of AE was low at the beginning of loading, increased rapidly to high values, and finally maintained relatively constant levels. An obvious change of evolution tendency can be identified from the AE evolution curve immediately after the initial rapid rising period. This feature was in good agreement with the bearing load development as shown in Figure 6.1, which also confirmed the validity of AE technique in pile penetration monitoring.

The AE counts for dense case T1-Si-D were more than two times greater than the loose case T3-Si-L at the end of each loading. It suggests that the dense ground tended to be more emissive than the loose ground. By contrast, the difference between T1-Si-D and T2-Si-M was not obvious. After pile penetration exceeded 70mm, T2-Si-M with lower relative density had similar AE rate. It demonstrated that the ground density may not be the only factor influencing the AE behavior. Possible explanations will be discussed later.

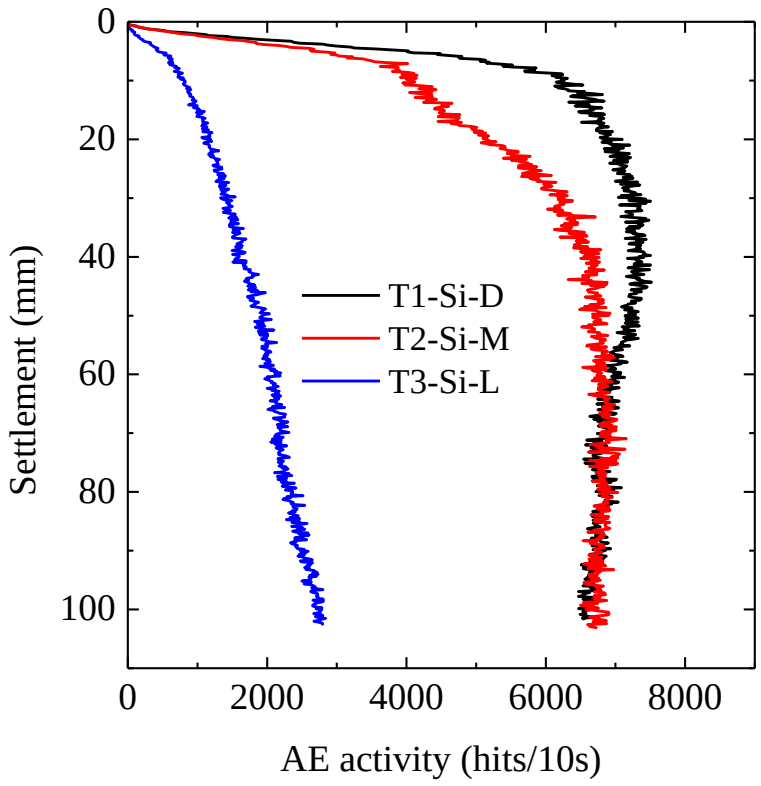

Figure 6.3 AE count evolution during pile penetration in silica sand

6.3.2.2 AE Amplitude

Besides the AE count, the amplitude of the AE signal is another important parameter indicating the strength of the released energy. Figure 6.4 shows the evolutions of average AE amplitude during the process of pile loading, which were calculated by averaging all detected AE amplitudes within 10 seconds. It can be seen that the AE amplitude tendency appeared in the same manner with AE count. The average amplitude rose with increased pile penetration, and turned to be relatively constant after a certain penetration depth. Dense case generally showed higher AE amplitude than loose case. For dense case, certain fluctuation is observed, while for loose case, it is more stable after the initial rising period. The difference among the three type of ground conditions is more obvious compared with AE count, because clear difference can be identified between T1-Si-D and T2-Si-M. This suggests that during the latter stages of pile loading, although the number of AE events appeared to be similar, individual events may had higher amplitude when the ground was denser.

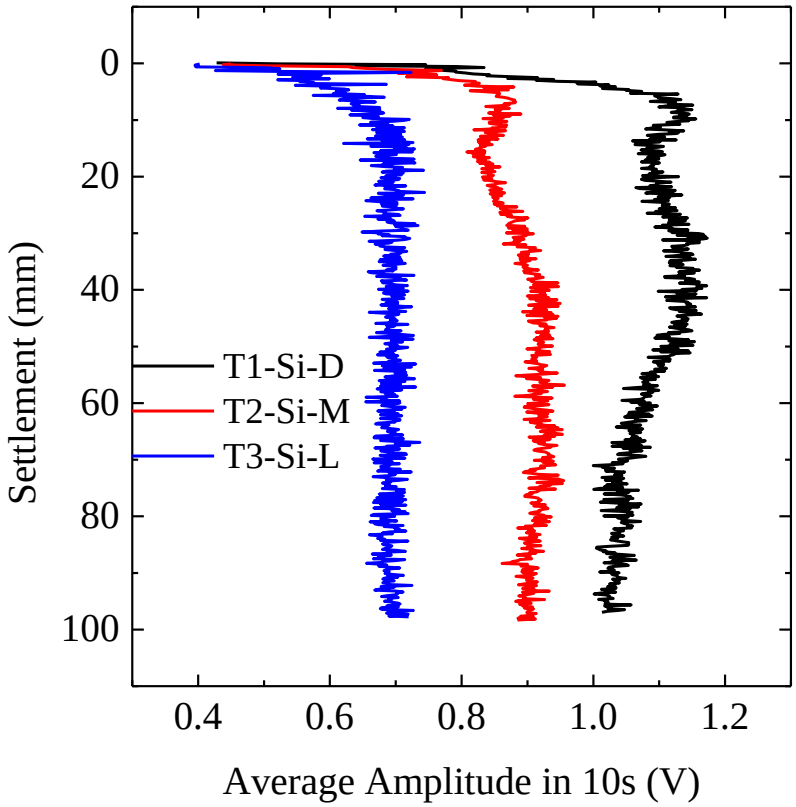

Figure 6.4 Average amplitude evolutions during pile penetration in silica sand

6.3.2.3 AE Energy

AE energy is considered as a more preferable parameter in the analysis because it is sensitive to both signal amplitude as well as signal duration, which are the indices of signal strength. As mentioned in Chapter 3, the AE energy discussed here mainly refers to the $E_{MARSE,}$ computed from the Measured Area under the Rectified Signal Envelop (MARSE) (ASM Handbook, 1992). The true energy, measured by integrating the squared AE signal voltage within signal duration, was presented only in the current section for comparison.

Figure 6.5 shows the AE energy (E_{MARSE}) development during pile penetration in three different ground conditions. The result turned out to be quite similar with AE count as well. The released AE energy was relatively low at the beginning of penetration, followed by a rapid increase period and eventually reached certain stable value. The E_{MARSE} can be regarded as the combination of AE count and AE amplitude. The difference between T1-Si-D and T2-Si-M was less obvious than AE amplitude as shown in Figure 6.4, while more significant than AE count as shown in Figure 6.3.

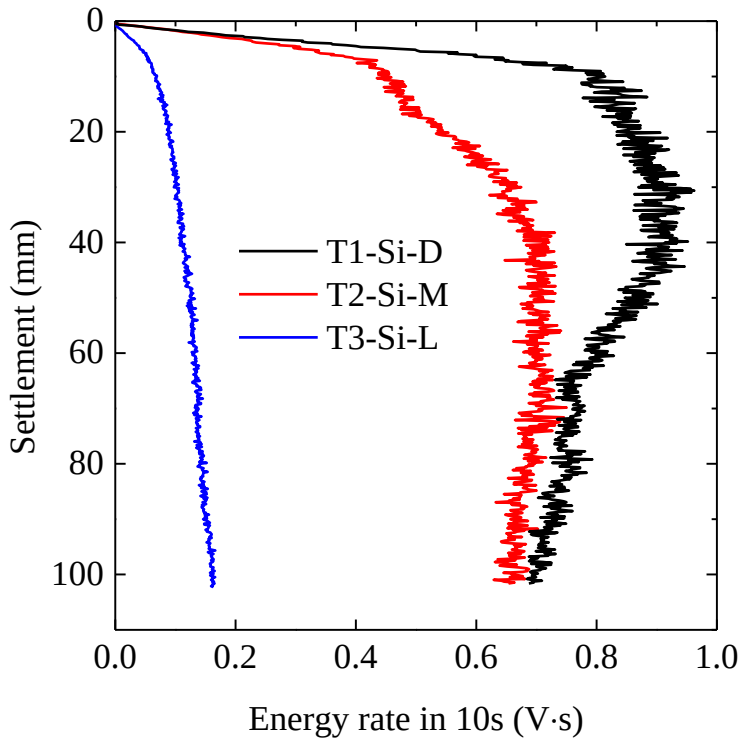

Figure 6.5 E_{MARSE} evolution during pile penetration in silica sand

For comparison, the results of true energy evolutions from three tests are also presented below. As can be seen in Figure 6.6, the shape and tendency of true AE energy were almost same with E_{MARSE}. Due to the squared signal voltage, the value of T3-Si-L became smaller, and T1-Si-D became larger. This is in assistance with the average amplitudes features shown in Figure 6.4, where T1-Si-D is larger than 1 and T3-Si-L is smaller than 1. The gap in between was amplified after squaring. Because of similar observations, only E_{MARSE} is presented in the following sections.

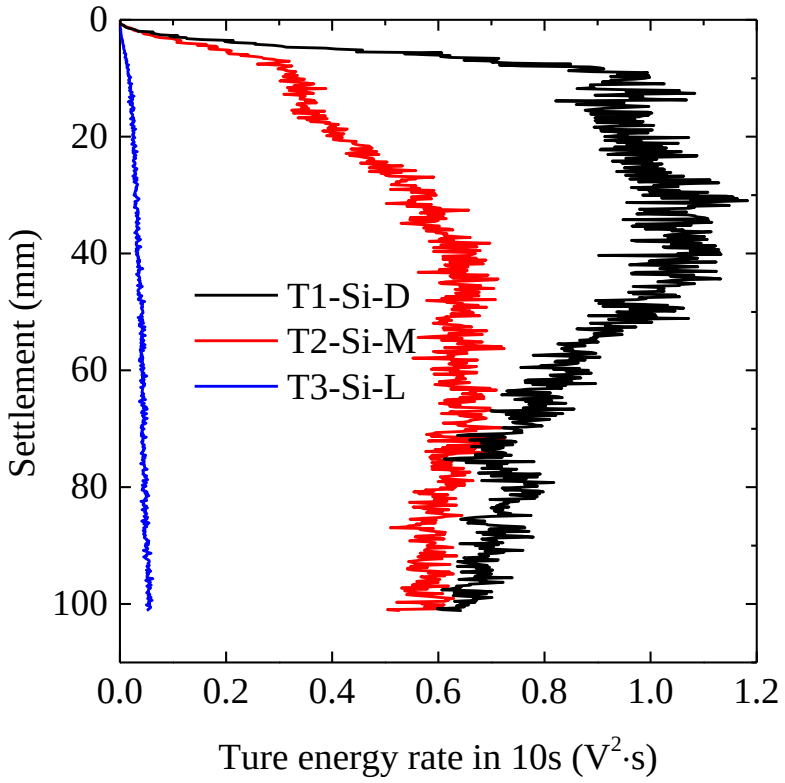

Figure 6.6 True energy evolution during pile penetration in silica sand

6.3.3 AE Characteristics during Pile Unloading in Silica Sand

The pile unloading process was also monitored with AE. As shown in Figure 6.7, the AE activity decreased rapidly after the initiation of unloading. In dense case T1-Si-D, notable rising of AE was observed after the AE dropped to a minimum value at the beginning of unloading. Such behavior was also seen in T2-Si-M, but invisible in loose case T3-Si-L. The AE in unloading is closely related to the ground rebounding capacity, which is supposed to be related with ground density and stress level. More observations will be presented from sequential loading tests later in this chapter.

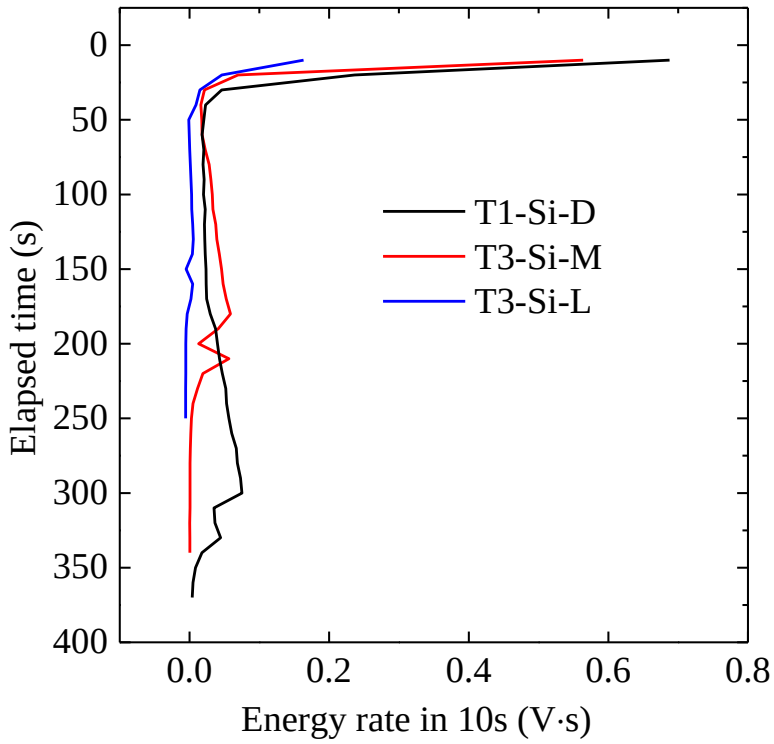

Figure 6.7 AE activity during pile unloading in silica sand

6.3.4 Activity of High Frequency Component

The emission of elastic waves from the sandy ground under pile loading may be caused by two main causes: sand sliding due to particle rotation or relative displacement, and sand crushing due to particle breakage at high pressure. As discussed in Chapter 5, the significant difference in the frequency content between these two types of events helped interpret the AE signals recorded during the pile penetration tests.

To evaluate the intensity of sand crushing, a high-pass filter (>100 kHz) was applied to the AE signals from above mentioned tests to eliminate low frequency signals. The AE signals after the filter were believed to be related with grain fracture source as discussed above. Figure 6.8 shows the high-pass AE evolutions with pile penetration in different ground conditions. The overall tendencies are quite similar with those of the total AE, with the absolute magnitude deceased due to the loss of low frequency components. It demonstrated that the phenomenon of particle breakage accompanied the whole process of pile penetration, although at the very beginning of loading the

crushing is not notable. Figure 6.8 also suggests that an almost constant rate of crushing happened after the ground fully yielded.

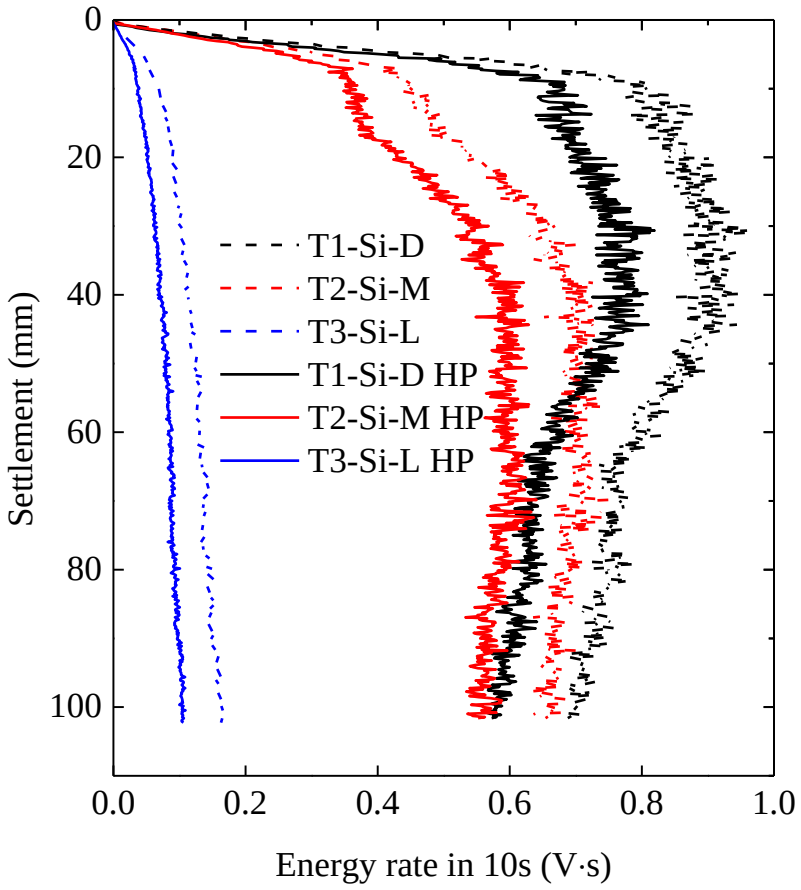

Figure 6.8 High-pass (f > 100 kHz) AE energy rate (E_{MARSE}) during pile penetration in silica sand

6.3.5 AE Characteristics during Sequential Pile Loading

6.3.5.1 Load-settlement Behavior

Figure 6.9 illustrates the relationship between the load and settlement during five sequential loadings. It shows that the ground resistance increased with the increasing of ground density. The resistance of dense case T4-Si-Se-D was almost twice as large as loose case at the same penetration depth. The settlements in the unloading stages illustrated that the rebound displacement for dense ground was more prominent than loose ground. Figure 6.10 shows the secant modulus in each loading step in three tested conditions, calculated by the following equation:

$$E_{sec} = \frac{F}{s * d} \tag{5-1}$$

where *Esec* is the secant modulus, *S* is the sectional area of pile end, *F* is the pile bearing load increment between 0.5 to 1.0 mm settlements of each loading sequence and d (equals to 0.5mm) is the corresponding settlement. Generally, dense ground showed larger secant modulus than that of loose ground, and the moduli tended to increase with loading steps due to ground compaction. It is suggested that the stiffness of the ground was closely associated with soil densification. The dependence of the AE characteristics on ground conditions will be discussed next.

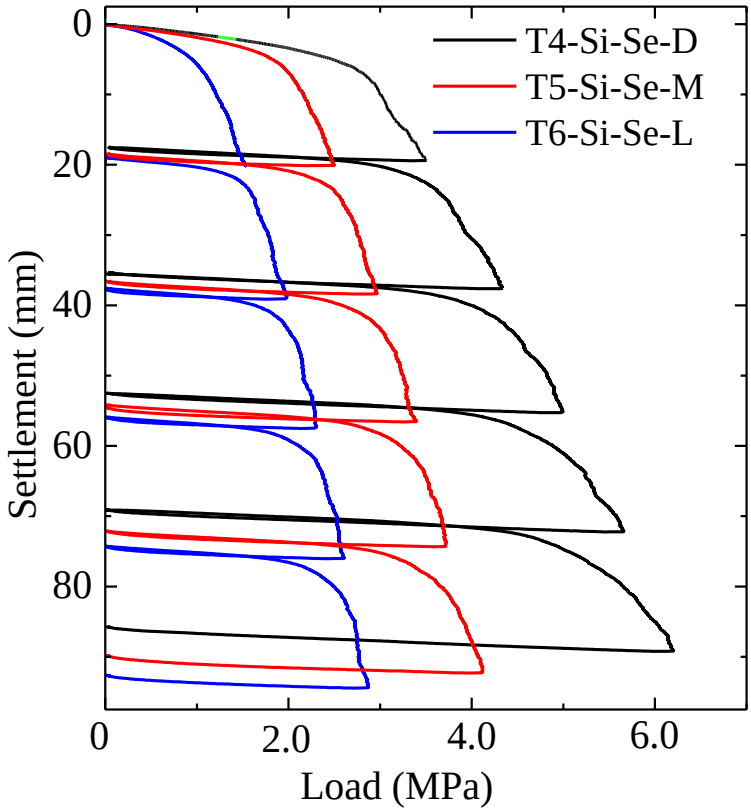

Figure 6.9 Load-Settlement relationship in sequential pile loading conditions

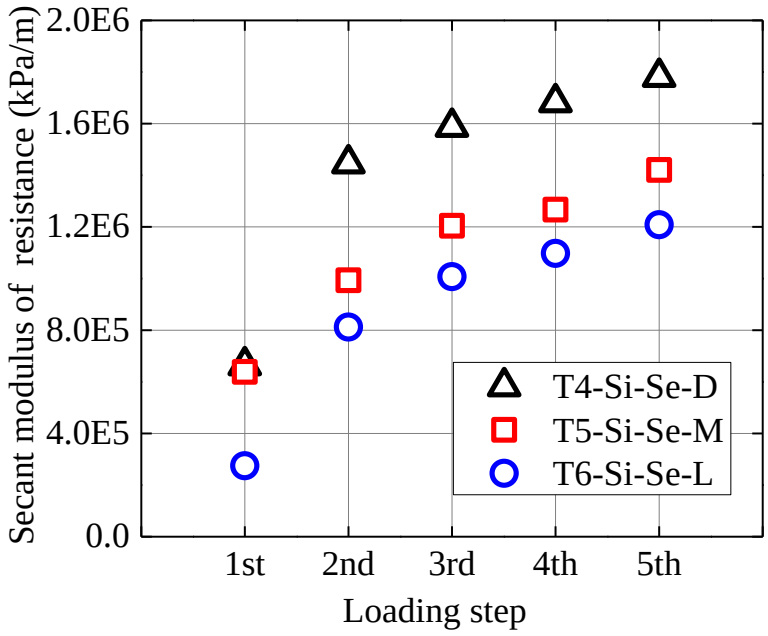

Figure 6.10 Secant modulus of ground resistance during sequential loadings

6.3.5.2 AE Characteristics during Sequential Pile Loading

The results of AE count rate evolutions during three tested cases are summarized in Figure 6.11, Figure 6.12 and Figure 6.13 (threshold all set at 0.25V). Similar with one-time penetration tests, the activity of AE during different loading sequences underwent a low rate at the beginning of loading, increased rapidly to high values, and finally maintained at relatively constant level. This tendency became more obvious during the reloading tests in case of loose ground T6-Si-Se-L. In general, dense ground was more emissive than the looser ground. The subsoil subjected to sequential loading underwent a process of densification (dilatancy may also exist around the shear zone). Accordingly, reloading stages were expected to generate more AEs. The results from loose case T6-Si-Se-L and medium case T5-Si-Se-M confirmed this assumption well where significant gaps between 1st and the latter loading steps can be observed. For the dense case T4-Si-Se-D, however, the AE counting showed no obvious difference between 1st and 2nd loadings and decreased slightly during 3rd-5th loadings, suggesting that there are also other factors affecting the AE behavior, which will be discussed later.

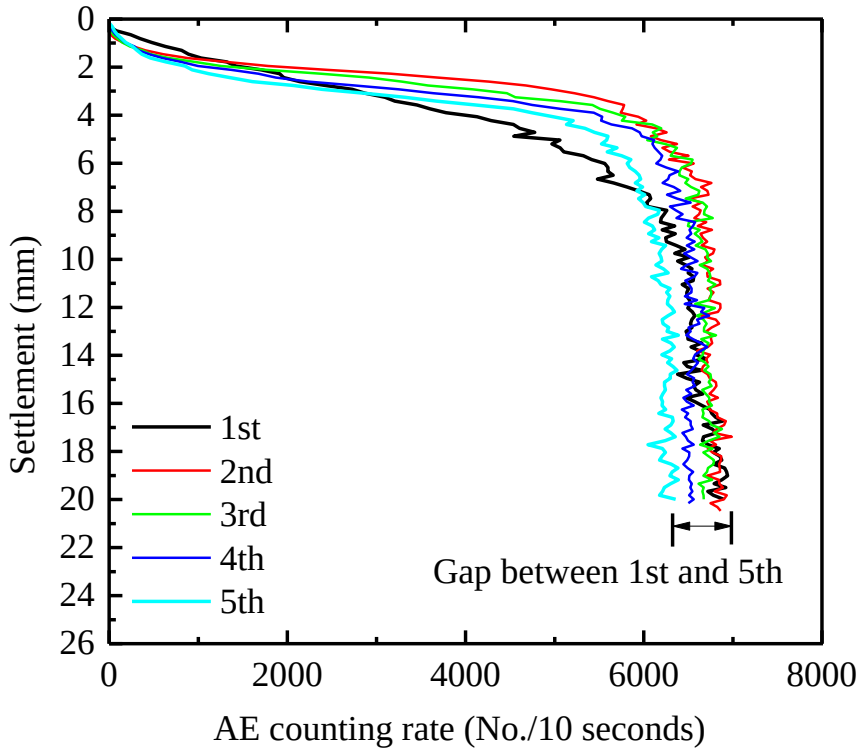

Figure 6.11 AE count evolution during sequential pile loading: T4-Si-Se-D

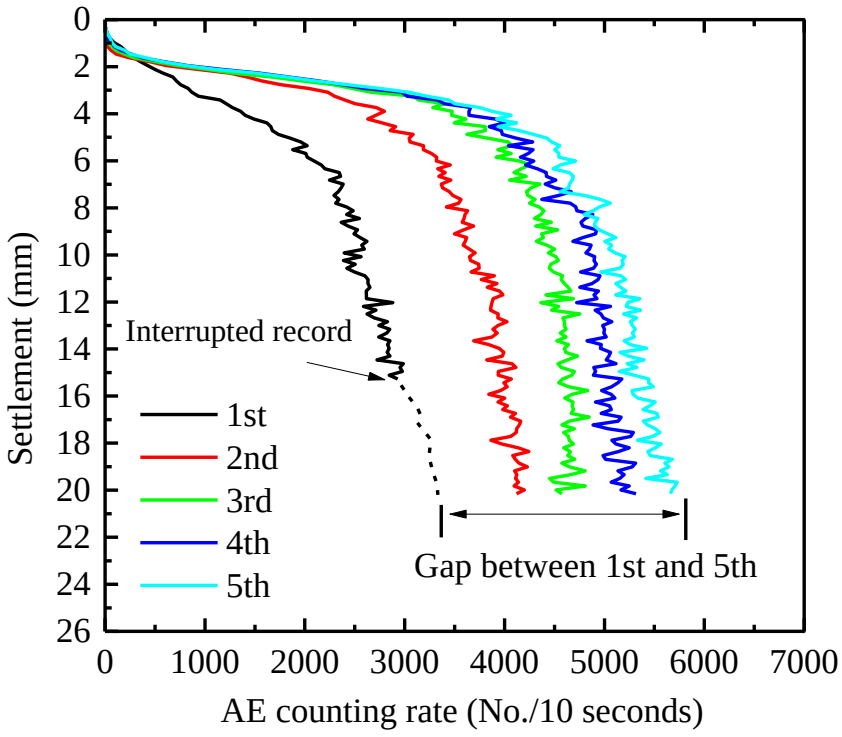

Figure 6.12 AE count evolution during sequential pile loading: T5-Si-Se-M

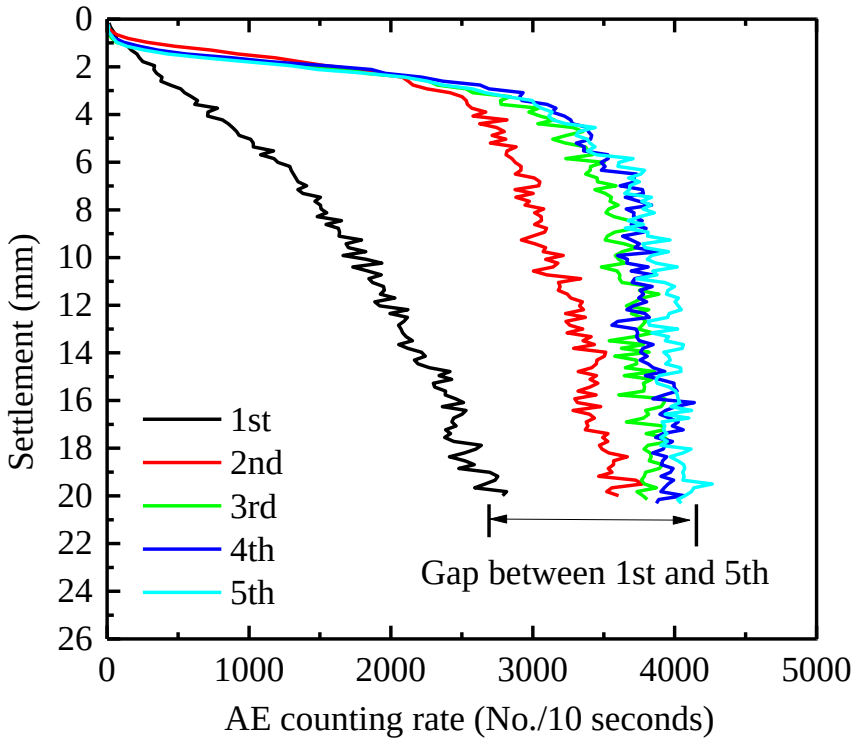

Figure 6.13 AE count evolution during sequential pile loading: T6-Si-Se-L

Figure 6.14, Figure 6.15 and Figure 6.16 show the AE energy development during pile penetration in case of dense, mid-dense and loose condition, respectively. Again, the AE energy was relatively low at the beginning of penetration, followed by a rapid increase period and eventually reached certain stable value. For loose case T6-Si-Se-L, the AE in the initial loading (1st) showed significant difference compared with the reloading processes. The rapid AE increasing period was longer and the increasing rate was much lower. By contrast, AE during reloading stages exhibited relatively consistent tendency. For dense case T4-Si-Se-D, slight increments of AE energy from the initial loading to the 2nd re-loading can be found, during the first 10mm penetration. However, it was observed to subsequently decrease during the 3rd and the 4th re-loadings. This decrease may be a result of densification of sand, and the micro-movement of sand particles were restrained. Moreover, a lower void ratio in the re-loading stage provides more contact points for individual particles, which might improve the sand grain strength and decrease the crushing rate. The overall behavior of medium case T5-Si-Se-M lay between the dense and loose cases, with less change

between the initial loading and 2nd-reloading, but also saw decreasing from the 3rd to 5th loading.

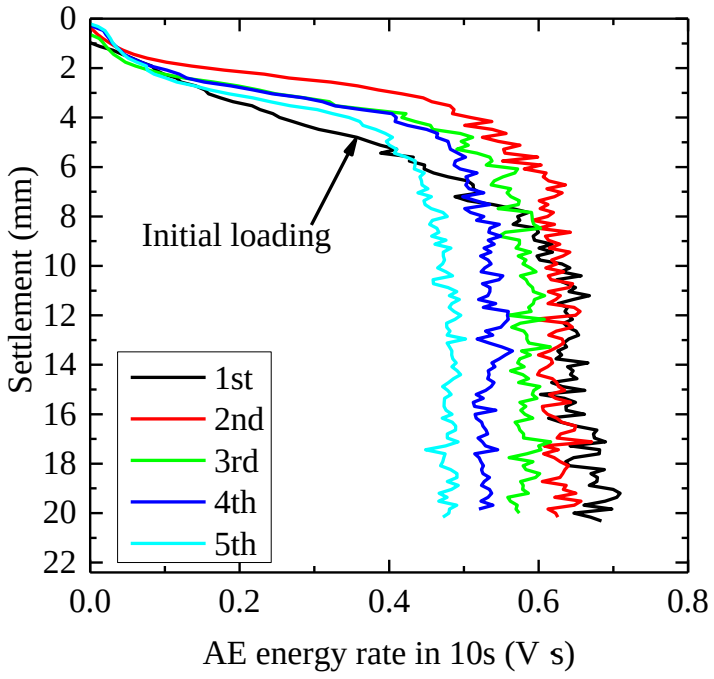

Figure 6.14 AE energy rate during sequential pile loading: T4-Si-Se-D

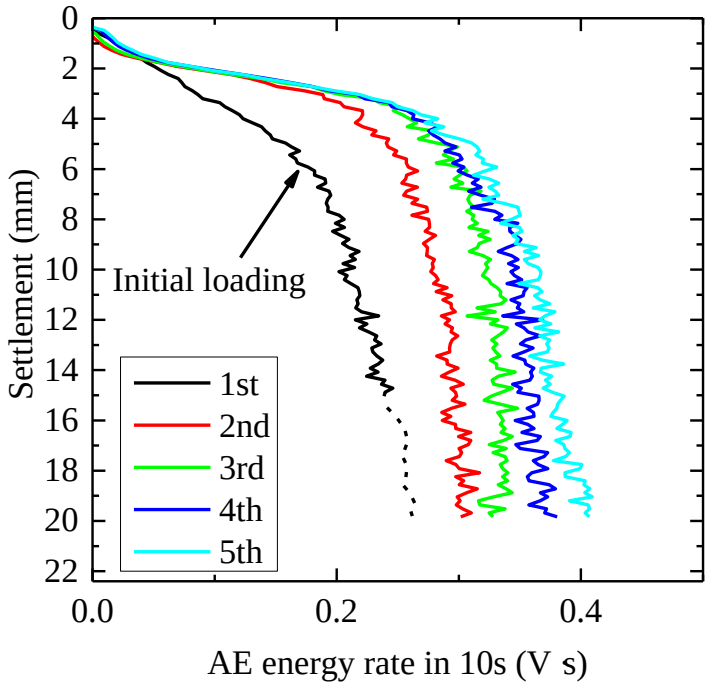

Figure 6.15 AE energy rate during sequential pile loading: T5-Si-Se-M

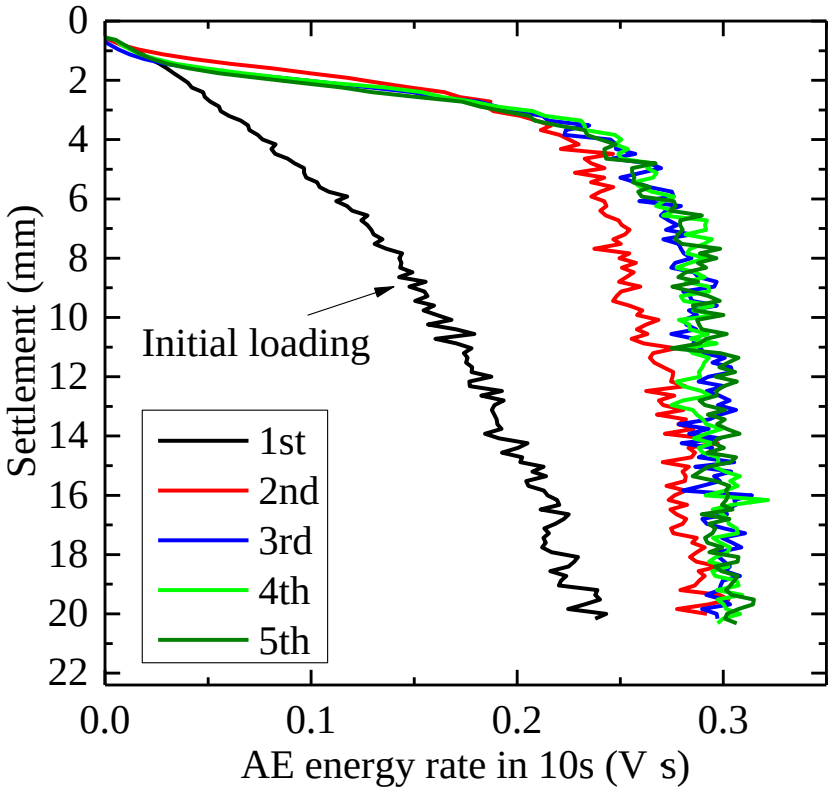

Figure 6.16 AE energy rate during sequential pile loading: T6-Si-Se-L

Figure 6.17 shows the ratio of sand crushing and sliding AE counting changing with pile penetration in dense case. All curves show that at the very beginning of each loading sequence, the ratio was low and then rose sharply with the process of pile penetration. This observation suggests that the sand crushing was not significant under low stress conditions. Conversely, it occurred substantially when stress was high. Another notable feature in Figure 6.17 is that during the first loading, it took more time to reach the reference line where the counting number of crushing and sliding is the same. All three re-loading sequences exhibited a significantly higher rate of reaching the reference line. Additional loading sequences took even less time, although to a less notable extent. This observation of hysteresis demonstrates the effect of previous loading history on the crushing behavior of the highly stressed sand. Therefore, it can be argued that the ground was gradually densified by the previous

loadings, which consequently makes the sand grains more prone to reach the crush limit in the latter loading sequences.

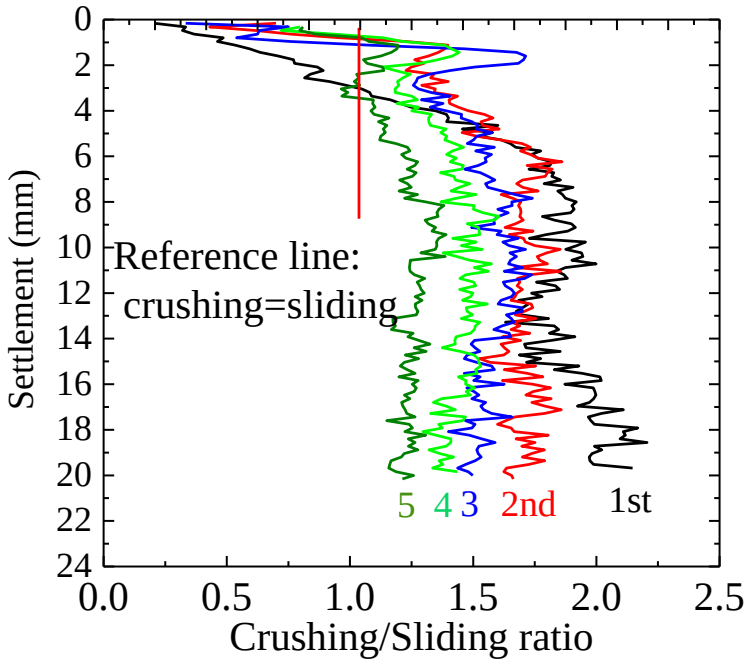

Figure 6.17 Count ratio of crushing and sliding events

6.3.5.3 AE Characteristics during Sequential Pile Unloading

Figure 6.18, Figure 6.19 and Figure 6.20 show the AE energy evolutions during the unloading stages. The unloading was initiated about 5 seconds after the loading stopped at the same speed (1mm/min). It can be seen that the AE energy decreased rapidly to a negligible level after the unloading initiation, then it rose slightly until the loading unit was disconnected the pile, and finally decreased to zero after a certain period of stabilization. It is also seen that the maximum AE energy (indicated by arrows in Figure 6.18 that was reached at the end of each unloading increased slightly compared with the previous unloading sequences, and the absolute values in the dense cases were generally higher than the loose case. In addition, the elapsed time for AE stabilization became longer during the latter loading steps in both dense and loose cases. Such properties may be potentially used for assessment of subsoil status, e.g. estimating the ground density/stress conditions via monitoring of AE.

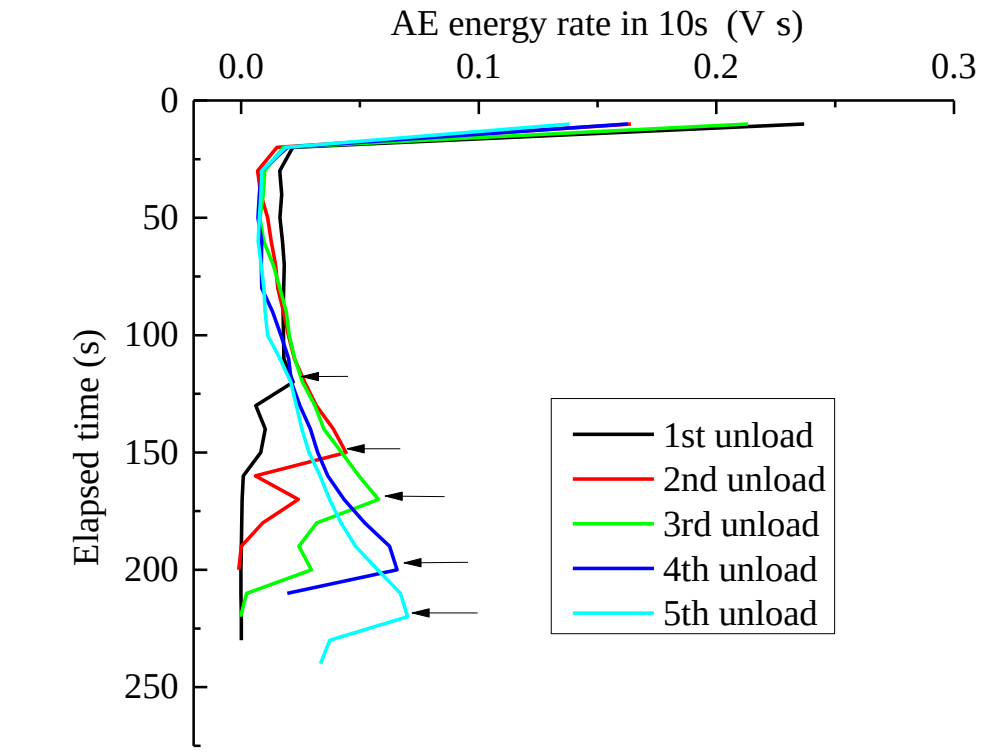

Figure 6.18 AE energy rate during sequential pile unloading: T4-Si-Se-D

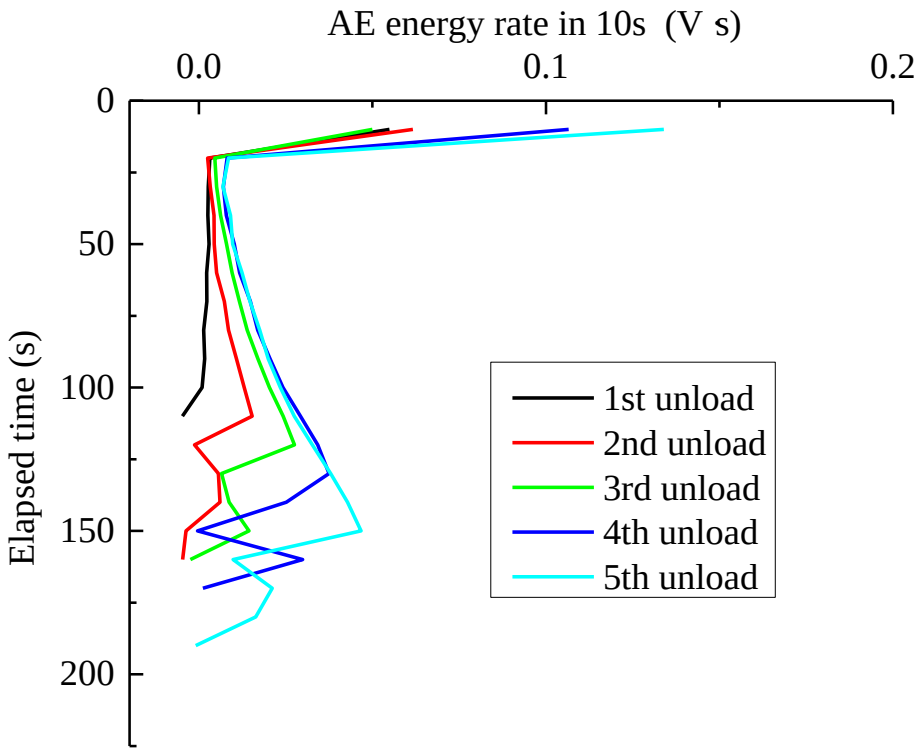

Figure 6.19 AE energy rate during sequential pile unloading: T5-Si-Se-M

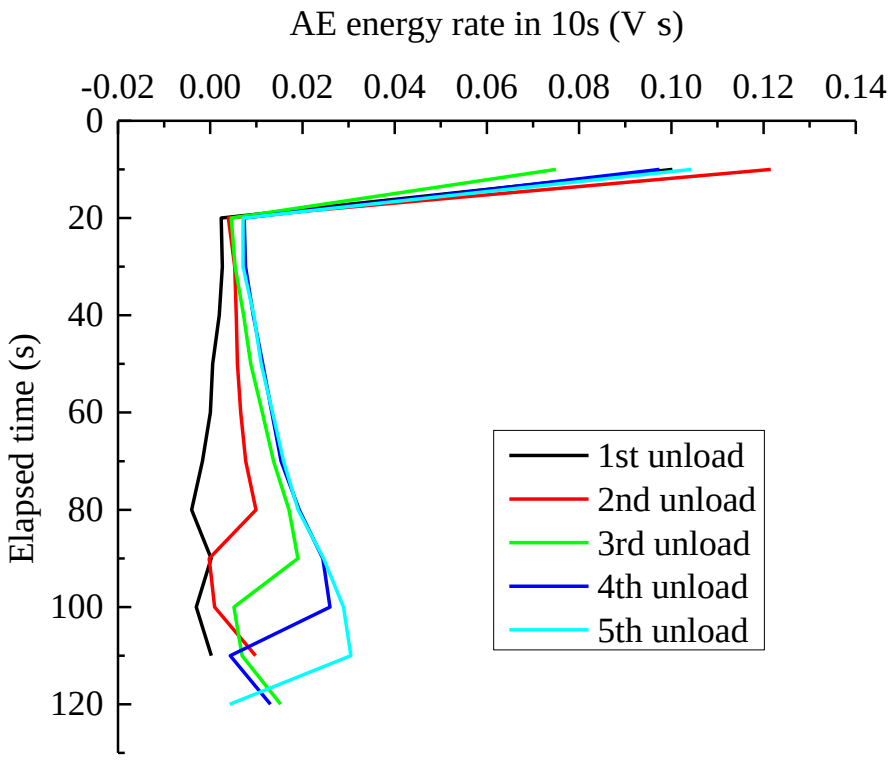

Figure 6.20 AE energy rate during sequential pile unloading: T6-Si-Se-L

6.4. EXPERIMENTAL RESULTS ON CORAL SAND NO.1

6.4.1 Load-settlement Behavior

Figure 6.21 illustrates the load-settlement relationship obtained from coral sand testes. Been similar with silica sand results, an increased relative density of the model ground yielded a larger tip resistance. Figure 6.21 shows a continuous rising of bearing stress. The bearing load of dense coral sample was even larger than that of silica sample as shown in Figure 6.1. It may be cause by a greater friction angle in case of coral sand. Yu (2014) found that the friction angle for silica sand No.5 was around 37 degrees. While for coral sand No.3, the friction angle reached around 44 degrees. Although coral sand No.3 tested by Yu (2014) had a larger grain size than the coral sand used in the current study. It may be the reason that the coral sand ground exhibited greater bearing capacity than silica sand ground. Another possible reason may be the limited confining pressured (10kPa) applied in the current study. Kuwajima et al. (2009) found that for crushable carbonate sands, although with

greater friction angles, the bearing capacity failed to increase significantly when the confining stress was high. Therefore, is can be expected that when the confining pressure increase to a significant high level, the silica sand will exhibit greater ground resistance than that of coral sand.

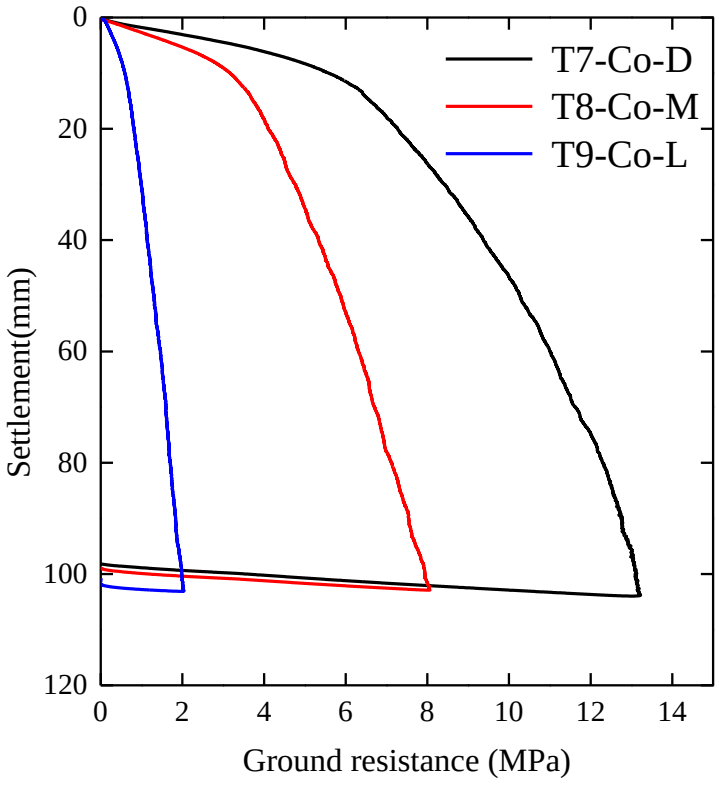

Figure 6.21 Ground resistance-settlement behaviors of coral sand cases: T7-T9

6.4.2 AE Characteristics during Pile Loading in Coral Sand

Figure 6.22 shows AE energy (EMARSE) evolutions for the three tested coral sand samples. Similarly, AE was rising from the initial low rate to certain high values. Loose case T9-Co-L was less emissive compared with denser cases T7-Co-D and T8-Co-M. However, there is no significant difference between the two denser cases. To some extent, T8-Co-M with lower relative density was even more emissive than T7-Co-D.

A notable feature that contrasts sharply with those of silica sand results can be seen from T7-Co-D and T8-Co-M. The overall tendency of AE evolution was separated

from the peak point, where a continuous decreasing of AE is observed in the succeeding period.

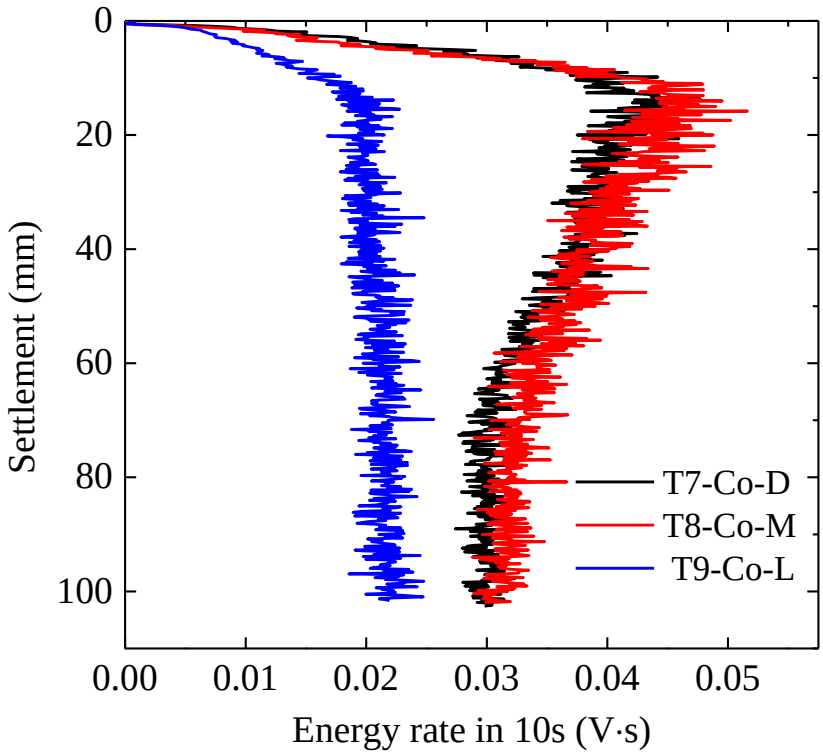

Figure 6.22 AE energy evolution during pile penetration in coral sand

6.4.3 Activity of High Frequency Component

The high-pass filter (>100 kHz) was further applied to the above AE signals to evaluate the intensity of sand crushing. Figure 6.23 shows the high-pass results of three test conditions. The overall tendencies are also similar with those of the total AE, with the absolute magnitude deceased due to the loss of low frequency components. A notable feature in Figure 6.23 is the clear difference between test T7-Co-D and T8-Co-M, where higher AE rate can be seen in the dense test T7-Co-D. By contrast, no obvious difference was seen before the signals were filtered as shown in Figure 6.22. This feature is consist with the common expectation that denser ground packing should be subjected to more crushing, which in turn verifies the argument that high frequency AE is correlated with fracture mechanism.

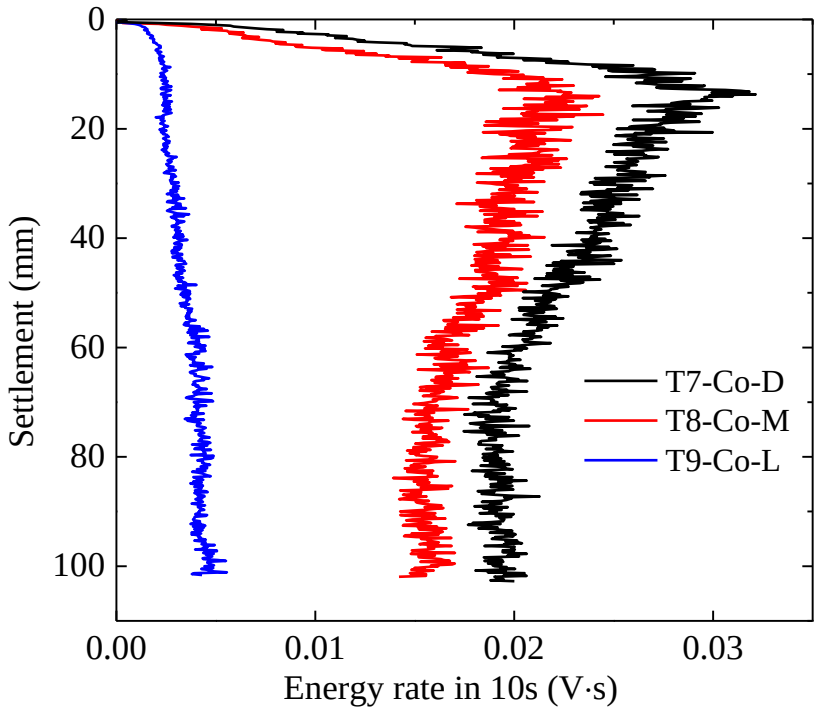

Figure 6.23 High-pass (f > 100 kHz) AE energy rate (E_{MARSE}) during pile penetration in coral sand

6.4.4 AE Characteristics during Pile Unloading in Coral Sand

Figure 6.24 shows the AE activity during pile unloading in coral sand. Although the emission level in coral sand was much lower than that in silica sand, the same tendency can be observed. The AE decreased rapidly to a negligible level immediately after the initiating of unloading, and slightly increased to a certain value. Dense ground took a longer time to reach the final silent status.

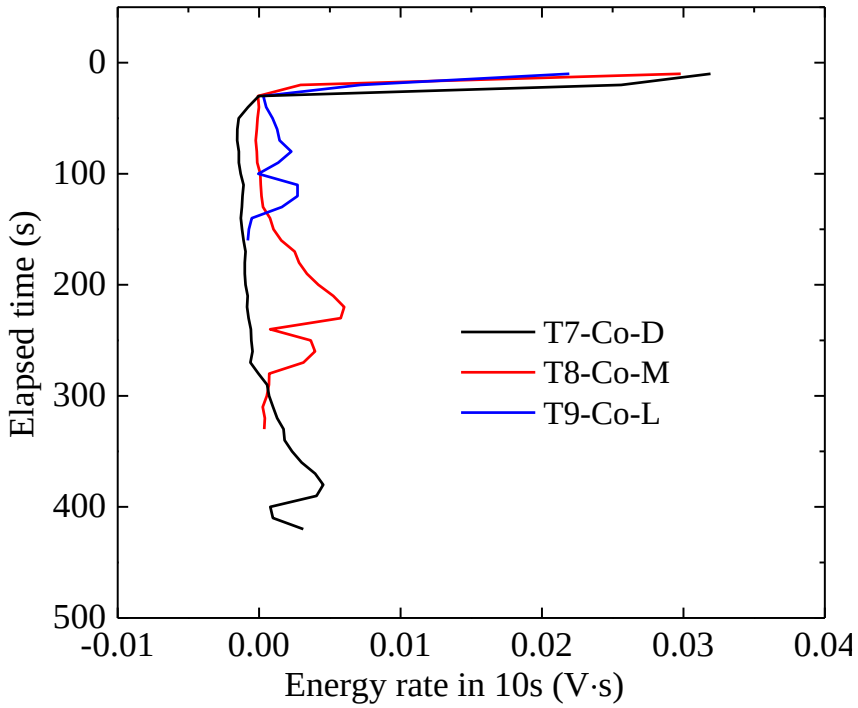

Figure 6.24 AE activity during pile unloading in coral sand

6.5. SIGNIFICANCE OF SAND CRUSHING

Figure 6.25 shows notable sand crushing observed in a pile penetration test. The sands immediately below the pile tip were crushed into "powders." Modifications of GSD were frequently used to evaluate the extent of crushing. In order to get a straight impression of sand crushing extent, sieve analysis were conducted to obtain the grain size distributions after each test (100mm pile penetration). Samples were taken from the cylindrical zone immediately below the pile tip as illustrated in Figure 6.26 from silica sand tests and Figure 6.27 from coral sand tests. It can be seen that the finer content of the sand increased significantly even when the ground condition was relatively loose, and became more profound when the ground turned to be dense, which provides a direct evidence of sand crushing after pile loading.

The GSD gives a general impression of the crushing extent at the timing of excavation, while the onset and rate of crushing remain unknown. Through AE monitoring, it is possible to evaluate the onset and rate of crushing. The application of the two

combined methods may provide useful information for the analysis of particle crushing problems.

Figure 6.25 Notable sand crushing observed below the pile tip after pile penetration

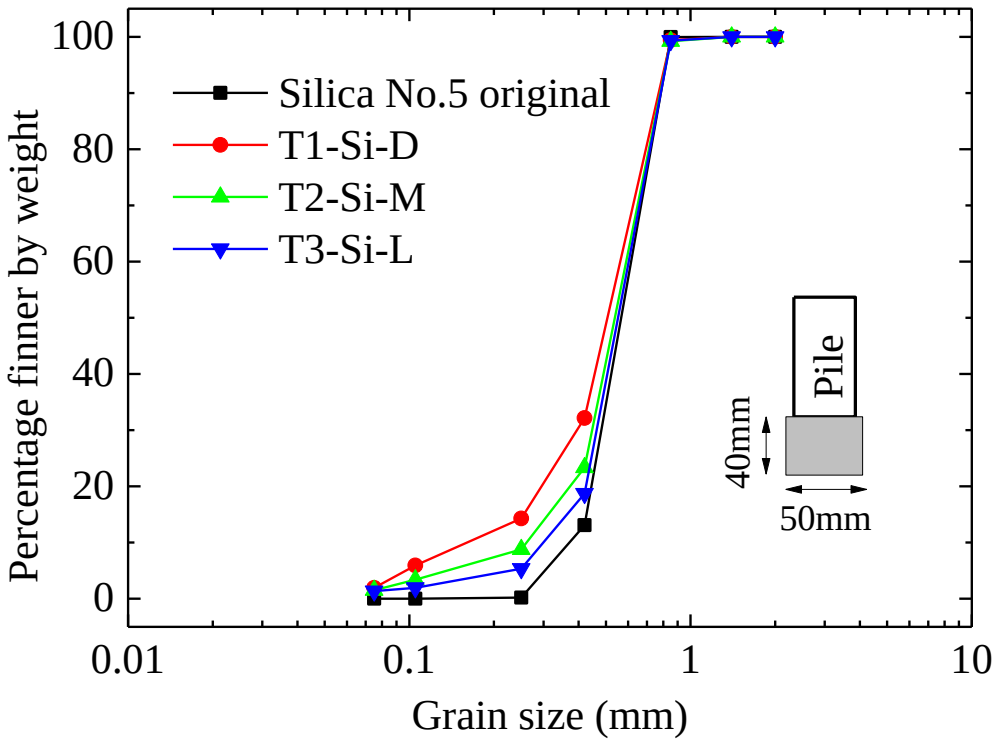

Figure 6.26 Grain size distribution curves from silica sand tests

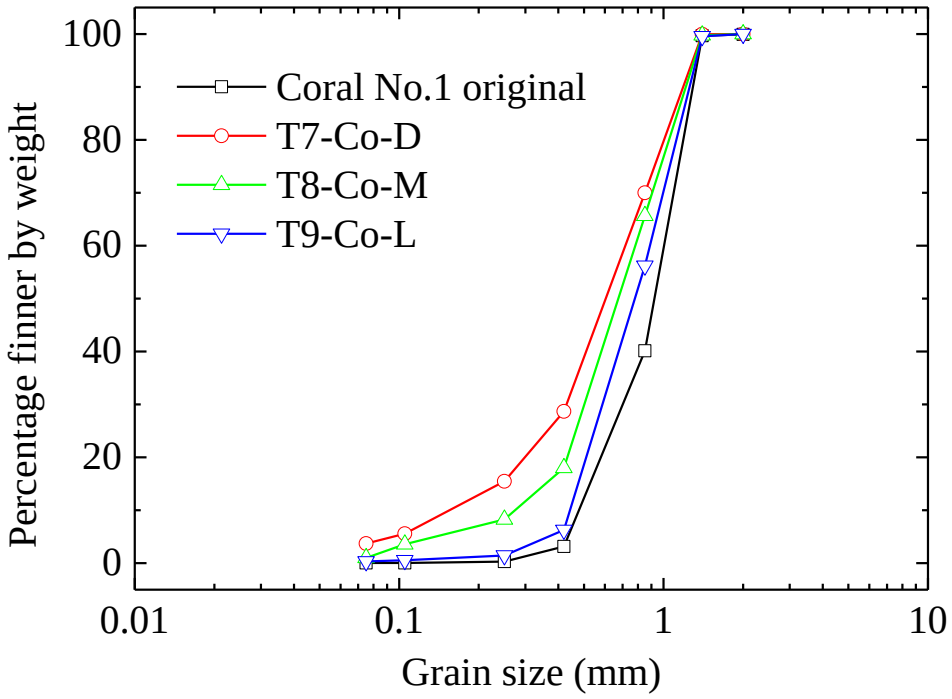

Figure 6.27 Grain size distribution curves from coral sand tests

6.6. AE AND SUBSOIL BEHAVIOR

6.6.1 AE and Ground Yielding

The "yielding" is a basic concept in soil mechanics and is usually determined by stress-strain relationships. In plasticity theory, it is of great importance to describe the yielding behavior of soils properly in constitutive models. After yielding, the soils is dominated by plastic deformation and small amount of load increment could result in large deformation. The yielding of soils is associated with irrecoverable plastic deformation and releases energy in form of thermal energy or stress waves. Tanimoto and Tanaka (1986) stated that such dissipated energy could be monitored by means of AE and correlated the onset of soil yielding with AE characteristics through a series of triaxial tests.

According to the above revealed AE features, it is found that the yielding of ground was also highly distinguished by AE characteristics in case of pile penetration. Two

testing cases from sequential pile loading were selected for a detailed analysis: T4-Si-Se-D representing for dense ground and T6-Si-Se-L representing for loose ground. The arrows in Figure 6.28 and Figure 6.29 indicate the yielding points, which were derived from the two tangent lines drawn at the beginning and final linear part of the load-settlement curves (Casagrande method for e-logp analysis). The intersection of the bisector of the two tangent lines and the curve was defined as the yielding point. Although the yielding point depicted herein is slightly scale sensitive, the method provides an overall impression of ground status. The semi-log scale provides a better observation of the load-settlement/AE-settlement relationships when the pile settlement is small. By applying the same method to the AE-settlement curve, another "yield point" can be obtained. A summary of the yielding settlement is shown in Figure 6.30. Although the yield settlements determined by AE turned to be slightly higher than those determined from load measurements, still it can be stated that the yielding of the ground is marked by the AE characteristics. The high consistency between AE and bearing load behavior make it possible to substitute one for the other under certain circumstances, e.g. AE monitoring during displacement pile installation.

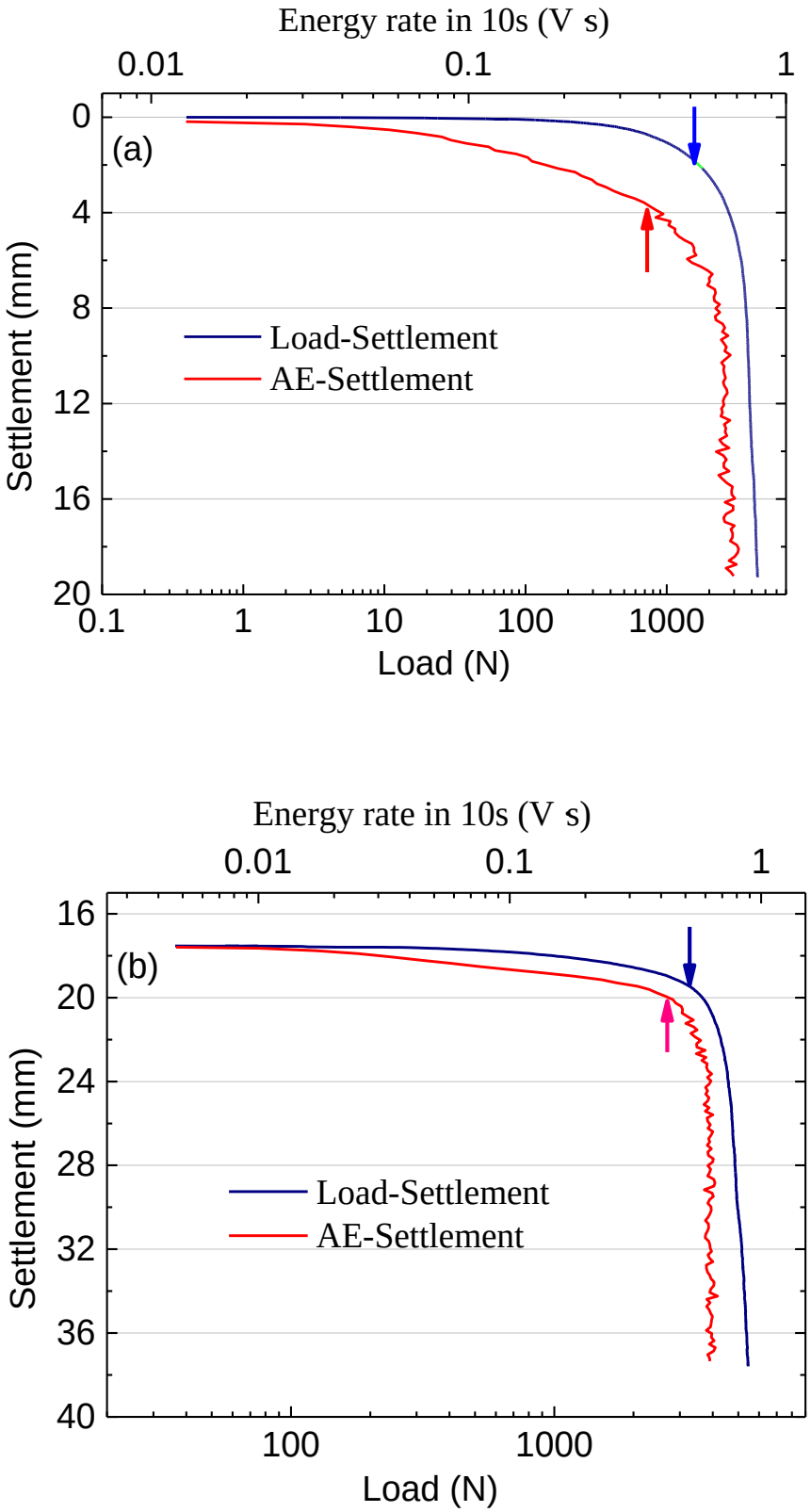

Figure 6.28 Load-settlement and AE characteristics in test T4-Si-Se-D for (a) initial loading and (b) 2nd-loading

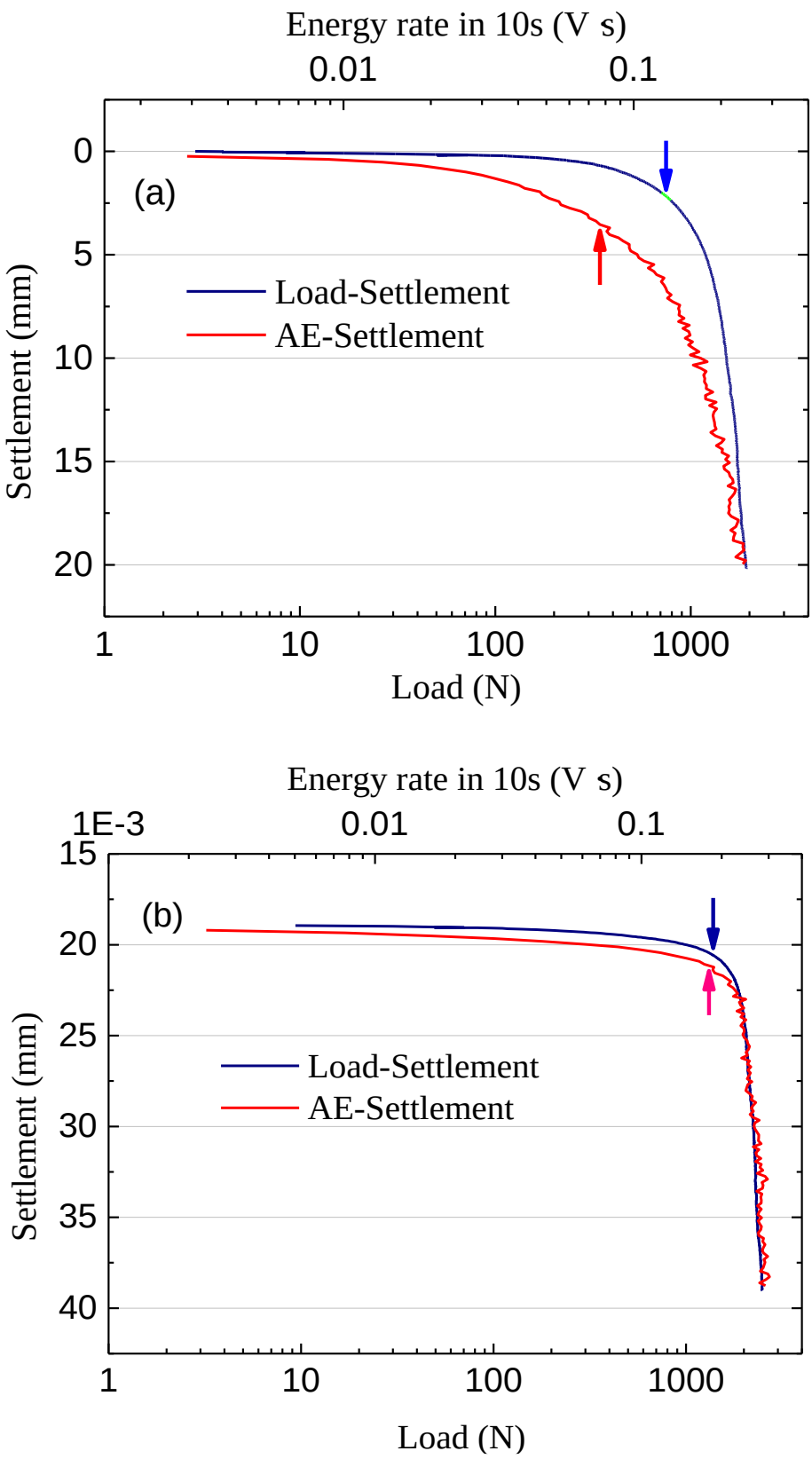

Figure 6.29 Load-settlement and AE characteristics in case T6-Si-Se-L for (a) initial loading and (b) 2nd-loading

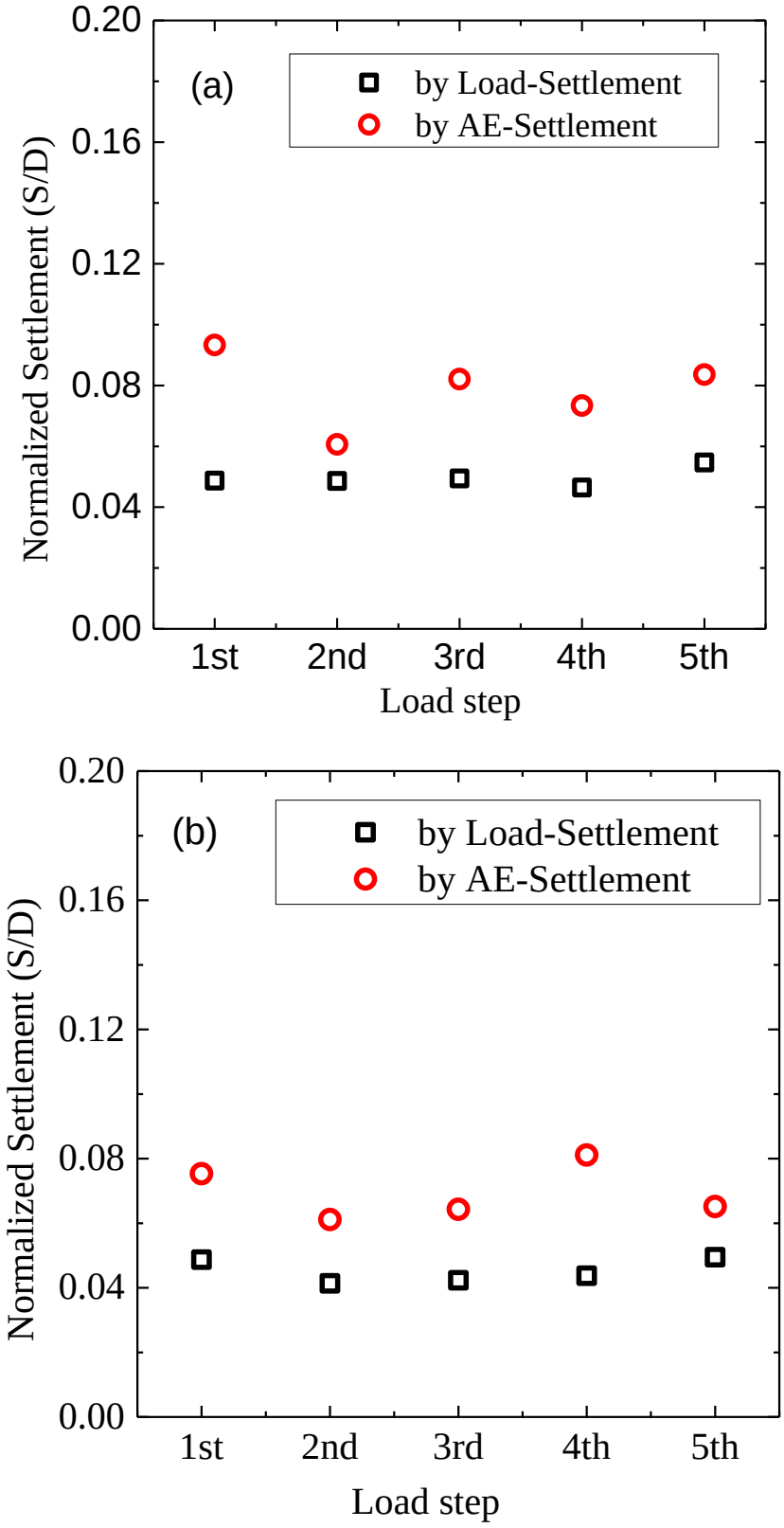

Figure 6.30 Yield settlement normalized by pile diameter in case of (a) T4-Si-Se-D (b) T6-Si-Se-L

6.6.2 Insights into Subsoil Behavior

According to the above results, the AE activity was observed to increase together with the load untile ground yielding, while turned to be relatively constant after yielding. Such tendency was closely related with the ground stress status during pile penetration. Before the ground yielding, the sand below the pile tip was densified and the bearing capacity was built gradually. It may be stated that the ground remained in the elastic status before the stabilization of AE rate, which was also evidenced by the linear load-settlement curve within this period. Microscopically, the increased stress among sand particles caused significant sliding and crushing, resulting in increased releasing of elastic waves. However, after the ground yielding, due to continuous pile penetration, the failure zone was well formed and the bearing capacity of the ground failed to increase notably. As a result, AE sources from the particle sliding and crushing turned to be constant as well due to the mobilized failure surface. Relative constant bearing load after yielding resulted in constant particle contacts, which also demonstrates that AE is consistent with the ground stress status.

Figure 6.31 shows a typical failure pattern below a pile tip. The failure surface was restrained within a limited region and the shape was analogous to half-sphere. Such failure shape was well observed by other researchers as well (Yasufuku and Hyde 1995; Kuwajima et al. 2009). A closer observation made by Yang et al. (2010) also showed that sand crushing was most significant along this failure surface.

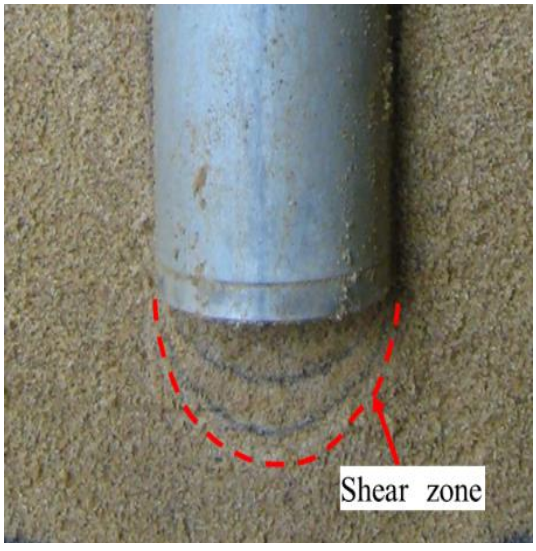

Figure 6.31 Shear surface developed below a pile tip

The shear zone developed along the failure surface is closely related to the observed AE behavior mentioned above, where upper boundaries of the AE activities were detected. The block of soil below the pile tip moved steadily and progressively downwards along the failure surface, resulting in constant AE rate after the ground yielding. This may also explain the reason that the shape and tendency of high-pass frequency AEs were similar with total AEs, since crushing is highly depended on the interface shearing. Constant interface shearing after the ground yielding resulted in relatively constant high frequency AEs.

In view of sequential loading, it may be generally stated that the overall density of the subsoil was gradually increased, as was revealed by the increased secant modulus shown in Figure 6.10. Meanwhile, dense ground was more emissive than loose ground as revealed in Figure 6.5 and Figure 6.22. However, the AE observed in sequential loading steps showed different tendency (Figure 6.32). During the pre-yielding periods (Figure 6.32 (a)), the average AE energy rates (calculated during 1-3mm pile settlement in Figure 6.11 and Figure 6.13) of both dense T4-Si-Se-D and loose cases T6-Si-Se-L were increased from the 1st loading to the 2nd loading, and then deceased to a relatively stable level during 3rd-5th loading steps. In view of the absolute AE energy value, the dense case T4-Si-Se-D exhibited higher level than the loose case T6-Si-Se-L during the first two loading steps and turned to be almost identical during the 3rd-5th loading steps. During the post-yielding periods (Figure 6.32 (b)), in the dense case T4-Si-Se-D, the average AE energy in the constant period (calculated during 15-20mm pile settlement in Figure 6.11 and Figure 6.13) exhibited a decreasing trend. While in the loose case T6-Si-Se-L, AE increased notably from the 1st loading to 2nd loading, and turned almost constant during 2nd~5th loading cycles.

During different loading steps, the AE evolution was not always showing the increasing trend with the sequential loading. It seems that apart from soil density, there are other aspects affecting the AE behavior. One reason could be the failure surface formed in the previous loading steps. The sand particles within failure zone underwent severest movement, accompanied by particle sliding and crushing which initiated substantial AE waves. After the failure zone was formed in the 1st-loading step, the AE contribution from this zone may decrease notably during the reloading

stages. Because the particles within this zone had better arrangement and directivity during reloading, which caused less sliding compared with randomly distributed condition in case of 1st-loading. In dense case, the AE increment from ground densification was not as significant as in loose case, and consequently, the overall AE was dropping. Furthermore, the dilatancy of soil around the shear zone may create a zone of soil less dense, which could be more evident in case of dense ground and attributed to the decreased AE observed in Figure 6.32(b). In loose case, the densification effect might be still dominant, and therefore the overall AE increased significantly in the 2nd-loading step despite of the pre-existed failure surface. However, from the 3rd-loading step, it seemed that the ground started to behave like dense ground, since the increment was not obvious. This demonstrates the effect of initial ground condition on the AE characteristics.

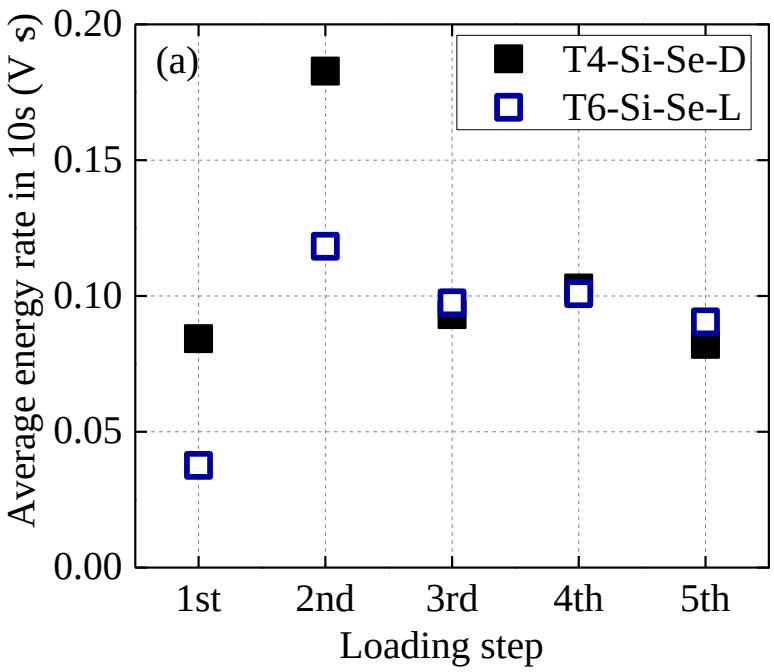

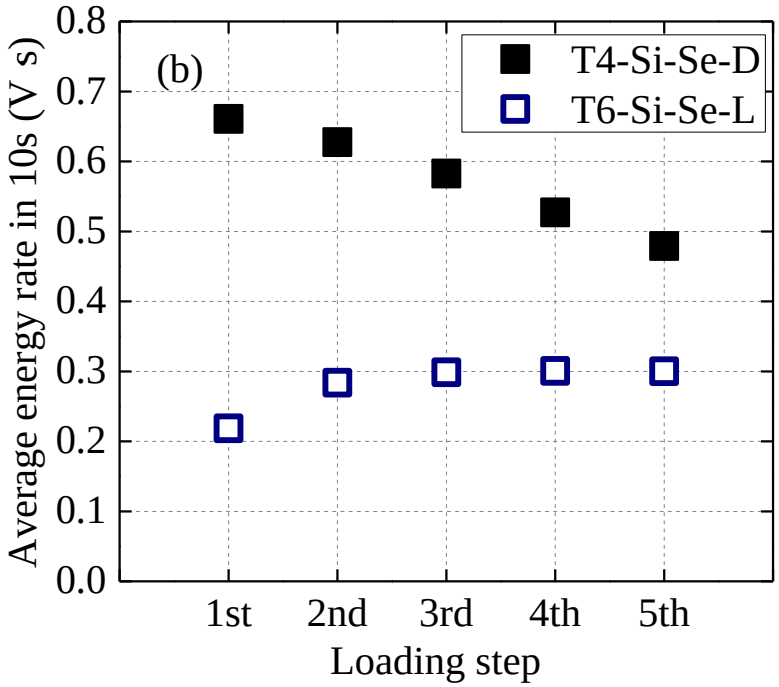

Figure 6.32 Average AE energy rate during (a) 1-3mm and (b) 15-20mm pile settlement in case of T4-Si-Se-D and T6-Si-Se-L

6.7. SUMMARY

This chapter summarizes test results and discussions related to the AE characteristics during pile penetration in sand. Different types of sand, loading procedure and relative density were examined. It is generally found that the process of pile penetration was highly distinguished by AE activities. The evolution tendency of the AE count, AE amplitude and AE energy showed high similarity with load-settlement curves. The AE at the beginning of the pile penetrating was relatively low, followed by a rapid rising period and eventually became relatively constant. A detailed comparison of load-settlement and load-AE relationship found that AE could be a reliable indicator of ground yielding.

Significant difference revealed in the frequency content of various AE signals can be used for distinguishing sand crushing and sand sliding events. It is found that sand crushing occurred throughout the pile penetration process, and became significant after the ground yielding. Since the ground is characterized by shear deformation

along the shear zone after initial yielding, the continuation of sand crushing AE events is in accordance with previous studies that indicate sand particles are more prone to crushing under shear than compression.

6.8. REFERENCES

Altaee, A., Fellenius, B. H., & Evgin, E. (1992). Axial load transfer for piles in sand. I. Tests on an instrumented precast pile. Canadian Geotechnical Journal, 29(1), 11-20.

Jardine, R. J., Zhu, B., Foray, P., & Dalton, C. P. (2009). Experimental arrangements for investigation of soil stresses developed around a displacement pile. Soils and Foundations, 49(5), 661-673.

Kuwajima, K., Hyodo, M., & Hyde, A. F. (2009). Pile bearing capacity factors and soil crushability. Journal of Geotechnical and Geoenvironmental Engineering, 135(7), 901-913.

Talesnick, M. (2013). Measuring soil pressure within a soil mass. Canadian Geotechnical Journal, 50(7), 716-722.

Tanimoto, K., & Tanaka, Y. (1986). Yielding of soil as determined by acoustic emission. Soils and foundations, 26(3), 69-80.

Yang, Z. X., Jardine, R. J., Zhu, B. T., Foray, P., & Tsuha, C. H. C. (2010). Sand grain crushing and interface shearing during displacement pile installation in sand. Géotechnique, 60(6), 469-482.

Yasufuku, N., & Hyde, A. F. L. (1995). Pile end-bearing capacity in crushable sands. Geotechnique, 45(4), 663-676.

Yu, F. (2014). Experimental study on particle breakage under high pressure. Doctoral dissertation, the University of Tokyo, Tokyo.

Zhu, B., Jardine, R. J., & Foray, P. (2009). The use of miniature soil stress measuring cells in laboratory applications involving stress reversals. Soils and Foundations, 49(5), 675-688.

CHAPTER 7

SOURCE LOCATION OF AE SIGNALS

7.1 INTRODUCTION

The AE evolution characteristics indicate the intensity of subsoil crushing and sliding during pile penetration processes. For the investigation of underlying ground bearing mechanism, it was further necessary to determine the location of the AE signals. AE is part of the irrecoverable energy dissipations due to plastic straining of the stressed material. It is expected that active AE should be associated with locations of severest stress concentration or strain mobilization. The spatial distribution of AE hypocenters provides direct insights into such regions, which is relatively difficult to identify by traditional measurements. For this purpose, an AE source location method based on multiple sensor array was firstly developed. Furthermore, a series of pile penetration tests were conducted to explore the subsoil behavior subjected to pile penetration. The developed methodology, experiments, and the related discussions are presented in this chapter.

7.2 METHODOLOGY

7.2.1 Fundamentals of AE Source Location

Figure 7.1 shows the illustration of transducer arrangement adopted for the AE source location in this study. The AE sensors were set to surround the target area, i.e. 1-2D to the pile tip. In a Cartesian coordinate system, the distance (*d*) between two points, e.g. AE source and sensor, can be calculated using the following equation:

$$d_i = (t_i - t) * v = \sqrt{(x - x_i)^2 + (y - y_i)^2 + (z - z_i)^2} \qquad (7\text{-}1)$$

where d_i: distance between signal source and *i*-th sensor;

t: real signal onset time;

t_i: arrival time at the *i*-th sensor;

v: wave velocity;

x, y, z: coordinates of the signal source;

x_i, y_i, z_i: coordinates of the *i*-th sensor;

In the above equation, only four parameters (x, y, z, t) correlated with AE source are unknown if a constant wave velocity is assumed. Suppose one event signal is captured by four sensors (No.1-4), an equation system shown in Equation (7-2) can be subsequently obtained. By solving the Equation (7-2), the location and the onset time of the signal were therefore derived. Theoretically, a four-sensor array would be able to localize one AE event based on the Time Difference of Arrival (TDOA) among sensors. In practice, more sensors are arranged in order to eliminate the potential errors. In the current study, an eight-sensor array was applied to capture the AE signals around the pile tip.

$$\begin{cases} (t_1 - t) * v = \sqrt{(x - x_1)^2 + (y - y_1)^2 + (z - z_1)^2} \\ (t_2 - t) * v = \sqrt{(x - x_2)^2 + (y - y_2)^2 + (z - z_2)^2} \\ (t_3 - t) * v = \sqrt{(x - x_3)^2 + (y - y_3)^2 + (z - z_3)^2} \\ (t_4 - t) * v = \sqrt{(x - x_4)^2 + (y - y_4)^2 + (z - z_4)^2} \end{cases} \quad (7\text{-}2)$$

In Equation (7-2), the coordinates of sensors can be determined during experimental setting, while the velocity of the elastic wave can be estimated from pre-testing measurements (around 200 m/s in the current study). However, the arrival time of the signals to the sensor array needs to be picked up one by one. Reliable signal source location required accurate determination of the arrival times picked by the sensors. Millions of individual events from a pile loading test prevent the use of manual pick-up method. Therefore, an automatic arrival time picking algorithm was developed. The following sections describes the details of the mathematical derivations for arrival time determination, as well as the iteration step of solving Equation (7-2).

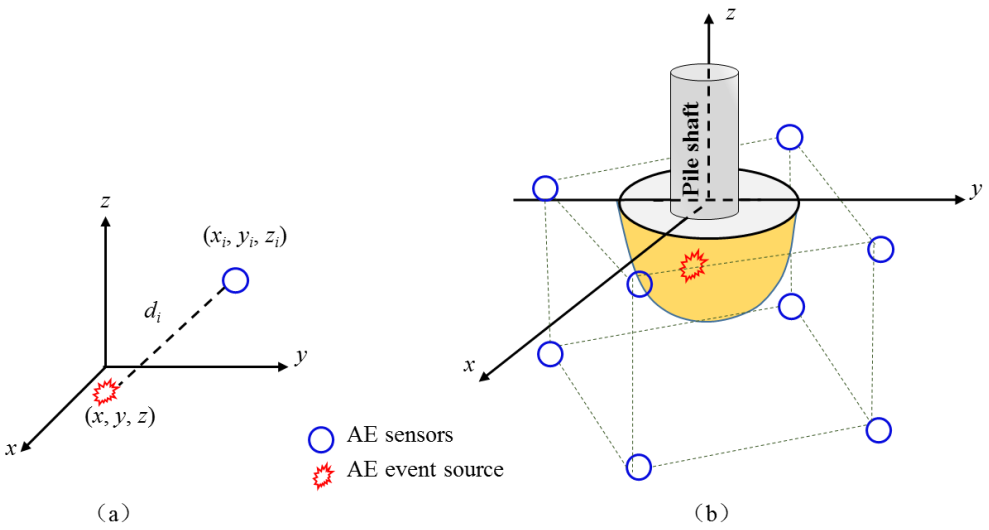

Figure 7.1 Schematic diagram of sensor array for AE source localization

7.2.2 AR-AIC Model for Signal Onset Time Determination

7.2.2.1 Derivation of AR-AIC Model

In signal processing, the time series of a stationary signal can be represented in autoregressive process. The current observations of a signal in the autoregressive (AR) model can be described as the linear combination of the *p* predecessors. (Takanami and Kitagawa 1988, Sleeman and van Eck 1999, Niccolini et al. 2012). A general form of an AR (*p*) model is:

$$X_t = c + \sum_{i=1}^{p} \varphi_i X_{t-i} + \varepsilon_t \tag{7-3}$$

where φ_i (i=1, 2, 3, …p) are the parameters of the AE model

c: constant value;

ε_t : white noise

p:order of AE model

Referring to the AR-AIC model for arrival time determination, the non-stationary AE signals are described as locally stationary AR processes, using Akaike Information

Criteria (AIC, Akaike 1973). Figure 7.2 shows a schematic illustration of the computation process of AR-AIC model. Suppose $\{x_1, x_2, x_3, \ldots, x_N\}$ is a signal obtained from the sensor, containing both background noise and the signal part. Therefore, this time series here can be divided in two segments: the noise part $\{x_1, x_2, x_3, \ldots, x_M\}$, and the signal part $\{x_{M+1}, x_{M+2}, x_{M+3}, \ldots, x_N\}$, where M here identifies the unknown signal onset time. Two intervals before and after the onset time are assumed to be two different pseudo-stationary time series. Each of the two intervals is modeled as an autoregressive process of order p^i with coefficients a_m^i (i=1, 2 corresponding to noise and signal part respectively). An estimated arrival time is assumed at first, computing the AIC and then approaching to the next point.

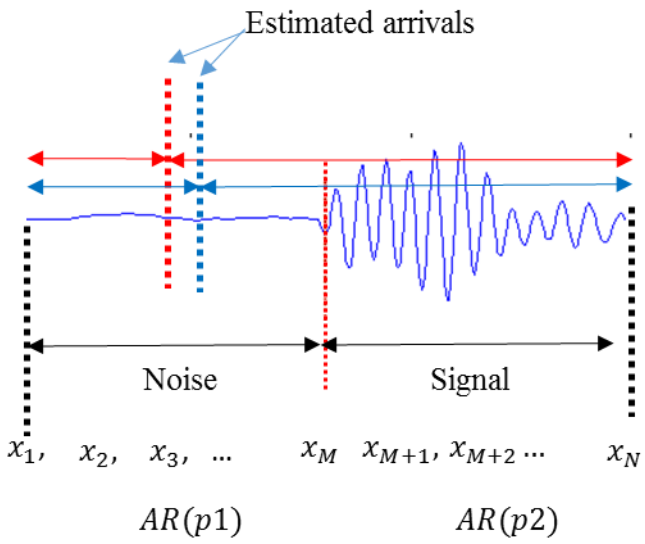

Figure 7.2 Schematic illustration of the computation process of AR-AIC model

For noise part AR (*p1*):

$$x_m^n = \sum_{j=1}^{p1} \alpha_j^n x_{m-j} + \varepsilon_n^n \tag{7-4}$$

where m=1, 2, 3, … M. *p1* is the order of the noise part AR model. a_j^n is the autoregressive coefficient, and ε_n^n is a Gaussian white noise with mean zero and variance σ_n^2.

For signal part AR (*p2*):

$$x_m^s = \sum_{j=1}^{p2} \alpha_j^s x_{m-j} + \varepsilon_n^s \tag{7-5}$$

where $m=M+1, M+2, M+3, \ldots N$. *p2* is the order of the signal part AR model. a_j^s is the autoregressive coefficient, and ε_n^s is a Gaussian white noise with mean zero and variance σ_s^2.

Taking noise part for example, Equation (7-4) can be rewritten as:

$$\boldsymbol{Y^n} = \boldsymbol{X^n a^n} + \boldsymbol{\varepsilon^n} \tag{7-6}$$

where

$$\boldsymbol{Y^n} = [x_{p1+1}\ x_{p1+2}\ x_{p1+3} \ldots x_{p1+M}]^T \tag{7-7}$$

$$\boldsymbol{a^n} = [a_1\ a_2\ a_3 \ldots a_M\ ]^T \tag{7-8}$$

$$\boldsymbol{\varepsilon^n} = [\varepsilon_1\ \varepsilon_2\ \varepsilon_3 \ldots \varepsilon_M\ ]^T \tag{7-9}$$

$$\boldsymbol{X^n} = \begin{bmatrix} x_{p1} & x_{p1-1} & \cdots & x_1 \\ x_{p1+1} & x_{p1} & \cdots & x_2 \\ \cdots & \cdots & \cdots & \cdots \\ x_{M-1} & x_{M-2} & \cdots & x_{M-p1} \end{bmatrix} \tag{7-10}$$

By applying the least square method, $\boldsymbol{a^n}$ can be estimated as

$$\boldsymbol{a^n} = (\boldsymbol{X^{nT} X^n})^{-1} \boldsymbol{X^{nT} Y^n} \tag{7-11}$$

Therefore, the variance $\sigma_{n,\max}^2$ is

$$\sigma_{n,\max}^2 = (\boldsymbol{Y^n} - \boldsymbol{X^n} * \boldsymbol{a^n})^T (\boldsymbol{Y^n} - \boldsymbol{X^n} * \boldsymbol{a^n}) / (M - p1) \tag{7-12}$$

The AIC value of the noise part is given by the equation below (Niccolini et al. 2012, Takanami and Kitagawa 1988).

$$AIC_{noise} = M \log(\sigma_{n,\max}^2) + 2p1 \tag{7-13}$$

Being similar to the noise part, the $\sigma^2_{s,\max}$ of the signal part can also be obtained. Consequently, the AIC of the whole signal is derived:

$$AIC_{total} = AIC_{signal} + AIC_{noise} \tag{7-14}$$

The arrival time of the signal corresponded to the minimum AIC value of the whole time window derived from Equation (7-14).

7.2.2.2 Signal Searching Tactics

For determination of individual signal arrival from a long time series, a threshold is firstly applied to search the large amplitudes in the record, as shown in Figure 7.3. Then, the time window is consist of +/- X points from the point over the threshold in order to include both background noise and the arriving signal. The length of time window may differ in case of different signal sampling speed. For example, when the sampling rate is set at 500 kHz/s, a length of 400 points corresponding to 0.8ms is usually enough for AR-AIC analysis. It is important to confirm the validation of time window selection by checking the data manually before computing the whole time series.

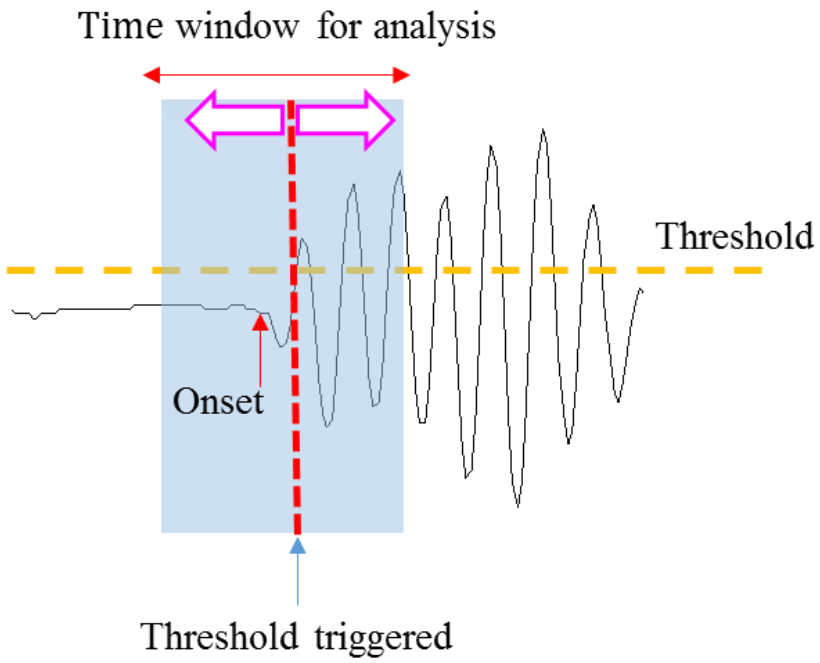

Figure 7.3 Illustration of time window selection

7.2.2.3 Performance of the AR-AIC Model

Two examples of the algorithm performance are shown in Figure 7.4 and Figure 7.5. Both high frequency and low frequency signals are verified. It can be seen that the arrival time determined by the AR-AIC model gave reasonable results. Therefore, the developed method was applied to the entire dataset of eight channels from a pile test, yielding a list of signal arrival times for further analysis.

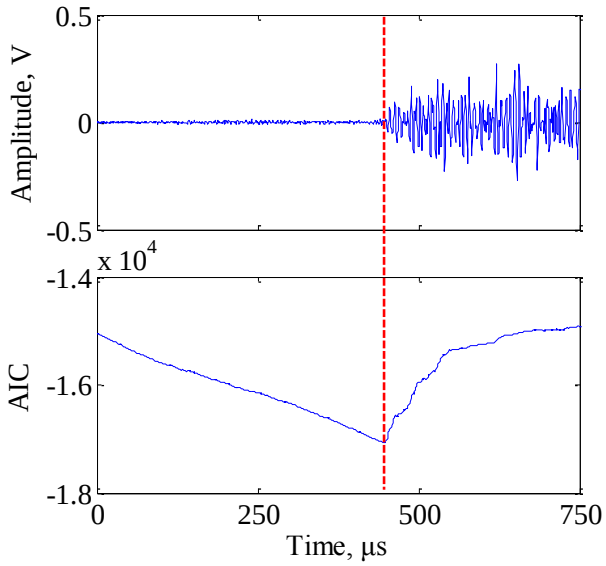

Figure 7.4 Performance of AR-AIC model applied to high frequency signal

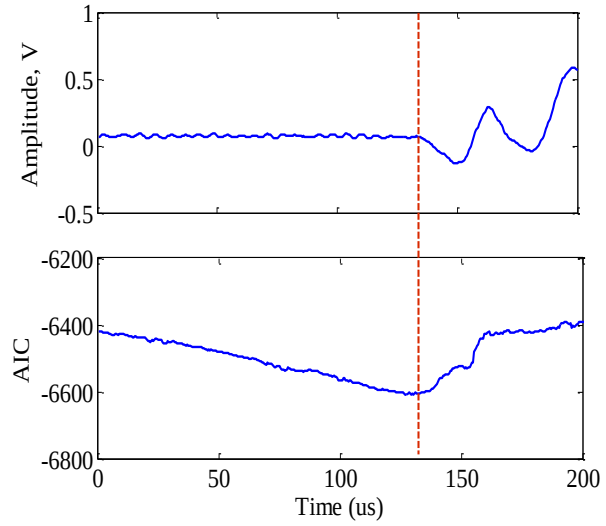

Figure 7.5 Performance of AR-AIC model applied to low frequency signal

7.2.3 Computation of Signal Source

7.2.3.1 Determination of Wave Velocity

In order to simplify the computing process, a constant value of wave velocity was assumed in the current analysis. The assumed wave velocity was measured by an additional test before the source location test. Figure 7.6 shows the schematic view and the photo of the test layout for determination of the compression wave velocity *Vp*. The sensors were embedded in the sand at a certain distance. The source of the signal were excited by hitting the metal plate placed on the sand surface. Therefore, the velocity of the wave can be calculated based on the time difference of signal arrival and the distance between the sensors.

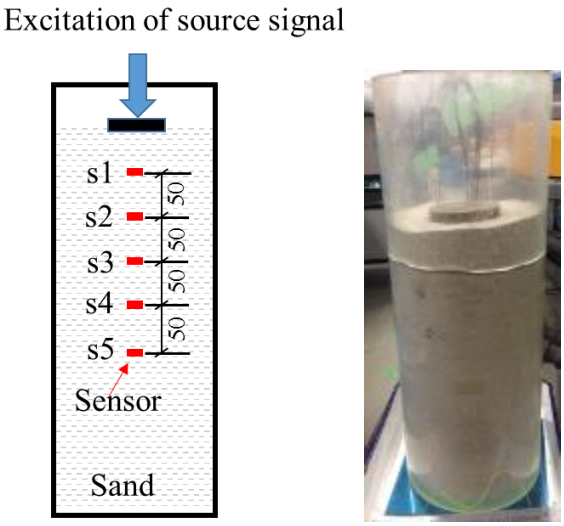

Figure 7.6 Illustration of wave velocity estimation

Table 7.1 Measured compression wave velocity

Sensor range	s1-s2	s2-s3	s3-s4	s4-s5	Average
Velocity (m/s)	189.5	196.2	195.4	203.3	196.1

Table 7.1 shows the measured wave velocity when the ground relative density was 79%. It should be noted that the velocity of wave propagation in soil is affected by a variety of factors including the ground density, stress level as well as grain size distribution of the soil. According to Irfan (2014), the increased stress condition will result in the increased wave velocity. During pile penetration, it is expected that a

high stress zone would appear below the pile tip. Therefore, the wave velocity within that zone should become higher. However, it is also noted that the source region of the AE is limited to a small area, and the higher stress will decrease rapidly as it become distant from the pile (Jardine et al. 2013). As a result, the zone of higher wave velocity is restrained to a limited area as well. In addition, the AE sensors were placed almost symmetrically around the pile tip. Therefore, to some extent, the influence of the changed wave velocity can be balanced out among sensors. For simplification, the wave velocity was simply set at 200m/s in the current analysis.

7.2.3.2 Derivation of Solution

Equation 7-2 can be rewritten as:

$$\begin{cases} f_1 = (x-x_1)^2 + (y-y_1)^2 + (z-z_1)^2 - (t_1-t)^2 v^2 \\ f_2 = (x-x_2)^2 + (y-y_2)^2 + (z-z_2)^2 - (t_2-t)^2 v^2 \\ f_3 = (x-x_3)^2 + (y-y_3)^2 + (z-z_3)^2 - (t_3-t)^2 v^2 \\ f_4 = (x-x_4)^2 + (y-y_4)^2 + (z-z_4)^2 - (t_4-t)^2 v^2 \end{cases} \quad (7\text{-}15)$$

Think of (x_1, x_2, x_3, x_4) as a vector $\boldsymbol{x}$ and (f_1, f_2, f_3, f_4) as a vector-valued function $\boldsymbol{f}$. With this notation, Equation 7-15 can be written as

$$\boldsymbol{f}(\boldsymbol{x}) = 0 \quad (7\text{-}16)$$

Figure 7.7 illustrates the procedure of how the solution of $\boldsymbol{f}(\boldsymbol{x})$ is found by using the Newton-Raphson method (Ben-Israel 1966). The equation $\boldsymbol{f}(\boldsymbol{x}) = 0 \approx \boldsymbol{f}(\boldsymbol{x_0}) + \boldsymbol{f}'(\boldsymbol{x_0})(\boldsymbol{x_1} - \boldsymbol{x_0})$, which is the first order terms in a Taylor expansion series. It is a straight line tangent to $\boldsymbol{y} = \boldsymbol{f}(\boldsymbol{x})$ at $\boldsymbol{x} = \boldsymbol{x_0}$. This straight line intersects the x-axis at the point x_1, which can be calculated by $\boldsymbol{x_1} = \boldsymbol{x_0} - \boldsymbol{f}(\boldsymbol{x_0})/\boldsymbol{f}'(\boldsymbol{x_0})$**.** By applying the same method to the point x_1, another point x_2 is subsequently obtained. The actual root of the equation can be found by continuing this process of iteration. For the other parameters including y**, *z, t***, same idea can be applied.

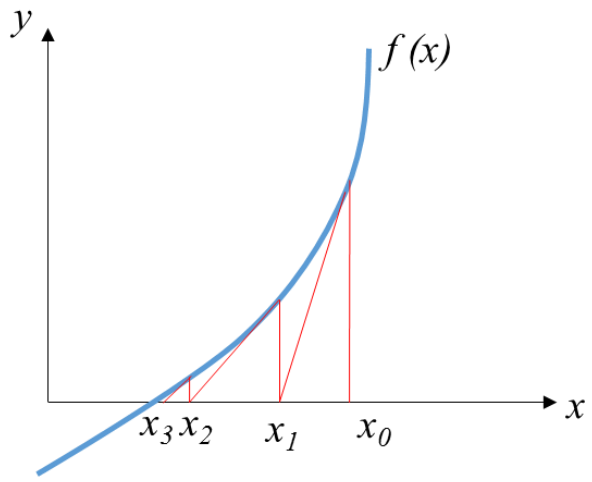

Figure 7.7 Illustration of Newton-Raphson method for equation solution

Detailed steps to solve Equation (7-15) are listed below:

(1) Assign an initial value to x_k (k=0); note x_k here is a vector of *x*, *y*, *z*, *t*

(2) Let $\Delta x_k = x_{k+1} - x_k$

Hence $x_{k+1} = x_k + \Delta x_k$

$$f(x_k) + f'(x_k)(\Delta x_k) = 0 \quad k = 0, 1, 2, \ldots \tag{7-17}$$

(3) Iteration format is

$$x_{k+1} = x_k - f(x_k)/f'(x_k) \tag{7-18}$$

where

$$f(x_k) = \begin{pmatrix} f_1(x_k, y_k, z_k, t_k) \\ f_2(x_k, y_k, z_k, t_k) \\ f_3(x_k, y_k, z_k, t_k) \\ f_4(x_k, y_k, z_k, t_k) \end{pmatrix} \tag{7-19}$$

$$f'(x_k) = \begin{pmatrix} 2(x_k - x_1) & 2(y_k - y_1) & 2(z_k - z_1) & -2v^2(t_k - t_1) \\ 2(x_k - x_2) & 2(y_k - y_2) & 2(z_k - z_2) & -2v^2(t_k - t_2) \\ 2(x_k - x_3) & 2(y_k - y_3) & 2(z_k - z_3) & -2v^2(t_k - t_3) \\ 2(x_k - x_4) & 2(y_k - y_4) & 2(z_k - z_4) & -2v^2(t_k - t_4) \end{pmatrix} \tag{7-20}$$

(4) If$|x_{k+1} - x_k| < \varepsilon$, iteration end. $x = x_{k+1}$

7.2.3.3 Flow Chart of AE Source Location

As described above, a list of arrival times is obtained from different channels (totally eight channels in the current study). However, it is still unknown which arrival times share a common AE event. Therefore, the following strategy is used to find matches.

The time at the beginning of pile penetration was set as 0. For each channel, if the difference of the arrival times is less than 0.4ms, they are grouped as the arrivals corresponding to the same event. The measured wave velocity before the test was found to be around 200m/s. Therefore, an absolute difference of 0.4ms duration yielding a 16cm long propagation distance, which is almost reaching the longest distance between sensors. In such case, all signals originated within the range of the sensor coverage is able to be localized. Although at minimum case, four channels is possible to identify one event, usually at least five channel are used in order to eliminate the errors. Therefore, in a specific time duration, if the number of arrival channels is less than five, then the signal is deemed insignificant. The searching time indicator will jump an interval of 0.4 for the next round.

When there are more than five channels matching as a group, the subsequent step is followed. First, a four-equation system is assembled by randomly selection of four matched channels. In this step, the total sets of equation system depend on the number of channels in the group, which is mathematically given by N=C_n^4. The solution of the equation systems is done by the Newton-Raphson method as explained in the previous section. After all potential equation systems are solved, the candidate positions of the AE event are obtained. Finally, the source position with the smallest root mean square of the computed arrival time minus observed arrival times is selected as the actual location. Figure 7.8 shows the overall flowchart of the described source location algorithm.

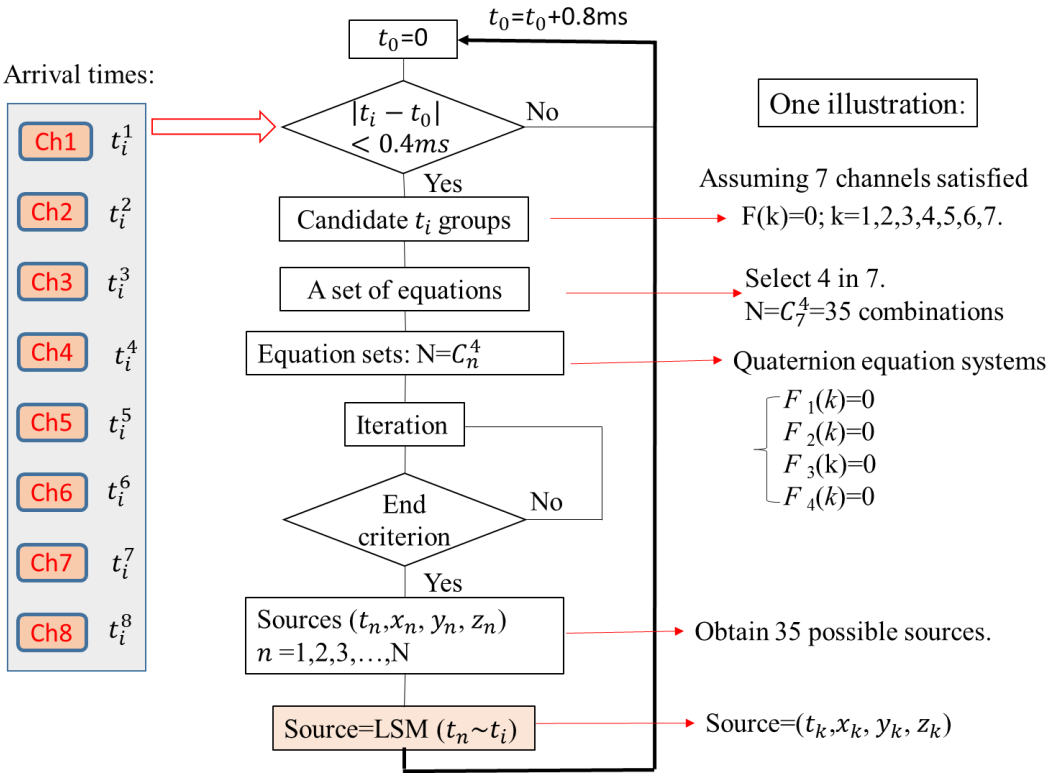

Figure 7.8 Flowchart of AE source location computation algorithm

7.2.4 AE Source Location during Pile Penetration in Silica Sand No.5

7.2.4.1 General Setup

During AE sensor location tests, eight sensors were set around the pile tip. Figure 7.9 shows the detailed positions of the sensor arrangement. For the convenience of installation, the sensors were placed at two layers only, which is 10mm and 70mm below the pile end respectively. Horizontal distance between the sensor and pile center was set as 70mm. Table 7.2 summarizes the coordinates of the sensors. The following sections show the performance of the above developed methodology applied to pile penetration tests.

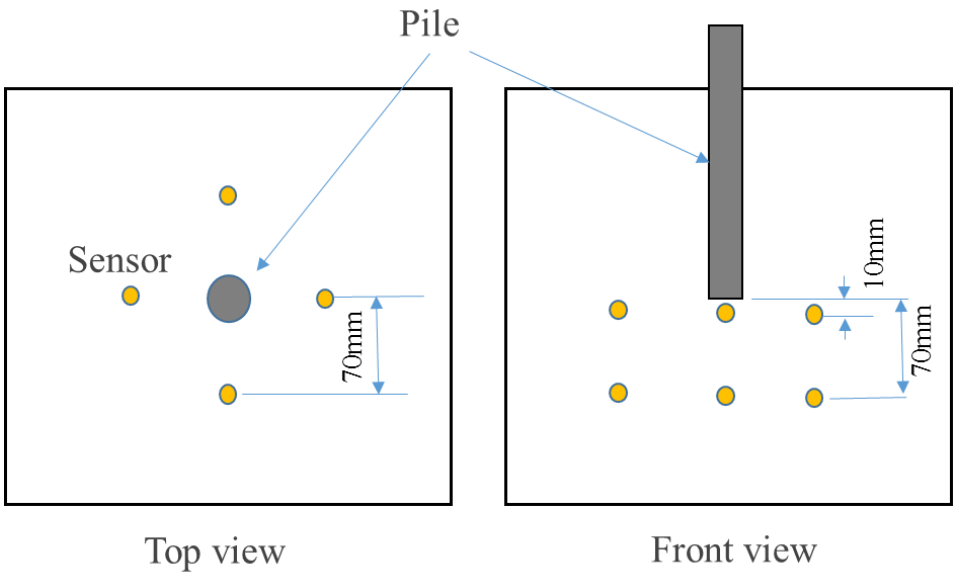

Figure 7.9 Layout of the sensor arrangement

Table 7.2 The coordinates of the sensor array

Sensor No.	*Coordinate (m)		
	x	y	z
S1	0	-0.07	-0.07 or -0.09
S2	0.07	0.07	-0.07 or -0.09
S3	-0.07	0	-0.01
S4	0.07	0	-0.01
S5	-0.07	0	-0.07 or -0.09
S6	0.07	0	-0.07 or -0.09
S7	0	0.07	-0.01
S8	0	-0.07	-0.01

*The origin of coordinates was set at the center of pile end before loading initiation.

7.2.4.2 Results of Source Location in Dense Silica Sand

Figure 7.10 shows the spatial distribution of individual events. The obtained results are displayed by every 2mm (0.05D) penetration. Only the results of the first 8mm penetration are presented, since it became similar during the subsequent plots. The events during the first 2mm penetration were almost randomly distributed. As the penetration proceeded, more events were found to be clustered together. Figure 7.11 and Figure 7.12 show the distribution of the localized AE sources at every 2mm pile penetration in terms of pseudo colour and contour plotting. The first 20mm penetration was presented. Quantified distribution of the events can be seen from the figures.

A notable feature in Figure 7.11 and Figure 7.12 is that the AE sources were not uniformly distributed below the pile tip, but concentrated within a limited region about 0.5-1D below pile tip. It is illustrated that the distribution of events was in form of radially extended manner, with density reduced outwards, indicating that the soils within this region underwent severest dislocation or crushing.

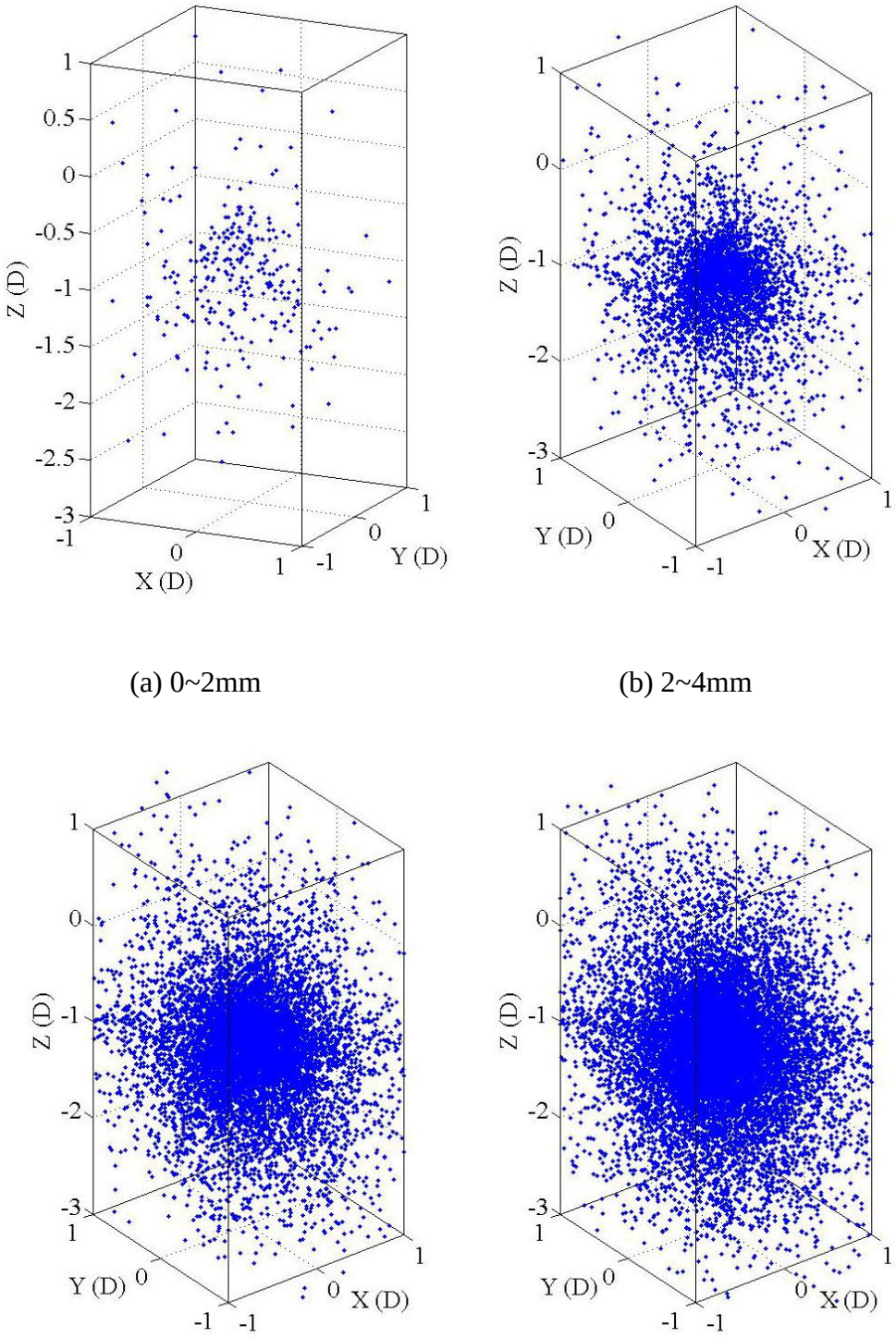

(a) 0~2mm (b) 2~4mm

(c) 4~6mm (d) 6~8mm

Figure 7.10 Spatial distribution of AE events (0-8mm penetration)

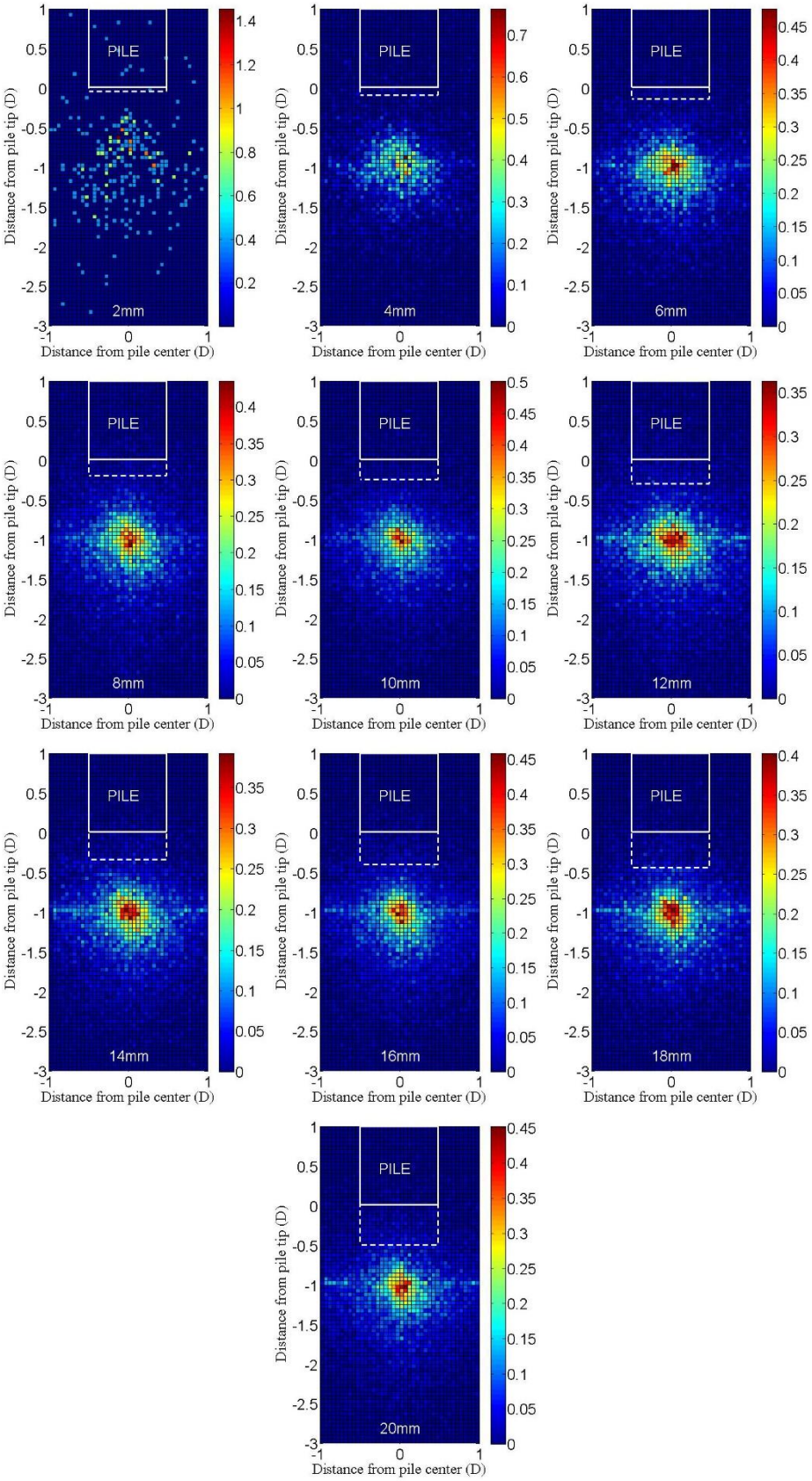

Figure 7.11 Distribution of AE source: Dense silica No.5

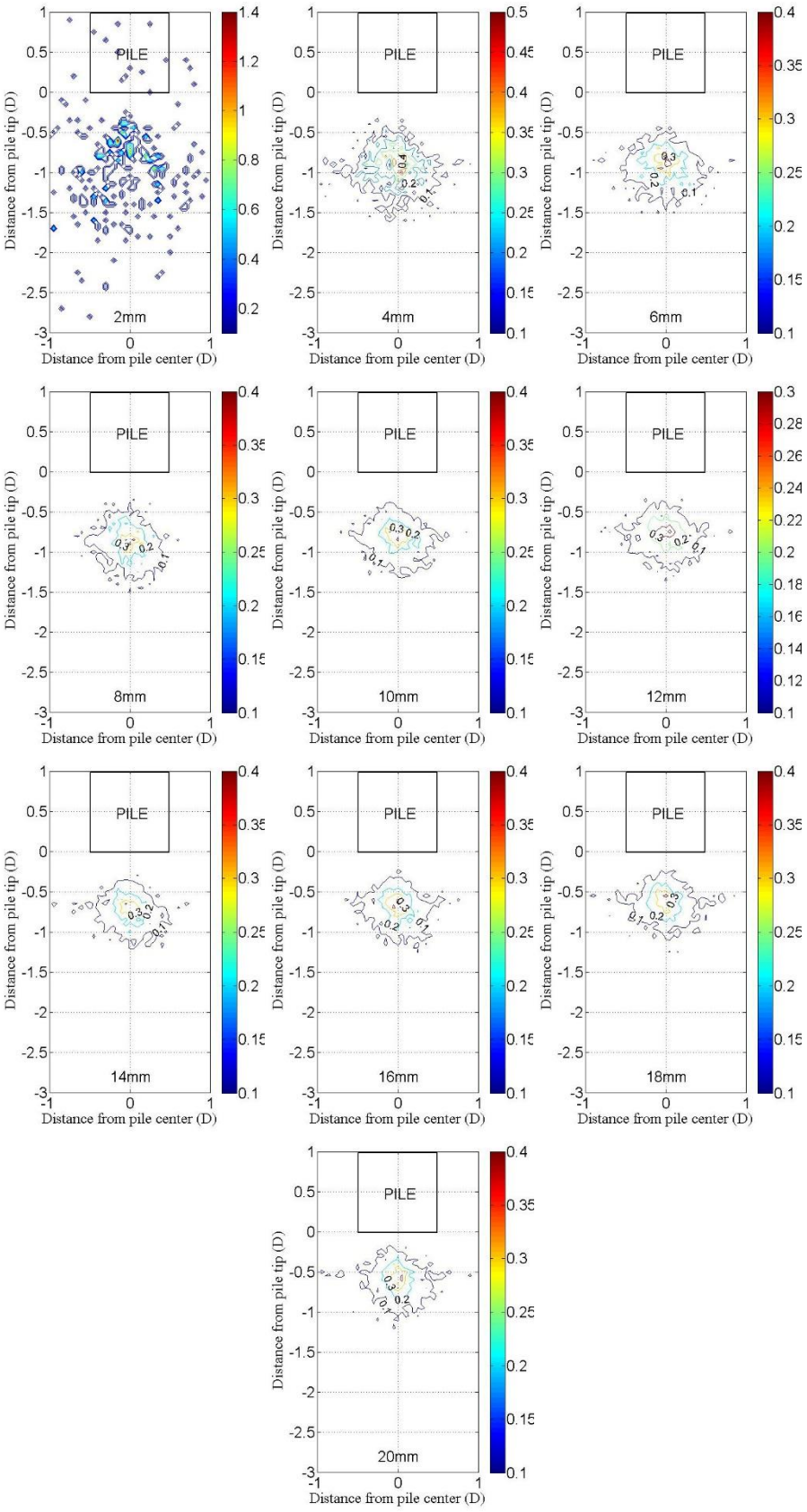

Figure 7.12 Contour distribution of AE sources in silica sand with corrected pile depth

7.2.4.3 Results of AE Source Location in Loose Silica Sand

Figure 7.13 shows the source distributions in case of loose silica sand (Dr=31.2%). Compared with dense case, the event distribution appeared more scattered below the pile tip in loose sand. Therefore, contour plotting is not presented every 2mm because the shape become rather distorted. Figure 7.14 shows the distribution of all localized AE in one plotting. Clear clustering of AE events can be identified. It demonstrates that the overall behaviour of dense and loose ground may be of a similar trend.

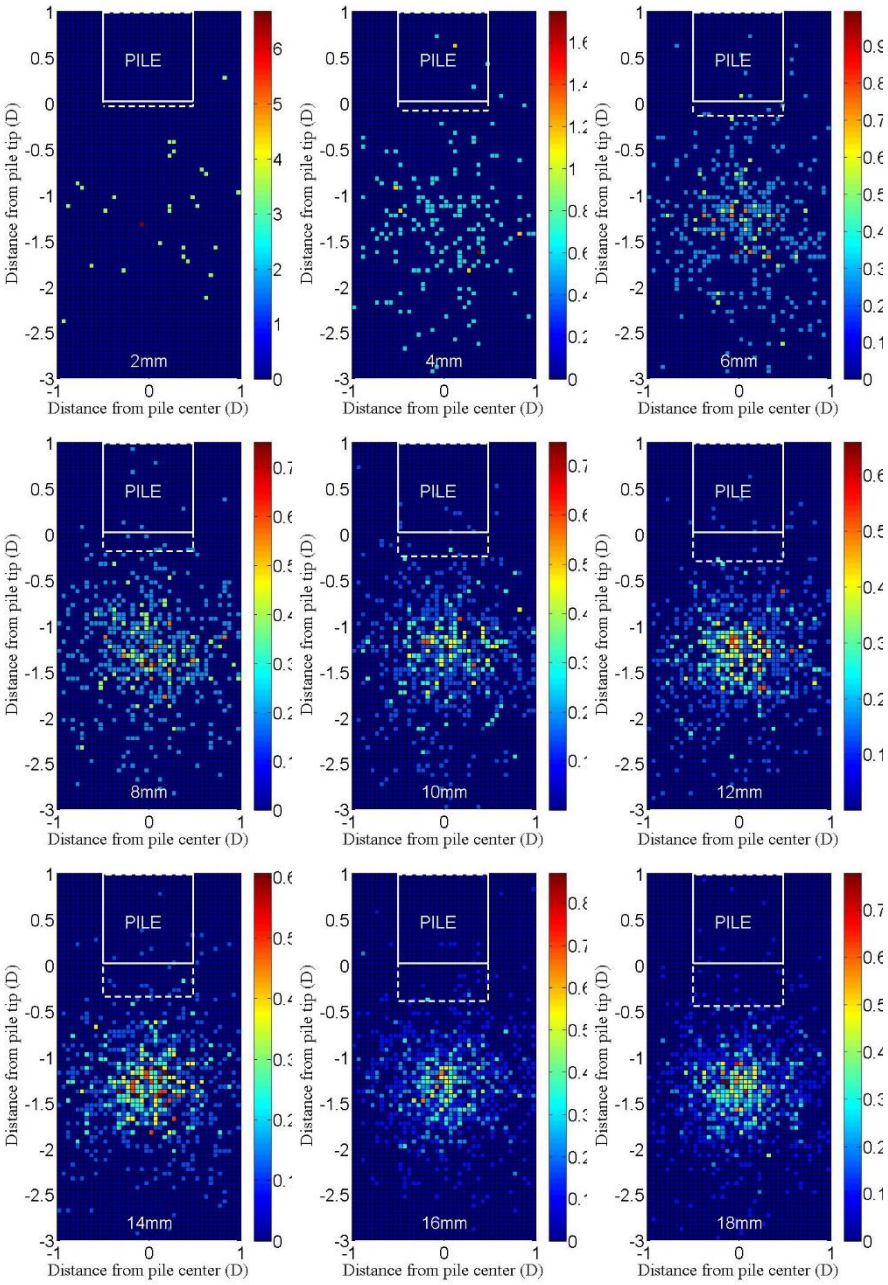

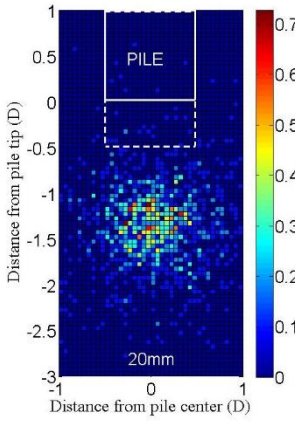

Figure 7.13 AE source distribution in loose silica sand

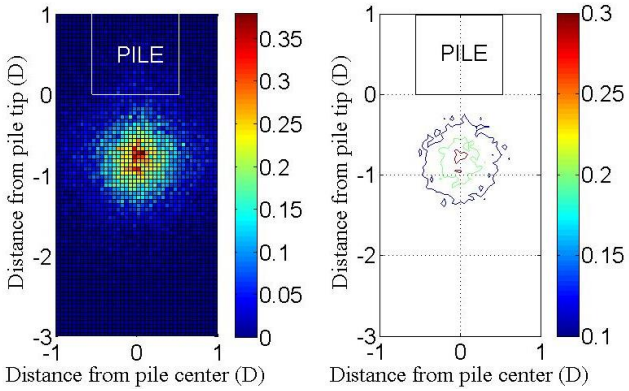

Figure 7.14 Distribution of all localized AE in loose silica sand

7.2.5 AE Source Location during Pile Penetration in Coral Sand No.1

Considering low emission level of coral sand, only dense case was tested, with relative density of 97.2%. Figure 7.15 shows the 3D spatial distribution of AE events in case of pile loading in coral sand. In general, all AE events were spread within a limited region, with almost no AE signals located in the distant area. This observation contrasted sharply with silica sand results. Figure 7.16 and Figure 7.17 shows the pseudo color plotting and contour plotting of all results up to 20mm penetration.

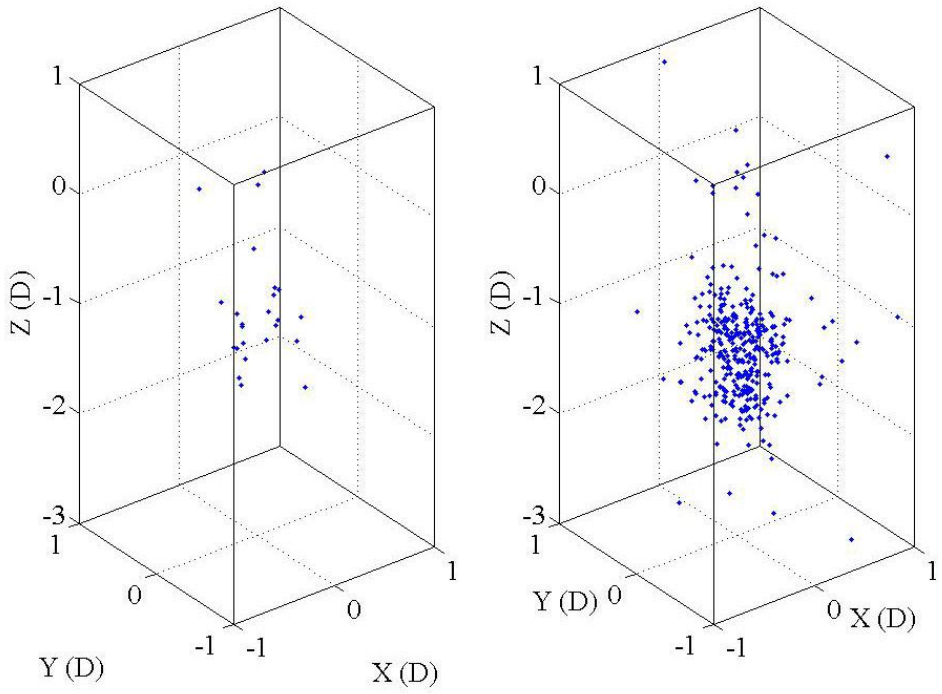

(a) 0~2mm

(b) 2~4mm

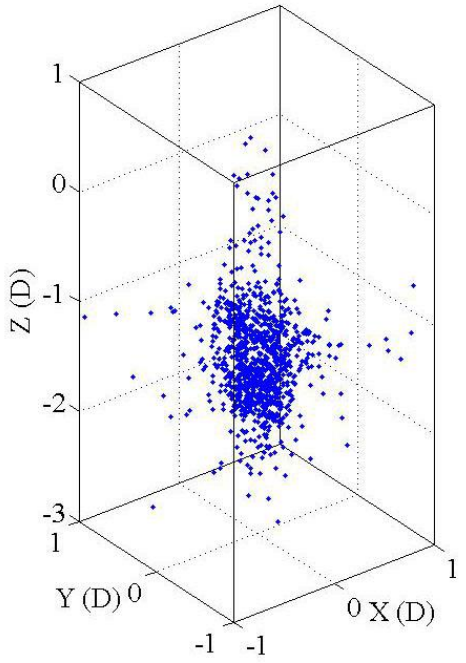

(a) 4~6mm

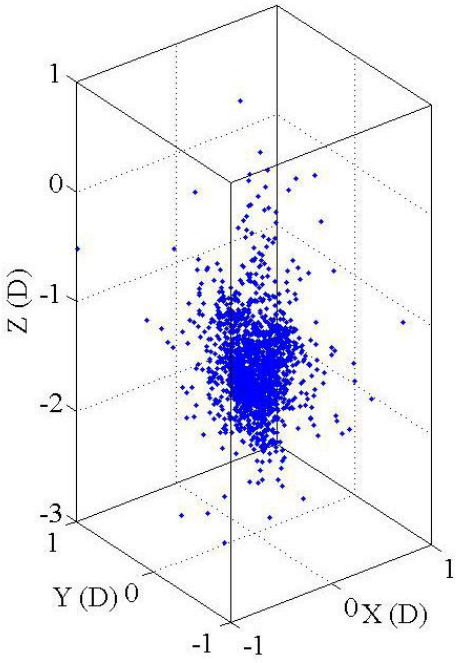

(b) 6~8mm

Figure 7.15 Spatial distribution of AE events in coral sand (0-8mm penetration)

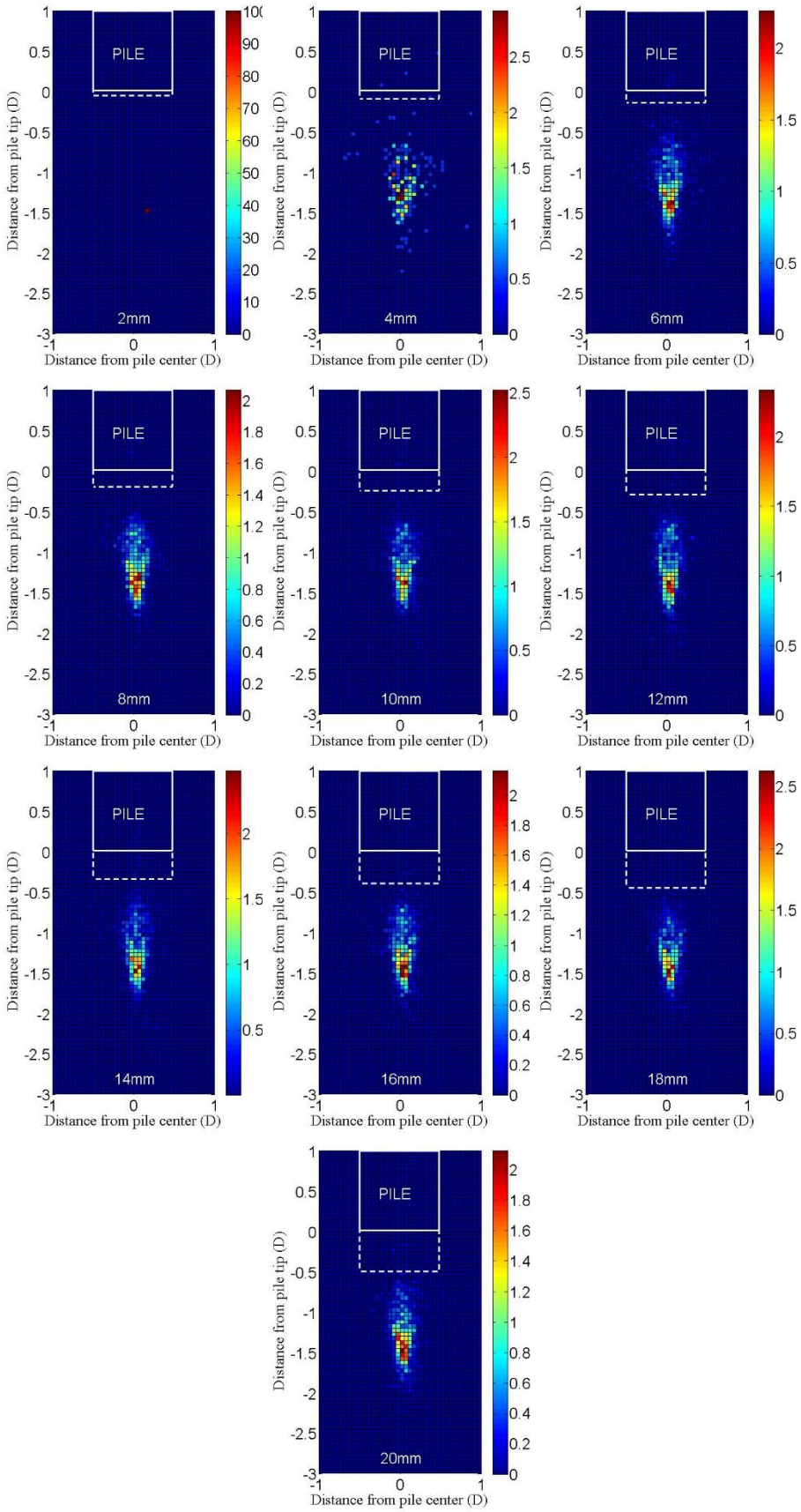

Figure 7.16 AE source distribution in coral sand

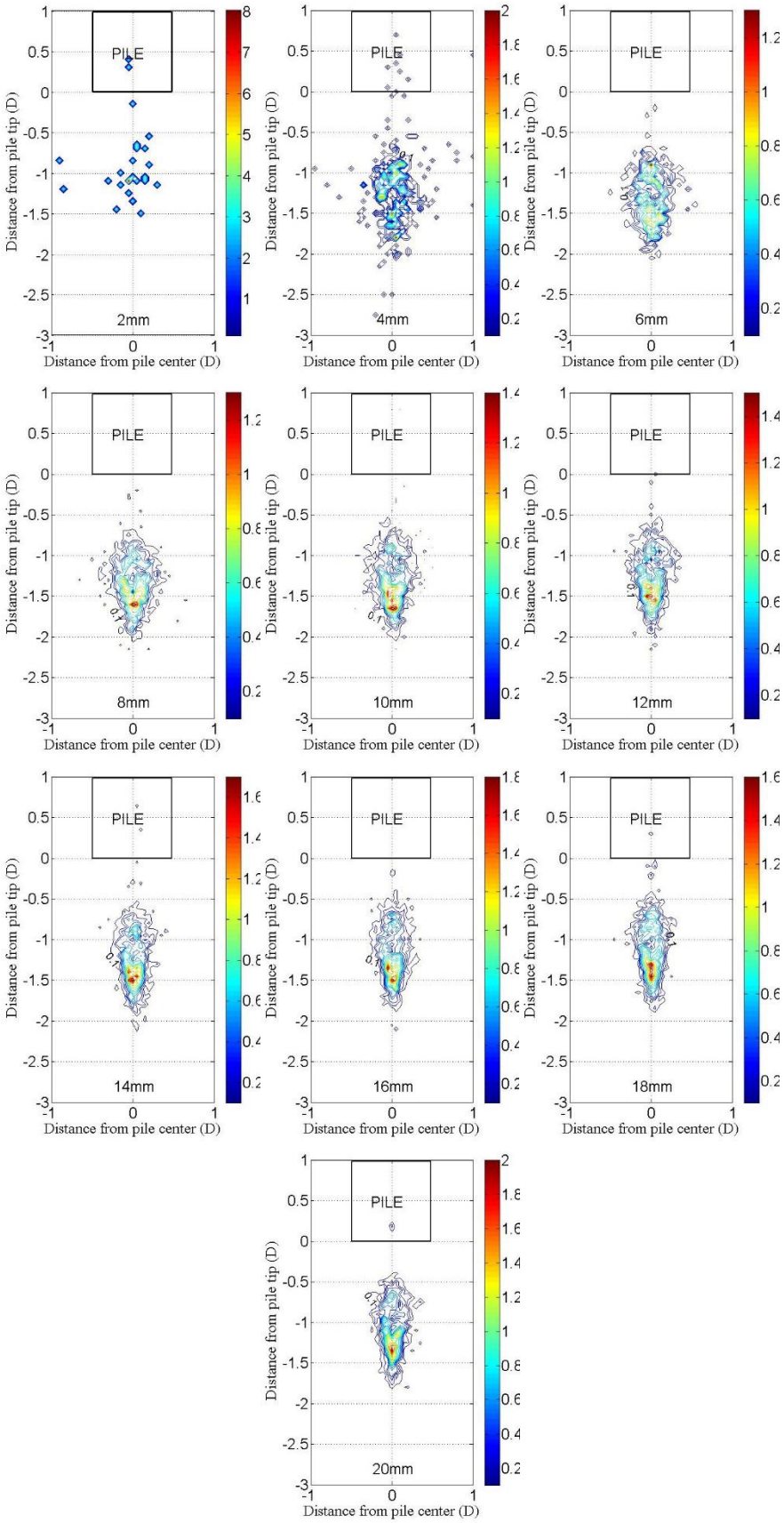

Figure 7.17 Contour distribution of AE sources in coral sand with corrected pile depth

7.2.6 Comparison between Silica Sand and Coral Sand

7.2.6.1 Comparison of Dense and Loose Silica Sand

Figure 7.18 shows the number of the localized AE events during every 2mm penetration. For dense case, the number of localized events at the beginning of loading was much less compared with that in the latter periods. It grew with the penetration and became relatively constant. By contrast, the loose case showed a continuous increasing trend as the penetration proceeded. Such a feature is similar with the AE activity evolution in forms of count, amplitude and energy, where loose case also exhibited more evident increasing trend after ground yielding.

It was also seen from Figure 7.11 and Figure 7.13 that the source distribution of loose case is more scattered compared with that of dense case. The smaller number of total events in loose case may be responsible for the observed scattering distribution, because the number of events localized in loose case was only one-tenth compared with that of dense case. Therefore, a set of data (first 900 events) extracted from the dense case during 6-8mm pile penetration was re-plotted, comparing with the loose case at the same penetration depth (849 events during 6-8mm penetration), as shown in Figure 7.19. Still, it can be seen that the dense case shows more significant clustering. This observation indicates the different subsoil behaviours below the pile tip. For dense sand, a cone shaped core area is formed below the pile tip, generating a shear surface around the outer boundary. For loose sand, the compression of the soil directly below the pile end was more dominant during penetration. Therefore, the stress concentration or strain localization at the cone head would take more time to be reached. Detailed discussion on the subsoil behaviour below the pile tip will be presented in the next section.

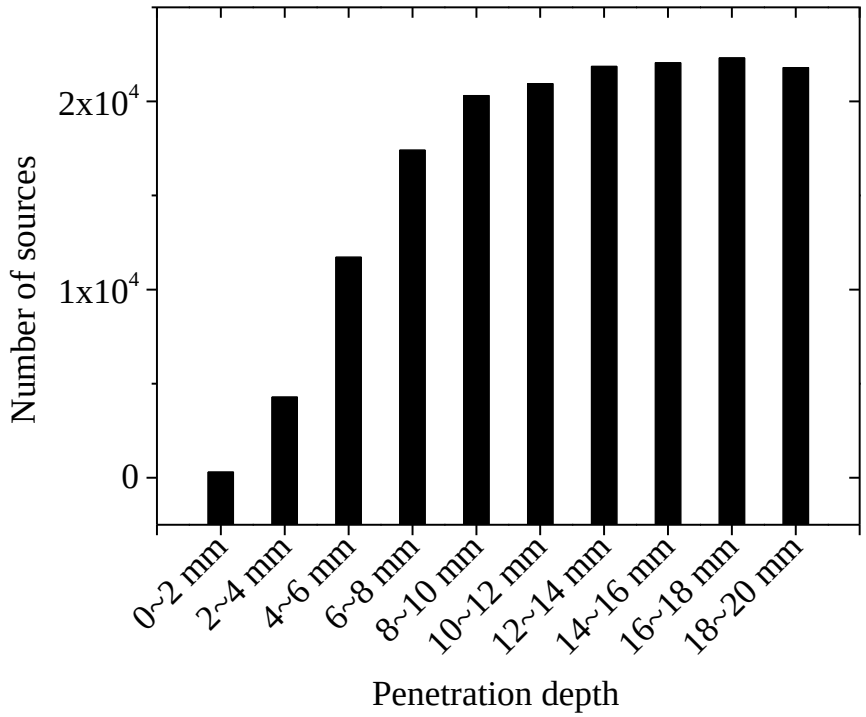

(a) dense case

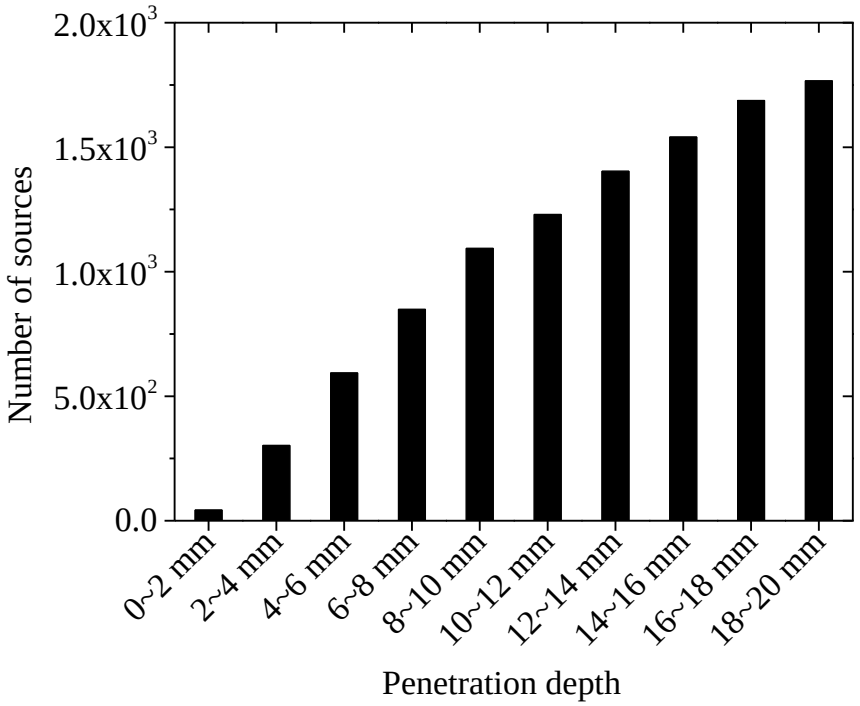

(b) loose case

Figure 7.18 Number of source localized in dense and loose silica sand

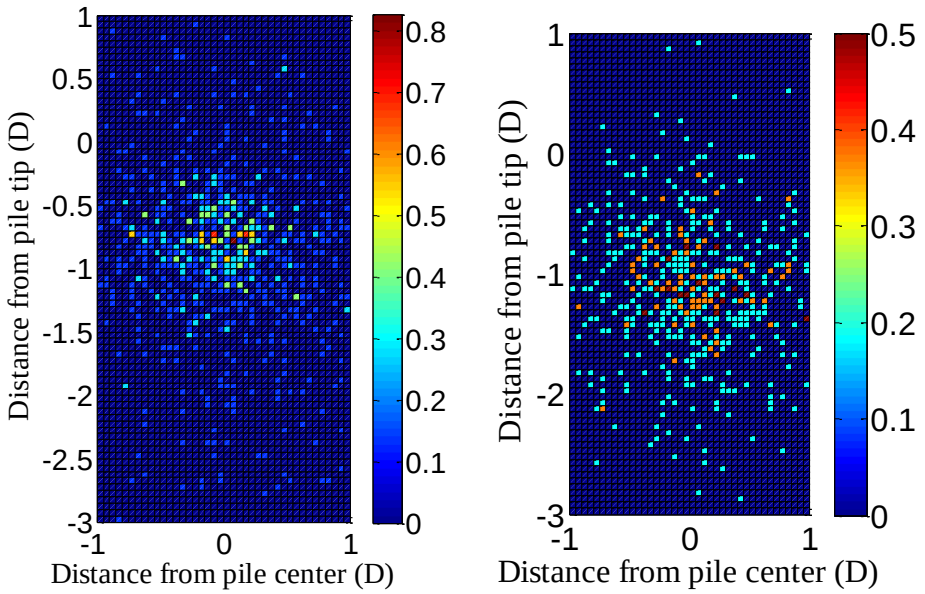

(a) (b)

Figure 7.19 Comparison of density distribution of (a) dense case (first 900 events) and (b) loose case (849 events)

7.2.6.2 Comparison of Silica Sand and Coral Sand

As was discussed in the previous chapter, the emission level of coral sand is much lower than that of silica sand. Although dense ground sample was tested for coral sand, the localized events were limited and the number was only comparable to that of loose silica case, as shown in Figure 7.20. However, the distribution of the AE events (Figure 7.16) was concentrated in a certain region, which is similar with dense silica case (Figure 7.11).

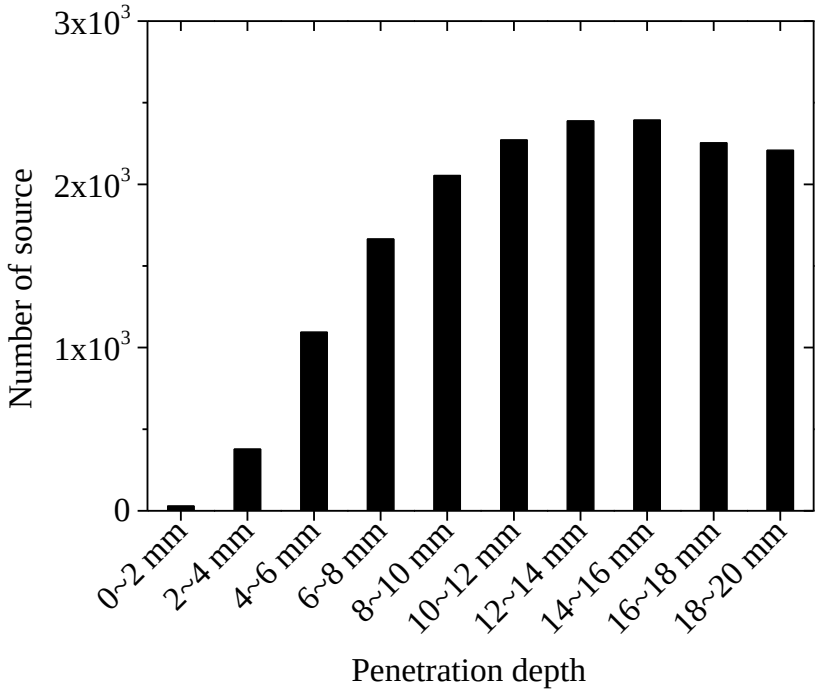

Figure 7.20 Number of source localized in coral sand

7.2.7 AE Source Location in Large Model Pile Test

The AE source location was further applied to the large pile testing system. Some key experimental settings are listed in Table 7.3. Two loading cycles were conducted and the penetration depth of each loading was 20mm. Detailed results of AE source location are shown in Figure 7.21 and Figure 7.22 with pseudo color plotting, and Figure 7.23 and Figure 7.24 with contour plotting.

Table 7.3 Experimental settings during large pile testing

Material	Silica sand No.5
Relative density	85.1%
Loading speed	0.5mm/min
Surcharge pressure	100kPa
Channels of sensor	8
AE sampling rate	500kHz

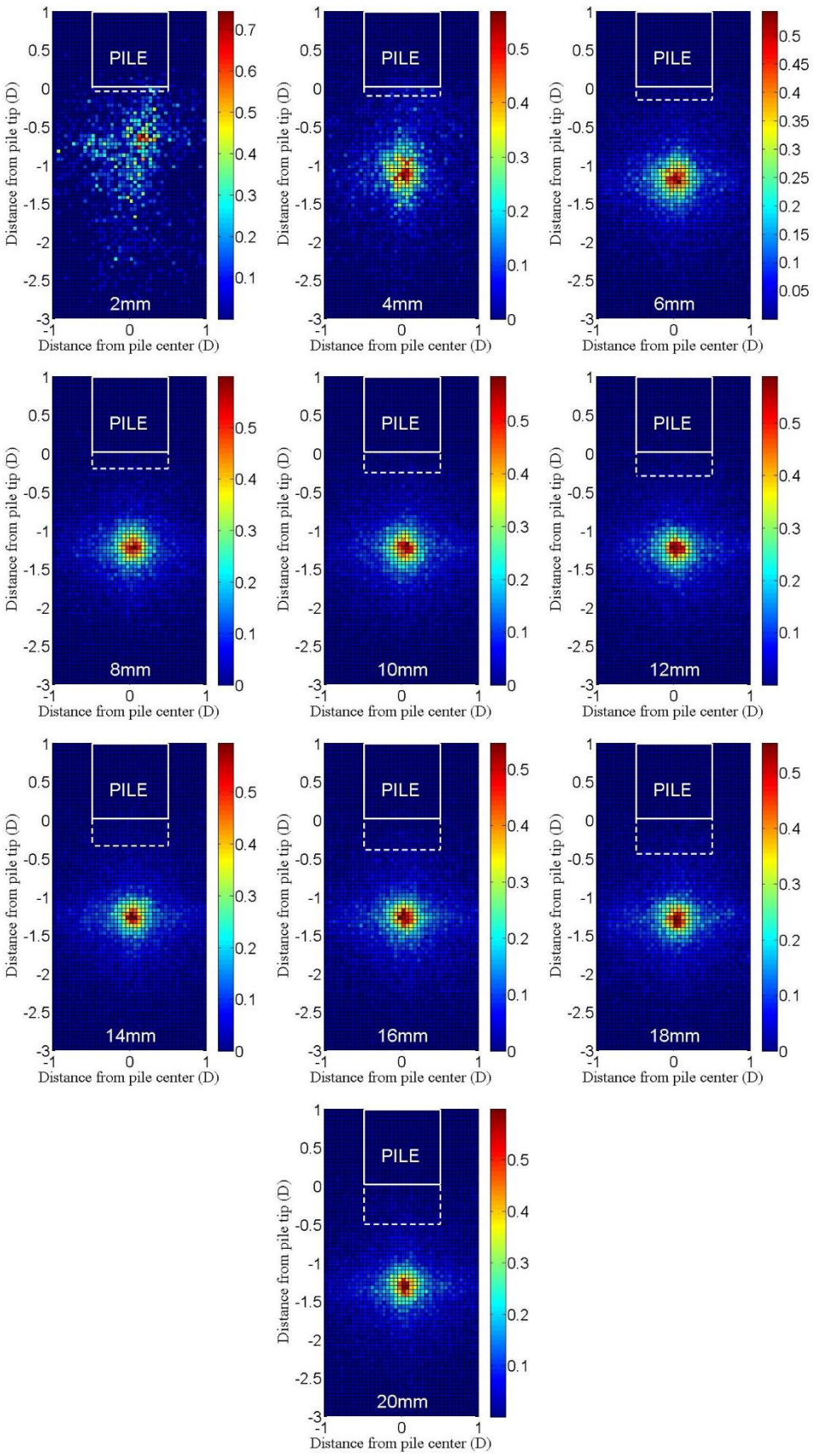

Figure 7.21 Distribution of AE source in large box: 1st loading

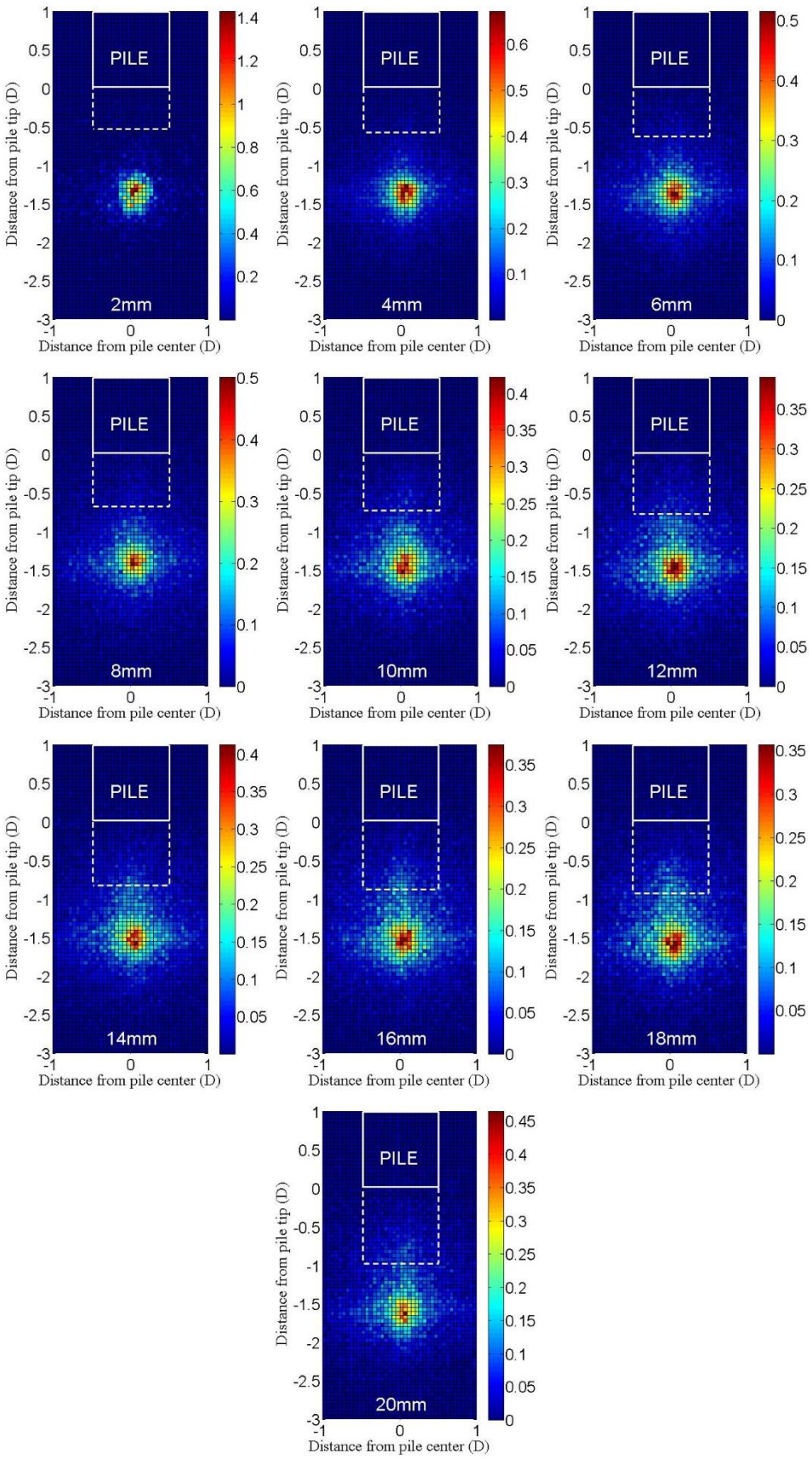

Figure 7.22 Distribution of AE source in large box: 2nd loading

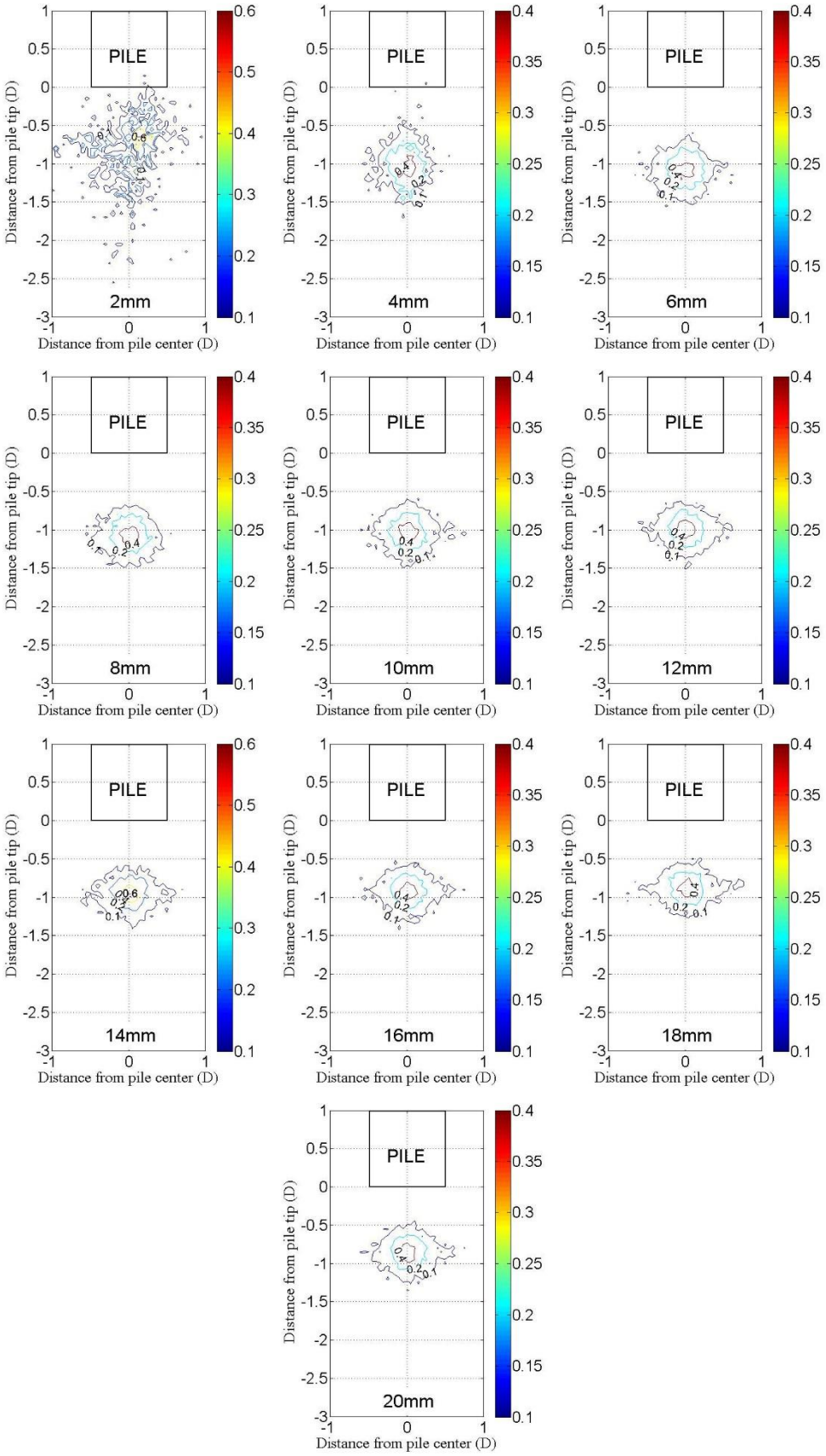

Figure 7.23 Contour distribution of AE sources in large box: 1st loading

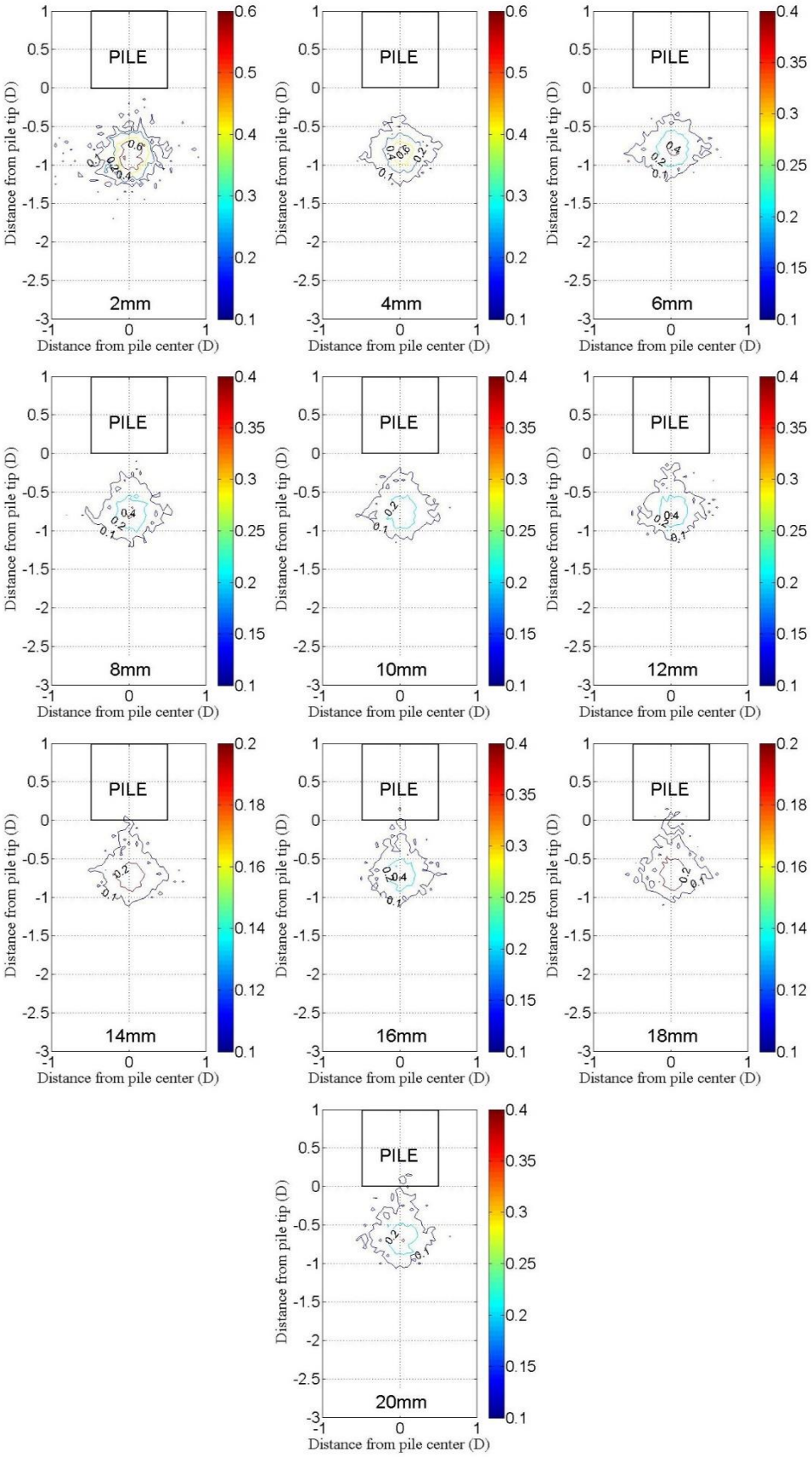

Figure 7.24 Contour distribution of AE sources in large box: 2nd loading

7.2.8 Insights into Subsoil Behavior

7.2.8.1 Observation of Sand Crushing Zone

To observe the zone of crushing, an additional test was conducted with colored sand with larger grain size (same material with silica No.5 but with D_{50}=1.7mm). Figure 7.25 shows the excavated horizontal plane after 100mm pile penetration. Figure 7.25(a) shows the pile tip condition before pile was removed, where crushed fines can be observed around the pile tip. Figure 7.25(b-f) show the top view of the ground configurations after removing the sand layer by layer. For sand immediately below the pile tip, it appears that there was a circular crushing zone around the pile edge, inside which no obvious crushing can be noticed. The non-crushing region shrank as the excavation advanced deeper and finally disappeared. At 43mm below the pile tip, the crushing of sand became insignificant, and fresh sand occupied the entire scope again at 54mm below the pile tip. It seems that the crushing of sand was originated from a certain point below pile tip, and spread up toward the pile tip to form a cone shaped crushing zone.

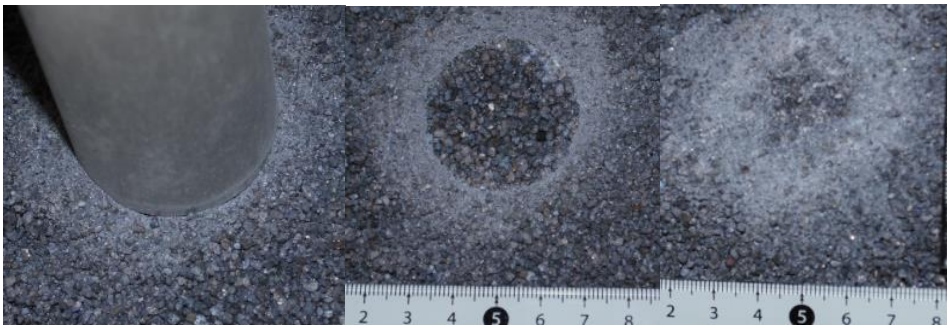

(a) pile tip (b)0mm (c)-10mm

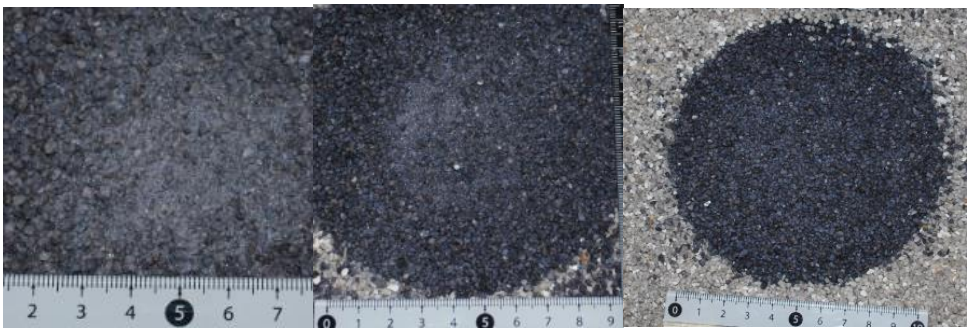

(d)-30mm (e)-43mm (f)-54mm

Figure 7.25 Observation of sand crushing below pile tip

Figure 7.26 shows the microscopic observation of sand crushing after 40mm pile penetration. Again, it is demonstrated that there was almost no crushing immediately below the pile tip, while the most crushed zone appeared at around 20mm below the pile tip. About 45mm below the pile tip, the crushing became insignificant again.

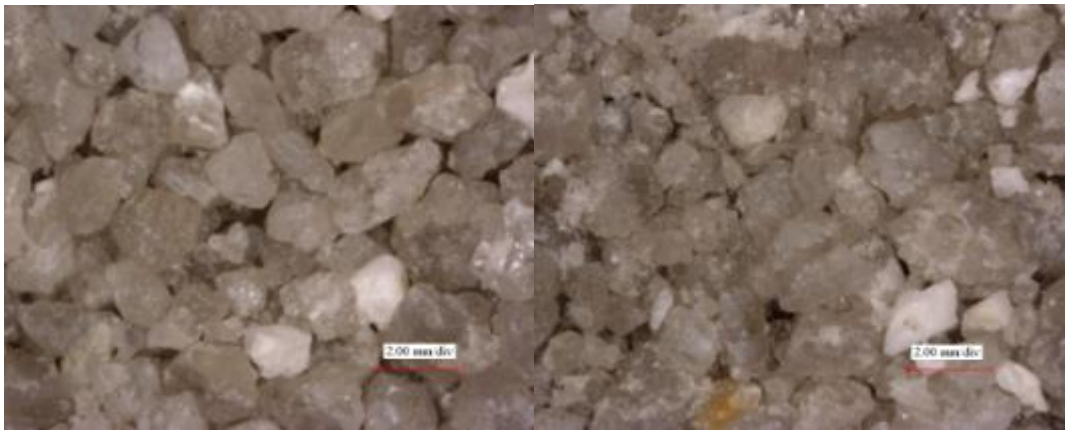

(a)0mm (b)-5mm

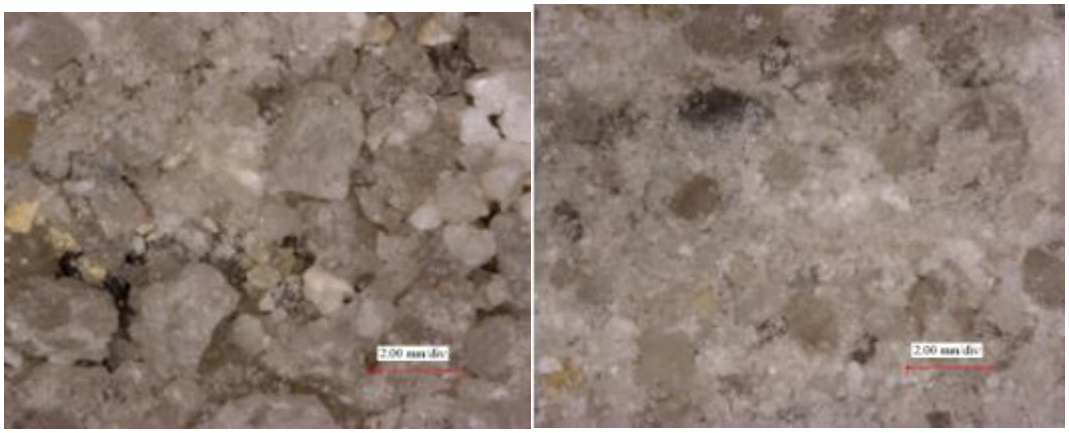

(a)-10mm (b)-20mm

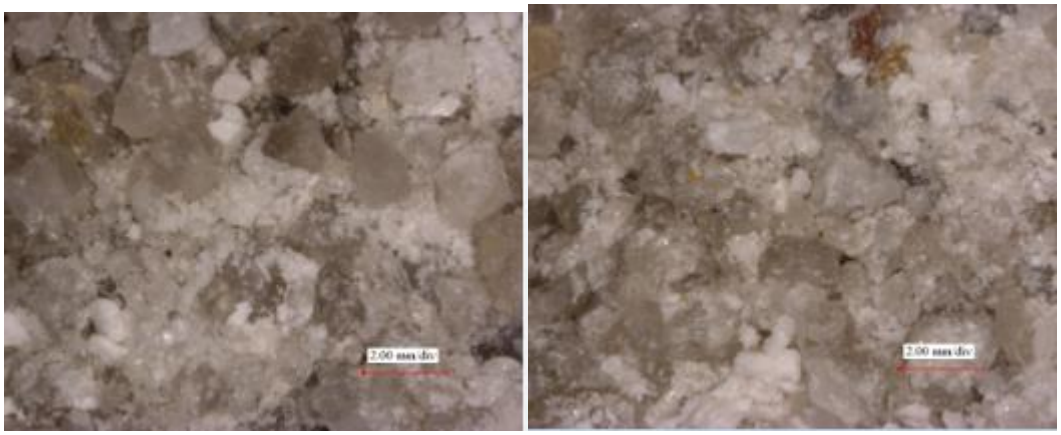

(a)-25mm (b)-30mm

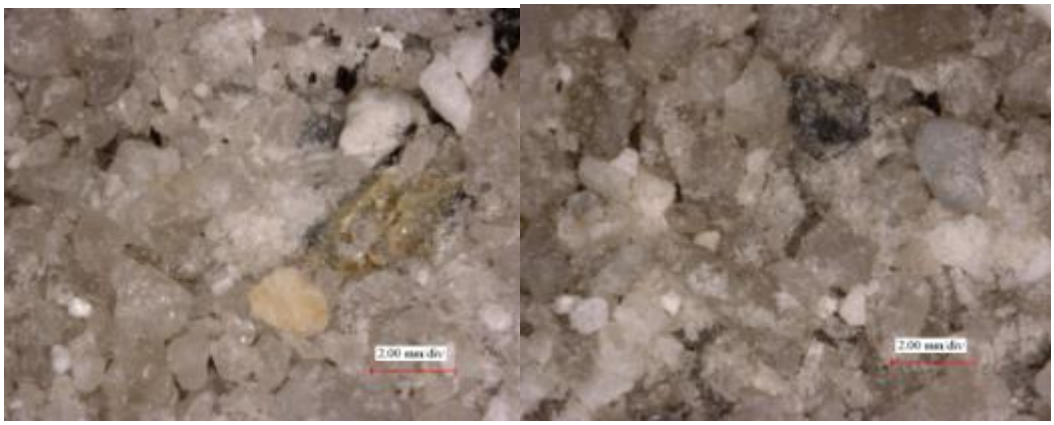

(a)-35mm (b)-40mm

(a)-45mm (b)-50mm

Figure 7.26 Microscopic observation of silica sand crushing

7.2.8.2 Zone Description of Crushing

White and Bolton (2004) described the crushing zone as the "nose cone" as observed in a calibration chamber test. Based on the observation of the current study, it is evident that the extent of crushing within the "nose cone" is not uniformly distributed. Yang et al. (2010) classified the crushing zone into three zones based on the stress conditions of each zone. The soils in the shear band subjected to extreme normal and shear stress underwent highest crushing rate, followed by the non-shear band zone with high normal stress (significant crushing) and reduced normal stress (moderate crushing). Due to the cone-shaped pile end, the crushing status of sand immediate below a flat ended pile was not observed.

According to White and Bolton (2004), the process of a displacement pile installation can be regarded as soil streams passing through a stationary pile. The path of sand stream formed the shear zone where severest crushing occurred as observed by Yang

et al. (2010). In view of sand stream, the crushing of sand below a flat ended pile can be roughly divided into four zones as shown in Figure 7.27: the outer transition zone, the shear zone, the inner transition zone and the compression zone. The sand in the shear band underwent severest crushing and is supplied with fresh sand from the frontal of fresh sand stream. The continuous fresh sand flowed into the shear band resulting in substantial crushing with the advancing of pile penetration, and consequently generated considerable AE. The sands localized around the center of the bottom shear zone would change the direction of flow most sharply when entering the shear band. This region is expected to be most "noisy" in terms of AE, which is consistent with AE source distributions shown in the previous sections. The distribution of crushing zones demonstrated that particle crushing more easily occurs under shearing than compression. Sadrekarimi and Olson (2010) reported that particle breakage can be observed when normal stress is very small during ring shear test. In addition, although Zone I exhibited no notable crushing in this study, one-dimensional compression of sands showed that substantial crushing can occur at high pressures (Hagerty et al. 1993, Yamamuro et al. 1996, Nakata et al. 2001). This suggests that Zone I may shrink or even disappear when the ground bearing pressure is high enough. However, since shear failure is more likely to happen in case of pile foundation, it is more important to concern sand crushing within the shear band.

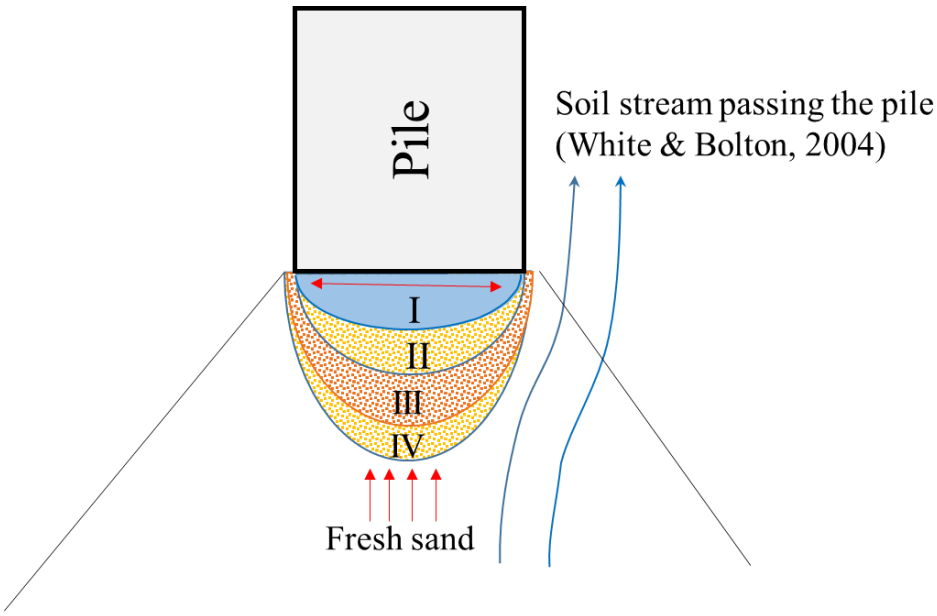

Zone I: Compression zone, insignificant crushing

Zone II: Inner transition zone, medium crushing

Zone III: Shear zone, severe crushing

Zone IV: Outer transition zone, medium crushing

Figure 7.27 Schematic illustration of crushing zones below the pile tip

7.2.8.3 Observation from PIV Analysis

The particle image velocimetry (PIV) technique allows a direct observation of the ground deformation subjected to pile penetration. Detailed descriptions of the PIV testing procedures are summarized by Luki (2013), and the theoretical background should be referred to White et al. (2001), White et al. (2003) and White and Bolton (2004). Figure 7.28 illustrates a typical vector displacement field around a pile tip, which is combined by a vertical displacement shown in Figure 7.29(a) and a horizontal displacement shown in Figure 7.29(b). The vertical displacement of the soils is mainly restrained to the pile tip. It demonstrates that the soils immediately below the pile tip are "pushed" downward. Meanwhile, in the horizontal direction, the soils are "pushed" to the two sides of the pile. It should be noted that the maximum horizontal displacement occurs around the side of the pile tip, while considerably small within the region immediately below the pile tip. This observation is consistent with the previous assumption that the soils deform (flow) along the pile and change

their directions most severely at certain point below pile tip (corresponding to the AE source concentration zone).

The PIV method traces the trajectories of the soil patch based on the ratio of matching between different images. However, when the soil is subjected to crushing, the PIV method fails to function well since the original searching patch no longer exists. In addition, the scratching between pile surface and the observation window, as well as the sand penetrating into the gap add to the errors of PIV analysis. Figure 7.30 illustrates the change of observation conditions during PIV testing. It clearly shows that the soils immediately below the pile tip crushed into fines (white color). This zone was also describe as the "nose cone" by White and Bolton (2004). However, this crushing is mainly due to the interface shearing of the sands in the gap and the scratching, which does not represent the three dimensional conditions. Therefore, the accuracy of the PIV method decreases when the penetration depth becomes large.

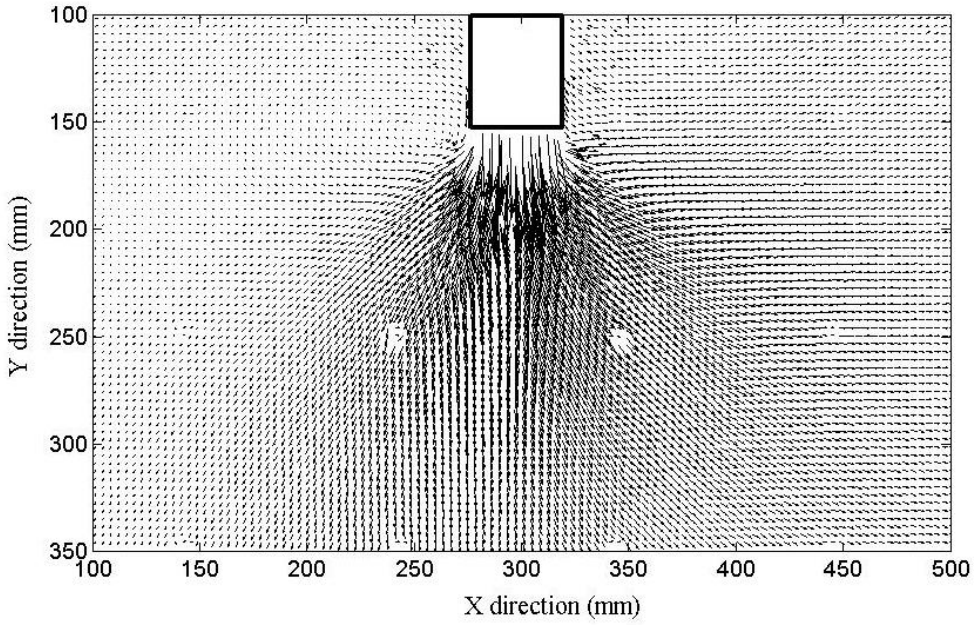

Figure 7.28 Vector displacement field around a pile tip (9-13mm penetration)

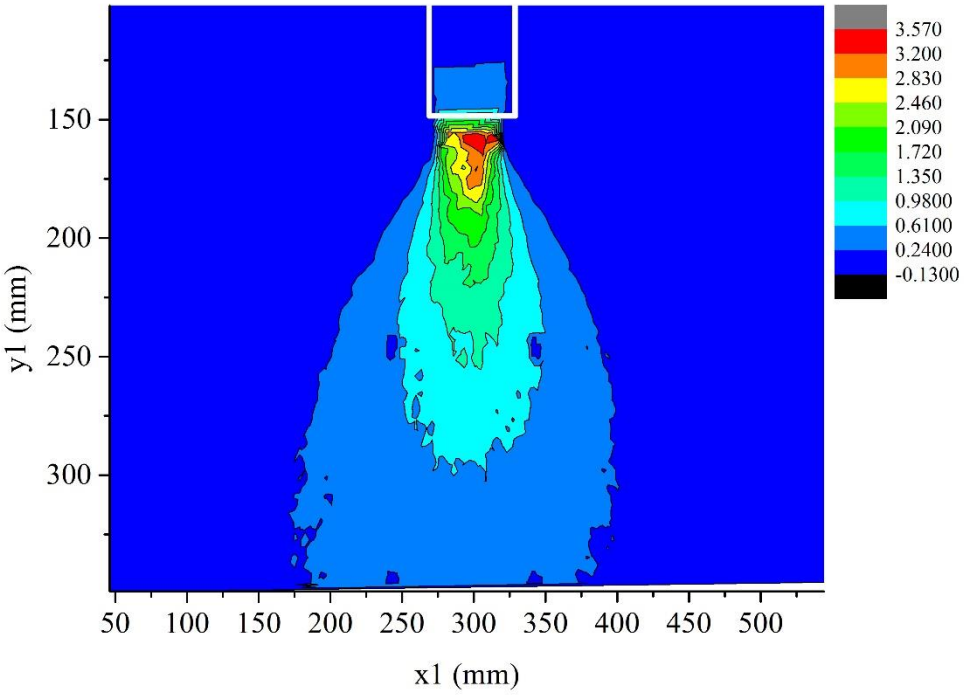

(a)

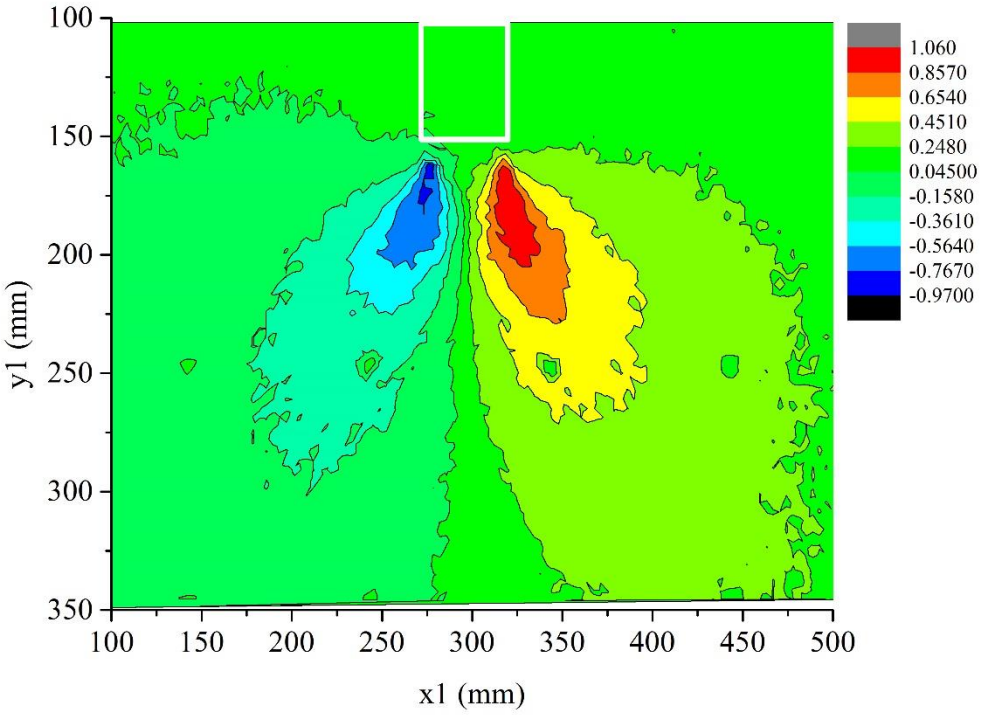

(b)

Figure 7.29 (a) Vertical and (b) Horizontal displacement field (9-13mm penetration)

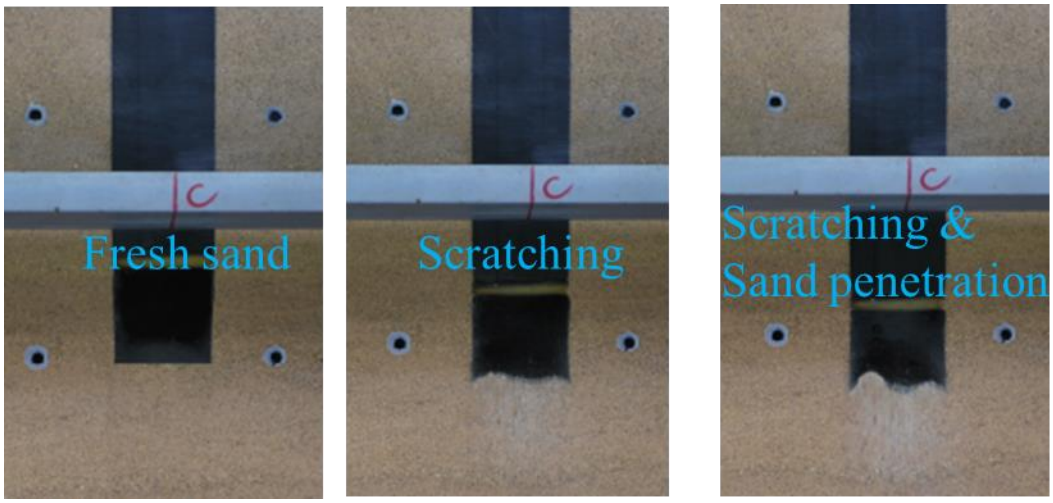

Figure 7.30 Change of observation conditions during PIV testing

7.3 SUMMARY

This chapter summarizes the mathematical derivation of the AE source localization algorithm, including signal arrival times determination using AR-AIC model and signal source localization based on TDOA. The source characteristics of AE from silica sand and coral sand were identified and compared through experimental exploring. It is found that the AE sources were concentrated within certain zones, usually around 0.5~1D below the pile tip. Effects of the initial relative density on AE source distribution revealed that loose ground underwent a longer period of subsoil densification. More scattered AE distribution was found in loose case, however, the overall distribution still fell into a limited zone.

A close-up observation of the sand crushing zone illustrated that the sand in the shear zone underwent severest crushing, while in the compression zone immediately below pile tip, the crushing was insignificant. Consequently, based on the extent of crushing, the subsoil below the pile tip was divided into four zones, and source of crushing was believed to be originated from the head of cone shaped area below pile tip, corresponding to the most active area of AE source.

7.4 REFERENCES

Akaike, H. (1973). Information theory and an extension of the maximum likelihood principle. In 2nd International Symposium on Information Theory. Academiai Kiado.

Ben-Israel, A. (1966). A Newton-Raphson method for the solution of systems of equations. Journal of Mathematical analysis and applications, 15(2), 243-252.

Hagerty, M. M., Hite, D. R., Ullrich, C. R., & Hagerty, D. J. (1993). One-dimensional high-pressure compression of granular media. Journal of Geotechnical Engineering, 119(1), 1-18.

Irfan M. (2014). Elastic wave propagation through unsaturated soils concerning early warning of rain-induced landslides. Doctoral dissertation, The University of Tokyo, Tokyo.

Jardine, R. J., Zhu, B., Foray, P., & Yang, Z. X. (2013). Measurement of stresses around closed-ended displacement piles in sand. Geotechnique, 63(1), 1-17.

Luki D. (2013). Image analysis on deformation of ground around group pile foundation undergoing vertical loading. Master's thesis, the University of Tokyo, Tokyo.

Nakata Y, Kato Y, Hyodo M Hyde AFL & Murata, H. (2001). One-dimensional compression behavior of uniformly graded sand related to single particle crushing strength. Soils and Foundations, 41(2), 39-51.

Niccolini, G., Xu, J., Manuello, A., Lacidogna, G., & Carpinteri, A. (2012). Onset time determination of acoustic and electromagnetic emission during rock fracture. Progress In Electromagnetics Research Letters, 35, 51-62.

Sadrekarimi, A., & Olson, S. M. (2010). Particle damage observed in ring shear tests on sands. Canadian Geotechnical Journal, 47(5), 497-515.

Sleeman, R., & van Eck, T. (1999). Robust automatic P-phase picking: an on-line implementation in the analysis of broadband seismogram recordings. Physics of the earth and planetary interiors, 113(1), 265-275.

Takanami, T., & Kitagawa, G. (1988). A new efficient procedure for the estimation of onset times of seismic waves. Journal of Physics of the Earth, 36(6), 267-290.

White, D. J., & Bolton, M. D. (2004). Displacement and strain paths during plane-strain model pile installation in sand. Géotechnique, 54(6), 375-397.

White, D. J., Take, W. A., & Bolton, M. D. (2001). Measuring soil deformation in geotechnical models using digital images and PIV analysis. Proc. 10th Int. Conf. Computer Methods and Advances in Geomechanics, 997-1002.

White, D. J., Take, W. A., & Bolton, M. D. (2003). Soil deformation measurement using particle image velocimetry (PIV) and photogrammetry. Géotechnique 53 No 7, 619-631.

Yamamuro, J. A., Bopp, P. A., & Lade, P. V. (1996). One-dimensional compression of sands at high pressures. Journal of Geotechnical Engineering.

Yang, Z. X., Jardine, R. J., Zhu, B. T., Foray, P., & Tsuha, C. H. C. (2010). Sand grain crushing and interface shearing during displacement pile installation in sand. Géotechnique, 60(6), 469-482.

CHAPTER 8

AE MONITORING IN GROUP PILE TESTING

8.1. INTRODUCTION

Group pile has been a common design in modern infrastructure construction. The capacity of group pile depends on the individual capacities of piles, and influenced by the spacing between the piles (Poulos 1988, Lee 1993, Zhang and Small 2000). It was found that there is a certain value of pile spacing at which the mechanism of group failure changes (Whitaker 1957). For those spacing larger than this value, the failure of group pile is analogous with local penetration of individual piles; for those spacing smaller than this value, the failure of group pile occurs together as a block. In case of narrow spacing, the bearing behavior of group pile is substantially different from the superposition of the single piles. Rollins et al. (2005) conducted full scale pile group tests with different spacing and found that group effects decreased considerably as pile spacing increased from 3.3 to 5.65 times pile diameter. Similarly, Lee and Chung (2005) conducted vertically loading experiment of 3X3 pile group in granular soil. Their results showed that the group effect of pile installation due to superimposed densification of soil between neighboring piles increased the load carrying capacity of a pile at the narrow pile spacing up to 3D. Based on optimization analysis, Leung et al. (2009) found that the role of nonlinearity in pile interaction becomes more significant when pile spacing is less than 2.5 times of pile diameter. It is expected that the group pile effect would become more significant while the spacing get narrower.

Moreover, the bearing load distribution within the pile group was not uniform among different pile positions. Whitaker (1957) conducted loading tests of group pile in clayey ground and showed that bearing capacity of the group pile became smaller than the summation of the bearing capacity of single piles, and the corner piles carried more load than the center pile. Similar results were also observed by Comodromos et

al. (2009) using numerical analysis. In contrast, Vesic (1969) showed that the group pile could carry more than the summation of single piles in sandy ground, and that the center pile carried more load than corner pile. This feature differs sharply from the block failure mechanism like the group pile in clayey ground. It seems that the features of the ground stratum have a significant effect on the group pile behavior. Aoyama et al. (2015) conducted a series of group pile (3×3) tests with 5D and 2.5D spacing. It was found that the secant modulus of the center pile was greater than that of other piles in case of 2.5D group pile. By contrast, in 5.0D group, the modulus is almost same among all piles in the group. However, this location effect was not always observed in 2.5D group pile. When the group loading was disturbed by the intermission of individual loading, the bearing load of the center pile showed no significant difference compared with the other piles. This observation suggests that the interaction in group pile was caused not only by the current loading condition but also by the loading history. The specific grain fabric which developed during the previous loading affects the modulus in the subsequent step.

The present study conducts the group pile loading with AE instrumentation. The behavior of group pile in terms of different spacing (2.5D and 5D) were monitored by AE. In order to compare with the previous studies, both group loading and individual loading were performed. The following sections show the details of the AE monitoring results.

8.2. TEST CONDITION

The experimental arrangements for group pile tests were described in detail in Chapter 3 and Chapter 4. Two types of pile spacing, 2.5D and 5D, were tested to represent strong and weak group effects. Being similar with the sequential pile testing in the small pile loading system, the loadings for group pile were also conducted at every 20mm penetration, and followed by unloading. In order to examine the influence of induced soil fabric caused by group loading, individual loadings were performed after two group loadings, followed by another two group loading. Figure 8.1 shows the schematic illustration of group pile loading steps.

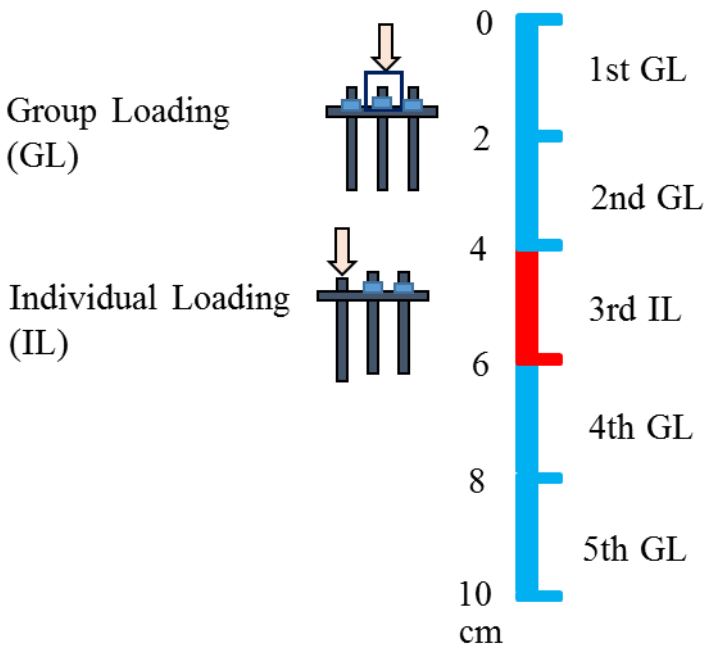

Figure 8.1 Schematic illustration of loading procedure

Three piles in the group as well as the loading footing were selected for AE monitoring as shown in Figure 8.2. The selected three piles represent three different positions corresponding to center, middle and corner pile respectively. And the footing was monitored to exam the influence of the surrounding piles.

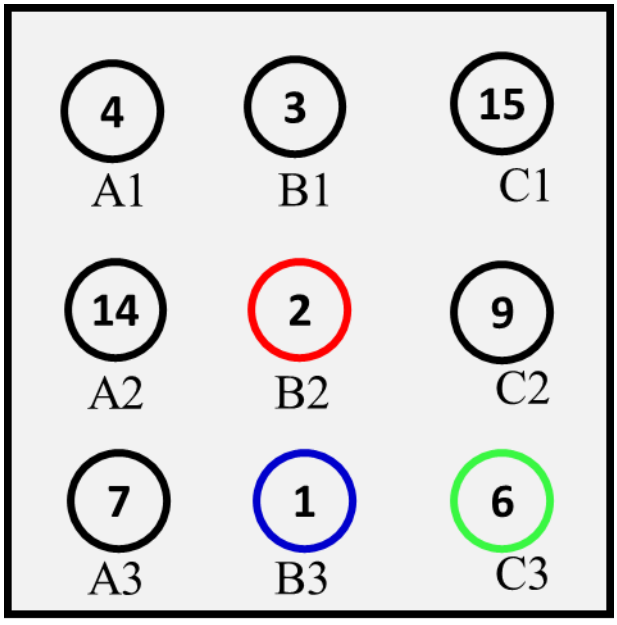

Figure 8.2 Pile arrangement for AE monitoring

8.3. RESULTS OF GROUP PILE LOADING

8.3.1 5D Group Pile

8.3.1.1 Load-settlement Behavior

Figure 8.3 shows the load-settlement behavior of all piles during 5D group loading. The load here refers to the pile tip resistance measured by the strain gauges, which were located at 50mm above from the pile tip. It can be seen that, for all individual piles, the load-settlement curve of the 1st loading showed notable difference compared to the reloading steps, especially at the very beginning of penetration. A clear transition point indicating ground yielding can be identified from the reloading curves. The load-settlement curves of the three piles monitored with AE were plotted separately in Figure 8.4. It can be generally found that, except for the 1st loading, the load-settlement of the three piles were close to each other before ground yielding. Since the ground behavior before yielding is more concerned in the practical application, further discussion in term of secant modulus will be presented next.

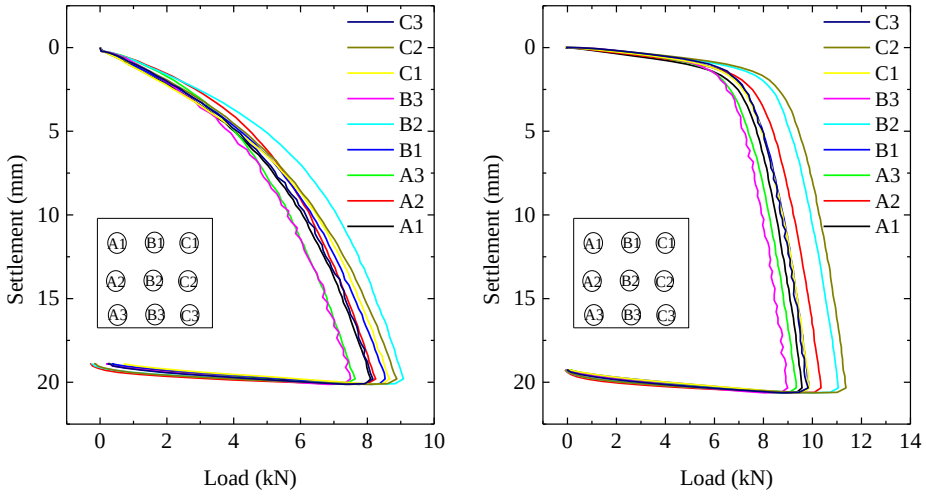

(a) 1st group loading (b) 2nd group loading

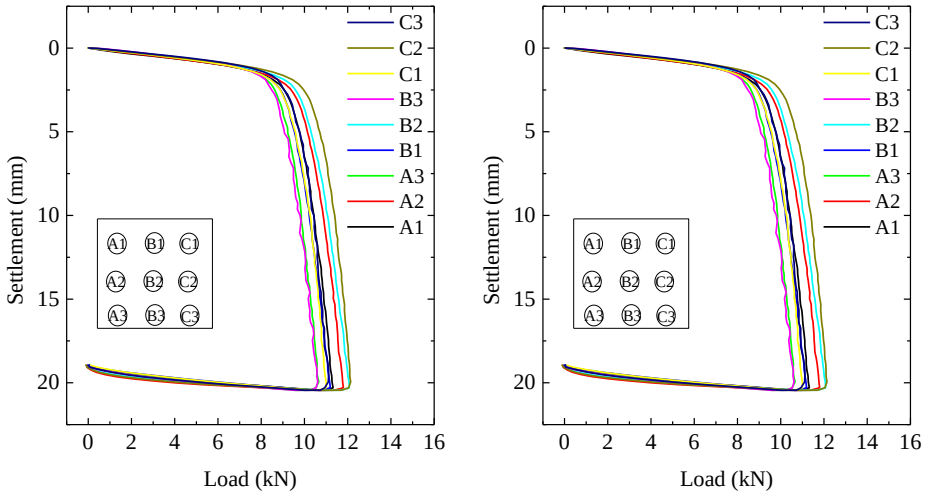

(c) 4th group loading (d) 5th group loading

Figure 8.3 Load-settlement behavior during 5D group loading

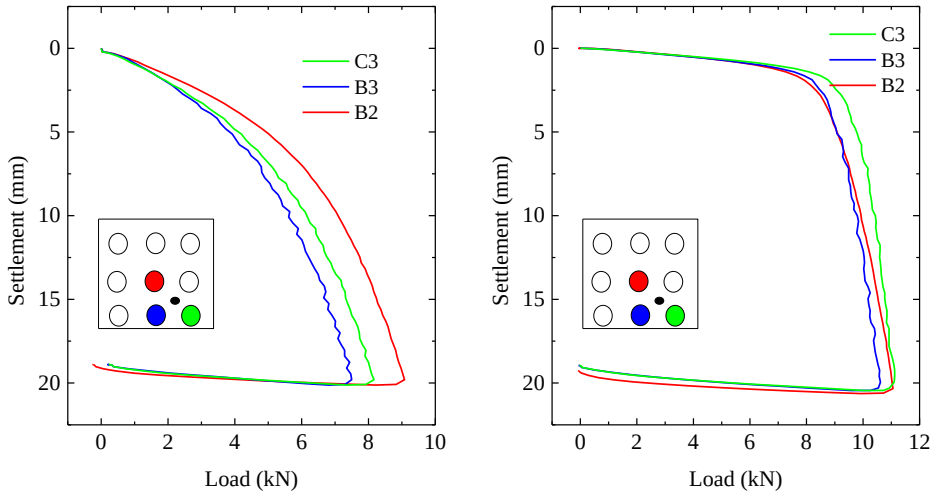

(a) 1st group loading (b) 2nd group loading

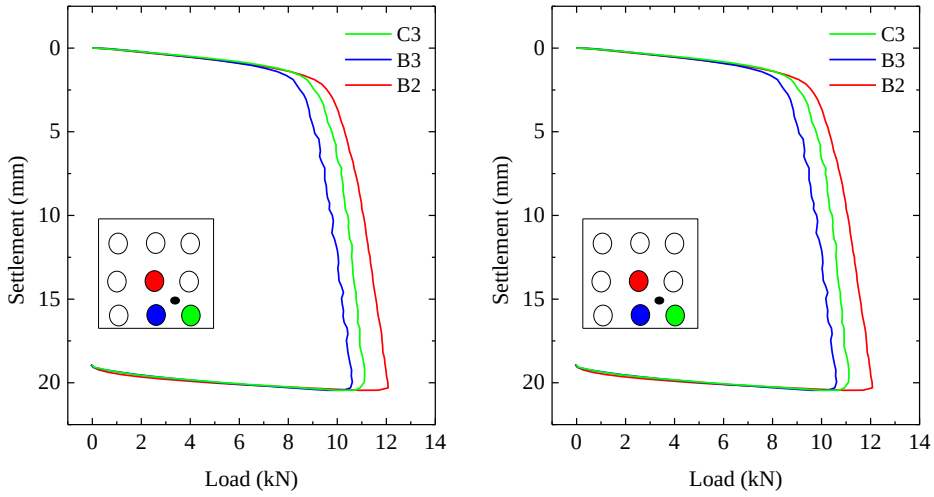

(c) 4th group loading (d) 5th group loading

Figure 8.4 Load-settlement behavior of the three piles monitored with AE during 5D group loading

8.3.1.2 AE Activity

Figure 8.5 shows the AE evolution during 5D group pile loading. Similar tendencies can be observed compared with the load-settlement curves as shown in Figure 8.4. Higher tip resistance of piles yielded higher level of AE. In Figure 8.5, the center pile and corner pile showed no obvious difference. However, the middle pile had much lower AE level. This may be caused by the local ground conditions since the soil below the middle pile was subjected to a smaller load. Another notable feature is that the AE sensor placed on the footing detected a relatively low level of AE, which suggests that the influence of the surrounding piles was not so significant.

The AE signals were further treated with a high-pass filter to eliminate the low frequency components. Figure 8.6 shows the results of high-pass AE activity during 5D group pile penetration. The overall tendency was similar with the total energy cases. Figure 8.7 shows the ratio of high-pass AE to the total AE energy. Again, the center pile and the corner pile shared similar ratio levels during all group loading steps. The middle pile, during the 1st and 2nd group loading, showed notable difference from the center and corner piles. However, such difference became insignificant during the 4th and 5th group loading.

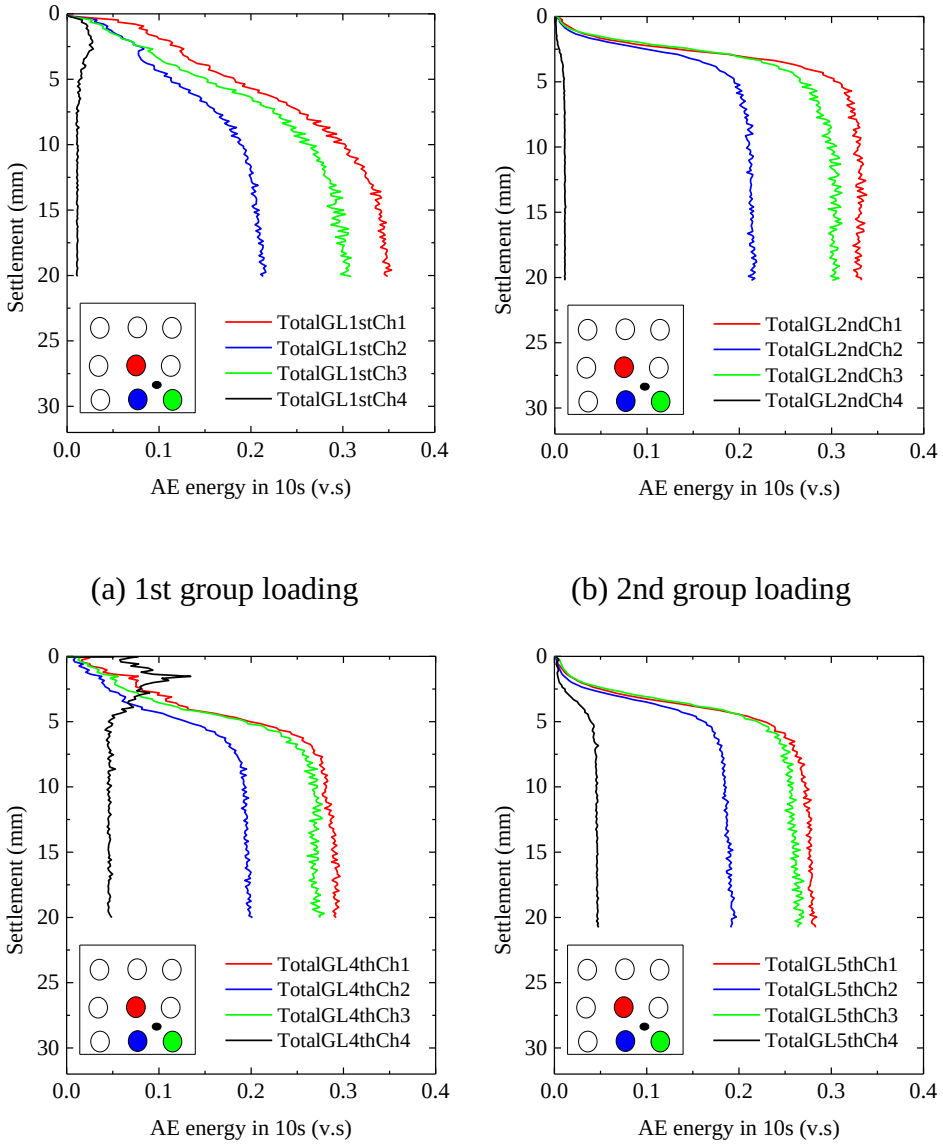

(a) 1st group loading (b) 2nd group loading

(c) 4th group loading (d) 5th group loading

Figure 8.5 AE activity evolution during 5D group pile penetration

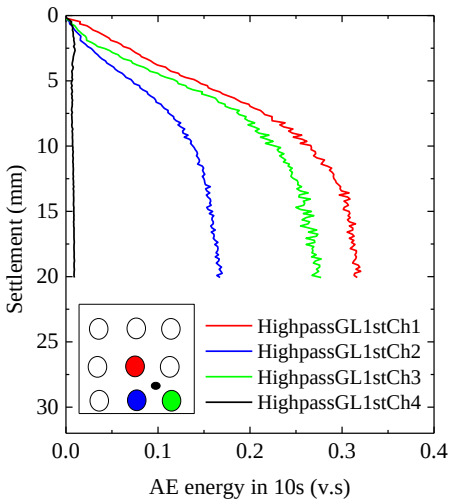

(a) 1st group loading

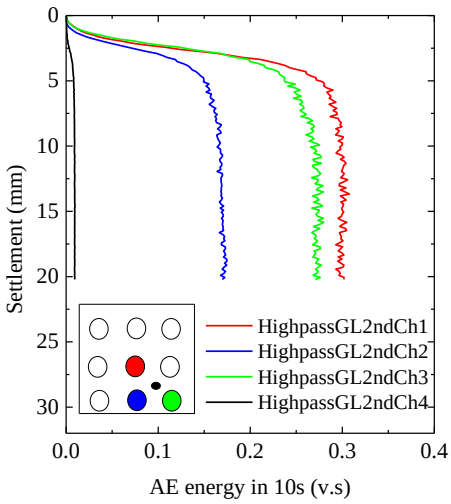

(b) 2nd group loading

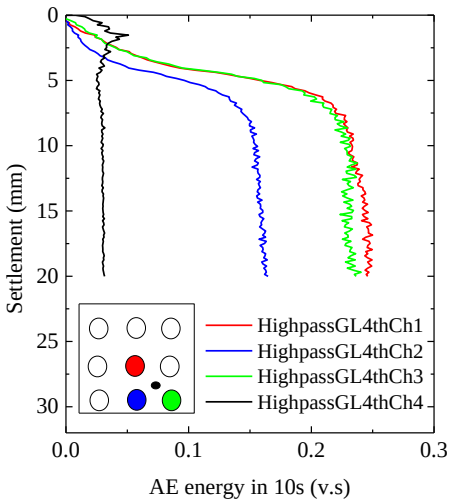

(c) 4th group loading

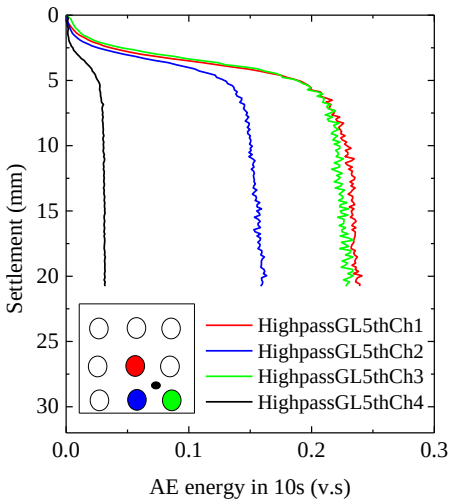

(d) 5th group loading

Figure 8.6 AE activity after high-pass filter (100 kHz)

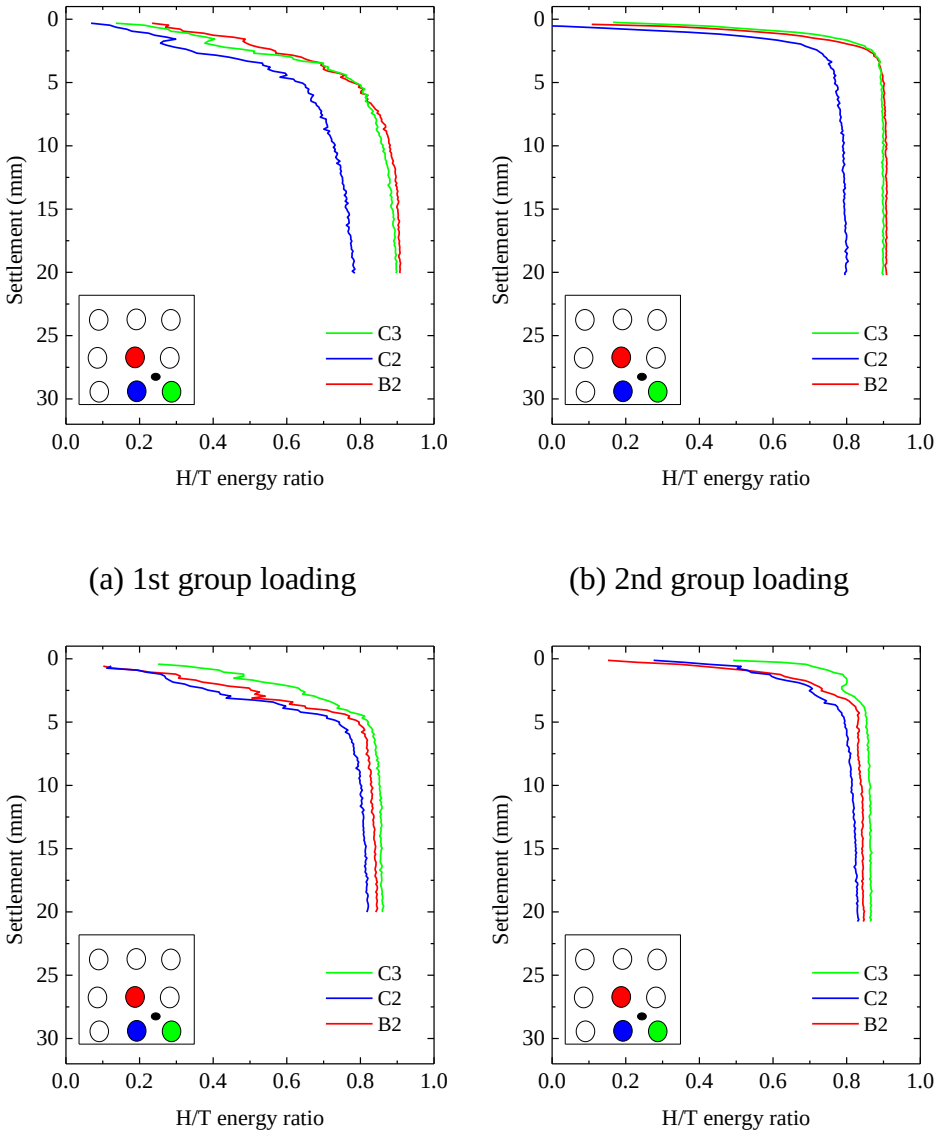

(a) 1st group loading (b) 2nd group loading

(c) 4th group loading (d) 5th group loading

Figure 8.7 Ratio of high-pass AE energy to the total AE energy

8.3.1.3 Secant Modulus and AE Behavior

Figure 8.8 exhibits the relationship between loading step and the secant modulus of all piles during 5D group loading. The modulus was calculated between 0.5mm and 1.0mm settlement for each pile. In general, the secant modulus increased with the loading step (slight decrease after individual load). In this figure, the center pile showed no notable difference in the bearing load after group loading, which demonstrated that the group effect in case 5D pile spacing was not significant. This

observation is consistent with previous studies by Aoyama et al. (2015). The secant modulus of the three AE monitored piles is shown in Figure 8.9. The center pile here carried a slightly more load than the middle and corner piles, especially in the 2nd group load step. Referring to this three piles, the decreasing of bearing load after individual loading is more substantial.

A comparison of the current secant modulus results with the previous study by Aoyama et al. (2015) was shown in Figure 8.10. Note that the depth of penetration of each step in 20mm in the current study, which is different with 30mm in the reference. Therefore, the load step in Figure 8.10 was adjusted to realize comparable settlement. The corner and middle piles were averaged value from same positons. It can be seen that the secant modulus of the current study matched well with the previous study. Center pile showed no significant difference with the other piles.

The AE energy rate was also calculated during the same penetration period (0.5-1mm), as shown in Figure 8.11. Again, it shows remarkable similarity in view of overall distribution compared with the secant modulus shown in Figure 8.9. The AE rose from the 1st loading to the 2nd loading, while decreased during the 4th reloading due to individual loading, and increased again during the 5th reloading. The AE from the center pile showed no obvious difference compared with the other piles.

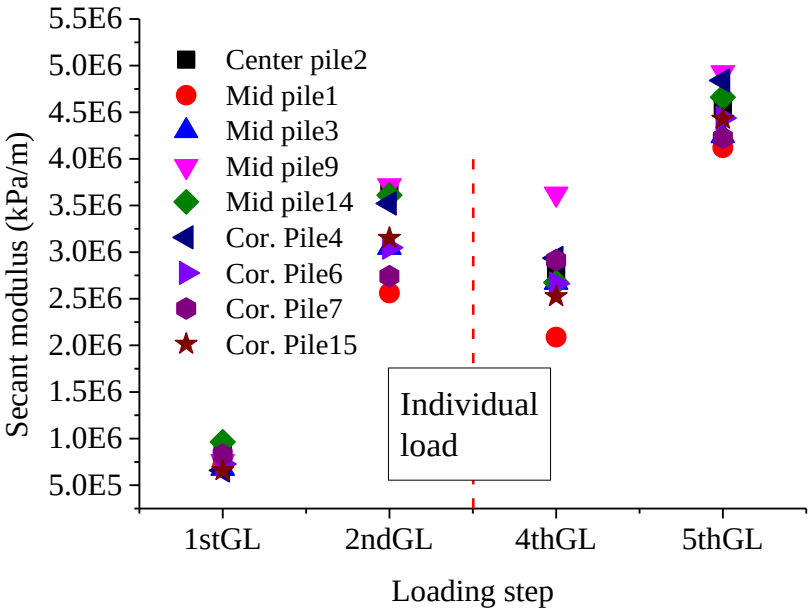

Figure 8.8 Secant modulus of all piles in group during 5D group loading

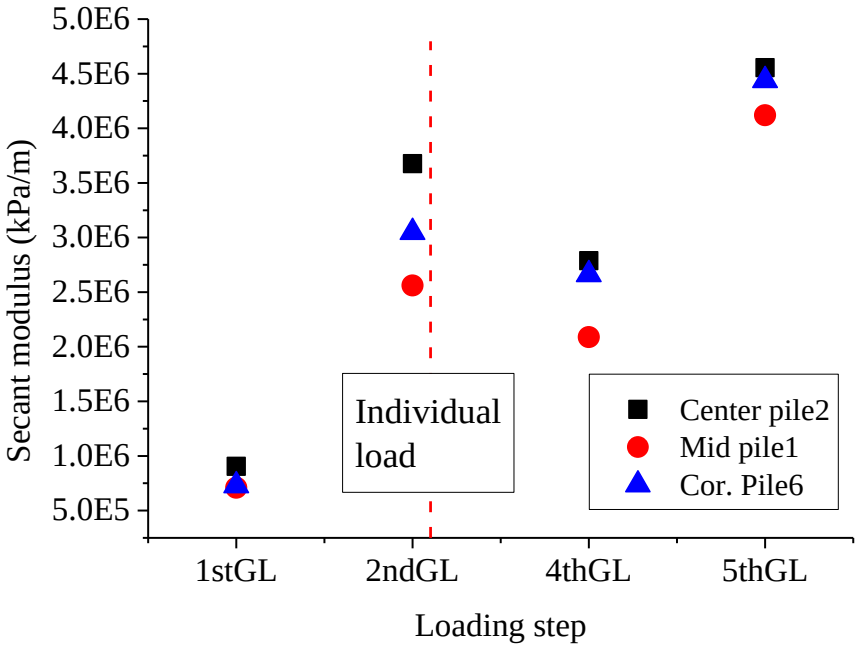

Figure 8.9 Secant modulus of the three piles monitored with AE

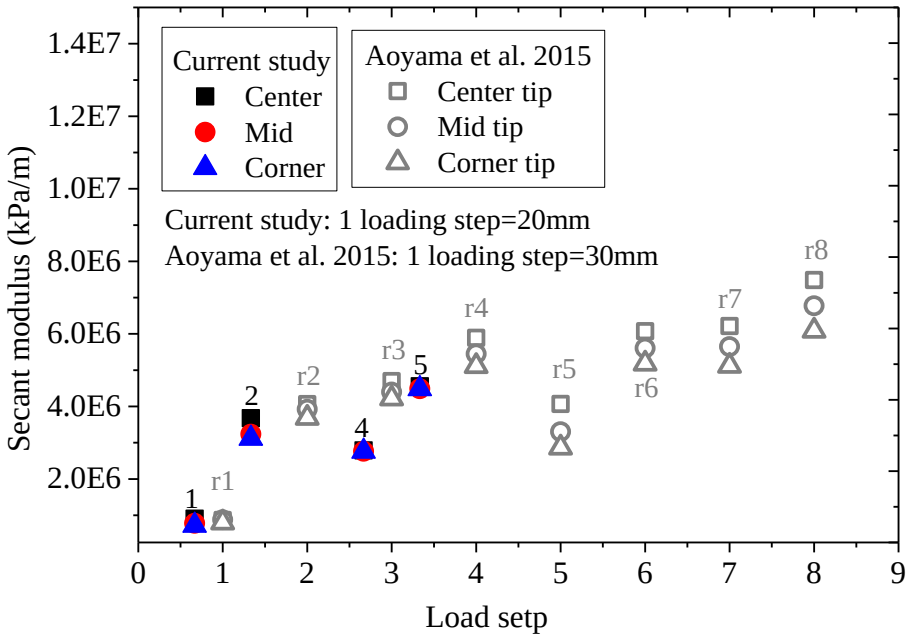

Figure 8.10 Comparison of secant modulus results with Aoyama et al. (5D)

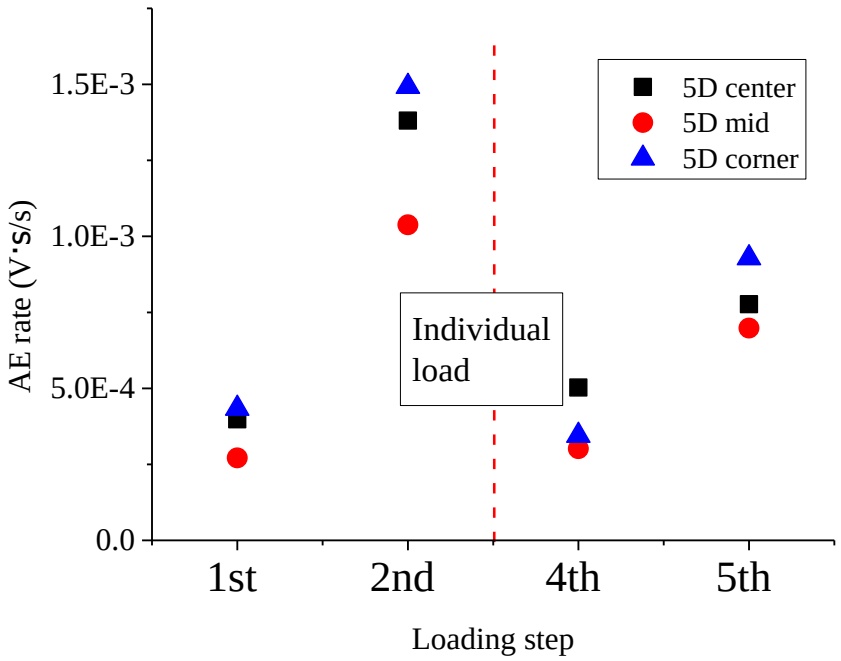

Figure 8.11 AE energy increasing rate during 0.5-1mm group pile penetration

8.3.2 2.5D Group Pile

8.3.2.1 Load-settlement Behavior

Figure 8.12 shows the results of load-settlement relationship in case of 2.5D group loading. The load-settlement behavior appears more scattered among different piles compared with 5D group loading. Meanwhile, the center pile seems to carry more load. This will be compared in detail by focusing on the pre-yielding period in term of secant modulus. The bearing load at the end of the 5th loading was smaller than 5D condition. The load-settlement curves of the three piles monitored with AE were plotted separately in Figure 8.13. It clearly shows that the center pile carried more load compared with middle and corner piles.

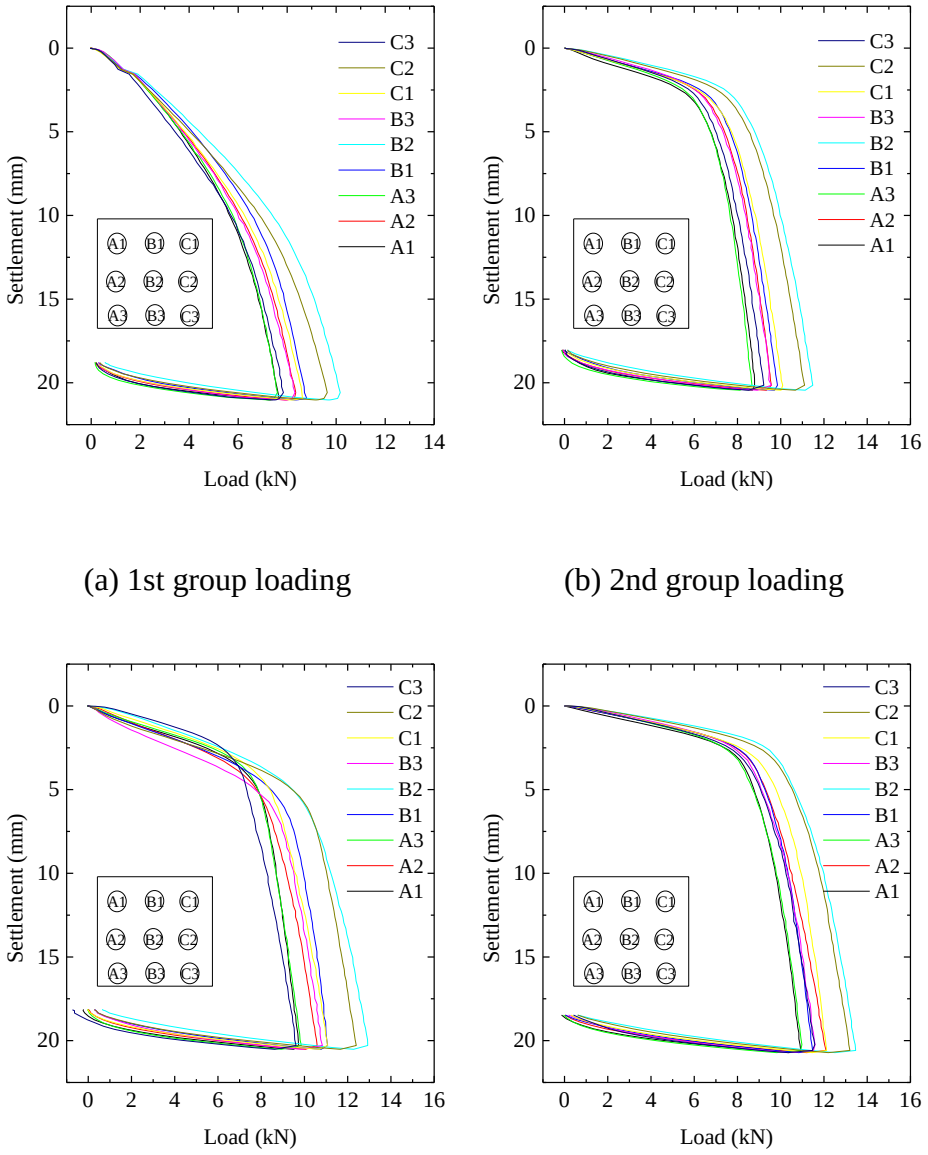

(a) 1st group loading (b) 2nd group loading

(c) 4th group loading (d) 5th group loading

Figure 8.12 Load-settlement behavior during 2.5D group loading

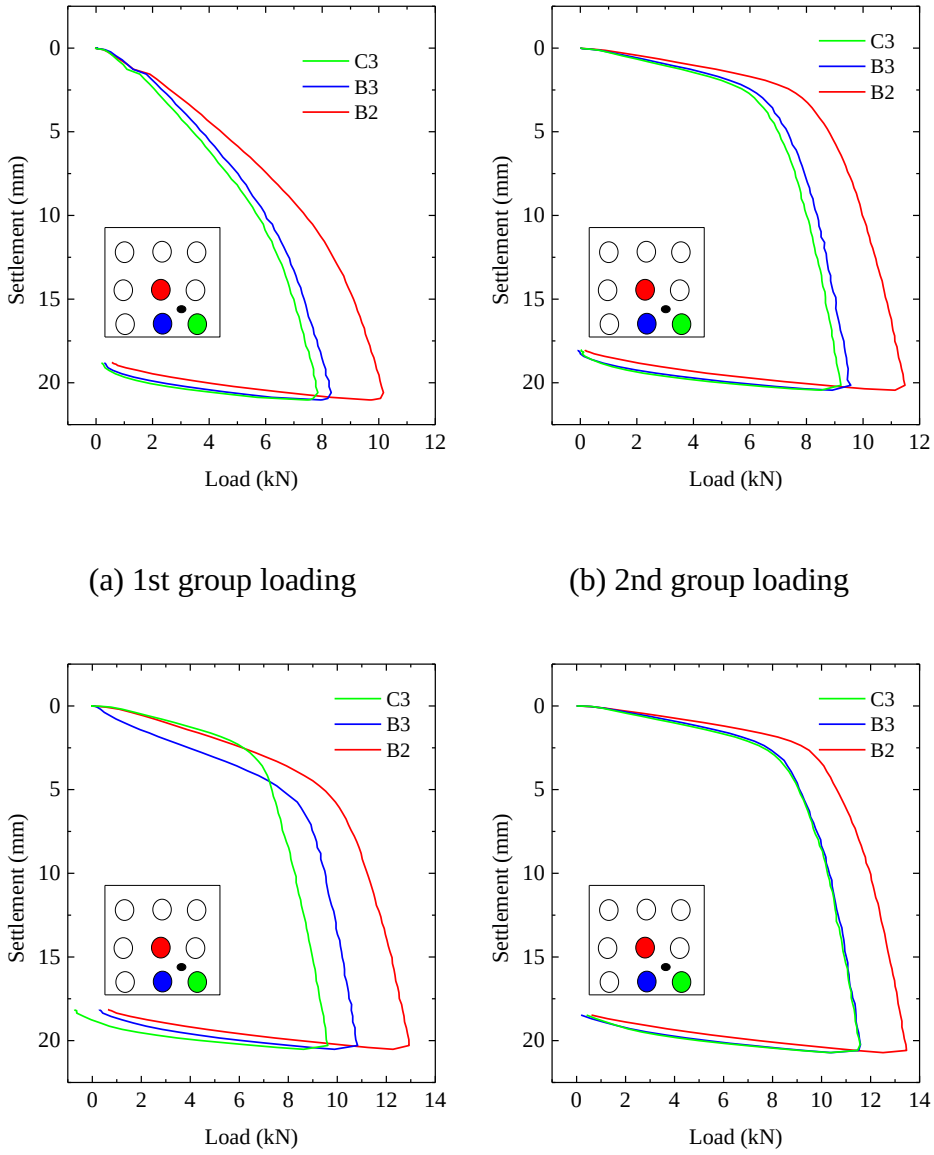

(a) 1st group loading (b) 2nd group loading

(c) 4th group loading (d) 5th group loading

Figure 8.13 Load-settlement relationship of the three piles monitored with AE during 2.5D group pile

8.3.2.2 AE Activity

Figure 8.14 shows the AE evolution during 2.5D group pile loading. Similar tendencies can be observed compared with the load-settlement curves as shown in Figure 8.13. The center pile showed much higher level of AE than the middle and corner piles. This trend was not affected notably by the individual loading. By contrast, the AE from middle and corner piles had similar level of AE activity. The

distinct difference between the center pile and the other piles suggested that the pile interaction in case of 2.5D group pile was more significant than that of 5D group pile.

In addition, the results of high-pass AE activity was shown in Figure 8.15, which also shows a similar tendency with the total AE activity. Figure 8.16 shows the ratio of high-pass AE to the total AE energy in case of 2.5D group pile. The center pile exhibits much higher ratio compared with middle and corner piles, indicating that there was more sand crushing occurring below the center pile. This is also consistent with the observation that the center pile carried higher level of bearing load.

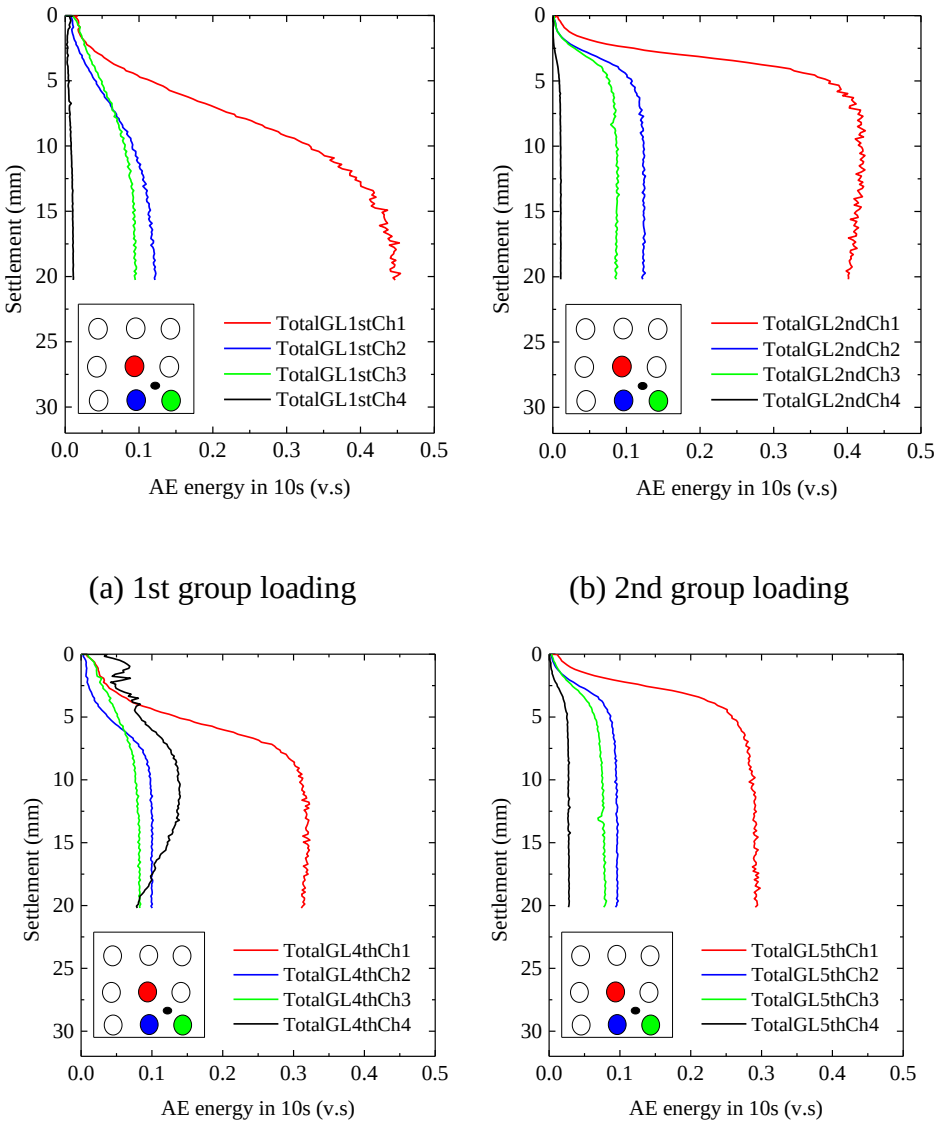

(a) 1st group loading (b) 2nd group loading

(c) 4th group loading (d) 5th group loading

Figure 8.14 AE activity evolution during 2.5D group pile penetration

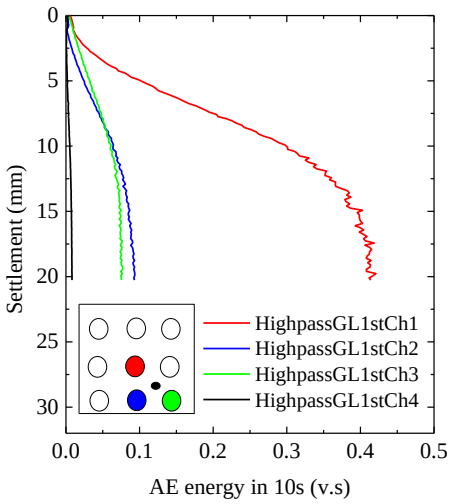

(a) 1st group loading

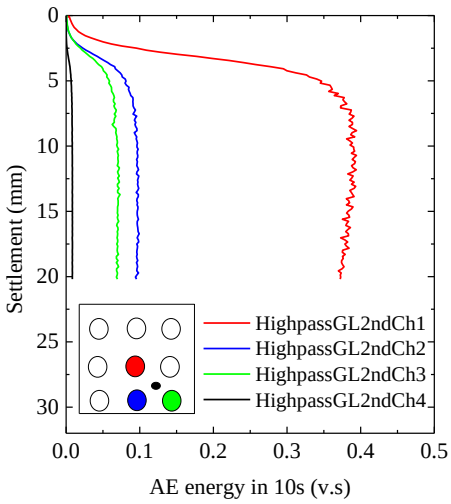

(b) 2nd group loading

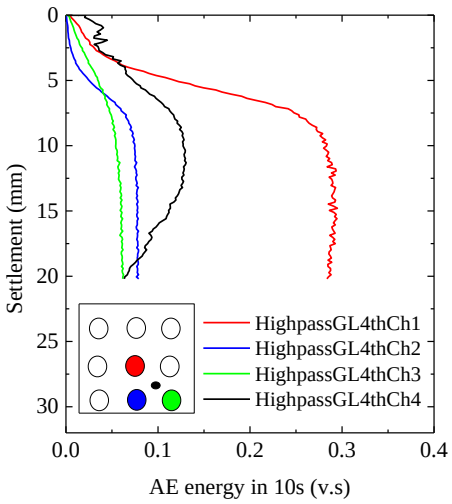

(c) 4th group loading

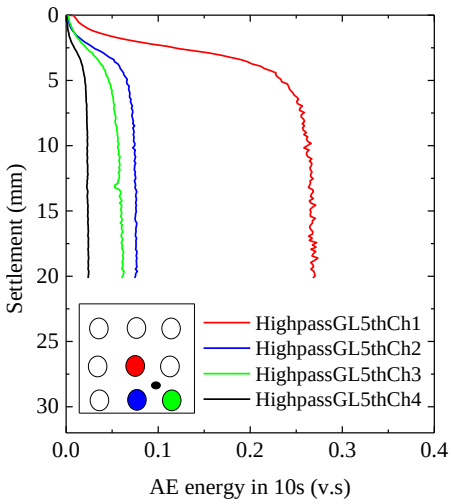

(d) 5th group loading

Figure 8.15 AE activity after high-pass filter (100 kHz)

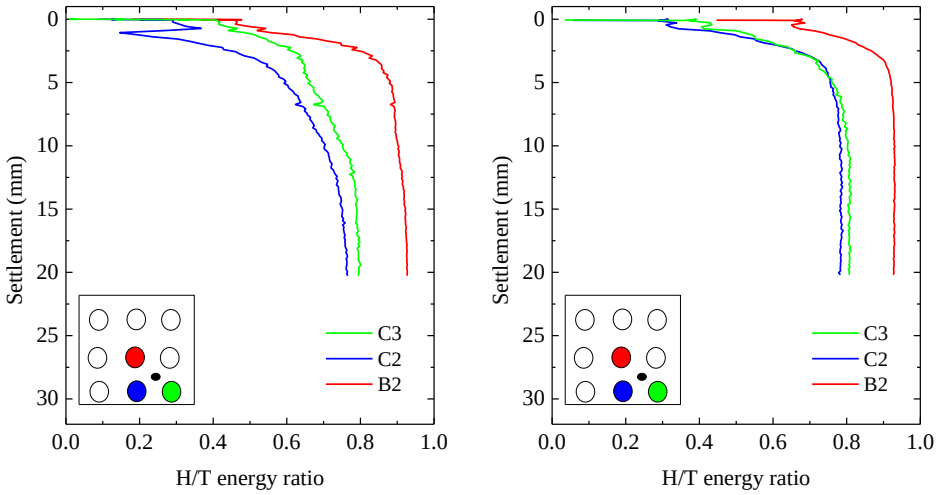

(a) 1st group loading (b) 2nd group loading

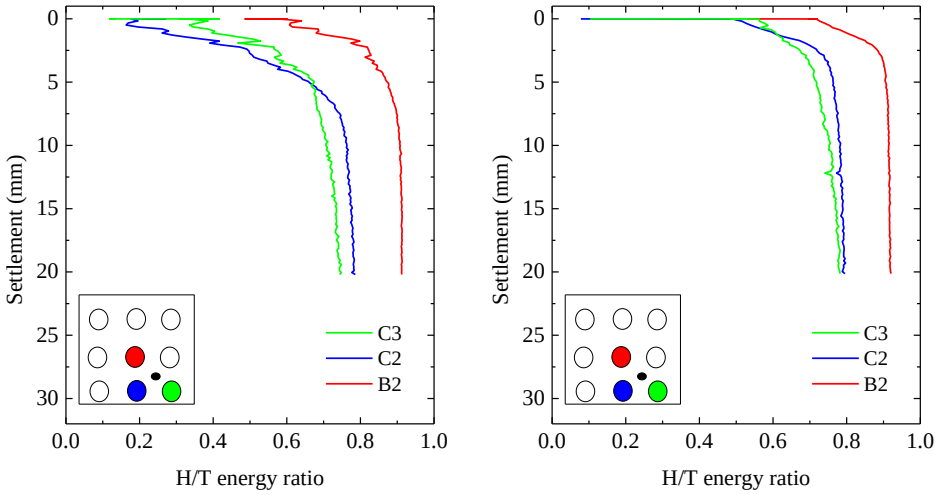

(c) 4th group loading (d) 5th group loading

Figure 8.16 Ratio of high-pass AE energy to the total AE energy

8.3.2.3 Secant Modulus and AE Behavior

Figure 8.18 exhibits the relationship between loading step and the secant modulus of all piles during 2.5D group loading. The secant modulus increased with the loading step (decreased after individual load). Note that the modulus in case of 2.5D was smaller than 5D conditions during the same loading step (compared with 5D case shown in Figure 8.9). A notable feature from Figure 8.18 is that the modulus of the center pile becomes greater than that of other piles after group loading (2nd and 5th).

However, for the 4th group loading which was performed after individual loading, the center pile showed no higher secant modulus. In other words, only the group loading following another group loading showed the pile location effects. This observation suggests that this kind of the interaction in group pile was caused not only by the current loading condition but also by the history of loading. The specific grain fabric which developed during the previous loading affects the modulus in the subsequent step.

Figure 8.19 shows the secant modulus of the three AE monitored piles and a similar trend can be observed compared with the other piles plotted in Figure 8.18.

A comparison of the secant modulus results in case of 2.5D with Aoyama et al. (2015) was shown in Figure 8.17. The missing steps in the figure were individual loadings. The value of the secant modulus showed reasonable consistence with the previous results. Particularly, higher value of the secant modulus was observed from both cases after group loading, and this phenomenon disappeared after individual loading.

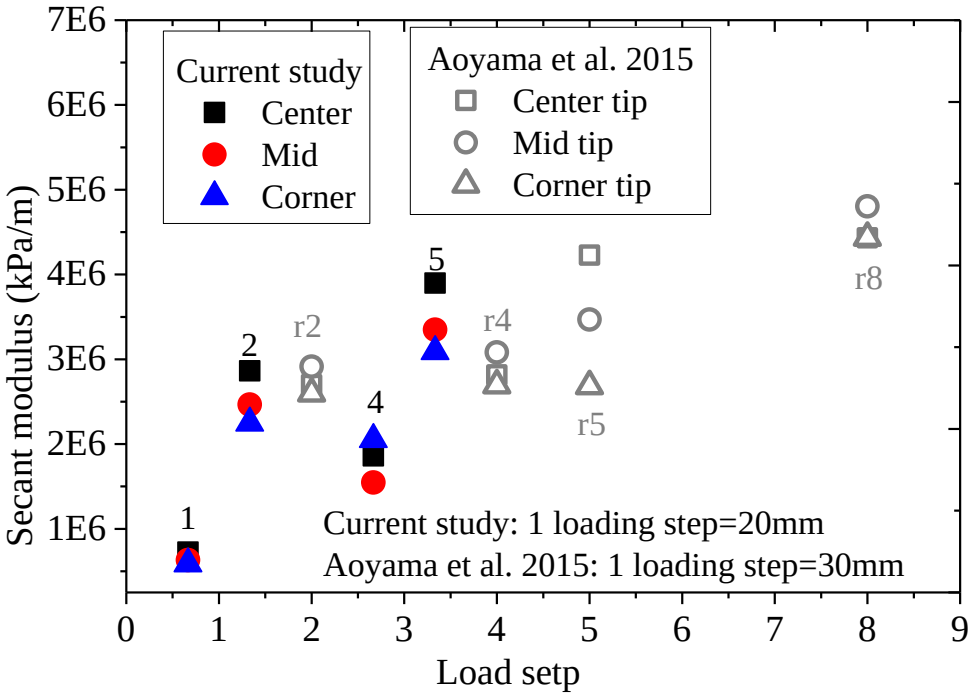

Figure 8.17 Comparison of secant modulus with Aoyama et al. (2.5D)

The AE energy rate for 2.5D group pile was shown in Figure 8.20. It can be seen that the AE from center pile was substantially higher than the other piles for all loading steps. On the whole, the effect of individual loading was not obvious in view of AE, and limited effect can be seen from middle and corner piles, where the two piles showed some difference after individual loading.

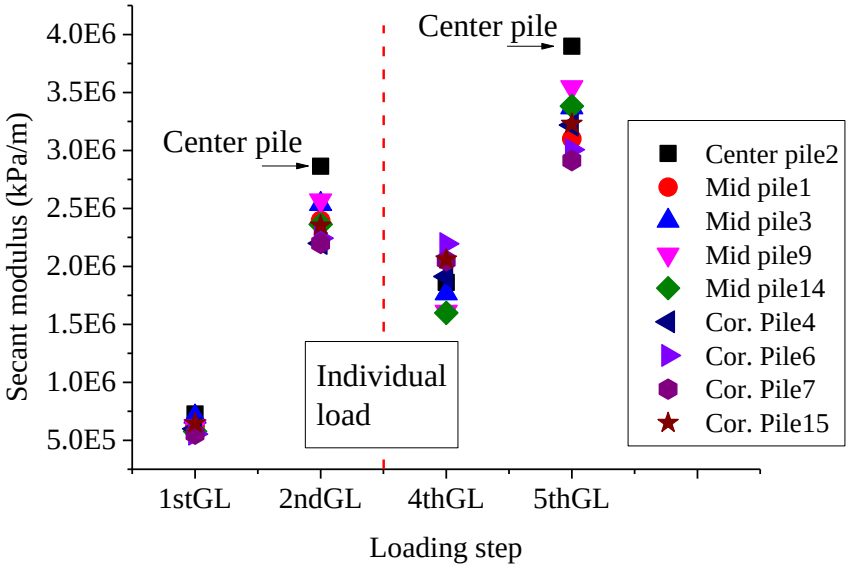

Figure 8.18 Secant modulus of all piles in group during 2.5D group loading

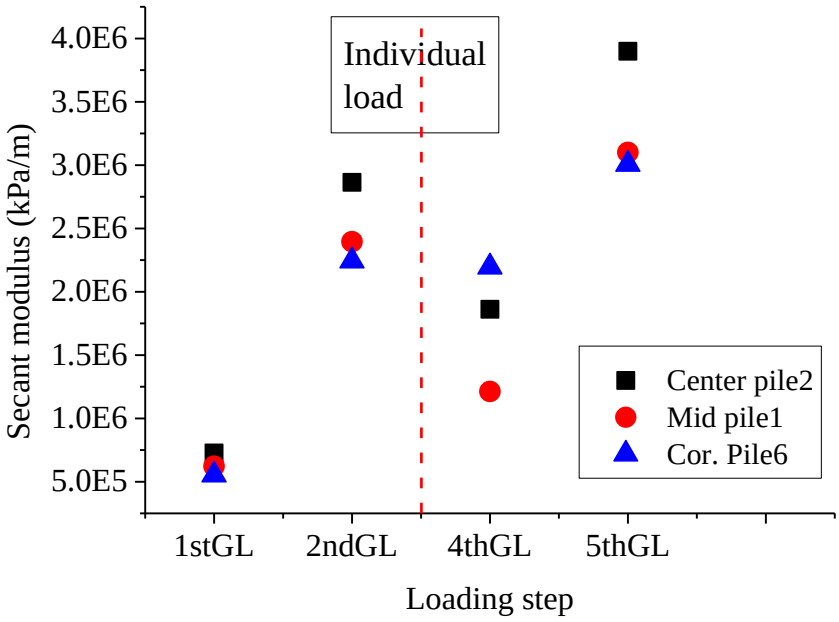

Figure 8.19 Secant modulus of the three piles monitored with AE

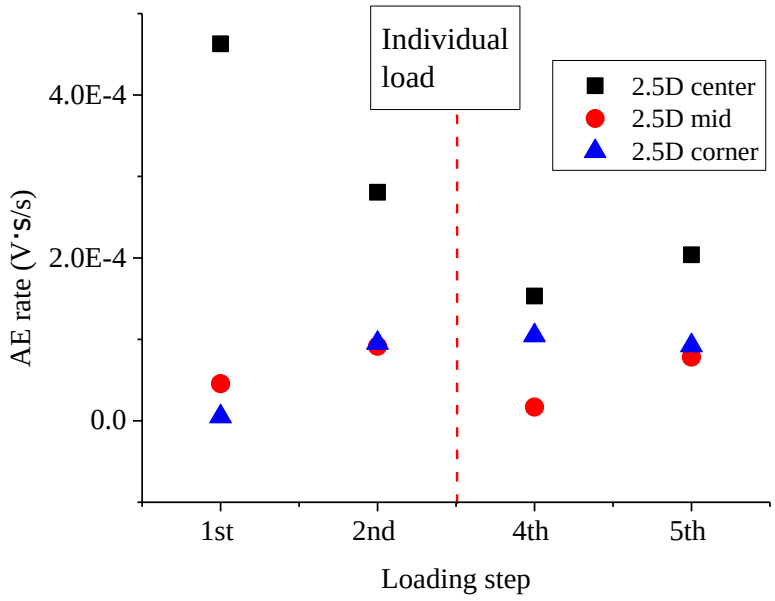

Figure 8.20 AE energy increasing rate during 0.5-1mm group pile penetration

8.4. SUMMARY

This chapter summarizes the test results of AE monitoring in 5D and 2.5D group pile loading tests. Three piles representing center, middle and corner positons were monitored with AE. The evolution of AE activity, ratio of high-pass signal energy during group pile penetration were revealed. The feature of AE rising rate during the 0.5-1mm pile penetration was compared with the secant modulus of the piles. It is generally found that the group pile in case of narrow spacing may significantly reduce the stiffness of the ground, since lower secant modulus was observed in case of 2.5D group pile. The effect of individual loading on the behavior of group pile can be clearly identified in 2.5D group pile, while not significant in 5D group pile, suggesting that a narrower spacing may result in stronger subsoil interaction. However, such effect is not significant in view of AE monitoring.

8.5. REFERENCES

Aoyama, S., Mao, W., Goto, S., & Towhata, I. (2015) Application of advanced procedures to model tests on the subsoil behavior under vertical loading of group pile in Sand. Published online. Indian Geotechnical Journal.

Comodromos, E. M., Papadopoulou, M. C., & Rentzeperis, I. K. (2009). Pile foundation analysis and design using experimental data and 3-D numerical analysis. Computers and Geotechnics, 36(5), 819-836.

Lee, C. Y. (1993). Settlement of pile groups-practical approach. Journal of Geotechnical Engineering, 119(9), 1449-1461.

Lee, S. H., & Chung, C. K. (2005). An experimental study of the interaction of vertically loaded pile groups in sand. Canadian geotechnical journal, 42(5), 1485-1493.

Leung, Y. F., Klar, A., & Soga, K. (2009). Theoretical study on pile length optimization of pile groups and piled rafts. Journal of geotechnical and geoenvironmental engineering, 136(2), 319-330.

Poulos, H. G. (1988). Modified calculation of pile-group settlement interaction. Journal of geotechnical engineering, 114(6), 697-706.

Rollins, K. M., Lane, J. D., & Gerber, T. M. (2005). Measured and computed lateral response of a pile group in sand. Journal of Geotechnical and Geoenvironmental Engineering.

Vesic, A. S. (1969) Experiments with Instrumented Pile Groups in Sand, Performance of Deep Foundations, ASTM STP444, 177-222.

Whitaker, T. (1957). Experiments with Model Piles in Groups*. Geotechnique, 7(4), 147-167.

Zhang, H. H., & Small, J. C. (2000). Analysis of capped pile groups subjected to horizontal and vertical loads. Computers and Geotechnics, 26(1), 1-21.

CHAPTER 9

CONCLUSIONS & RECOMMENDATIONS

9.1. INTRODUCTION

Nowadays, pile foundations has been well developed in modern infrastructure constructions. However, the underlying bearing mechanism of pile foundations is still a subject of great uncertain. A crucial process to work this out is via clarifying the subsoil behavior subjected to pile loading. Conventional studies focus on the macro scale investigation of piles based on load-settlement analysis, which is doomed to provide a compendium of information. As an attempt to overcome such limitations, the current study used the acoustic emission technique aiming to capture the microscale stress/strain variations.

Laboratory investigations were conducted through pile penetration tests with AE instrumentation. The activity of AE accompanied with pile penetration was revealed. Further insights into particle crushing were realized by FFT analysis, which characterized the signal source mechanism. The positions of AE source were localized to image the subsoil behavior. Major conclusions derived from these studies are summarized in the following section.

9.2. CONCLUSIONS

9.2.1 AE Evolution

(a) The process of pile penetration was highly distinguished by AE activities. The evolution tendency of the AE count, AE amplitude and AE energy showed high similarity with load-settlement curves. The AE at the beginning of the

pile penetrating was relatively low, followed by a rapid rising period and eventually became relatively constant.

(b) The yield settlements obtained from both load and AE data were close. Considering that the yielding of the soil is closely related to the release of irrecoverable energy, therefore, the use of AE energy measurement for yielding determination seems reasonable. This suggests a new method of studying the yielding of soil other than the traditional stress-strain-based method.

(c) In generally, dense ground was more emissive than loose ground. However, under sequential loading conditions, despite the subsoil generally became denser, the AE energy dropped after each loading step in dense case. By contrast, loose ground showed significant increment from the 1st to 2nd-loading, and turned to be relatively constant from the 3rd~5th loading cycles. It suggested that the loose ground turned to behave like dense ground after being densified by the previous loading steps.

(d) Apart from the density effect, it is believed that the dislocations of sand particles in the shear zone resulted in better arrangement and directivity, which decreased the AE activity within this zone during the latter sequential loadings. The effect of dilatancy may also attribute to the decreased AE activity in dense case.

9.2.2 Particle Crushing

(a) The spectra of AE originated from the fracture failure of the particles exhibited a significant rising of high frequency components (>100 kHz). The dominant frequency distributions during single particle crushing process showed that high frequency components were mostly observed when the stress level was high, especially when there was an obvious decreasing in bearing load. This suggests a profound correlation between particle fragmentation and high frequency AEs.

(b) The AE signals originated from sliding generally dominated by low frequency components.

(c) The activity of high-pass (>100 kHz) signals corresponding to sand crushing showed similar tendency compared with that of total AE during pile penetration.

(d) Sand crushing occurred throughout the pile penetration process, and became significant after the ground yielding. Since the ground is characterized by shear deformation along the shear zone after initial yielding, the continuation of sand crushing AE events is in accordance with previous studies that sand particles are more prone to crushing under shear than compression.

(e) Dense ground was subjected to more crushing. This is evidenced by both AE analysis and GSD analysis.

9.2.3 AE Source Location

(a) Automatic signal arrival time determination method was developed based on AR-AIC model; AE source location algorithm was developed based on TDOA.

(b) AE sources were not uniformly distributed below the pile tip, but concentrated within a limited region about 0.5-1D below pile tip.

(c) The distribution of AE source in case of dense and loose ground showed significant difference. Dense ground was more concentrated, while loose ground was more scattered.

(d) AE sources in coral sand were distributed within a more limited region, suggesting a higher level of stress concentration

(e) Microscopic observation of subsoil below pile tip after tests showed that the sand crushing mostly occurred in the shear zone. In the compression zone immediately below the pile tip, the crushing was not significant. The lower limit of sand crushing located approximately 1D below the pile tip. This is consistent with AE source concentration results.

9.2.4 AE in Group Pile Monitoring

(a) The center pile in case of 2.5D group pile showed much higher level of AE activity compared with the corner and middle pile While in case of 5D group pile, the center pile showed no obvious difference compared with the other piles. This suggests greater interactions between piles in case of narrower pile spacing.

(b) The effect of individual loading on the group pile behaviors was evident in view of secant modulus for 2.5D group pile. Center pile exhibited higher value of secant modulus after group loading. Such feature disappeared after the disturbance of individual loading, and reappeared after subsequent group loading. However, in view of AE, the effect of individual loading is not well revealed, always higher AE observed in center pile. For 5D group pile, the variation of secant modulus was less significant in view of both load-settlement and AE behaviors, and center pile showed no notable difference of AE activity.

(c) The high-pass AE ratio in case of 5D group turned to be similar among different pile positons. By contrast, center pile always showed much higher ratio of high-pass AE in case of 2.5D group pile, suggesting greater pile interaction lead to higher crushing possibility.

9.3. RECOMMENDATIONS FOR FUTURE RESEARCH

Due to the limitation of time, apparatus and the scope of the current study, the finding of this study may be further extended in several aspects. Some recommendations for future researches are summarized below;

(a) The scope of present study was limited to dry sand only. This can be expanded to other aspects which may better represent the in-situ ground conditions, such as anisotropy, water content effect and wave attenuation.

(b) The idea of sand stream and resultant sand crushing mechanism revealed herein is derived from indirect analysis based on AE activity and its locations. Validity of said findings in actual pile penetration conditions is yet to be proved by a more direct observation method.

(c) The sensors used for AE source location in the present study only responded to limited range of frequency. Future studies may use more broad-band AE sensors so that the high frequency AE sources can be localized accurately. And consequently, the locations of sand crushing can be better identified.

(d) The wave velocity used in the AE source location was assumed to be constant. This may not consistent with the real situation. Future study may consider

variable values of wave velocity, e.g. by using AE data from more than five channels and treating wave velocity as unknown.

(e) The characteristics of subsoil behaviors revealed in the current study including extent of crushing as well as the location of crushing can be further utilized to modify the traditionally developed pile bearing theories, e.g. the cavity expansion theory, to achieve a better prediction of the pile bearing capacity.

Appendix 1

LabView VI for splitting a large file into small files

(In courtesy of Jie Zheng, National Instruments Corporation)

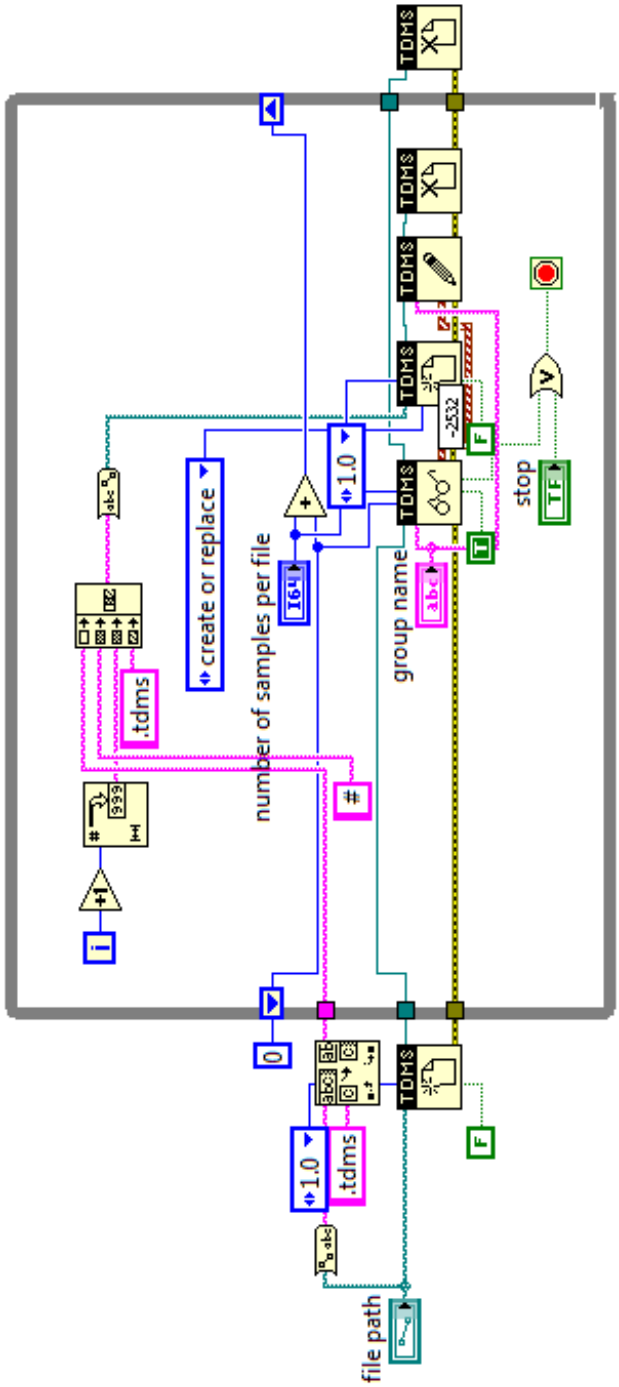

Appendix 2
MATLAB code to load *.tdms file

```
% --function read_in_tdms_file-----------------------------

%Recreate needed property constants defined in nilibddc_m.h
DDC_FILE_NAME                       =     'name';
DDC_FILE_DESCRIPTION                =     'description';
DDC_FILE_TITLE                      =     'title';
DDC_FILE_AUTHOR                     =     'author';
DDC_FILE_DATETIME                   =     'datetime';
DDC_CHANNELGROUP_NAME               =     'name';
DDC_CHANNELGROUP_DESCRIPTION        =     'description';
DDC_CHANNEL_NAME                    =     'name';

%Check if the paths to 'nilibddc.dll' and 'nilibddc_m.h' have been
%selected. If not, prompt the user to browse to each of the files.
if exist('NI_TDM_DLL_Path','var')==0
      [dllfile,dllfolder]=uigetfile('*dll','Select nilibddc.dll');
      libname=strtok(dllfile,'.');
      NI_TDM_DLL_Path=fullfile(dllfolder,dllfile);
end
if exist('NI_TDM_H_Path','var')==0
      [hfile,hfolder]=uigetfile('*h','Select nilibddc_m.h');
      NI_TDM_H_Path=fullfile(hfolder,hfile);
end

%Prompt the user to browse to the path of the TDM or TDMS file to read

%Load nilibddc.dll (Always call 'unloadlibrary(libname)' after finished using the library)
loadlibrary(NI_TDM_DLL_Path,NI_TDM_H_Path);

%Open the file (Always call 'DDC_CloseFile' when you are finished using a file)
fileIn = 0;
[err,dummyVar,dummyVar,file]=calllib(libname,'DDC_OpenFileEx',Data_Path,'',1,fileIn);

%Read and display file name property
filenamelenIn = 0;
%Get the length of the 'DDC_FILE_NAME' string property
[err,dummyVar,filenamelen]=calllib(libname,'DDC_GetFileStringPropertyLength',file,DDC_FILE_NAME,fi
lenamelenIn);
if err==0 %Only proceed if the property is found
      %Initialize a string to the length of the property value
      pfilename=libpointer('stringPtr',blanks(filenamelen));

[err,dummyVar,filename]=calllib(libname,'DDC_GetFileProperty',file,DDC_FILE_NAME,pfilename,filenam
elen+1);
      setdatatype(filename,'int8Ptr',1,filenamelen);
      disp(['File Name: ' char(filename.Value)]);
```

```
end

%Read and display file description property
filedesclenIn = 0;
%Get the length of the 'DDC_FILE_DESCRIPTION' string property
[err,dummyVar,filedesclen]=calllib(libname,'DDC_GetFileStringPropertyLength',file,DDC_FILE_DESCRIP
TION,filedesclenIn);
if err==0 %Only proceed if the property is found
    %Initialize a string to the length of the property value
    pfiledesc=libpointer('stringPtr',blanks(filedesclen));

[err,dummyVar,filedesc]=calllib(libname,'DDC_GetFileProperty',file,DDC_FILE_DESCRIPTION,pfiledesc,
filedesclen+1);
    setdatatype(filedesc,'int8Ptr',1,filedesclen);
    disp(['File Description: ' char(filedesc.Value)]);
end

%Read and display file title property
filetitlelenIn = 0;
%Get the length of the 'DDC_FILE_TITLE' string property
[err,dummyVar,filetitlelen]=calllib(libname,'DDC_GetFileStringPropertyLength',file,DDC_FILE_TITLE,file
titlelenIn);
if err==0 %Only proceed if the property is found
    %Initialize a string to the length of the property value
    pfiletitle=libpointer('stringPtr',blanks(filetitlelen));

[err,dummyVar,filetitle]=calllib(libname,'DDC_GetFileProperty',file,DDC_FILE_TITLE,pfiletitle,filetitlelen
+1);
    setdatatype(filetitle,'int8Ptr',1,filetitlelen);
    disp(['File Title: ' char(filetitle.Value)]);
end

%Read and display file author property
fileauthlenIn = 0;
%Get the length of the 'DDC_FILE_AUTHOR' string property
[err,dummyVar,fileauthlen]=calllib(libname,'DDC_GetFileStringPropertyLength',file,DDC_FILE_AUTHOR,
fileauthlenIn);
if err==0 %Only proceed if the property is found
    %Initialize a string to the length of the property value
    pfileauth=libpointer('stringPtr',blanks(fileauthlen));

[err,dummyVar,fileauth]=calllib(libname,'DDC_GetFileProperty',file,DDC_FILE_AUTHOR,pfileauth,fileaut
hlen+1);
    setdatatype(fileauth,'int8Ptr',1,fileauthlen);
    disp(['File Author: ' char(fileauth.Value)]);
end

%Read and display file timestamp property
yearIn = 0;
monthIn = 0;
dayIn = 0;
hourIn = 0;
```

```
minuteIn = 0;
secondIn = 0;
msecondIn = 0;
wkdayIn = 0;
[err,dummyVar,year,month,day,hour,minute,second,msecond,wkday]=calllib(libname,'DDC_GetFileProperty
TimestampComponents',file,DDC_FILE_DATETIME,yearIn,monthIn,dayIn,hourIn,minuteIn,secondIn,msec
ondIn,wkdayIn);
if err==0 %Only proceed if the property is found
    disp(['File Timestamp: ' num2str(month) '/' num2str(day) '/' num2str(year) ', ' num2str(hour) ':'
num2str(minute) ':' num2str(second) ':' num2str(msecond)]);
end

%Get channel groups
%Get the number of channel groups
numgrpsIn = 0;
[err,numgrps]=calllib(libname,'DDC_GetNumChannelGroups',file,numgrpsIn);
%Get channel groups only if the number of channel groups is greater than zero
if numgrps>0
    %Initialize an array to hold the desired number of groups
    pgrps=libpointer('int64Ptr',zeros(1,numgrps));
    [err,grps]=calllib(libname,'DDC_GetChannelGroups',file,pgrps,numgrps);
end
for i=1:numgrps %For each channel group
    %Get channel group name property
    grpnamelenIn = 0;

[err,dummyVar,grpnamelen]=calllib(libname,'DDC_GetChannelGroupStringPropertyLength',grps(i),DDC_C
HANNELGROUP_NAME,grpnamelenIn);
    if err==0 %Only proceed if the property is found
        %Initialize a string to the length of the property value
        pgrpname=libpointer('stringPtr',blanks(grpnamelen));

[err,dummyVar,grpname]=calllib(libname,'DDC_GetChannelGroupProperty',grps(i),DDC_CHANNELGRO
UP_NAME,pgrpname,grpnamelen+1);
        setdatatype(grpname,'int8Ptr',1,grpnamelen);
    else
        grpname=libpointer('stringPtr','');
    end

    %Get channel group description property
    grpdesclenIn = 0;

[err,dummyVar,grpdesclen]=calllib(libname,'DDC_GetChannelGroupStringPropertyLength',grps(i),DDC_C
HANNELGROUP_DESCRIPTION,grpdesclenIn);
    if err==0 %Only proceed if the property is found
        %Initialize a string to the length of the property value
        pgrpdesc=libpointer('stringPtr',blanks(grpdesclen));

[err,dummyVar,grpdesc]=calllib(libname,'DDC_GetChannelGroupProperty',grps(i),DDC_CHANNELGROU
P_DESCRIPTION,pgrpdesc,grpdesclen+1);
    end
```

```
    % figure('Name',char(grpname.Value));
     %hold on;

     %Get channels
     numchansIn = 0;
     %Get the number of channels in this channel group
     [err,numchans]=calllib(libname,'DDC_GetNumChannels',grps(i),numchansIn);
     %Get channels only if the number of channels is greater than zero
     if numchans>0
          %Initialize an array to hold the desired number of channels
          pchans=libpointer('int64Ptr',zeros(1,numchans));
          [err,chans]=calllib(libname,'DDC_GetChannels',grps(i),pchans,numchans);
     end

     channames=cell(1,numchans);

     for j=1:numchans %For each channel in the channel group
          %Get channel name property
          channamelenIn = 0;

[err,dummyVar,channamelen]=calllib(libname,'DDC_GetChannelStringPropertyLength',chans(j),DDC_CHA
NNEL_NAME,channamelenIn);
          if err==0 %Only proceed if the property is found
               %Initialize a string to the length of the property value
               pchanname=libpointer('stringPtr',blanks(channamelen));

[err,dummyVar,channame]=calllib(libname,'DDC_GetChannelProperty',chans(j),DDC_CHANNEL_NAME,
pchanname,channamelen+1);
               setdatatype(channame,'int8Ptr',1,channamelen);
               channames{j}=char(channame.Value);
          else
               channames{j}='';
          end
          %Get channel data type
          typeIn = 0;
          [err,type]=calllib(libname,'DDC_GetDataType',chans(j),typeIn);

          %Get channel values if data type of channel is double (DDC_Double = 10)
          if strcmp(type,'DDC_Double')
               numvalsIn = 0;
               [err,numvals]=calllib(libname,'DDC_GetNumDataValues',chans(j),numvalsIn);
               %Initialize an array to hold the desired number of values
               pvals=libpointer('doublePtr',zeros(1,numvals));
               [err,vals]=calllib(libname,'DDC_GetDataValues',chans(j),0,numvals,pvals);
               setdatatype(vals,'doublePtr',1,numvals);

               %Add channel values to a matrix. The comment, #ok<AGROW>, at
               %the end of the line prevents warnings about the matrix needing
               %to allocate more memory for the added values.
               chanvals(:,j)=(vals.Value);
```

```
            end

        end
        %% data input from here


%Close file
err = calllib(libname,'DDC_CloseFile',file);

%Unload nilibddc.dll
unloadlibrary(libname);
```

Reference:
www.ni.com